BIOMIMETIC ZWITTERIONIC SULFOBETAINE POLYMERS AS FUNCTIONAL BIOINTERFACES

Zur Erlangung des akademischen Grades eines

DOKTORS DER INGENIEURWISSENSCHAFTEN
(Dr.-Ing.)

Von der KIT-Fakultät für Chemieingenieurwesen und Verfahrenstechnik
des Karlsruher Instituts für Technologie (KIT)
genehmigte

DISSERTATION

von

M.S. **Gowthamy Venkidasubramonian**
aus Thirunelveli, Indien

Erstgutachter: Prof. Dr.-Ing Matthias Franzreb

Zweitgutachter: Prof. Dr. Jörg Lahann

Tag der mündlichen Prüfung: 11.12.2018

Die vorliegende Arbeit wurde unter der Leitung von Prof. Dr. Jörg Lahann von Februar 2014 bis Dezember 2018 am Institut für Funktionelle Grenzflächen des Karlsruher Instituts für Technologie (KIT) durchgeführt.

Hiermit erkläre ich, die vorliegende Arbeit selbständig verfasst und keine anderen als die angegebenen Quellen und Hilfsmittel verwendet sowie Zitate kenntlich gemacht zu haben.

Die Dissertation wurde bisher an keiner anderen Hochschule oder Universität eingereict.

Out of purity and silence come the words of power

Swami Chinmayananda

People will forget what you said, people will forget what you did, but people will never forget how you made them feel

Maya Angelou

Dedicated to my mother Nalini

You are my strength

ACKNOWLEDGEMENTS

I would like to thank everyone who helped and supported me during the most stressful but the most rewarding chapter of my life. First and foremost, I would like to thank my advisor Prof. Dr. Jörg Lahann, who not only accepted me into his lab, but also believed in my potential even at times when I did not. The confidence he placed in me has pushed me through some of the darkest moments of my life. I have been very fortunate to have worked with him, he cheered me on through my personal difficulties and patiently waited for me to find myself, even though I began my journey later than most people in life and was going through the most tumultuous personal crises. His deep thinking, sharp wit and wisdom helped guide me over the years. His trust and optimism, and his subtle ways of bringing me back on track when I strayed has made me a better scientist. His persistent support for me pushed me harder to succeed. I am very grateful and humbled to work with someone with a brilliantly critical mind, and an equally generous and empathetic human being.

Further, I would like to thank Prof. Dr. Matthias Franzreb for his valuable time, useful suggestions, mentoring and support for my research projects. I am grateful to my former colleague Dr. Sahar Rahmani for having my best interests at heart, and for taking the time to give me feedback, advice, care and love, regardless of the time of day. She has been a friend, mentor, critic and more, and she has helped me grow both personally and professionally.

Again, my successes as a graduate student cannot be solely attributed to the work that I performed by myself, but many thanks must be given to all the collaborators I had during my time here. I must thank all my collaborators – Prof. Paul Krebsbach, and his lab members Dr. Tuğba Topal and Dr. Xu Qian, each provided me with technical expertise in pluripotent stem cell culture that were critical to numerous portions of this dissertation. A special thanks to Tuğba for her unwavering friendship and support. She spent many hours working on the cell culture studies on the IGT-modified substrates. Hematopoietic stem cell culture and analyses was performed by Dr. Lisa Rödling. Many thanks also need to be extended to Dr. Nicolas Zydziak for the vast amount

of intellectual contributions towards my work. Prof. Jürgen Hubbuch, including Dr. Josephine Morgenstein, must also be thanked for providing me with the opportunity to work on new protein-polymer conjugates which were not included in this dissertation.

Birgit Huber deserve much more than this simple mention, for the hard work she put into providing me the SEC data whenever I asked for it. Vanessa Trouillet has been a huge source of support and insight for her role in XPS. ToF-SIMS analysis was done by Dr. Alexander Welle at Institute for Applied Materials – Energy Storage System (IAM-ESS), KIT. Dr. Christoph Hussal, Dr. Domenic Kratzer, Fabian Becker and Dr. Mirella Wawryszyn helped with the synthesis of the various paracyclophanes.

While there were many contributors to my work, the members of the Lahann Lab at Karlsruhe Institute of Technology and University of Michigan, Ann Arbor, have not only helped me develop my research, but they were also fantastic friends that made the lab my home away from home. Dr. Aftin Ross, Dr. Thomas Eyster, Dr. Jaewon Yoon, Dr. Xiaopei Deng, Dr. Asish Misra and Dr. Kenneth Cheng went out of their way to teach me and help me start my own journey. Dr. Ramya Kumar worked on the zeta potential measurements, and I would like to thank her for countless hours of discussion, and all her help when I was in Michigan. Dr. Domenic Kratzer was my mentor during my first few months of research in KIT. He made me feel welcome in a foreign country and taught me a lot of what I know about organic and polymer chemistry. He put up with a lot of questions from me in my first years here, and I cannot thank him enough for his patience and guidance through these years. I thank him for being my family in Karlsruhe. My undergrads Jonathan and Enrique have been a joy to work with. Both were instrumental in providing CVD coatings for me, without which this dissertation would not have happened.

My research also benefitted from other members of the Lahann Lab who were not directly involved in my projects. I would like to thank Dr. Mirella Wawryszyn, Dr. Azam Jeihanipour, Dr. Artak Shahnas and Dr. Denise Paula de Cunha for their tremendous help, insightful discussions and friendship along the way. What makes them stand out from other lab members is that they helped the lab feel like a family, which made me look forward to every day I went to work. I am also thankful to Dr. Amit Sitt, who became a mentor in the short amount of time he was here. I am also thankful for getting to know Dr. Jake Jordahl, Dr. Stacy Ramcharan, Dr. Sangyeul Hwang,

Dr. Hakan Durmaz, Dr. Jan Weiß, Fabian Becker, Marvin Kleiber and Hyesun Jun who all helped make my time in the Lahann Lab a great experience.

The administrative staff Astrid, Steffie, Annette and Angela deserve special thanks, for providing the comprehensive and most dedicated help with administration at Institute of Functional Interfaces (IFG).

I dedicate this degree, firstly, to my family – my parents, my brother Shravan, my husband Bala, Deepak anna, Anusha and Anvi, the newest member of our family. Their motivating words, unwavering support and motivation throughout this PhD, having stood by me despite being far away, for their encouragement to work harder, and their unconditional love are what made the difference. I am grateful for the friendship and camaraderie of Dr. Divya Varadharajan, for her direction and expertise regarding polymer science, and for her motivation which was invaluable. I am indebted to Aswathi, Harsha, Sandeep and Siva for the support, encouragement, laughter, countless dinners and movies. A special mention to Celina, Ann Katherine and Katharina for welcoming me into their hearts. My best friends Laks, Shradz, Krithi, KK, Cherry, Venkat and Neeti kept reminding me who I was. Kalpana, Bhawna, Nagashree, Dr. Ravi Peravalli, Meenal and Fritz kept me grounded and connected to my roots. I am forever grateful to Meera akka and Mani Sir for providing me a home, comforts, love and treating me like their daughter.

I wonder whether I could have paced myself more wisely and whether I could have somehow exceeded my limits. This PhD journey has taught me to be friends with adversities, and take away wisdom, courage and experience. As I move on to the next phase of my life, I know that the journey is important and not the destination. There are still miles to go before I sleep.

TABLE OF CONTENTS

ABSTRACT

Human pluripotent stem cells (hPSC) self-renew and differentiate extensively, bringing unprecedented opportunities for research in the field of regenerative medicine. To tap into such potential, the development of biocompatible polymer brushes as human stem cell culture platforms that closely mimic the biological milieu is vital to grow these cells *in vitro*. This dissertation focuses on developing biomimetic zwitterionic sulfobetaine polymer brush systems with tunable material properties, in relation to hPSC adhesion and proliferation. For this purpose, chemical vapor deposition (CVD) polymerization was first used to obtain functionalized substrates, followed by "grafting-from" and "grafting-to" methods to graft polymer brushes on these substrates, encompassing controllable thickness, wettability, and surface roughness.

Alkyne functionalized coatings prepared by CVD polymerization were generated to introduce reversible addition-fragmentation chain transfer (RAFT) agents with a clickable azide group via metal-free click reactions. Biomimetic polymer brushes, poly[2-(methacryloyloxy)ethyl dimethyl-(3-sulfopropyl) ammonium hydroxide] (PMEDSAH), were grown from these surfaces using a "grafting-from" approach to obtain polymer brushes up to 20 nm thick, and surface roughness of 3.6 nm possessing high wettability were achieved.

Further, for the first time, a modular molecular polymer brush system called interfacial Gemini transformers (IGT) containing a central benzaldehyde group flanked by zwitterionic sulfobetaine polymer segments on either side were designed and synthesized for the growth of human embryonic stem cells (hESC) *in vitro*. They were immobilized on functional coatings made via CVD polymerization using a "grafting-to" approach. IGTs with different molar masses exhibited tunable surface thickness and surface charge. These IGT-modified substrates were suitable for the adhesion and subsequent proliferation of hESC in an undifferentiated state. In addition, spatially controlled immobilization of IGT using microcontact printing on substrates coated with reactive functional coatings resulted in controlled protein deposition with spatiotemporal control. Thus, biomimetic zwitterionic polymer brush systems were developed to be used for biomedical applications and regenerative medicine due to their unique structure-property relationship and scalability potential.

KURZZUSAMMENFASSUNG

Humane pluripotente Stammzellen (hPSC) besitzen die Fähigkeit zur Selbsterneuerung und können darüber hinaus in alle möglichen Zelltypen differenzieren. Aus diesen Gründen bieten hPSCs beispiellose Anwendungsmöglichkeiten auf dem Gebiet der regenerativen Medizin. Die vollständige Ausnutzung dieses Potenzials erfordert neue Techniken der in vitro Kultivierung um Kontrolle über Differenzierung und Proliferation der Zellen zu erhalten. Zu diesem Zweck kommen unter anderem biokompatible Polymerbeschichtungen als Kulturplattformen zum Einsatz, welche das native Milieu der Zellen so gut wie möglich nachahmen sollen. Diese Dissertation konzentriert sich auf die Entwicklung entsprechender biomimetischer Polymerbeschichtungen auf Basis von Sulfobetainen, welche abstimmbare Materialeigenschaften in Bezug auf hPSC-Adhäsion und Proliferation aufweisen sollen. Dazu wurde zunächst die CVD-Polymerisation (Chemical Vapor Deposition) angewendet um funktionalisierte, reaktive Substrate zu erhalten. Diese wurden im Folgenden mittels "*grafting-from*" und "*grafting-to*" Methoden modifiziert, um Polysulfobetain-schichten auf diesen Substraten anzubringen, welche eine Kontrolle im Hinblick auf Schichtdicke, Benetzbarkeit und Oberflächenrauhigkeit erlauben.

Mittels der CVD-Polymerisation wurden Alkin-funktionalisierte Beschichtungen hergestellt, um anschließend ein RAFT-Agenz (Reversible-Additions-Fragmentierungs-Kettenübertragung) mit einer klickbaren Azidgruppe über eine metallfreie Klickreaktionen anzubinden. Aus diesen Oberflächen wurden biomimetische Polymerbeschichtungen, bestehend aus Poly[2-(Methacryloyl-oxy)ethyldimethyl-(3-sulfopropyl)ammoniumhydroxid] (PMEDSAH) mittels eines "*grafting-from*"-Ansatzes hergestellt. Dadurch konnten Polymerbesichtungen mit einer Schichtdicke von bis zu 20 nm und einer Oberflächenrauhigkeit von 3,6 nm mit hoher Benetzbarkeit in kontrollierter Art und Weise hergestellt werden.

Darüber hinaus wurde erstmals ein modulares, molekulares System zur Polymerbeschichtung mit dem Namen *Interfacial Gemini Transformers* (IGT) entwickelt um das Wachstum humaner embryonaler Stammzellen (hESC) auf künstlichen Substraten zu ermöglichen. Dabei handelt es sich um Makromoleküle, bei denen eine zentrale Benzaldehydgruppe auf beiden Seiten von zwitterionischen Polysulfobetainsegmenten flankiert wird. Diese Segmente wurden nach ihrer

Synthese auf funktionellen CVD-Beschichtungen mittels einer "*grafting-to*"-Methode immobilisiert. Die resultierenden Schichtdicken und Oberflächenladungen konnten über die Molmassen der IGTs gesteuert werden. Diese IGT-modifizierten Substrate waren für die Adhäsion und anschließende Proliferation von hESC in einem undifferenzierten Zustand geeignet. Darüber hinaus führte die räumlich kontrollierte Immobilisierung der IGTs mittels Mikrokontaktdruck zu einer entsprechenden räumlich definierten Proteinabscheidung auf CVD-modifizierten Substraten. Somit wurden biomimetische, zwitterionische Polymerbürstensysteme entwickelt, welche aufgrund ihrer einzigartigen Beziehungen zwischen Struktur und Materialeigenschaften und ihres Skalierbarkeitspotenzials für die Bereiche Biomedizin und Regenerative Medizin ein hohes Anwendungspotential besitzen.

CHAPTER 1 INTRODUCTION

Human pluripotent stem cells (hPSC) can be expanded indefinitely in culture while maintaining the ability to differentiate to all specialized cell types in a manner that parallels aspects of human development.[1–3] Consequently, hPSC offer the opportunity for numerous biomedical applications and to advance the development of cell-based therapies.[4,5] By 2025, the global stem cell market is estimated to reach $15.6 billion, up from $5.2 billion in 2016.[6] However, these applications require large numbers of hPSC-derived cells of high quality.[5] For example, in cell transplantation, ~10^9 cardiomyocytes are required for treating myocardial infarction, ~10^9 insulin-producing β cells for type I diabetes mellitus, and ~10^{10} hepatocytes for hepatic failure.[7] To obtain these large numbers of cells, there is a need to develop simple, efficient, defined, scalable, and good manufacturing practice-compatible culture systems for cell proliferation and harvesting in vitro.[7] The systems must show ease of use and potential scalability, in order to make them suitable for numerous technological applications from the laboratory towards the clinic.

However, to date, high-yield expansion of hPSC has not been possible. Currently, there is a lack of robust, scalable technologies for manufacturing the quantities of cells anticipated to be required for widespread patient access. While large-scale manufacturing of other mammalian cells in bioreactors using industrial processes have been widely demonstrated, high-yield-expansion of hPSC has not been reported. Our limited understanding of process related risks such as cell transformation, that influence hPSC production processes, restrict the strategies at our disposal for resolving these technology gaps.[8] Clinical adoption of stem cells for therapeutic applications is hindered by the availability of culture systems that lack animal products, leading to a host of immunogenic concerns. Furthermore, ideal cell culture substrates would be generated from scalable processes, be compatible with sterilization techniques, display long-term stability, have compatibility with multiple stem cell lines, be relatively inexpensive, and maintain stem cell pluripotency during long-term expansion.[9]

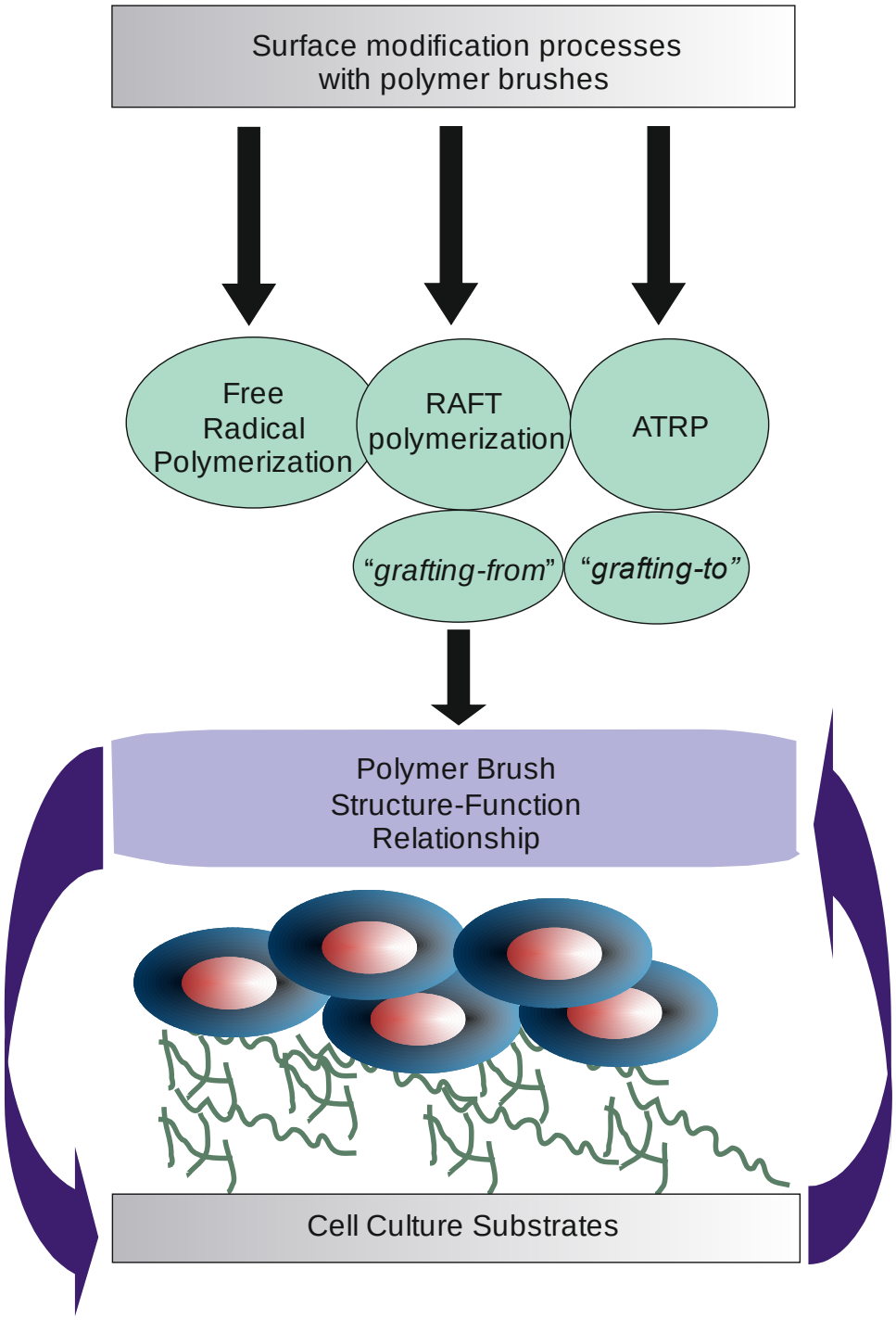

Figure 1.1: Dissertation outline. Biomimetic polymer brushes are synthesized by free radical polymerization and reversible deactivation radical polymerization processes. The surfaces are characterized, and the structure and function of the polymer interfaces are probed. Tunable zwitterionic polymer brushes are then used as model systems to examine the roles of polymer brush architecture and interfacial properties on human pluripotent stem cell-biomaterial interactions.

The aim of this dissertation was, therefore, to develop a chemically defined, scalable and good manufacturing practice-compatible two-dimensional (2D) culture platforms for hPSC expansion *in vitro* and to characterize the interfacial properties of these substrates as schematically represented in Figure 1.1. The engineered substrates had to meet the following requirements:

1. The substrate material developed needs to be consistent, defined, biocompatible, free of xenogeneic components and mimic cell culture environments.

2. The cell culture substrates should be easy to scale up, reproducible and safe.

3. The cell-surface interactions should be understood in detail to optimize defined culture conditions to support hPSC self-renewal. To elucidate the role of the biomaterial on hPSC culture, the physicochemical properties like structure, topography, wettability and elasticity should be tailored.

4. They should maintain and expand the cells in the pluripotent state, and should have the ability to direct cell differentiation into the right phenotypes on cue for potential use in regenerative medicine. Also, multiple hPSC cell types need to be cultured on the substrates.

Firstly, the surfaces (silicon, gold, glass, tissue culture polystyrene (TCPS)) were coated with polymers containing suitable chemical functional anchors. In a subsequent step, biomimetic polymer brushes were either directly grown from these substrates (grafting-from) or were independently synthesized and immobilized on them (grafting-to).

Specifically, polymer brushes were chosen as they provide an attractive functional interface, wherein composition, architecture and polymer functionality can be controlled precisely and independently. Such an optimal stem cell/material interface would allow a dynamic regulation of one another's fate: the cell by remodeling its surroundings, and the material controlling the cell fate through its local physicochemical environment.

Chemical vapor deposition (CVD) is a polymer chemical vapor deposition technique for preparing reactive coatings in substrate independent manner from functional paracyclophane precursors. CVD polymerization method was employed to prepare a polymer coating decorated with functional groups and subsequently modified for the introduction of polymer brushes on the surface. One common technique for effective introduction of such brushes for both grafting-from

and grafting-to approaches is reversible deactivation radical polymerization (RDRP) processes. RDRP is a technique used to synthesize a variety of precise polymers with good control over their molecular weights, dispersity, architecture, as well as their functionality.[10] Subsequently, a strategy was envisioned to combine CVD and RDRP to obtain robust hPSC cell culture substrates.

Strategy 1 (Grafting-from). A polymer coating containing 2-bromoisobutyryl functional groups providing atom transfer radical polymerization (ATRP) initiators was deposited by CVD polymerization. Polymer brushes were then grown from this surface by ATRP.

Strategy 2 (Grafting-from). A polymer coating decorated with activated alkynyl groups[11] was prepared by CVD polymerization and was utilized to immobilize reversible addition-fragmentation chain transfer (RAFT) agents to surfaces in a copper-free click reaction.[12] The controlled polymer brushes were grown from this surface by RAFT polymerization.

Strategy 3 (Grafting-to). A polymer coating decorated with aldehyde groups was prepared by CVD polymerization on the surfaces, and further reacted with a dihydrazide linker. Interfacial Gemini transformer (IGT) was pre-synthesized containing a central reactive aldehyde group, and subsequently covalently attached to the hydrazide moiety exposed at the surface to obtain polymer brushes by the grafting-to approach.

Villa-Diaz *et al.* developed a standardized and fully defined synthetic polymer coating, poly[2-(methacryloyloxy)ethyl dimethyl-(3-sulfopropyl) ammonium hydroxide] (PMEDSAH) by ultraviolet/ozone (UVO)-initiated free radical polymerization, which could sustain the undifferentiated growth of human embryonic stem cell (hESC) and induced pluripotent stem cell (hiPSC) growth in several different culture media, including commercially available defined media for 25 passages.[13,14] However, the molecular mechanisms and the material properties responsible for this support is not evident, and need to be evaluated. Drawing inspiration from these findings and to engineer surfaces with tunable material properties that interact with different kinds of hPSC, the following investigations have been performed on appropriate substrates as described in Sections 4.1-4.5.

1. Multiplication of hematopoietic stem and progenitor cells (HSC), a type of hPSC, *in vitro* with current approaches suffer from limited scalability and are emerging as a bottleneck for clinical applications of these cells. They quickly lose their multipotency and self-renewal capacities in culture because of their fast differentiation. UVO-grafted biomimetic PMEDSAH hydrogel coatings have been found to be effective in sustaining the long-term expansion of hESC and hiPSC. Therefore, Section 4.1 deals with the preparation of PMEDSAH substrates by UVO-initiated free radical polymerization, and Section 4.6.1 deals with the investigation of their ability to adhere and proliferate HSC.

2. UVO-grafting is a free radical polymerization process, which means, the process is not well-controlled, leading to polydisperse PMEDSAH polymer brushes. Widespread clinical applications of stem cells require substrate materials with tunable physical properties.[15] The second objective in this dissertation is to control the composition, architecture and biological functionality of the zwitterionic polymer brushes precisely. Controlling the physicochemical properties by fine-tuning the polymer brush thickness, and in turn, its molar mass, could identify reaction parameters that would yield the optimum cell growth. For that reason, PMEDSAH brushes were introduced on to the functional CVD-coated surfaces using a "grafting-from" approach using ATRP and RAFT polymerization. Then, the possible physicochemical properties were measured, like, thickness, wettability, surface roughness and zwitterionic charge distance, and the information was used to tailor the polymer brushes for biomedical applications. In particular, hPSC cell adhesion on the polymer brushes have been used to understand the structure-property relationships of the biomaterial and guide the tuning of interfacial properties.

3. After growing biomimetic polymer chains from substrate-bound sites through RDRP, the next challenge was to develop engineered biointerfaces for a potentially scalable hPSC cell culture platform. For this, the "grafting-to" approach was used, as it enables the control of substrate physicochemical properties, is relatively inexpensive, and a scalable process. For this, a novel modular molecular system consisting of a small hydrophobic functional segment at the center (benzaldehyde initiator) flanked by zwitterionic polymer segments was synthesized. Such a system was coined interfacial gemini transformer (IGT). The IGT

brushes were covalently grafted onto the vapor-based reactive substrates decorated with surface reactive orthogonal groups by a “grafting-to” approach.

4. The last section focuses on the use of the developed 2D hPSC cell culture platforms for the growth and expansion of hPSC in a defined media. Further, maintenance of pluripotency on the culture surface was investigated. The versatility of the substrates has also been investigated, exploring the advantages of using the developed hPSC cell culture platform over the existing ones.

CHAPTER 2 THEORETICAL BACKGROUND

2.1 Human Pluripotent Stem Cells

Stem cells are defined by their ability to self-renew, which is termed pluripotency, and their potential differentiation into specific tissue types.[16] The two major classes of stem cells are pluripotent stem cells that can become any cell type in the adult body, and adult stem cells that can differentiate to yield some of the population of cells of their tissue of origin. Pluripotent stem cells include embryonic stem cells and induced pluripotent stem cells.

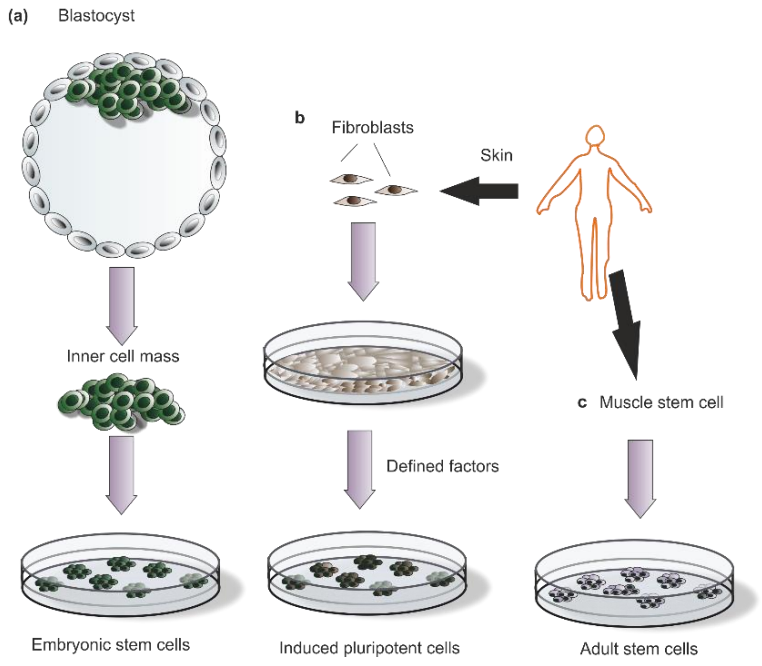

Figure 2.1: Schematic representation of the origin of stem cells. (a) Embryonic stem cells shown in green are derived from blastocysts. (b) Induced pluripotent stem cells shown in brown generated from skin fibroblasts which are somatic cells. (c) Tissue-specific adult stem cells (for example skeletal muscle stem cells) shown in purple are derived from muscle fibers. Adapted from Lutolf *et al.*[17]

Embryonic stem cells, induced pluripotent stem cells and adult stem cells are derived from three different sources, and each have advantages and disadvantages in regard to their potential use in regenerative therapies (Figure 2.1).[17] The discovery of human embryonic stem cells (hESC) from blastocysts by Thomson *et al.* in 1998[1] provided the first human source of pluripotent stem cells. Though their clinical translation is impeded by the ethical concerns of using embryos. Human induced pluripotent stem cells (iPSC) were reprogrammed from somatic cells such as skin fibroblasts by Takahashi *et al.* in 2007.[3] The reprogrammed cells have similar morphology as natural pluripotent stem cells; and are able to differentiate into a variety of cell types. Some ethical issues associated with hESC could be side stepped by using iPSC.

Successful reprogramming of adult stem cells, also called somatic stem cells, into a pluripotent state would allow generation of stem cells that differentiate into specialized cell types.[3] For example, the hematopoietic stem cells (HSC) are found in stem cell niches in the bone marrow. They maintain homeostasis by balancing the inactive and active cells in the blood.[18] HSC can be generated from Umbilical cord blood (UCB),[19] and could be used to differentiate to regenerate the tissue that has been damaged or worn out. Somatic stem cells are lucrative as they have lower rejection rates and there are no ethical concerns associated with their usage. They can be cultured on substrates derived from animal sources, conventional tissue culture polystyrene (TCPS) dishes, or microcarriers.

However, major challenges are associated with culturing hPSC, firstly, controlled proliferation while the ability to maintain pluripotency in culture; and secondly, the capability to direct stem cell differentiation reliably.[20] hPSC either do not attach or spontaneously differentiate in conventional substrates used for adult stem cells. Safety is yet another issue preventing hPSC from becoming a viable therapy in regenerative medicine. Traditionally, these cells are cultivated on mouse embryonic fibroblasts (MEF) feeder layers.[1] MEF feeder layers secrete soluble factors and deposit ECM required for hPSC self-renewal.[21] However, they induce xenogeneic contaminants or undefined factors into the culture systems.[22] Matrigel™ (Corning, NY) is another widely used cell culture substrate consisting of extracellular components.[23] It is a commercially available solubilized complex basement membrane matrix containing laminin, collagen IV, and heparan sulfate proteoglycan purified from Engelbreth-Holm-Swarm tumor. It also consists up to 1,800 different proteins whose levels vary significantly from batch to batch. Accordingly, it is limited by being an undefined substrate and also contains unwanted xenogeneic materials.[24] Now xeno-free

methods, including the use of human fibroblast feeders,[25] amniotic mesenchymal cells,[26] and adipose-derived mesenchymal stem cells[27] have been developed. However, the batch-to-batch variation of feeder cells still pose a challenge for the large scale production of hPSC.[28] Also, sterilization by irradiating feeder cells with gamma rays impede their proliferation and induce apoptosis.[29] These shortcomings associated with culturing hPSC on feeder cells negatively affect their self-renewal and limit their use in therapeutic applications.

One potential solution would be to develop a chemically defined, xeno- and feeder-free culture system. A synthetic surface could minimize the risk of xenogeneic contamination and yield more reproducible and homogenous stem cell cultures while lowering the cost of production.

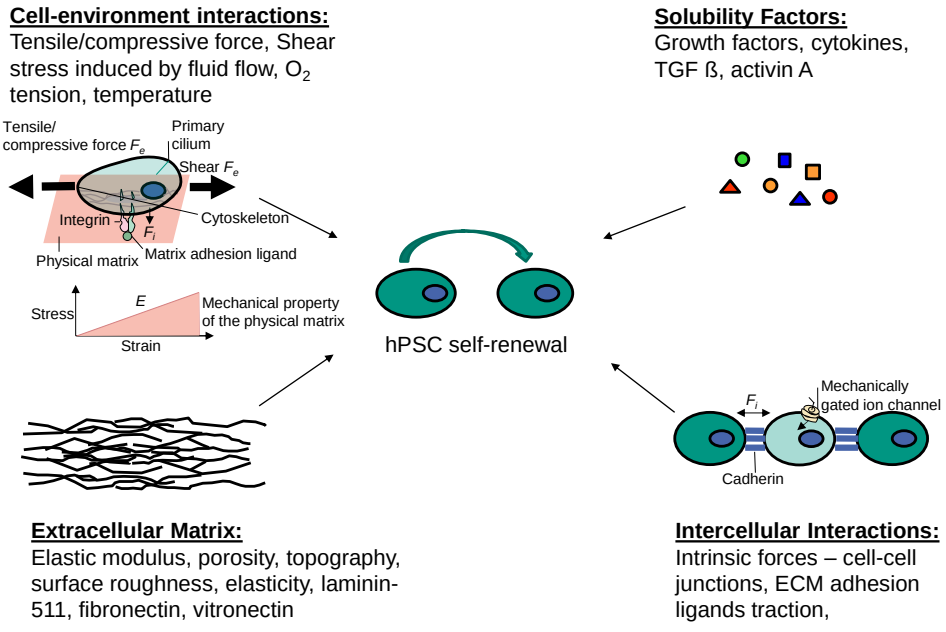

Figure 2.2: Environmental factors that regulate hPSC self-renewal, adapted from Azarin *et al.*[30] and Vining *et al.*[31]

These advances would help produce a near limitless source of hPSCs for deriving specific cell types required for regenerative medicine.[32] The first step in developing substrates for the expansion of hPSC *in vitro* is to identify the environmental cues facilitating their undifferentiated expansion (Figure 2.2).

The stem cell niche is a complex microenvironment comprising of an ensemble of soluble signals from cytokines and growth factors, direct interactions with other cells, and the extracellular

matrix (ECM).[33] In combination with one another, these components act on stem cells to maintain their pluripotent state, physically tether them, and regulate self-renewal.[34] The stem cell niche serves as a protective environment that provides supportive conditions to maintain the functional propertied of stem cells. The loss of contact with the niche can result in the loss of stem cell functions. In the next section, the factors that affect stem cell expansion in synthetic cultures are elucidated.

2.1.1 Extracellular Matrix

Different ECM molecules play vital roles in cell behavior such as cell anchorage, proliferation, mechanical buffering, survival, aiding intercellular communication and differentiation.[35] Cells can also sense structural and mechanical stimuli of the ECM such as elasticity, surface topography, directional motility guided by gradients in adhesion, and rigidity.[36–38] The cell adhesion and spreading are controlled by intra-cellular signaling pathways that are originally triggered by transmembrane proteins interacting with the engineered substrate[39] (Figure 2.2). Understanding the effects of the physical aspects of the ECM in regulating hPSC behaviors is essential in improving their survival and self-renewal in synthetic cell culture platforms. Synthetic substrates need to have defined material properties that mimic the ECM physically and biochemically. Comprehensive reviews about the physical aspects of cell culture substrates have been detailed by Ross *et al.* and Vining *et al.*[31,38] A few of the important aspects will be focused in the sections below.

Material Stiffness

Mechanical cues provided by material stiffness is an essential characteristic by which cells sense the external forces (F_e) and subsequently respond to the environment (F_i, response force) in an appropriate manner.[31] There are various F_e and F_i that modulate cell adhesion. Mechanically gated ion channels sense the F_e caused by applying tension on cells. The ion channels rearrange the cytoskeleton in response to the shear.[31] The cytoskeleton then transfers forces (F_i) to the intracellular structures, such as the nucleus. These mechanotransductions correlate with changes in gene expression and cell fate.[40] Thus, optimal stiffness of the substrate correlates to optimal stem cell growth.

From literature, human embryo stiffness was found to range from 3-14.2 Pa by deducing stiffness values of African clawed frog embryo, which has a close evolutionary relationship with humans.[41] Stiffness of traditional cell culture substrates (plastic and glass) are outside the range of many functional tissues.[42] TCPS substrates have an elastic modulus of ~2 GPa, which is rigid and cause differentiation of hPSC. Rigid substrates cannot transfer the cellular traction forces (F_i) to nearby molecules. Consequently, cells are not able to remodel actin cytoskeleton to adhere to the substrates, which may suppress cell spreading and migration.

Substrates with lower stiffness could have higher adhesion rates due to the ability of the cells to better reorganize the surrounding material. This is done by clustering the integrin receptors into aggregates at the membrane, that bind ECM proteins at the membrane into a complex termed the focal adhesion[43] (Figure 2.2). These focal adhesion sites serve to signal bidirectionally to regulate cell adhesion and migration (Figure 2.2). Thus, the elasticity of the substrates directly influences the cellular responses. Modulation of the elastic modulus of biomaterials may also impact on the topography of the surface. For example, polydimethylsiloxane (PDMS) and polyacrylamide hydrogels have marked differences in porosity, spanning a range of micro- to nanometer pore sizes for different stiffness.[44] The pore sizes influences hPSC spreading, by reorganization of the cytoskeletal components.[45] In summary, modulating the stiffness of synthetic surfaces impact *in vitro* cellular signaling responses, which can be tapped for uses in biotechnology applications.

Material composition

The substrates need to display defined cell-binding groups. Substrate interface-mediated binding of ECM proteins (like laminin, proteoglycan, vitronectin, fibronectin, E-cadherin, etc.,) growth factors, and cell surface receptors (for example, integrins) create a microenvironment to support self-renewal of hPSCs.[46] Surface wettability measured by water contact angle, WCA, has been used to predict cell adhesion.[47] *In vitro* studies have helped to identify that the surface roughness of the substrate modulate cell adhesion, morphology, proliferation, as well as macrophage cytokine release, and protein expression of collagen and elastin (increases with increased surface roughness).[38,48] Hence, surface micro-structuring, like acid etching have been commonly used for increasing surface roughness and oxygen content.[49]

2.1.2 Biochemical factors

Soluble biochemical factors complement the ECM interactions in defining cellular fate.[50] Optimal culture conditions are required for the maintenance of hPSC *in vitro*. Multiple studies have shown that fibroblast growth factors (FGFs), Wnts, and transforming growth factor β (TGF β) are crucial in maintaining stem cell pluripotency and need to be present in the synthetic microenvironment.[51–53] Hence, several feeder- and serum-free culture media formulations containing these factors have been employed to support the culture of hPSC.[24,54,55] However, the cells still require Matrigel substrates, and therefore can be challenging to gain regulatory approval for manufacturing high numbers of cells. Hence, there is a need for biomaterial substrates, which might result in a more defined and xeno-free system that will allow optimal expansion of cells.

Culture medium supplemented with fetal bovine serum (FBS), insulin, transferrin, albumin[56] are used for hPSC culture because they adsorb to biomaterials and regulate hPSC responses.[15] In this dissertation, human cell conditioned medium (HCCM) is used for the growth of hESC. Adhesion and binding of plasma proteins on the biomimetic substrates depend on diverse biomaterial characteristics, such as surface roughness, charge and wettability, and is affected by the available protein repertoire in the culture medium.[57] Therefore, the complex interplay of substrate's inherent material properties and the resulting adsorption of molecules from the culture medium modulate cellular responses and it is not easy to separate the individual responses. This should be kept in mind while developing synthetic substrates.

2.1.3 Inter-cellular interactions

Mechanical and biochemical signals used for cell-cell adhesion interactions also govern hPSC self-renewal.[58] Specialized cell junctions occur at points of cell-cell and cell-substrate contact in hPSC. They play a key part in transmitting tensile forces, from cell-cell or from cell-substrate that regulate intracellular signaling pathways. This is done by adhesive molecules like integrins.[59] Individual cells and small clumps on the substrate have poor viability while large colonies on the culture plate are spontaneously differentiated. Colonies require an appropriate size for self-renewal. Hence, hESC are passaged regularly through mechanical or chemical means to regulate stem cell colony size and shape.[30]

Ultimately, the appropriate balance between cell-substrate interactions, soluble factors and cell-cell interactions controls the proliferation of hESC. Therefore, defined culture conditions that promote hPSC self-renewal need to be established. Identification of biomaterials that support long-term expansion of undifferentiated stem cells, appropriate cellular attachment, proliferation and gene expression patterns is critical.[9,60] The next section describes biomaterials, their properties and select examples.

2.2 Biomaterials

Biomaterials were incorporated into modern medicine with the use of polyurethanes as artificial heart pumping bladders.[61] From then on, there have been tremendous developments in materials that contribute to the medical field. Biomedical devices like coronary stents,[62] guide wires,[63] implants and biosensors have been surface coated with materials that are biocompatible and non-fouling.[64] A major characteristic of these materials is the prevention of nonspecific biomolecular and microorganism attachment on surfaces. Biomaterials with tunable biochemical and mechanical properties may recapitulate the ECM, providing cells with information that is important for pluripotency and self-renewal.[47,61,65,66]

Potential diverse biomaterials are reported in literature as promising materials for biomedical applications. As an example, poly(ethylene)glycol (PEG) is used extensively because they are hydrophilic, non-toxic, biocompatible and low fouling.[67] PEG polymers resist non-specific protein adsorption due to steric repulsion effect.[68] Adhesion peptides have been incorporated by PEG modification to create tunable tissue engineering substrates.[69] However, PEG-based coatings have disadvantages. They are susceptible to oxidation damage when oxygen and transition metal ions (most biochemically relevant solutions contain transition metal ions) are present.[70] Also, PEG dehydrates the cells in contact with it.

Other low fouling polymer brushes based on 2-hydroxyethyl methacrylate (HEMA) and poly(ethylene glycol) methacrylate (PEGMA) have been generated and have shown resistance to proteins.[71–73] PolyHEMA-based materials do not resist protein adsorption from undiluted human blood serum and plasma, making them unsuitable for biomedicine.[74] In our lab, hESC adhesion and propagation on PEGMA surfaces were investigated, and it was observed that hESC initially adhered to these surfaces, but did not promote extended cell culture.[13] The development of

materials that maintain their properties in tissue fluids is critically important in biomedical applications. Hence, scientists began to probe the role of zwitterionic polymer surfaces in protein resistance and stem cell self-renewal.[75]

2.3 Zwitterionic polymers

Zwitterionic-based materials such as phosphobetaines, sulfobetaines and carboxybetaines are hydrophilic and known to be much more oxidatively stable than PEG.

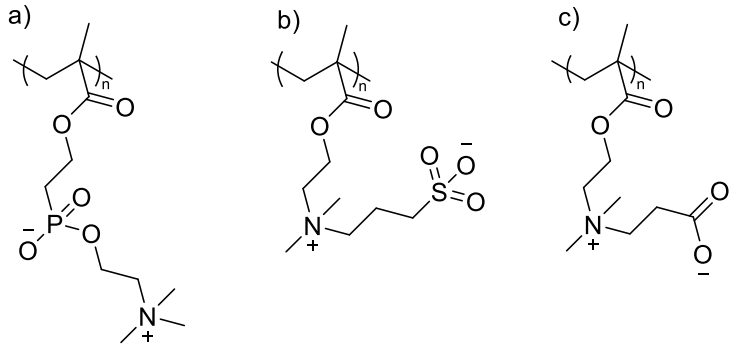

Figure 2.3: (a) Zwitterionic polyphosphobetaine, (b) zwitterionic polysulfobetaine and (c) zwitterionic poly(carboxybetaine) polymers. The polymer backbone shown in these examples is a polymethacrylate.

Zwitterionic polymers show strong electrostatic intramolecular interactions between the cationic and anionic groups on the same monomer residue while maintaining overall charge neutrality (Figure 2.3).[76] The water structure surrounding the zwitterionic brushes forms a physical and energetic barrier, thus preventing protein adsorption on the surface.[77] The strong ionic interactions between the monomeric units is influenced by temperature and molecular weight of the polymer brushes.[78–80]

Certain zwitterionic hydrogels are thermoresponsive and upper critical solution temperature (UCST) transitions could be observed.[81] The inter- and intramolecular ion associations between the zwitterionic groups at low temperatures render them insoluble in water. The electrostatic attractions are broken at sufficiently high temperatures, resulting in isolated polymer chains that are completely soluble.[82,83] UCST behavior can be understood via the Flory-Huggins mean-field theory.[84] Upon increasing the temperature, the Flory-Huggins parameter χ reduces. Therefore, the entropic mixing contribution of the free energy will dominate over the enthalpy at high

temperatures and, consequently the components mix. For many applications, e.g. in drug delivery,[85] bio-adhesion,[86] etc., temperature is used as a stimulus inducing a response of the polymeric system. The development of antifouling, thermoresponsive zwitterionic coatings on interfaces to meet the challenges of biomedical devices development is therefore beneficial.[87]

Phosphobetaine-based polymer surfaces such as poly(2-methacryloyloxyethyl phosphorylcholine) (polyMPC), have been studied because they mimic the lipid components that constitute the outside layer of cell membranes. PolyMPC coatings are protein-resistant.[88]. MPC-based copolymers have been used commercially in contact lenses.[67] MPC, however, is difficult to synthesize. The zwitterionic structure of poly(carboxybetaine methacrylate) (polyCBMA) has a comparable structure to glycine betaine, a molecule that is essential to the osmotic regulation of living organisms.[89] PolyCBMA has cationic quaternary ammonium and anionic carboxylate functional group moieties. It has been demonstrated to prevent non-specific protein adsorption while permitting covalent decoration with bioactive proteins.[90,91]

The structure of sulfobetaines is similar to that of 2-aminoethane sulfonic acid, which is present in high concentrations in nature.[92] A 60 kg human contains up to 60 g of 2-aminoethane sulfonic acid. Due to its biomimetic nature, antifouling properties, simple synthesis, and commercial availability of the monomer [2-(methacryloyloxy)ethyl]dimethyl-(3-sulfopropyl)ammonium hydroxide (MEDSAH), our research focuses on the study of PMEDSAH polymers.[93,94] PMEDSAH was first synthesized by Liaw *et al.* in 1987.[95] The chemical structure of PMEDSAH features a terminal sulfonate (SO_3^-) group and a cationic quaternary ammonium group on each monomer unit. It exhibits an "anti-polyelectrolyte effect" salt-responsive behavior. Zwitterionic PMEDSAH brushes exhibit a UCST behavior that is thickness- and grafting density-dependent.[80,96] A 28 kDa PMEDSAH has a cloud point temperature of 36 °C in water,[97] a value close to the body temperature, thereby making it promising for biomedical applications. PMEDSAH brushes are also capable of modifying the surface wettability as a function of brush thickness.[96] PMEDSAH is utilized in "smart" micelles,[98] polymer nanoparticles,[99] hydrogels[100–102] and polymer brushes.[103] Owing to such attractive properties, this dissertation further deals with the development of substrates for hESC culture using PMEDSAH material. The engineering aspect of manufacturing such materials with respect to scaling up processes are discussed in the next section.

2.4 Synthetic Engineered Environments

Robust, scalable technologies are necessary for large-scale hPSC expansion for regenerative medicine purposes.[104] There is an inescapable need to engineer synthetic microenvironments to have more reproducible culture conditions and lower the cost of production without introducing xenogeneic components. Maintenance of viability, pluripotency as well as homogeneity of cell populations are essential. Diffusion of oxygen, growth factors and nutrients to the cells are important.[105] The cells need to be protected against mechanical stresses like the hydrodynamic shear forces that negatively affect cell viability and pluripotency.[22] Then, these cells need to be conditioned efficiently so that they survive and integrate into the tissue *in vivo.* All these factors require microenvironments that emulate *in vivo* conditions and incorporate biomaterials specifically modified for the growth and proliferation of hPSC. This need for the synthetic hPSC cell culture systems design led to the development of two dimensional (2D)[13,106,107] and 3D biomaterials, including hydrogels, microwells, microcarriers[108,109] and scaffolds[110,111]. 2D biomaterials are the most commonly used for hPSC culture to date. Though it has proved to be a viable option, the limitation of 2D substrates is the lack of 3D environment that is native to cells. Progressing from 2D to 3D biomaterials could lead to faster clinical translation of hPSC cells grown in vitro. Scaffolds using decellularized tissues represent an attractive solution, but many engineering design constraints manifest.[112] Some examples of hPSC cell culture platforms explored by researchers are elucidated below.

2.4.1 Natural biomaterials

Naturally derived biomaterials are like biological macromolecules that are recognized by and metabolized in the biological environment. But these biomaterials do not induce chronic inflammatory or immune response and toxicity like biological macromolecules do.[113] The use of functional fragments of ECM proteins like the arginylglycylaspartic acid (RGD)-peptides to functionalize the substrates for culturing hPSC was desirable to reduce immunological reactions.[106] Kiessling and coworkers prepared a range of thiolated peptides and spotted them onto gold-coated glass slides to prepare peptide-functionalized self-assembled monolayer (SAM) microarrays that support hESC growth and self-renewal.[114] Decellularized ECM coated substrates derived from MEF allowed hESC adhesion and proliferation.[115] Encapsulation of hESC in 3D hyaluronic acid (HA) hydrogels maintained their pluripotency, and could be differentiated into

embryoid bodies.[116] HA hydrogels can be cross-linked to modulate material properties such as stiffness, to direct stem cell fate.[117,118]

There are disadvantages in using naturally derived biomaterials as cell culture systems. First, they are exposed to the external environment during production, and, therefore, microbial and heavy metal contamination may occur. Second, batch-to-batch variation and slow processing hinder the mass production of natural biomaterials for hPSC culture use.[119] To overcome these limitations, synthetic biomaterials incorporating biologically active components were explored.

2.4.2 Synthetic biomaterials

The use of synthetic biomaterials to maintain hPSC provide an ideal tool to elucidate the molecular mechanisms that control stem cell fate because material parameters can be tightly controlled. Synthetic peptides and polymers have been developed that support long term expansion of hPSC.

ECM proteins

An alternative to materials harvested from natural sources is the use of protein-engineered biomaterials. They are made entirely out of recombinant ECM proteins. As mentioned before, laminin, vitronectin, fibronectin, heparin and collagen are major ECM proteins. Culture on human recombinant laminin proteins has been demonstrated to be a robust substrate for hESC self-renewal.[107] However, mass production of full length recombinant laminins is very difficult as they are large structures.[120] Therefore, Miyazaki *et al.* went on to show that recombinant laminin fragments, instead of the whole laminins, could support increased adhesion and undifferentiated proliferation of hESC for 10 passages,[120] thereby reducing the size and complexity of laminin required.

Substrates with recombinant vitronectin has been shown to sustain hESC pluripotency and survival.[121] This is done by the binding of integrins to vitronectin. This discovery led Higuchi *et al.* to develop synthetic surfaces consisting of polyvinylalcohol-co-itaconic acid hydrogels with a stiffness of 25 kPa grafted with an oligopeptide derived from vitronectin.[122] They showed that the cells maintained their pluripotency for 20 passages. This is also a good example of tuning physical cues and biological cues by the biomaterial to direct stem cell fate. Chang *et al.* developed heparin-

based hydrogels as a matrix platform for hESC culture. They found that they exhibited good attachment of hESC via direct interaction with heparin moieties and supported long-term expansion maintaining their pluripotency for >20 passages.[123] Fibronectin surfaces (Cellstart™, Thermo Fisher) supported hPSC cultures in chemically defined medium.[124,125]

2D synthetic polymer substrates

Biomaterials may be useful to mimic the ECM properties, in turn affecting stem cell function. To discover novel biomaterials satisfying such conditions, Anderson *et al.* used an unbiased high-throughput approach using 576 different combinations of 25 acrylate-based polymers to find their effects on cell attachment, proliferation and lineage induction.[47] The different polymers were synthesized through photopolymerization onto a poly(hydroxyethyl methacrylate) (pHEMA) coated glass slide. They found combinations of materials that influenced hESC attachment, proliferation and differentiation. This study confirmed the dependence of cell-material interaction on surface chemistry. Materials with resistance to cell attachment contained hydrophobic moieties such as aromatic and aliphatic carbon groups. The conclusion of this study was that weakly polar groups support cell attachment. The same group later studied material properties of all polymeric substrates such as surface topography, wettability, surface chemistry and indentation elastic modulus to develop structure-function relationships between material properties and hPSC culture.[15] They demonstrated that hESC substrates having moderate wettability support pluripotency.

Poly(methyl vinyl ether-alt-maleic anhydride) (PMVE-alt-MA) synthesized by free radical polymerization supported attachment, proliferation and self-renewal of hESC for five passages.[126] Hydrogel interfaces of aminopropylmethacrylamide (APMAAm) were developed by free radical polymerization for hESC growth and self-renewal for 20 passages.[127]

There are only four commercially available synthetic hPSC culture surfaces available in the market today, StemAdhere™, Synthemax™, Geltrex™ and Vitronectin XF™. StemAdhere surfaces™ is made up of a human protein. Vitronectin XF™ (Nucleus Biologics) is a defined, recombinant fusion protein containing the full length human vitronectin sequence. Synthemax™ (Corning) is a chemically defined, xeno-free synthetic peptide substrate consisting of the RGD motif. Geltrex™ consists of reduced growth factor basement membrane matrix. However, none of

them are commonly used. As seen in Figure 2.4, Matrigel is still the most widely used as a substrate for stem cell culture. In our group, a novel synthetic polymer coating made up of PMEDSAH[13] was shown to replace feeder cells and Matrigel in 2D hPSC culture systems. hPSC could be expanded for 25 passages in PMEDSAH synthetic polymer coatings.[13]

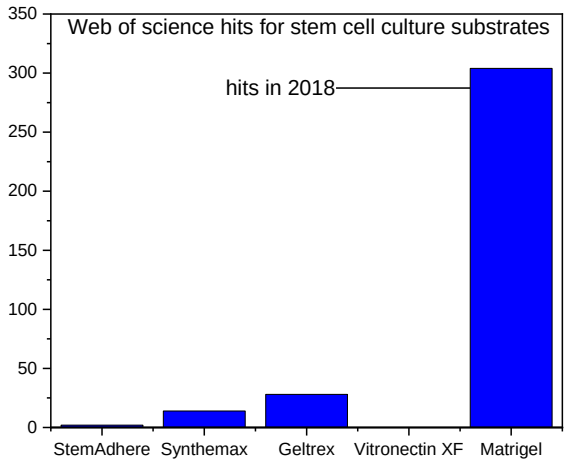

Figure 2.4: Number of hits for the search term for each substrate. The search term "Matrigel" provided 9,775 hits, with 304 hits alone in 2018.

Three dimensional substrates

hESC could be cultured on micron scale wells consisting of soft lithography formed PDMS stamps mold polymer substrates. Generally, their surfaces are functionalized with a material that adsorbs protein.[128] Mohr *et al.* outlined a modification strategy for achieving selective adhesion of cells. Microwells with tri-ethylene glycol terminated SAMs were constructed, where cells adhered only on SAMs. This method yielded defined 3D geometries that permit undifferentiated hESC growth in monodisperse colonies for 3 passages and expressed pluripotency markers. A natural ECM analog was engineered de novo from *in vitro* cultured fibroblasts called decellularized fibroblast-derived matrices (FDM).[112] Tuning the stiffness of the matrices with genipin modulated cell adhesion and pluripotency. Naturally derived 3D microenvironments could be developed in this way to grow hPSC with high efficiency.

2.5 Surface Modification Techniques

Biomaterial surfaces can be modified by controlling the physical and chemical characteristics of the surface. The surface properties can profoundly alter cell attachment and proliferation. General methods of surface modification using synthetic materials are detailed below.

2.5.1 Self-assembled monolayers

Alkanethiols are known to form reproducible and well-ordered surfaces on top of gold surfaces via chemisorption of the sulfur atom to gold, when gold is immersed in thiol solutions.[129] They can be engineered for generating arrays with defined elements.

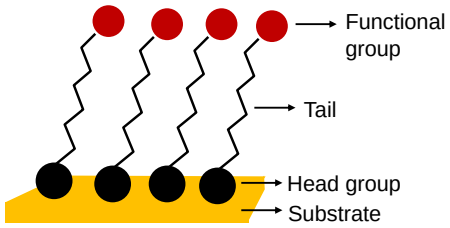

Figure 2.5: Description of self-assembled monolayers.

Alkanethiols used to construct SAMs typically contain an anchoring (head) group, a 11-18 carbon chain (tail) and are capped with a functional group which gives rise to the SAM interfacial properties (Figure 2.5). The choice of head group will determine the affinity for the surface. The tail will determine, in part, the intermolecular interaction between the neighboring molecules on the surface. SAMs of alkanethiols have been studied as potential cell substrates for human umbilical vein endothelial cells.[130] Nonetheless, the use of SAMs have been known to desorb from surfaces when exposed to biological serum during prolonged culture.[131]

2.5.2 Langmuir-Blodgett films

The Langmuir-Blodgett (LB) deposition, invented by Langmuir[132] and Blodgett,[133] organizes a single layer of molecules on a liquid surface, usually water, before transfer to a solid substrate by immersing the solid into the liquid.[134] A thin organic film is formed with the thickness of just one molecule due to the distinct affinity of the monolayer for each of the phases involved.[135,136] LB films enable molecular-level control over the structure of films that are difficult to otherwise achieve. LB technique offers the possibility for the immobilization of proteins or enzymes and

subsequent application in bio-catalysis, drug delivery and tissue engineering.[137,138] However, LB films require expensive instrumentation and may only be used for the encapsulation of amphiphilic components.[139] An alternative to LB deposition is layer-by-layer (LbL) assembly.

2.5.3 Layer-by-layer self-assembly

Layer-by-layer (LbL) self-assembly of thin films, introduced in 1992, is a simple deposition process with broad applications in optics, biosensors, surface coatings, controlled drug-delivery devices and tissue engineering.[139,140] LbL films are created through the sequential deposition of biomolecules in aqueous solution containing functional groups that drive self-assembly.[141] The LbL technique is basically formed by alternate deposition of positively and negatively charged materials on a solid substrate with washing steps in between.[140] Electrostatic interactions between oppositely charged polyelectrolytes are the dominant driving force to drive the LbL assembly during sequential deposition. It is a low-cost process with precise control of coating thickness under mild assembly conditions on versatile coating materials.

2.5.4 Chemical Vapor Deposition polymerization

Chemical vapor deposition (CVD) polymerization is a surface modification platform for the fabrication of thin films using a vacuum deposition method in which volatile precursors are deposited from the vapor phase by their decomposition on the substrate to form a coating.[142] Most frequently the process is thermally driven but photo- and plasma-assisted methods are also used. The deposition of the film is controlled by a chemical reaction. Hence, this technique has successfully overcome some of the issues faced by wet fabrication methods such as LbL. CVD is employed in several thin film and coating applications, such as those used for dielectrics, semiconductors, passivation layers, oxidation barriers, and tribological coatings.[143]

There are many CVD processes; for example, initiated CVD (iCVD),[144] plasma-enhanced CVD (PECVD),[145] oxidative CVD (oCVD),[146] vapor deposition polymerization (VDP),[147] and CVD of parylene and its derivatives.[148] Amongst them, parylene CVD, originally pioneered by Gorham *et al.*, employs heat to crack vapor phase reactants related to [2.2]paracyclophane while under vacuum (~0.3 mbar).[149] Polymerization of the resulting radical species on cooled substrates proceeds via a chain growth mechanism. By varying the functional groups attached to the

[2.2]paracyclophane, polymer films with high retention of functionality can be produced via the this process. A depiction of the CVD set-up and process is provided in Figure 2.6.

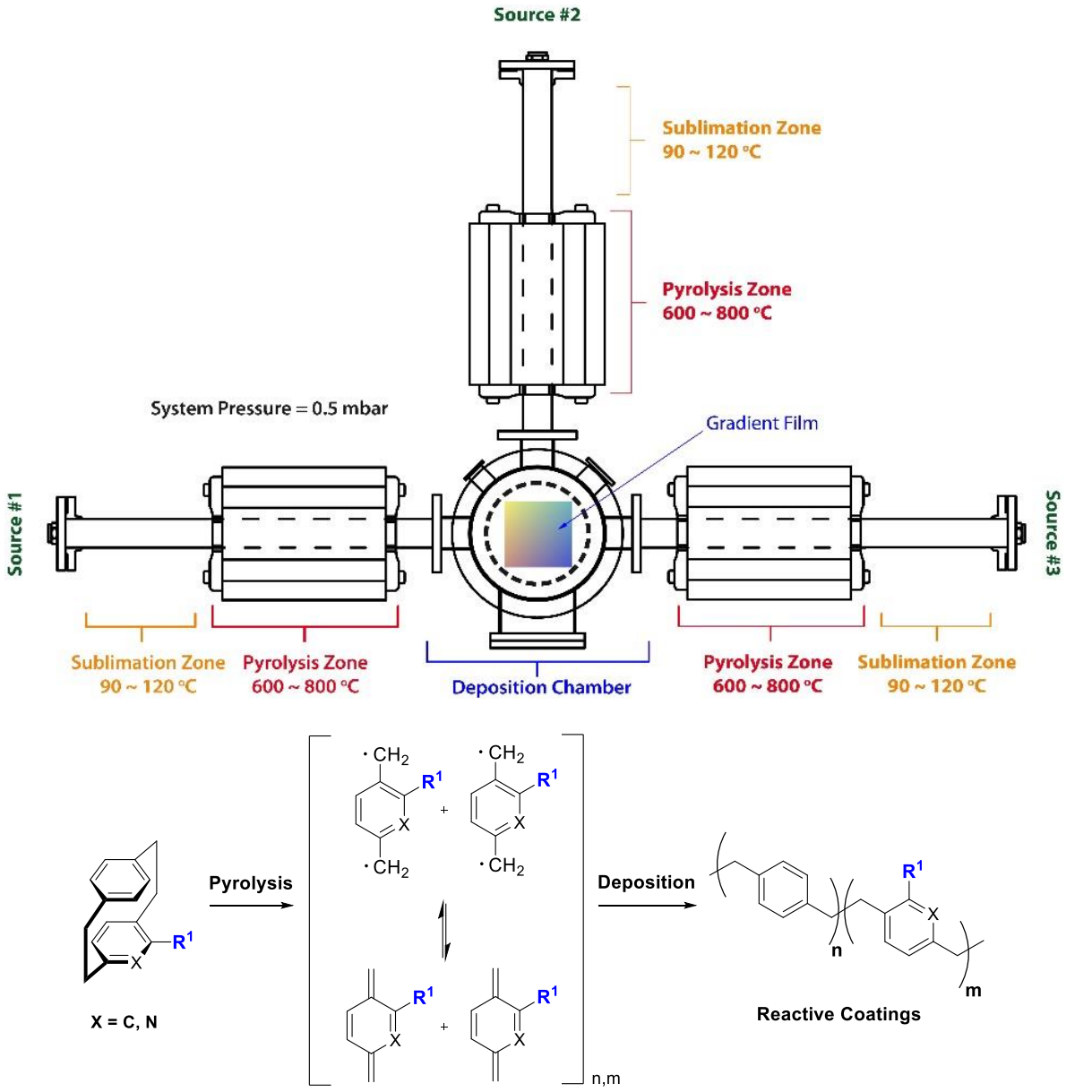

Figure 2.6: The schematic represents the three-source chemical vapor deposition (CVD) copolymerization system containing three inlet sources that each contain a sublimation zone and a pyrolysis zone, and the three sources are connected to a center deposition chamber. [2.2]paracyclophanes are sublimed at 90-120 °C in the sublimation zone, transported to the pyrolysis zone and deposited in the deposition chamber. Adapted from Kratzer.[157]

CVD of poly(*p*-xylylenes) (trade name: parylene) possessing reactive functional groups including amino, hydroxyl, anhydride, triflate, trifluoroacetyl moieties, etc., have been used to prepare submicron coatings with distinct chemical and optical properties in our lab and other labs.[150–156] Technically relevant substrates such as polystyrene, PDMS, polyvinyl chloride, steel, etc. can be functionalized with a library of chemical moieties, irrespective of substrate chemistries and properties.[158] The CVD process yields conformal coatings with pinhole-free coverage for large areas and can also be applied to complex 3-dimensional geometries.[153] The coatings are deposited in a solvent-free process, and also the by-products evaporate, giving the possibility of achieving, reproducibly, very high levels of purity in the films. The process also allows flexibility during deposition such as co-deposition of different materials. Some members of the poly-*p*-xylylene family have gained commercial acceptance due to their high solvent resistance, low dielectric constants, and excellent barrier properties.[159,160] Parylene coatings are extensively used as a barrier medium for implantable chemical sensors,[161] stainless steel implants,[162] pacemakers,[163] stents and catheters.[164]

The CVD technique, LbL assembly, SAMs, LB films, etc. have been made by free radical polymerization. But it is useful to have defined responsive polymer brushes for regenerative medicine.[165] They can be synthesized by reversible-deactivation radical polymerization (RDRP) techniques nowadays. In this dissertation, employing CVD polymerization, the initiator coatings (2-bromoisobutyryl groups for atom transfer radical polymerization (ATRP)),[166] or alkyne groups that can anchor chain transfer agents (CTA) for reversible addition fragmentation chain transfer polymerization (RAFT),[11,167] or amino or aldehyde groups to immobilize functional polymers by the grafting-to process, is prepared and subsequently used for further modification. The generation of polymer brushes with tailored physical and chemical properties of interfaces by RDRP techniques is discussed in the next section.

2.6Reversible-deactivation radical polymerization

RDRP is a form of polymerization propagated by chain radicals, the majority of which, are held in a state of dormancy through an equilibrium process involving a dormant species.[168] The equilibrium ensures prolonging the lifetime of the growing polymer chains by keeping the concentration of the propagating radicals sufficiently low. Most of the radicals are in the dormant state at any second, however, they are not irreversibly terminated. Only a small fraction of them

are active, yet because of the activation-deactivation equilibrium process, simultaneous growth of all chains is ensured. Consequently, the molecular weights of the polymers generated have a narrow Poisson distribution, and in turn, a lower dispersity. RDRP methods have provided a robust synthetic approach to synthesize polymers with controlled composition, topology, functionalities and narrow molecular-weight distributions.[169] RDRP consists of four reactions: initiation, propagation, transfer and termination.

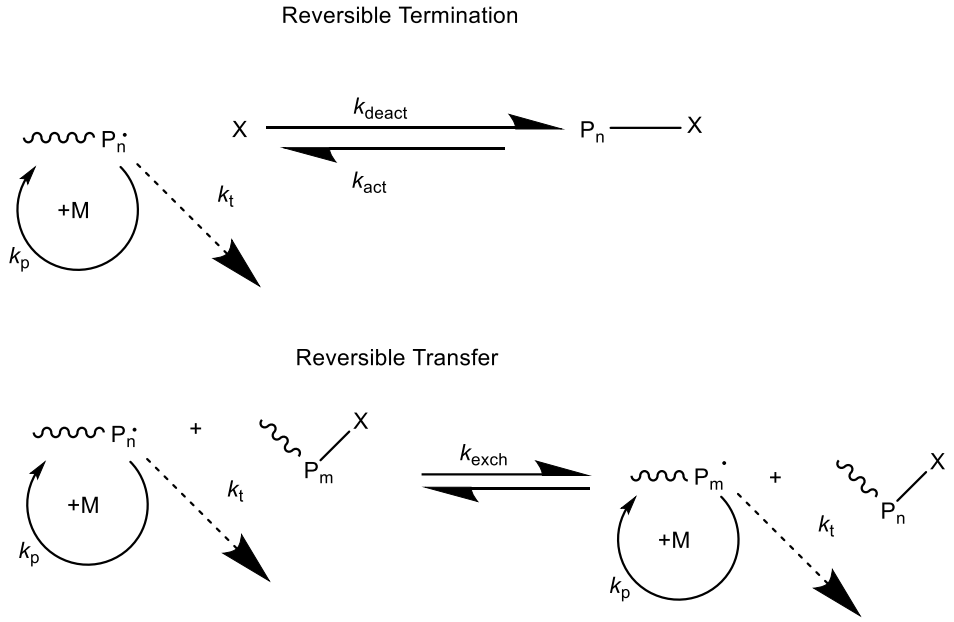

Scheme 2.1: Mechanisms for reversible-deactivation radical polymerization. They possess a dynamic equilibrium between a dormant and an active species which can be enabled by reversible activation/deactivation process or by degenerative chain transfer processes.

There are two initiation steps; the first being the decomposition of the initiator to yield a pair of free radicals. In the second step, a monomer is added to the free radical resulting in a chain radical. A combination of a fast initiation step and slow propagation step is characteristic of RDRP. This is achieved by an intermittent formation of radicals with added monomer units. The propagation step involves a dynamic equilibrium between a large concentration of dormant species and a low concentration of active propagating chain radicals as shown in Scheme 2.1.[170] The equilibrium can be achieved by one of two processes: (1) reversible deactivation (e.g. ATRP)[171] or (2) degenerative transfer (e.g. RAFT).[172] The molecular weight distributions in free radical polymerizations are broad, and not optimum for controlling polymer brush properties.[173] With

RDRP, the parameters could be varied in order to control polymer brush properties. The different RDRP methods include atom transfer radical polymerization (ATRP)[174–176], reversible addition-fragmentation chain transfer (RAFT) polymerization[177–179] and nitroxide-mediated polymerization (NMP).[180,181]

Using RDRP, polymer brushes can be obtained by three different methods: (1) "grafting-from", (2) "grafting-to" and (3) "grafting-through" (Figure 2.7). Polymer grafting provides a powerful technique for modification and functionalization of various surfaces.

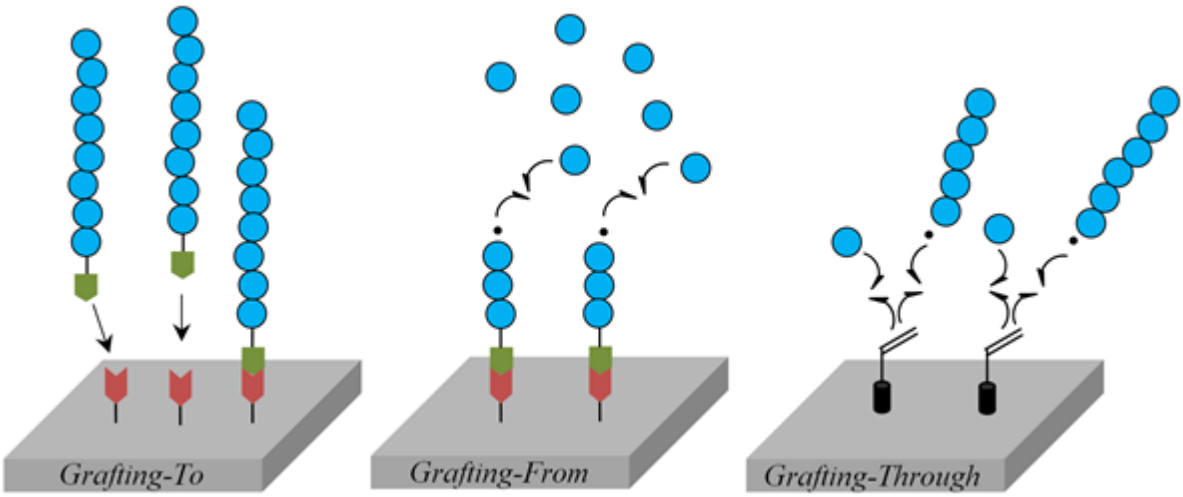

Figure 2.7: Preparation of polymer brushes by "grafting-to", "grafting-from" and "grafting-through" strategy. Cartoon adapted from Kratzer.[157]

The process of growing chains from a surface is termed "grafting-from", where the growth of polymer chains occurs from covalently bound small-molecule initiation sites on the surface.[182] The "grafting-from" approaches are able to produce dense, tunable and multifunctional polymer brushes. The grafting of polymer after the synthesis of polymer in solution with a reactive group on a surface is termed "grafting-to". The polymers have reactive functionalities that reacts with a complementary reactive group on the surface. This method offers the advantage of operational ease, controlled molecular weight distributions and improved polymer characterization before grafting. The "grafting-to" approach can be readily scaled, as pre-formed polymers with functional groups can be synthesized in large quantities. However, this approach usually yields low grafting density (number of chains per unit area of grafted surface) compared to the "grafting-from" process

due to steric hindrance of the chains at the surface of the polymer backbone.[183] Furthermore, the polymer coil has to diffuse to an empty unfilled spot on the surface, which is a diffusion-controlled process leading to a lower grafting density depending on the reaction time. In addition, the probability that a polymer coil does not bind covalently but instead adsorb onto the substrate surface will lower the grafting density. The chains lie on the surface forming a pancake structure at low surface concentrations, where the layer thickness will only be a couple of nm.[184] The "grafting-through" method consists of copolymerizing a macromonomer and low molecular weight monomer to synthesize polymers with defined side chains.[185]

2.6.1 Atom Transfer Radical Polymerization (ATRP)

Atom transfer radical polymerization (ATRP) is a versatile tool for the production of tailored polymer brushes with diverse architectures.[186–188]. Matyjaszewski *et al.*[175] and Sawamoto *et al.*[189] reported ATRP in 1995. It operates via a reaction between an initiator (R-X), which is an alkyl halide and a transition metal complex ((Lig)Mt^z) in its lower oxidation state, via a halogen (X) transfer.

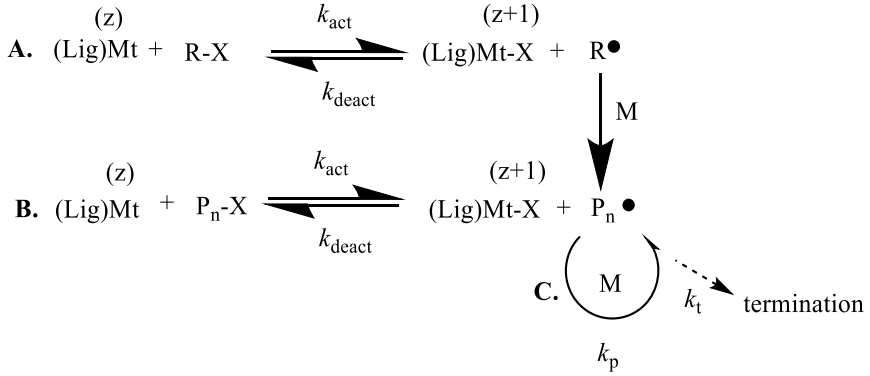

Scheme 2.2: Mechanism of Atom Transfer Radical Polymerization (adapted from [190]). (a) Initiation. (b) Equilibrium with dormant species. C) Propagation. (Lig)Mt^z = transition-metal complex; P_n-X = halogen-terminated dormant species; (Lig)Mt^{z+1}-X = Oxidized transition metal complex-halogen atom; $P_n^{\bullet}$ = active radicals; M = monomer; R-X = initiator; k_{act} = rate constant of activation; k_{deact} = rate constant of deactivation; k_p = propagation rate constant; k_t = termination rate constant.

This results in the formation of propagating radicals (P_n•) and the higher oxidation state transition metal complex ((Lig)Mt^{z+1}-X) (Scheme 2.2).[191] Once P_n• are generated, they react immediately with (Lig)Mt^{z+1}-X to form (Lig)Mt^z and the dormant species P_n-X. The formation of the

(Lig)Mt^{z+1}-X complex is characterized by the activation rate constant, k_{act}, whereas the transfer of X to P_n•, the ATRP deactivation rate coefficient of k_{deact}. Therefore, the activation-deactivation equilibrium constant (K_{ATRP}) is the ratio of the two rate constants k_{act}/k_{deact}. The P_n• propagate with a rate constant k_p. and terminate with a rate constant k_t. During termination reactions, radicals predominantly react with X to form dormant species P_n-X.[192] Initiators and propagating chains are alkyl halides. The initiation and propagation steps of ATRP are shown in Scheme 2.2.[193]

Monomer (M) disappears only due to propagation.

$$-\frac{d[M]}{dt} = k_p[P_n^{\bullet}][M] \quad (1)$$

If [P_n•] is constant, the concentration of monomer is reduced in accordance with first-order kinetics.

$$\frac{[M]}{[M]_0} = \exp(-k_p[P_n^{\bullet}]t) \quad (2)$$

However, [P_n•] is not necessarily constant. Fischer derived a rate expression for the radical by considering the initiation and termination reactions.[192]

$$\frac{d[P_n^{\bullet}]}{dt} = k_{act}[P_n - \mathrm{X}] - k_{deact}[P_n^{\bullet}] - k_t[P_n^{\bullet}]^2 \quad (3)$$

This expression for K_{ATRP} helps illustrate the conditions under which equilibrium can be achieved.

$$K_{ATRP} = \frac{k_{act}}{k_{deact}} = \frac{[P_n][(Lig)Mt^{z+1}X]}{[P_n - X][(Lig)Mt^{z}X]} \quad (4)$$

The polymerization rate (R_p) is governed by the ATRP equilibrium position which is defined by the structure of alkyl halide/monomer and catalyst. Assuming steady-state kinetics, R_p is given by:

$$R_p = k_p[\mathrm{M}]K_{ATRP}\frac{[P_n - X][(Lig)Mt^{z}]}{[(Lig)Mt^{z+1}X]} \quad (5)$$

R_p conforms to a first-order kinetic model with respect to [M] and Mt^z concentrations.[194] R_p is controlled by the ratio of Cu^I to Cu^{II} present in the reaction medium.

The degree of polymerization (DP) is determined by the molar ratio of concentration of reacted monomer to concentration of the initially introduced initiator $[initiator]_0$.[195]

$$DP = \frac{[M]_0}{[initiator]_0} \times conversion \quad (6)$$

ATRP has been employed to polymerize monomers, including acrylates, methacrylates, and acrylamides.[175,196–199] N-based ligands coordinated to Cu are commonly used,[200] but other metals including Ru, Fe, Mo, Os, etc could be used in ATRP.[190] The equilibrium involving active and dormant macromolecules are maintained by ligands during the polymerization reaction.[190] In addition, the ligand structure markedly affect activation.[169] The fast redox between Cu(I) and Cu(II) is directly affected by the ligand, and they must also have a high complexation constant to compete with the polymer for copper. Ligands also adjust the redox activity of the metal for the repetitive halogen exchange reaction.[201,202] Figure 2.8 depicts a series of ligands and initiators.

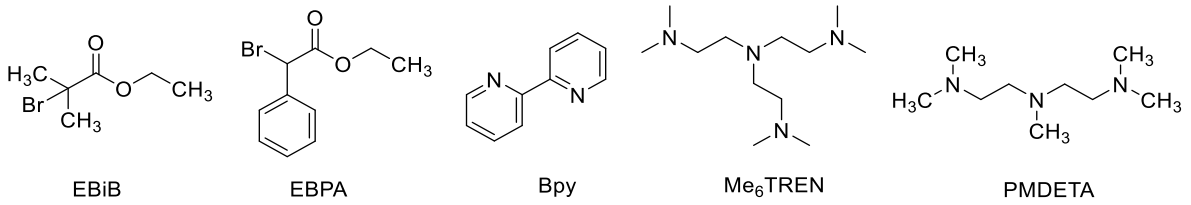

Figure 2.8: Examples of commonly used initiators and ligands for ATRP: ethyl α-bromoisobutyrate (EBiB), ethyl α-bromophenylacetate (EBPA), 2,2'-bypyridine (bpy) and tris[2-(dimethylamino)ethyl]amine (Me_6TREN), N,N,N´,N´´,N´´-pentamethyldiethylenetriamine (PMDETA).

The challenge of using ATRP techniques for cell culture applications is the presence of copper that end up in the material.[169] Cells are sensitive even to incredibly low amounts of copper. This scenario is not ideal for the development of cell culture substrates. Surface-initiated ATRP techniques have enabled polymer brush synthesis from various solid surfaces,[193,203] nanoparticles,[204] proteins[205] and cellulose fibers.[206] In this dissertation, ATRP is used to grow polymer brushes from polymer coatings polymerized employing CVD polymerization, decorated with 2-bromoisobutyryl group which act as ATRP initiators. The advent of oxygen-tolerant SI-ATRP[207] has eliminated the need for using glove boxes and Schlenk techniques, making polymer brushes easier to synthesize.[208]

In SI-ATRP, the amount of each deactivator is very small because of the small amount of immobilized initiator on the flat surface.[203] Xiao and Wirth calculated that the growth rate of polymer thickness was proportional to the rate of monomer consumption in solution,[193]

$$[M]_0 - [M] = k_p[R^\bullet][M]_0 \quad (7)$$

where $[R^\bullet]$ is the radical concentration, $[M]_0$ is the initial monomer concentration, [M] is the monomer concentration, and k_p. is the propagation rate coefficient. K_p values are available in the literature.[209] The radicals undergo bimolecular termination reactions

$$\frac{d[R^\bullet]}{dt} = -k_t[R^\bullet]^2 \quad (8)$$

with its initial concentration of $[R_0^\bullet]$ at time, $t = 0$. Combining Equations 7 and 8, an analytic expression for the monomer consumption was derived as follows:

$$[M]_0 - [M] = \frac{[M]_0 k_p [R^\bullet]_0 t}{1 + [R^\bullet]_0 k_t t} \quad (9)$$

ATRP kinetic model analysis is significant in determining the optimum parameters required for controlling the material properties of the polymer brushes.

2.6.2 Reversible addition-fragmentation chain transfer (RAFT) polymerization

RAFT polymerization was discovered at the Commonwealth Scientific and Industrial Research Organization (CSIRO) of Australia in 1998.[179] RAFT polymerization process enables the production of polymers with enhanced properties, as it can be adapted to the widest range of monomers.[210] RAFT polymerization is also a very tolerant technique, and thus could be used to polymerize functional monomers directly in aqueous solution, providing good control over the polymerization.[210] ATRP has a radical that is localized on a transition metal catalyst, and the monomers attach to them and polymerize. In contrast to ATRP, RAFT polymerization operates via a series of reversible addition-fragmentation steps based on the degenerate chain transfer mechanism.

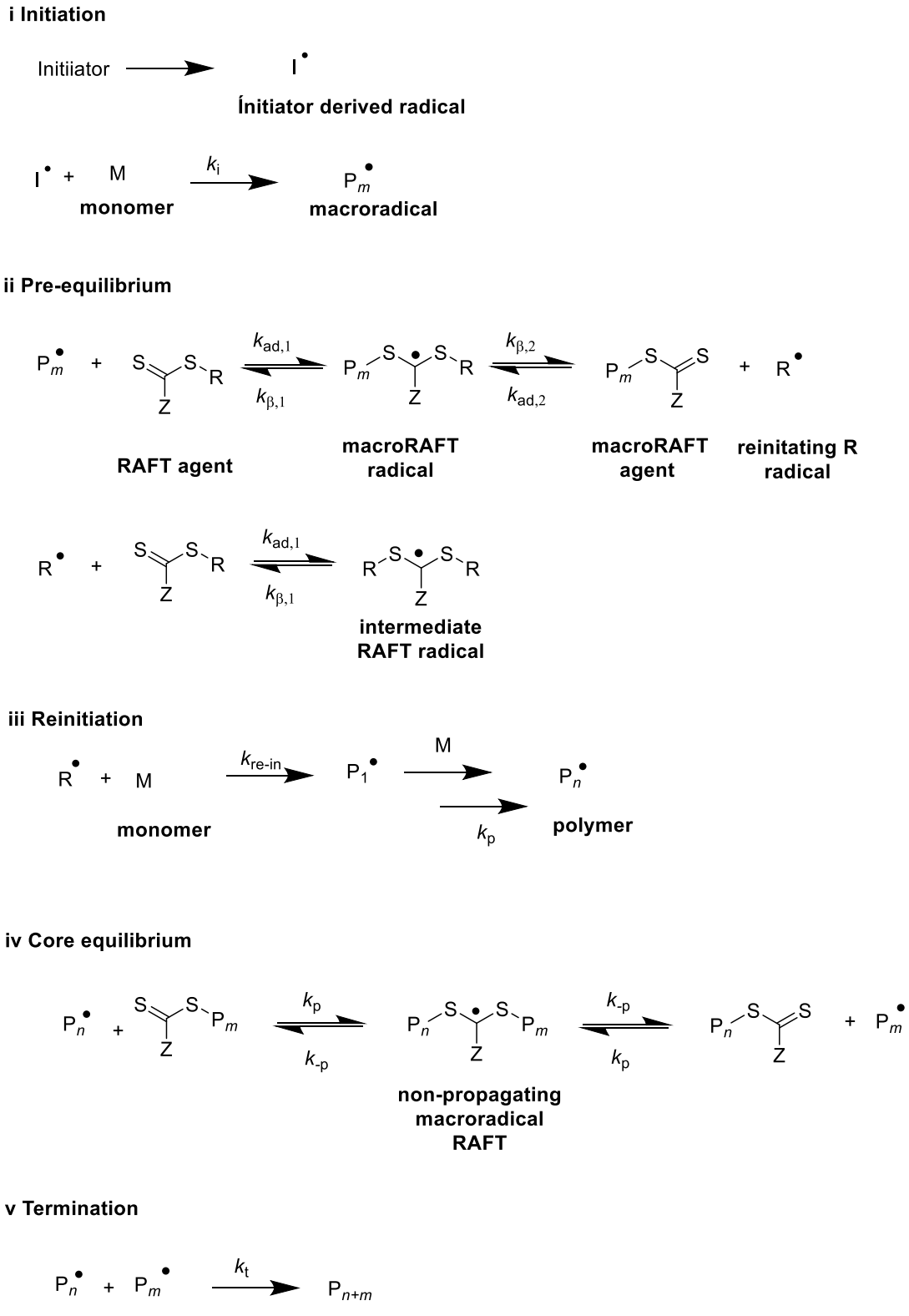

Scheme 2.3: Generally accepted mechanism for RAFT polymerization.

They are called degenerate because they only involve an exchange of functionality between dormant chains and active propagating radical.[211] The chain transfer events are mediated by a chain transfer agent (CTA), which is a dithioester compound S=C(-Z)-S-R, also called as a RAFT agent. CTA has an R-group and a Z-group, which help in controlling molecular weight and dispersity. The R-group is the homolytic leaving and re-initiating group, and Z-group is the stabilizing group[212] (Scheme 2.3). The scheme for the mechanism of a RAFT process is shown in Scheme 2.3.

A radical initiator is required for initiation in RAFT polymerization. The concentration of the radical initiator determines the polymerization rate and dispersity by an appropriate selection of polymerization conditions.[172] The first reaction step is the initiator dissociation into radical fragments. These radicals subsequently initiate polymerization by reaction with a monomer molecule. In the pre-equilibrium reaction step, an equilibrium is maintained between the initial RAFT agent and the macroradical $P_m^{\bullet}$. $P_m^{\bullet}$ (shown in step ii) can fragment back to the initial RAFT agent or fragment to yield a macroRAFT agent and a re-initiating R-radical $R^{\bullet}$.[211] $R^{\bullet}$ can also react with the initial RAFT agent and fragment back to the corresponding intermediate RAFT radicals. In the main equilibrium reaction, the polymer chains rapidly exchange between $P_m^{\bullet}$ and the species capped with the dithioester group. Reactions of these pre- and main equilibria are described by the kinetic parameters, the addition rate coefficient k_{ad} and the fragmentation rate coefficient k_{β} (as shown in Scheme 2.3). Finally, termination occurs by radical-radical reaction (step v). Due to the living character of the RAFT process, termination reactions play only a minor role.

The equilibrium constant (K_{eq}) is given by:

$$K_{eq} = \frac{k_{ad}}{k_{\beta}} \tag{10}$$

The rate of polymerization (R_p) is equal to

$$R_p = k_p[P^{\bullet}][M] \tag{11}$$

where k_p is the propagation rate coefficient, [$P^{\bullet}$] the concentration of propagating radicals and [M] the instantaneous monomer concentration.[172]

RAFT technique has also been used to produce controlled surface-grafted polymers.[213] In Surface RAFT (S-RAFT) polymerization, either the initiator or the CTA can be anchored to the surface.[214] When the initiator is immobilized on the surface, the resultant surface bound polymer layers have a lower polymer propagation rate compared to that of polymers formed in the solution.[215] Surface bounding of CTA can be done through the R-side or the Z-side. Immobilizing the R-group of S=C(Z)S-R graft only about half of the chains to the surface.[216] The Z-group approach, however, has shown to produce well-defined grafted polymers.[217]

Several methods have been reported for the immobilization of CTA onto surfaces. For instance, covalently attaching RAFT-silane agents have been used because it is experimentally simple.[218] Zamfir *et al.*[219] carried out RAFT polymerization of 2-hydroxyl methacrylate (HEMA) from surface-functionalized RAFT-silane agents. SAMs have also become a popular technique to introduce CTA on surfaces, but are limited to specialized substrates such as gold or silicon.[220] The CTA can also be anchored by UV-triggered photoreaction[221] and electrodeposition.[222] In this dissertation, vapor-based polymer coatings are used to immobilize the CTA onto the surface. A functional polymer containing ester bromide group was prepared via CVD polymerization. An azide-functionalized CTA was used for conjugation with the ester-alkyne groups decorated on the surface.

CHAPTER 3 MATERIALS AND METHODS

3.1 Materials

[2-(Methacryloyloxy)-ethyl]dimethyl-(3-sulfopropyl)ammonium hydroxide (MEDSAH) was purchased from Monomer Polymer Dajac Labs, Trevose, PA. MEDSAH (used for UVO-initiated graft polymerization), $CuBr_2$, 2,2'-bipyridine (bpy), ethyl 2-bromoisobutyrate (EBiB), triethylamine (TEA, 99%, stored over potassium hydroxide pellets), 4,4´-azobis(4-cyanopentanoic acid) (V501, >98%), phosphate-buffered saline (PBS, 10 mM), fluorescein labeled bovine serum albumin (FITC-BSA), albumin from bovine serum (BSA, molecular weight ~66 kDa, V fraction), lysozyme (molecular weight ~14.3 kDa) and ROCK inhibitor were purchased from Sigma Aldrich and used as received. Copper bromide (Cu(I)Br) was purified by stirring in glacial acetic acid and rinsing with ethanol and diethyl ether and then dried under vacuum. Deionized water was obtained using a Milli-Q plus system (Millipore, Schwalbach, Germany). [2.2]paracyclophane (PCP) was purchased from Curtiss Wright Surface Technologies, Galway, Ireland. Dichloromethane (DCM, >99%) was purchased from VWR International. Column chromatography was used to separate and purify products from mixtures. The stationary phase used was silica gel 60 (Merck KGaA, Darmstadt, Germany). Thin layer chromatography (TLC) using Silica gel coated aluminum plates (Merck KGaA, Darmstadt, Germany; silica gel 60, fluorescence indicator F_{254}) was used for routine monitoring of reactions; analysis was done using ultraviolet lamp (Merck KGaA, Darmstadt, Germany; 254 nm) or potassium permanganate reagent (1 g $KMnO_4$ and 5 g Na_2CO_3 in 250 mL water). Oven-dried glassware and Schlenk techniques were used in order to carry out reactions in inert atmosphere. Dry ice/acetone cooling bath (-78 °C) and an ice/water bath (0 °C) were used to maintain low temperatures for reactions. Screened FBS (Lot: 791291), Pen/Strep (10K units), Dulbecco's modified Eagle's medium/F12 (DMEM/F12), antibiotic-antimycotic, trypsin-EDTA, penicillin/streptomycin and L-glutamine were purchased from Gibco. Human embryonic stem cells (H9 and H1, NIH registration number#0062) were obtained from WiCell Research Institute, Madison, WI, http://www.wicell.org. Human-cell-conditioned media (HCCM)

was purchased from MTI-Global Stem, Gaithersburg, MD, http://www.mti-globalstem.com. Human recombinant basic fibroblast growth factor (bFGF) and Trizol Reagent was purchased from Invitrogen™, Carlsbad, CA, http://www.invitrogen.com. Falcon Tubes, Matrigel™ (Corning® hESC-Qualified Matrix, *LDEV-free, cat#354277) and 40 mm nylon mesh cell strainer were purchased from BD BioSciences. Accutase™ Cell Detachment Solution (cat#07920) was purchased from Stemcell Technologies, Inc. Bio-Rad protein assay (cat#5000006), Precision Plus Protein™ Dual Color Standards (cat#1610374), Towbin buffer (cat#1610734) and blotting-grade blocker (cat#1706404) was purchased from Bio-Rad, Hercules, CA. Novex™ Tris-Glycine SDS Running Buffer (10X, cat#LC2675-4), Novex™ WedgeWell™ format 4-20% Tris-Glycine Mini Gels (cat#XP04205BOX), XCell SureLock® Mini-Cell Electrophoresis System (cat#EI0001), Novex™ Wedgewell™ 10% Tris-Glycine Gels, Tween™ 20 (cat#BP337-100), SuperSignal™ West Pico PLUS Chemiluminescent Substrate (cat#34078), donkey anti-mouse IgG secondary antibody, Alexa Flour® 488 (cat#R37114), donkey anti-rabbit IgG secondary antibody, Alexa Flour® 594 (cat#A-21207), SuperScript™ VILO™ Master Mix (cat#11755050) and the primers used for qPCR were purchased from ThermoFisher Scientific. HyBlot CL film (cat#e3018) was purchased from Denville Scientific. The primary antibodies used for Western blot analyses were purchased from Cell Signaling. The secondary antibodies used for Western blot analyses were purchased from Promega. Z-Fix solution (cat#170) was purchased from Analtech Ltd. The primary antibodies used for immunofluorescence analysis are Oct 4 (Santa Cruz Biotechnology, goat, cat#sc8629), Nanog (Abcam, mouse, cat#ab62734), Sox2 (Millipore, rabbit, cat#ab5603). TaqMan Universal PCR Master Mix was purchased from Applied Biosystems. SSEA-4 PE-conjugated antibody and Mouse IgG1 phycoerythrin (PE) isotype Control was purchased from R&D systems. HematoStem SF Kit was purchased from PAA, Pasching, Austria. Anti CD34-PE-Cy7 and the respective isotype control were purchased from eBioscience, Frankfurt, Germany. CellTrace™ Violet Cell Proliferation Kit (Life Technologies). The remaining chemicals used were purchased from Acros Organics, Sigma-Aldrich, Alfa Aesar or ABCR and used as received unless otherwise stated.

3.2 Synthesis

3.2.1 Reversible Addition Fragmentation Chain Transfer Polymerization in solution

All polymerizations were performed in a Schlenk tube and V501 was employed as an initiator. Monomer, CTA, initiator (molar ratio of CTA/V501 = 5/1) in 0.5 M NaBr solution were placed in the sealed Schlenk tube and degassed by three freeze-pump-thaw cycles and refilled with argon. The reaction mixture is then heated in an oil bath at 70 °C. Applied reaction times ranged from 1-8 h. Then, the polymerization was halted by exposing to air and being immediately cooled in ice. The resultant solution was dialyzed in water for 48 h with water changed every 2 h to remove salt and unreacted monomers. The final polymers were obtained as a light pink solid after lyophilization.

3.2.2 Synthesis of azido-CTA

Azido-CTA was prepared by modification of a method previously reported[223]. 3-azidopropan-1-ol was synthesized prior to the synthesis of azido-CTA.

Synthesis 3-azidopropan-1-ol: In a 250 mL flask equipped with a reflux condenser, sodium azide (9.37 g, 144 mmol, 2 eq.) and 3-bromopropan-1-ol were dissolved in water (100 mL). The mixture was heated to 60°C and stirred for 24 h. After cooling to room temperature, the mixture was extracted with DCM (3×100 mL). The combined organic phases were dried over magnesium sulfate ($MgSO_4$). After removal of the solvent under reduced pressure, the crude product was purified by vacuum distillation (56°C, 5 mbar) to yield 3-azidopropan-1-ol as a colorless liquid (6.19 g, 61.2 mmol, 86%). ^{1}H-NMR (500 MHz, $CDCl_3$): δ = 3.75 (t, *J* = 5.6 Hz, 2H, C*H*$_2$OH), 3.45 (t, *J* = 6.6 Hz, 2H, C*H*$_2$N$_3$), 1.83 (quin, *J* = 6.3 Hz, 2H, CH$_2$C*H*$_2$CH$_2$), 1.65 (s, 1H, O*H*). ^{13}C-NMR (125 MHz, $CDCl_3$): δ = 59.9 (–, *C*H$_2$OH), 48.5 (–, *C*H$_2$N$_3$), 31.4 (–, CH$_2$*C*H$_2$CH$_2$).

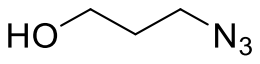

Synthesis of azido-CTA: In a 100 mL two-neck flask under an argon atmosphere, 3-azidopropan-1-ol (0.50 g, 4.95 mmol, 1.0 eq.), CPA (1.52 g, 5.44 mmol, 1.1 eq.) and 4-dimethylaminopyridine (70 mg, 0.57 mmol, 0.12 eq.) were dissolved in dry DCM and cooled to 0 °C. Over a period of 15 min, a solution of DCC (1.02 g, 4.95 mmol, 1.0 eq.) in dry

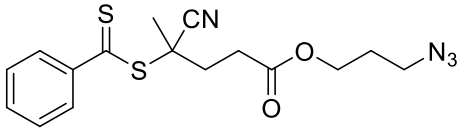

DCM (20mL) was added dropwise. The mixture was stirred for an additional 4 h at room temperature. Next, the reaction mixture was filtered to remove the formed urea byproduct. The organic phase was then washed with a 10% aqueous sodium bicarbonate solution (50 mL), water (50 mL), saturated NaCl solution (2×50 mL) and dried over $MgSO_4$. After removal of the solvent under reduced pressure, the crude product was purified by column chromatography (hexane/ethyl acetate 4:1, R_f = 0.41) to yield the target compound as a purple oil (987 mg, 2.72 mmol, 55%).

^{1}H-NMR (500 MHz, $CDCl_3$): δ = 7.92–7.90 (m, 2H, H_{Ar}), 7.59–7.56 (m, 1H, H_{Ar}), 7.42–7.39 (m, 2H, H_{Ar}), 4.21 (t, *J*= 6.2 Hz, 2H, COOC*H*$_2$), 3.41 (t, *J* = 6.6 Hz, 2H, C*H*$_2$N$_3$), 2.72–2.59 (m, 3H, C*H*$_2$C*H*$_2$COO), 2.46–2.40 (m, 1H, CH$_2$C*H*$_2$COO), 1.94–1.90 (m, 5H, CH$_2$C*H*$_2$CH$_2$, CC*H*$_3$). IR (ATR): $\tilde{\nu}$ = 2931 (w), 2094 (m), 1732 (m), 1589 (w), 1444 (m), 1378(w), 1291 (m), 1231 (m), 1178 (m), 1107 (w), 1080 (m), 1045 (m), 867 (m), 761(m), 686 (m), 650 (m), 616 (w), 576 (w) cm^{-1}.

MS (70 eV, EI), *m/z* (%): 362 (100) [M$^+$], 344 (20), 334 (51), 322 (29), 319 (20), 307 (11), 293 (16), 281 (17), 269 (35), 262 (43), 259 (25), 247 (92), 239 (33).

HRMS calculated for $C_{16}H_{18}N_4O_2{}^{32}S_2$ ([M$^+$]):362.0866; found: 362.0864 [M$^+$].

3.2.3 Benzaldehyde Initiator

The benzaldehyde initiator was developed by Dr. Artak Shahnas. In a typical run, 1 g of 3,5-hydroxybenzaldehyde (7.2 mmol, 1eq.) 3 g of trimethylamine (30 mmol) were dissolved in 20 mL of dichloromethane (DCM). The mixture was degassed by bubbling argon to the solution and cooled down in an ice bath. A solution of 3.4 g (14.6 mmol, 2 eq.) of 2-bromoisobutyryl bromide in 5 mL DCM was slowly added under argon flow using a dropping funnel. The reaction was then stirred for 4 h. The precipitated product was filtered and purified by column chromatography with mixtures of *n*-hexane/ethyl acetate (EtOAc) with a ratio of 6:1 yielding 2-bromo-2-methylpropionic acid 3-(2-bromo-2-methylpropionyloxy)-5-formyl-phenyl ester as a pale-yellow powder in 75 % yield (2.35 g, 5.4 mmol, 1 eq.). The successful synthesis of the initiator was proven by ^{1}H NMR in $CDCl_3$: δ = 10.0 (s, 1H, C***H***O), 7.61 (d, *J* = 2.4 Hz, 2H, Ar***H***), 7.29 (t, 1H, *J* = 2.4 Hz, Ar***H***), 2.08 (s, 12H, C***H***$_3$), ppm. - ^{13}C-NMR (125 MHz, $CDCl_3$): δ = 189.9 (***C***HO), 169.8 (***C***=O), 151.9 (***C***$_{Ar}$O),

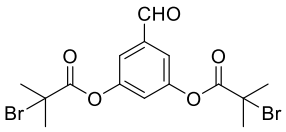

138.4 (***C***CHO); 120.7 (***C***$_{Ar}$); 120.0 (***C***$_{Ar}$), 54.8 (***C***Br), 30.6 (***C***H_3) ppm. HRMS (EI) *m/z* $C_{15}H_{17}O_5Br_2$, calculated: 436.0960, found: 276.0686.

3.2.4 Procedure for ATRP of IGT

Poly[2-(methacryloyloxy)ethyl dimethyl-(3-sulfopropyl)ammonium hydroxide] (PMEDSAH) was polymerized using an ATRP procedure. MEDSAH (2.8 g, 10 mmol) and the benzaldehyde initiator (43.6 mg, 0.1 mmol) were dissolved in a methanol/water (4/1 v/v) solvent mixture (previously degassed by four freeze-vacuum-thaw cycles) and placed in a Schlenk tube reactor. Subsequently, CuBr (14.3 mg, 0.1 mmol), $CuBr_2$ (2.2 mg, 0.01 mmol) and ligand 2,2'-bipyridyl (bpy, 46.9 mg, 0.3 mmol) were added to the solvent in another Schlenk tube reactor. Both tubes were placed under argon atmosphere and stirred. After the catalyst and the ligand were fully dissolved, the catalyst solution was added to the monomer reaction mixture and the reaction proceeded at room temperature with stirring. 0.1 mL aliquot samples were taken during the polymerization using an airtight syringe and purging the side arm of the Schlenk tube reactor with argon.

The samples were analyzed by ^{1}H NMR spectrometry to determine the monomer conversion and SEC to determine the molecular weight and molecular weight distribution of the polymer samples. The solvent was removed and PMEDSAH was re-dissolved in TFE and passed through a neutral alumina column to remove the metal catalysts. The sample was concentrated under reduced pressure in a rotary evaporator and dialyzed against water. The final product was obtained by freeze drying. δ ^{1}H NMR (500 MHz, D_2O): 10.01 (s, C**H**O, 1H), 7.72 (s, aromatic, 2H), 7.35-7.29 (d, aromatic, 2H), 4.54 (s, C**H**$_2$CH$_2$N), 3.85 (s, *J* = 107.5 Hz, CH$_2$C**H**$_2$N), 3.63 (s, NC**H**$_2$CH$_2$), 3.27 (s, N^+(C**H**$_3$)$_2$), 3.01 (s, NCH$_2$C**H**$_2$), 2.3 (s, CH$_2$C**H**$_2$S), 2.1-1.73 (m, C**H**$_3$CBr), 1.43-1.31 (d, C**H**$_3$, 12H), 1.25-1 (m).

3.2.5 Sample preparation for Structural Characterizations

Polymer solutions were prepared in D_2O. The polymer concentration was 3 g L^{-1} for turbidimetric measurements. All solutions were equilibrated for about 12 h at the starting temperature of measurement. Cloud points were determined using a Cary 300 Bio UV-vis photospectrometer (Varian) equipped with a temperature-controlled sample cell. Absorption was

measured at a wavelength of 522 nm at temperatures ranging from 5 to 40 °C (using a 0.5 °C min^{-1} heating rate).

3.3 Instrumentation

3.3.1 Nuclear Magnetic Resonance spectroscopy (NMR)

^{1}H NMR (500 MHz) and ^{13}C NMR (125 MHz) spectra were collected on a Bruker Avance III spectrometer using $CDCl_3$ or D_2O as solvent. Chemical shifts are reported in parts per million (ppm, δ) downfield from tetramethylsilane (TMS) using the residual solvent as internal standard ($CDCl_3$, 7.26 ppm; D_2O, 4.8 ppm). All coupling constants are absolute values, and *J* values are expressed in Hertz (Hz). The description of the signals includes s = singlet, d = doublet, dd = doublet of a doublet, ddd = doublet of a doublet of a doublet, m = multiplet. The spectra were analyzed according to first order. Theoretically expected number-average molecular weight, $M_{n,theo}$ for RAFT polymerizations are calculated according to

$$M_{n,theo} = \frac{c_M}{c_{CTA}} conversion \times M_M + M_{CTA} \quad (12)$$

where M_M is the molar mass of the monomer, M_{CTA} = RAFT agent molar mass, c_M = molar concentration of the monomer, and c_{CTA} = molar concentration of the RAFT agent.[224] Theoretically expected number-average molar molecular weight, $M_{n,theo}$ for ATRP are calculated according to

$$M_{n,theo} = \frac{c_M}{c_{initiator}} conversion \times M_M + M_{initiator} \quad (13)$$

where $c_{initiator}$ is the molar concentration of the ATRP initiator and $M_{initiator}$ is the molecular weight of the ATRP initiator.

3.3.2 Size exclusion chromatography (SEC)

Size exclusion chromatography (SEC) analysis was performed using water SECcurity^2 GPC system (PSS) with a UV-Vis and refractive index (RI) detectors consisting of a NOVEMA Max 10 µm guard column. Flow rate was set at 1 mL min^{-1}. The eluent used was 80% 0.5 M aqueous NaBr / 20% acetonitrile. The tests were conducted at 30 °C. Before injection (50 µL), the samples were filtered through a poly(tetrafluoroethylene) (PTFE) membrane with 0.2 µm pore. The M_n and

Đ of the polymer were determined by calibration with linear polyethylene glycol (PEG) standards between 600 and 970000 g mol^{-1}.

3.3.3 Differential scanning calorimetry (DSC)

DSC was performed using differential scanning calorimeter Netzsch STA 449 C. The samples with a weight of about 12 mg were put into an aluminum pan and hermetically sealed. The scans were carried out under nitrogen atmosphere. The samples were preliminarily heated from 35 to 450 °C, at a heating rate of 10 K min^{-1}. Thermograms were recorded and, among others, glass transition temperatures, crystallization temperatures and melting temperatures were evaluated.

3.3.4 Dynamic Light Scattering (DLS)

The size of the polymers dissolved in water at a concentration of 10 mg ml^{-1} were determined by DLS using Malvern Zetasizer Nano ZS (Malvern, Germany) equipped with a He-Ne laser (λ = 633 nm, max 4 mW) and operated at a scattering angle of 173°. In all measurements, 1 ml of polymer solution was employed in a 3 ml disposable polystyrene cuvette. The polymer solutions were filtered through 0.22 µm syringe filters (Millipore corporation) prior to measurements. Sample temperature was maintained at 25 °C.

3.4 Surface Preparation and Characterization

3.4.1 Surface Preparation

Silicon wafers with a native oxide layer (Siegert Wafer GmbH, Aachen, Germany) were cut into 10 × 10 mm^2 pieces using a diamond-tipped cutter. Silicon wafers were first silanized with 3-(trimethoxysilyl)-propyl methacrylate. Gold wafers were prepared on silicon wafers by physical vapor deposition, with 5 nm titanium followed by 100 nm of gold. Gold wafers were first cleaned with acetone, ethanol and deionized water, and air dried. 35 mm Tissue culture polystyrene (TCPS) petri dishes (Thermo Scientific) were used as received. Cover glasses (25 mm × 25 mm, VWR) were first cleaned with 100% ethanol (VWR), rinsed with deionized water, and air dried. PDMS samples were prepared by uniformly mixed PDMS prepolymer and curing agent (Sylgard 184, Dow Corning) at a ratio of 10:1 and were cured at 70°C for 1 h.[225]

3.4.2 Chemical vapor deposition polymerization of reactive coatings

A custom chemical vapor deposition (CVD) system composed of a sublimation zone, pyrolysis zone, and deposition zone was used to generate polymer coatings.[226] For UVO-initiated free radical polymerization application, reactive CVD coatings of parylene N (PPX-N) were developed as platforms for human stem cell growth. In this instance, gold and silicon substrates were used as surrogates for the cell culture substrates in subsequent materials characterization.

For RAFT polymerization application, around 80 mg of the precursor, PCP-alkyne[11] was sublimed at 100-120 °C under reduced pressure (0.1 mbar) and then pyrolyzed at 510 °C. Substrates were placed on a cooled stage (15 °C) to promote the physical adsorption of radical species on its surface. Subsequently, the radical species underwent polymerization to form coatings composed of poly[(*p*-xylylene-4-methyl propiolate)-*co*-(*p*-xylylene)] (PPX-alkyne).

The ATRP initiator coatings were deposited onto the substrates via spontaneous polymerization in the form of a thin film bearing bromoisobutyryl ester groups for subsequent ATRP initiation.[166] The starting material was [2.2]paracyclophane-4-methyl-2-bromoisobutyrate. The starting material was sublimed at 120 °C, followed by pyrolysis at 540-550 °C, and the materials were deposited in converted form as poly[(*p*-xylylene-4-methyl-2-bromoisobutyrate)-*co*-xylylene] (ATRP initiator coating). Deposition occurred on gold, silicon, and TCPS plates via spontaneous polymerization. The working pressure during the polymerization was 0.3 mbar and the deposition occurred on a rotating sample holder that was maintained at 15 °C.

Poly[(4-formyl-*p*-xylylene)-*co*-(*p*-xylylene)] (PPX-aldehyde) was first deposited onto the substrates (silicon, gold wafers, glass, polystyrene slides or TCPS) via spontaneous polymerization in the form of a thin film bearing reactive aldehyde groups on the surface.[227] 14 mg of 4-formyl[2.2]paracyclophane precursor was sublimed at 100-120 °C, underwent pyrolysis at 660 °C, after which a thin film of poly[(4-formyl *p*-xylxlene)-co-(*p*-xylylene)] was coated on target substrates. The TCPS, silicon, gold or glass substrates were placed on a cooled sample holder at 14 °C for polymer deposition. Sample holder was rotated to ensure uniform polymer deposition.

3.4.3 Ultraviolet/Ozone-Initiated Free Radical Polymerization

A 10 L reaction vessel was degassed via vacuum/argon purge. The cycle was repeated three times. While the reaction vessel was being evacuated, the solvent system consisting of a deionized

water/ethanol mixture (4:1 v/v) was purged with argon for 40 min. The solvent and the monomer MEDSAH at 0.06 g/ml were added to the reaction vessel after degassing, and heated to 68 °C. Free radicals were generated on the surface of TCPS plates to create initiation sites by exposing them to a 25 min UV/ozone treatment (Jetlight Inc.) prior to polymerization. Silicon and gold substrates with poly(p-xylylene) coatings were also treated with UV/ozone. These substrates were used to measure thickness and contact angle. After free radicals have been generated, TCPS and poly-p-xylylene substrates were placed in the reaction vessel and heated such that the temperature was raised to 77 °C. The polymerization occurred on the substrates over a 2.5 h time period under argon atmosphere. Once the process was complete, the substrates were removed rinsed overnight with a 1% saline (w/v) solution that was maintained at 50 °C to remove any excess monomer. Subsequent rinsing with 1% saline and deionized water ensured the removal of unreacted monomer.[228]

3.4.4 Immobilization of RAFT agent

10 mM azide-functionalized RAFT agent (azido-CTA) dissolved in ethanol was introduced onto PPX-alkyne surface. The substrate was placed under argon at 50 °C for 48 h. After the reaction, the surface-modified reactive polymer coating was thoroughly washed with copious amounts of EtOAc followed by ethanol to remove the residual azido-CTA. Finally, the CTA-modified reactive polymer coating (S-CTA) was dried and stored under argon.

3.4.5 Surface-Initiated RAFT Polymerization

After azido-CTA immobilization, the S-CTA substrates were subjected to SI-RAFT polymerization using typical Schlenk techniques. For the SI-RAFT polymerization of MEDSAH, the following procedure was employed. A solution of MEDSAH (0.1 g L^{-1}), free RAFT agent 4-Cyano-4-(phenylcarbonothioylthio)pentanoic acid (CPA) (0.5 mmol L^{-1}), initiator 4,4'-azobis(4-cyanovaleric acid) (V-501) (0.05 mmol L^{-1}) and a 1:1 2,2,2-trifluoroethanol (TFE)/water (v/v) mixture was prepared in a two-neck round bottom flask. V-501 was recrystallized from methanol before use. The mixture was degassed by three consecutive freeze-pump-thaw cycles, backfilled with argon and then transferred into each of 4 degassed Schlenk tubes containing the S-CTA substrates (3 mL/substrate). The reactions were carried out in a preheated oil bath at 80 °C. At designated time intervals, one vial was removed to determine percent monomer conversion and

molecular weight of the polymer in solution. Following polymerization, the modified substrates were washed with TFE, water and dried in a stream of argon. The polymer in solution was dialyzed against water and freeze dried for purification. Typical polymerization times for PMEDSAH brushes were 2-8 h.

3.4.6 Procedure for SI-ATRP of zwitterionic monomers

In a typical SI-ATRP run, a 25 mL Schlenk tube was charged with 60 mg (418 μmol) of CuBr, 10 mg (45 μmol) of $CuBr_2$ and 168 mg (1 mmol) of bpy. Another Schlenk flask was charged with 1 M monomer. Both the flasks were sealed with a rubber stopper and cycled between vacuum and argon three times to remove oxygen. The substrates were placed in individual degassed vials. A 20 mL solution of methanol/deionized water (4/1 v/v) in a Schlenk flask was degassed via three freeze-pump-thaw cycles. The degassed solution was then transferred to both the flasks via a syringe to prevent atmospheric contamination. After the catalyst was fully dissolved, the reaction solution from both the flasks were transferred to the vials containing the ATRP initiator-coated substrates.

3.4.7 Linker Immobilization

The substrate was incubated in acetate buffer containing adipic acid dihydrazide (500 mM, pH 4) overnight. Then, the substrates were washed repeatedly with deionized water.

3.4.8 Patterning of interfacial Gemini transporter

A solution containing PMEDSAH (20 μg/mL) in acetate buffer (pH 4) was prepared. This polymer solution was spread on PPX-aldehyde coatings and the substrates were dried using argon. Patterned PDMS stamps (square islands of 250 μm × 250 μm) were created as previously described.

3.4.9 Protein Adsorption & fluorescence microscopy

Fluorescein isothiocyanate-labeled bovine serum albumin (FITC-BSA) were dissolved in 10 mM phosphate buffer saline (PBS) solution (pH=7.4) at concentrations of 250 μg/ml. Glass cover slips patterned with interfacial Gemini transformer were incubated in the solution and was shaken at room temperature in the dark for 30 min. The patterned substrates were rinsed copiously

with PBS solution and water and blown dry in a stream of argon and then directly analyzed under a fluorescent microscope (Axiovert 200M, Carl Zeiss, Jena, Germany). The images were analyzed with the help of the AxioVision 4.8.2. software. Exposure time of 500 ms was used.

3.4.10 Surface Characterization Methods: Ellipsometry, Infrared Reflection Adsorption Spectroscopy, Water Contact Angle Goniometry and Atomic Force Microscopy

Thickness measurements using ellipsometry

Film thickness of the different coatings was measured by ellipsometry using a multi-wavelength rotating analyzer ellipsometer (J. A. Woollam M2000, wavelength range 400-800 nm, Woollam Co., Inc., Lincoln NE, USA) at an incident angle of 65°. It was operated at a wavelength of $\lambda = 532$ nm. The experimental data was evaluated using the CompleteEASE software program. Film thickness measurements were collected by fitting for the ellipsometric delta and psi values using a Cauchy dispersion multilayer model (Air, polymer brush, initiator, SiO_2, Si) with fixed values of the real and imaginary refractive index of the PMEDSAH coatings ($n = 1.58$ and $k = 0$).

Infrared Reflection Adsorption Spectroscopy

To verify whether the desired materials were present on surfaces, infrared reflection adsorption spectroscopy (IRRAS) was performed. We used a Bruker Vertex 80 spectrometer (Bruker Optics, Ettlingen, Germany) in the grazing angle configuration equipped with a liquid nitrogen cooled mid band MCT detector. SAMs of perdeuterated 1-hexadecanethiol on gold were used as a background. Gold wafers were coated with the desired material and scans were collected from 600 to 4000 cm^{-1} with a resolution of 4 cm^{-1} at an incidence angle of 80°. A baseline, smoothing, and carbon dioxide peak correction were applied to the spectra.

Atomic force microscopy

Roughness of the surfaces was measured at room temperature with the MFD-3D-BIO (Asylum Research, USA). Measurements were taken in tapping mode at room temperature in air. A Multi75Al-G (BudgetSensors, Bulgaria) probe tips with resonant frequency of 75 kHz and spring constants of 3 N m^{-1} were used for the analysis. Surface roughness measurements were taken at 0.1 Hz scan rate over a 20×20 μm^2 and 1 Hz scan rate over a 2×2 μm^2 area. AFM software

(Asylum Research) was utilized to calculate root mean square roughness (R_q). Three values were taken for each sample and averaged.

Contact angle measurements

Contact angle of a liquid drop is determined by the outermost atomic layers of a surface (0.1-1 nm). When a drop of liquid is placed on a solid substrate, the drop shape will change under the pressure of the different surface tensions around the perimeter of the drop, until equilibrium is reached.

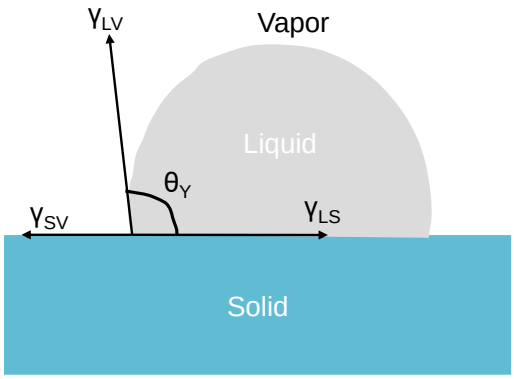

Figure 3.1: Components of interfacial tension used to derive Young's equation

In 1805, Thomas Young expressed the three-phase equilibrium in terms of the vector sum shown in Figure 3.1, resulting in the following equation of the interfacial equilibrium.[229]

$$\gamma_{SV} - \gamma_{SL} = \gamma_{LV} cos\theta_Y \quad (14)$$

The Young contact angle θ_Y is defined as the angle (measured in the liquid) that is formed at the junction of three phases, typically the solid-liquid-gas junction. In this dissertation, static contact angles were taken using a contact angle goniometer (Krüss DSA 100, Germany). Measurements were taken at three different locations on the same sample and averaged.

3.4.11 X-ray Photoelectron Spectroscopy

X-ray photoelectron spectroscopy (XPS) is a highly sensitive surface analytical technique. A surface is irradiated with photons from a soft X-ray source, exciting the electrons in the surface region. The excited electrons, called the photoelectrons are ejected from the atom. They escape the

surface with a kinetic energy (E_k) proportional to the difference between the incident photon energy (E_{hv}) and the binding energy of the electron to the nucleus (E_b) which can be described using Equation 14.[230]

$$E_k = E_{hv} - E_b - E_\Psi \tag{15}$$

where E_Ψ is the work function of the analyzer. E_k can be measured by an energy analyzer and E_Ψ is a constant and is known for a certain system.

Although X-rays can penetrate micrometers below the surface, only photoelectrons produced at the surface contribute to the XPS signals. The sampling depth of the XPS measurement varies with the E_k of the electrons being used. The average distance that electrons travel in the solid surface without undergoing an inelastic collision is the inelastic mean free path (λ) (Figure 3.2).

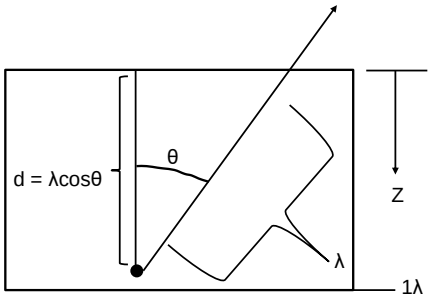

Figure 3.2: Electron attenuation depth d, inelastic mean free path λ and emission angle θ.

The sampling depth is determined by electron attenuation length, d:

$$d = \lambda cos\theta \tag{16}$$

where θ is the angle at which particles leave a specimen with respect to the normal to the specimen surface (z). Typical sampling depth is approximately 3d. The energy range of interest in XPS is 200-2000 eV. In that range, d is < 10 nm. That is the reason why XPS is highly surface specific. The sensitivity of the XPS measurement is dependent on the spectra background level and the photoelectron cross section.[231] Almost all elements in the periodic table after helium onwards can be measured.[232] XPS can be applied to all vacuum compatible materials.

In this dissertation, XPS was performed on a K-Alpha XPS spectrometer (Thermo Fisher Scientific, UK) equipped with a monochromated Al Kα X-ray source. The analysis region was a 400 μm spot size. A180° hemispherical energy analyzer operated in the constant analyzer energy mode (CAE) at 50 eV pass energy was used to measure the kinetic energy of the electrons for the survey elemental spectra. Thereafter elemental composition was determined by performing high resolution scans using the K-Alpha charge compensation with a pass energy of 8 eV, and low-energy argon ion beam was employed to prevent any localized build-up. The spectra were fitted with Voigt profiles (BE uncertainty ± 0.2 eV) and Scofield sensitivity factors were employed for quantification.[233] All spectra were referenced to the C_{1s} peak (C–C, C–H) at 285.0 eV binding energy controlled by the photoelectron peaks of Ag, Cu and Au. Data collection and analysis were performed using the Thermo Avantage software.[234]

The potential for the use of XPS in mapping is to identify regions of differing chemical structure in a sample surface, with a spatial resolution of the order of 15 μm.[235] XPS mapping is done by collecting images across a two-dimensional field-of-view, rectangular array of small-area XPS spectroscopy. At each pixel, a spectrum can be extracted and distribution of elements or chemical states at that pixel can be measured.[235] In this dissertation, The K-Alpha+ snap map option was used to image the different structures with a spot of 100 μm. (5 iterations were run to reach a better statistic). The obtained spectra were collapsed over the iterations and fitted with help of a principal component analysis routine to increase the quality of the images.

3.4.12 Tof-SIMS

Time-of-Flight Secondary Ion Mass Spectrometry (ToF-SIMS) provides detailed molecular and chemical information from the analyzed surface with an information depth of about 1-2 nm.[236] That makes it a powerful technique to study organic fragments with high mass and spatial resolution.[237] A focused, pulsed ion beam from a primary ion source (Bi cluster liquid metal or microfocused Ga) under ultrahigh vacuum conditions is used to bombard the surface of a material and dislodge molecules from the top 1-2 nm of the surface.[238] The resultant particles produced are then accelerated into a time of flight analyzer and their masses are determined by measuring the exact time at which they reach a detector.[238] The exact time can be detected on a scale of nano-seconds, producing high mass resolution, with a lateral resolution down to 100 nm.[239] Single ions (positive or negative) are generated from the closest impact site. Secondary ion mass spectra are

obtained by analyzing the mass to charge (m/z) ratio of the molecular fragments. The ToF-SIMS analysis collects both a positive and negative spectrum to give the complete picture over 1000 m/z. Figure 3.3 schematically shows how primary ion beams interact with a sample to remove material from the surface.

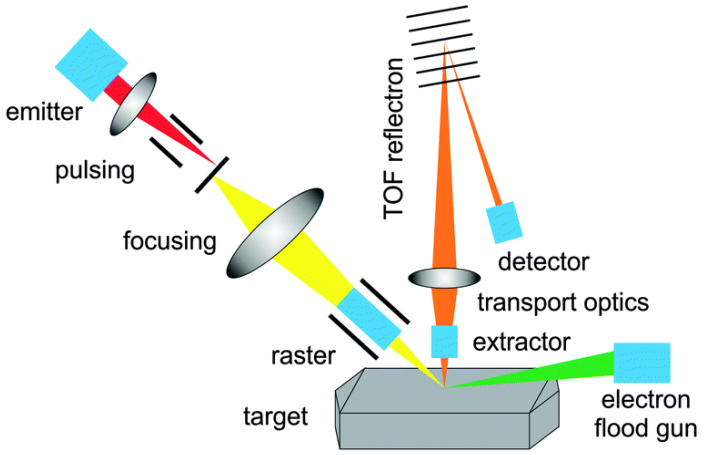

Figure 3.3: In Tof-SIMS, high energy focused beam is used to bombard the surface liberating single ions (positive and negative) and molecular fragments. Reproduced with permission from Hofmann *et al.*[240].

In this dissertation, ToF-SIMS experiments were performed using a TOF.SIMS5 instrument (ION-TOF GmbH, Munster, Germany). This spectrometer is equipped with a Bi cluster primary ion source and a reflectron type time-of-flight analyzer. The analysis beam used for this study was a Bi source providing short, pulsed 25 keV energy Bi_3^+. A high lateral resolution of approximately 4 μm, and a target current of 0.1 pA at a repetition rate of 5 kHz was maintained. Bi was set in the "bunched high current" mode for depth profiling (short pulses, high mass resolution). Samples were pumped down till the pressure in the analysis chamber was less than 5×10^{-8} mbar. The short pulse length of 0.8 ns allowed for high mass resolution. Primary ion doses were kept below 10^{11} ions cm^{-2} (static SIMS limit) for all measurements. Bi_3^+ was typically rastered over a 300 × 300 μm^2 area on the sample. 128 × 128 data points were recorded. Spectra were calibrated on the omnipresent C^-, CH^-, CH_2^-, OH^-, or on the C^+, CH^+ and CH_3^+ peaks. Based on these datasets the chemical assignments for characteristic fragments were determined. Bi was set in the "burst

alignment" mode for high lateral resolution imaging, providing long pulses and nominal mass resolution. Here, 100 × 100 μm^2 fields of view on the sample were analyzed, and 128 × 128 data points were recorded.

3.4.13 Streaming potential measurement

Most materials have charge-bearing surfaces that are sensitive to electrostatic effects.[241] When a charged surface is introduced into an ionic solution, the balancing counter charges from the solution concentrate near the charged surface. An electrical double layer model is used to describe the ionic environment near the charged surface. The charges will not be uniformly distributed throughout the liquid phase. The concentration of ions will be higher near the surface, and the concentration will decrease as the distance away from the charged surface is increased. This forms the diffuse layer. Some of the ions are specifically adsorbed by the surface. The layer between the charged surface and the diffuse layer where the adsorbed ions are present is called the Stern layer. The potential at the Stern layer is known as the zeta (ζ)-potential.[242,243] ζ-potential indicates the electric surface properties of a material. Typically, streaming potential measurements are used for the determination of ζ-potential of surfaces.[244]

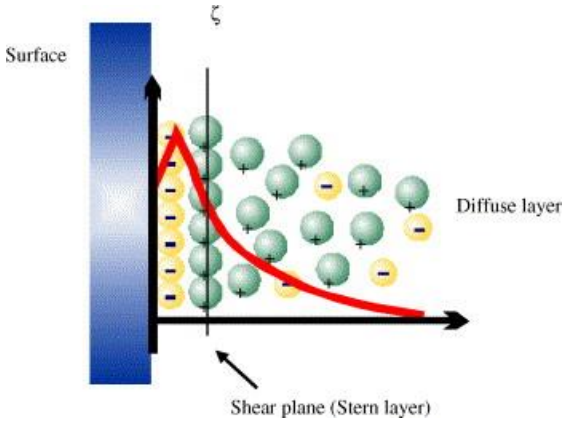

Figure 3.4: Schematic diagram of electrical double layer model at the surface. Bright grey (positive) and yellow (negative) ions from the ionic solution concentrate near the charged surface introduced in the ionic solution. This layer is called the Stern layer. The concentration of ions decreases further from the surface towards the extended liquid phase. The liquid phase between the surface and the extended liquid is called the diffuse layer. The potential between the Stern layer and the diffuse layer is known as the ζ-potential. Reproduced with permission from Cai *et al.*[245]

In this work, streaming current measurements for multiple pH values were collected by Dr. Ramya Kumar. Polymer coatings were prepared as described previously. Measurements were performed with a SurPASS (Anton Paar GmbH) electrokinetic analyzer. A clamping cell was used in asymmetric mode[246] to acquire all measurements from the sample across a pH range of 3 to 6. Polypropylene foil was used as reference. A gap of 100-120 µm was maintained between the sample and the polypropylene reference standard. For each sample, titration was performed from the neutral to the acidic range using 0.1 M hydrochloric acid as the titrant and 0.001 M potassium chloride solution as the electrolyte. The pH value was controlled using an automated titration unit, which effected pH ranges in increments of 0.3, while the electrolyte solution was stirred continuously. Streaming current was measured with a pair of reversible Ag/AgCl electrodes. The Helmholtz-Smoluchowski equation[247] was applied to compute the ζ-potentials. The streaming current was measured and recorded at a pressure of 400 mbar, with flow rates of 50-70 ml min^{-1}. The electrolyte solution was purged continuously by bubbling nitrogen gas to prevent carbon dioxide dissolution and unintended changes in the pH value. Samples were rinsed 3 min before each measurement to equilibrate the surface against the electrolyte solution.

3.5 Cell Culture

hMSC (a kind gift from Dr. Paul Krebsbach, University of Michigan) are cultured for 7 days on the various ATRP surfaces and the cell culture work for hMSC was completed together with Dr. Thomas Eyster. The media utilized was comprised of the following: alpha-MEM + 10% Screened FBS + 1% Pen/Strep. In this instance, UVO-grafted PMEDSAH is utilized as control. hMSC were seeded at a density of 6000 cells/cm^2 and were initially fed after 24 h and subsequently fed every 48 h thereafter.

hESC culture work was done by Dr. Xu Qian and Dr. Tugba Topal. Undifferentiated human embryonic stem cell (H9) colonies were washed with D-PBS and incubated with accutase non-enzymatic cell attachment passaging solution for 5-10 min at 37 °C for gentle dissociation of colonies. Lifted cells were collected with Accutase™ solution and HCCM was added. The solution was briefly centrifuged. The cell pellet was then dispersed in HCCM supplemented with 5 ng/mL of human recombinant bFGF and 10 mM ROCK inhibitor.[248] The cell aggregates were removed by passing the solution through a 40 mm nylon mesh cell strainer. 20,000 cells/mL were then plated on various ATRP surfaces, IGT-modified substrates and Matrigel-coated substrates and the

cells were cultured for 7 days. Culture medium was changed every second day. Differentiated cells were mechanically removed using a sterile pulled-glass pipet under a stereomicroscope (LeicaMZ9.5, Leica Microsystems Inc., Buffalo Grove, IL).

HSC culture and analyses were performed by Dr. Lisa Rödling. Umbilical cord blood (UCB) was obtained from the Cord Blood Bank of the German Red Cross (Mannheim, Germany) with ethics approval obtained from the local ethics committee (Ethik-Kommission bei der Landesärztekammer Baden-Württemberg, B-F-2013-111) and written informed consent of parents. After isolation, $CD34^+$ HSCs was determined by flow cytometry; cells were subjected to experiments if a minimum of 95% of the cells were $CD34^+$. The freshly isolated $CD34^+$ HSCs were cultivated in HematoStem SF Kit with 1% (v/v) penicillin/streptomycin, 2 mM L-glutamine.

"Interfacial Gemini Transformer" surface preparation

IGT-modified substrates were sterilized with UV-light overnight and washed with sterilized Dulbecco's phosphate buffer saline (D-PBS). Then the substrates were equilibrated with human cell-conditioned medium (HCCM) overnight before cell seeding at 37 °C in 5% CO_2 atmosphere.

Preparation of Matrigel-coated substrates

Matrigel preparation was done by Dr. Tugba Topal. Matrigel™, the gold standard in hESC culture is used as control. Matrigel™ was diluted to a concentration of 0.1 mg/mL in cold Dulbecco's modified Eagle's medium/F12 (DMEM/F12) and then applied to glass bottom TCPS dishes (35 mm, 10 mm glass diameter).[248] The coating polymerized during 2 h incubation at room temperature or 1 h at 7 °C. Excess Matrigel-DMEM/F12 solution was aspirated before plating cells, and the dishes were then washed with sterilized D-PBS.

3.5.1 Analysis of human pluripotent stem cell culture

The morphology, attachment, and differentiation of hMSC and hESC were evaluated. hMSC analysis was done along with Dr. Thomas Eyster. hESC analysis was done by Dr. Xu Qian and Dr. Tugba Topal. Morphology was assessed by determining the average cell area. For phalloidin staining, cells on UVO-grafted and ATRP PMEDSAH coatings were fixed in 4% paraformaldehyde at room temperature for 30 min and washed twice in PBS (5 min each) followed

by blocking in 1.5% BSA for 30 min. The resulting cells were stained with phalloidin (1:500 dilution from 1000× stock) and Hoechst 33342 (1 µm) in PBS for 1 h at room temperature followed by three additional washes in PBS (5 min each). Images of the cells were taken after 7 days of culture with the Nikon TE2000-S inverted microscope with a Nikon DS-Ri1 camera, and then Image J software (v1.48, NIH) was used to analyze the images. The area of hMSC was found by counting the total number of cells (as indicated by the number of DAPI stains) and dividing this number by the total cell area which is measured using the software. For hESC colonies, Image J software was used to quantify fluorescent intensity.[249,250] An outline was drawn around each cell, and area, integrated density and mean gray value was analyzed. Then several adjacent background readings were selected. The corrected total cell fluorescence (CTCF) was calculated.

CTCF = integrated density – (area of selected cell × mean fluorescence of background readings)

Cell attachment for hMSC was found by counting the number of cells/colonies present on the surface after 7 days culture.

3.5.2 Flow cytometry analysis

Flow cytometry was used to assess cell-surface expression of pluripotent markers. hMSC flow cytometry was done along with Dr. Thomas Eyster. After 7 days of proliferation in complete media (α-MEM + 10% FBS + 1% penicillin/streptomycin), the hMSC cells were trypsonized and labeled with 1 µg/ml of antibody conjugated with a fluorescent marker. Specifically, CD73 (PE), CD166, and CD105 (PE) are used as positive pluripotent markers for hMSCs. Hematopoietic stem cell markers CD34 (FITC) and CD45 (FITC) are also utilized as negative controls. Prior to flow analysis on the stained cells, cells that have not been stained are assessed in order to calibrate the baseline for subsequent measurements.

hESC flow cytometry was done by Dr. Xu Qian. After week 5, hESC cultured on different substrates were washed with PBS and harvested by incubation in 0.25% trypsin-EDTA. The trypsinization reaction was stopped by adding 1 ml HCCM. The cells were then incubated first with human IgG to block non-specific binding, washed and then incubated with human/mouse SSEA-4 PE-conjugated antibody, washing was repeated and then analyzed by flow cytometry. MoFloR® Astrios™ (Beckman Coulter) was used for analysis using standard procedures.

Background fluorescence and autofluorescence were recorded using cells incubated with Mouse IgG1 PE isotype control.

HSC flow cytometry was done by Dr. Lisa Rodling. For HSC, flow cytometry was applied to analyze CD34 expression and proliferation. To label CD34, 2×10^4 cells were stained with anti CD34-PE-Cy7 and the respective isotype control for 30 min on ice. After washing the cells were analyzed on a Cytomics FC 500 flow cytometer (Beckman Coulter, Krefeld, Germany).

3.5.3 Cell Trace Violet-Proliferation Assay

For analysis of cell divisions undergone during culture, the cells were stained with the CellTrace Violet Cell Proliferation Kit. In brief, freshly isolated HSCs were stained with 5×10^{-6} M CelTrace Violet in 1000 µL 0.1% (v/v) FBS in PBS and incubated for 20 min at 37 °C and 5%CO_2. 5 mL cold 10% (v/v) FBS in PBS was added to stop the reaction. After 5 min of incubation on ice the cells were resuspended in the appropriate medium and used for further experiments, following which the CellTrace Violet staining of the cells was analyzed by flow cytometry.

3.5.4 Western blot analysis

Western blot analysis was performed by Dr. Tugba Topal according to a procedure previously reported.[248] Cells were collected, washed once with PBS and lysed with NP-40 lysis buffer (150 mM NaCl, 1% NP-40 (w/v) and 50 mM Tris-HCL, pH 8), passed through a 30-gauge syringe 10 times and incubated in ice for 10 minutes to generate a whole cell lysate. Lysates were then centrifuged at 10,000 × *g* for 30 minutes. The supernatant was quantified for protein concentrations using the Bio-Rad protein assay with the Biotek Nova Spectrophotometer at 595 nm wavelength. 10 µg of protein lysate was mixed with 3X Laemmli loading buffer (0.125 M Tris-HCl; pH 6.8, 4% SDS, 20% glycerol, 0.004% bromophenol blue, 10% 2-mercaptoethanol) for using in SDS-PAGE. 10 µL of Precision Plus Protein Dual Color Standards were loaded in one lane for molecular weight estimation from 10-250 kDa. Novex™ Tris-Glycine SDS Running Buffer (10X) was diluted to 1X with milliQ filtered deionized water. The protein lysates were separated by electrophoresis on Novex™ Wedgewell™ 4-20% Tris-Glycine Gels and XCell SureLock® Mini-Cell Electrophoresis System. at 150 V for 85 min.

For optimal separation of proteins ranging from 50-75 kDa for S6 kinase 2 (S6K2) phosphorylation immunoprecipitation analysis, the Novex™ Wedgewell™ 10% Tris-Glycine Gels were used. Resolved proteins were transferred onto hydrophobic polyvinylidene difluoride (PVDF) membranes wetted with 100% methanol in Trans-Blot® SD semi-dry transfer cell (Bio-Rad, cat#170-3940) for 60 min at 24 V constant using 1X transfer buffer (25 mM Tris, 192 mM glycine, 20% methanol (v/v), 0.5% SDS at pH 8.3). After the transfer, the membranes were blocked with 2.5% blocking solution in 50 mL 1X Tris-buffered saline, 0.1% Tween20 (TBST, 50 mM Tris-HCl (pH 7.5), 150 mM NaCl, Tween 20) for 30 min at room temperature, followed by extensive washing with 1X TBST for 30 min.

Before incubating the antibodies, the membranes between the 75 kDa and 100 kDa bands were cut to optimize for proteins above 100 kDa in size, above 75 kDa and above the 37 kDa membrane for proteins within those ranges, and between 20-25 kDa for proteins above and below those ranges.[248] This allows for optimal antibody incubation with the appropriate membranes. The membranes are then incubated with primary antibodies overnight at 4 °C on a shaker. Then the membranes were washed with 1X TBST for 30 min (3 times). All washing, and antibody incubation steps were done on a shaker at room temperature to ensure even agitation. Next, the appropriate secondary antibody was added and incubated for 1 h. The membranes were washed with 1X TBST for 30 min. For visualization, membranes were incubated with ECL plus substrate for 3 min at room temperature and exposed to HyBlot CL autoradiography film. The primary antibodies used for Western blot analyses are: Oct4, Sox2, KLF4 and PRDM14. 1:1000 dilution of primary antibodies in 5% BSA in 1X TBST buffer with 0.04% sodium azide were used. Rabbit antibodies were used. Secondary antibodies for Western blot analyses: α-mouse IgG (H+L) HRP conjugate (1:4000 dilution), α-rabbit IgG (H+L) HRP conjugate (1:7500 dilution).

3.5.5 Cell immunofluorescence analysis

hESC on Matrigel coated substrates and IGT modified substrates were washed once with PBS for 5 minutes and the supernatant was aspirated out of each plate. Cells were fixed in 1 mL Z-Fix solution for 10 minutes, washed three times with 1 mL PBS for 10 min, added the unmasking solution (PBS, 2 N HCl, 0.5% Triton X) for 10 minutes and removed it, all at RT. Then, the cells were incubated in the quenching solution (TBS, 0.1% sodium borohydride) for 10 min, removed it, permeabilized with 0.2% Triton X-100 in PBS for 10 min and incubated in blocking solution

(1 mL 5% BSA/1X PBS) for 30 minutes. The samples were then incubated overnight at 4 °C with 1 mL primary antibodies diluted in 5% BSA/PBS. Next day samples were washed three times with 1X PBS for 10 min, followed by 1 h exposure to secondary antibodies. Samples were then washed twice in PBS for 10 min, incubated for 10 min with DAPI, followed by a wash step with 1X PBS for 10 minutes. These steps were at RT and in dark conditions.

Nikon Ti Eclipse Confocal Microscope with a water dipping lens (10X) was used to capture images. The images were recorded with or without 3X digital zoom, in about 1/8 frames per second, 512×512 pixels image capture, 1.0 Airy Units, two times line averaging, appropriate voltage and power settings optimized per antibody. Figures were prepared by rotation, image sizing or gray scale changes. No other modification was done. The following antibodies were used at the following dilution: Oct4 (1:500 dilution), Nanog (1:100 dilution) and Sox2 (1:500 dilution). Secondary antibodies used: donkey anti-mouse IgG, Alexa Flour® 488, donkey anti-rabbit IgG, Alexa Flour® 594. All secondary antibodies were used at a concentration of (1:1500) with a working volume of 1.5 mL in 5% BSA/PBS. DAPI stain was used for DNA.

3.5.6 Extraction and purification of total RNA

After washing the plates with PBS, cells were lysed directly on the plated by adding 1 mL of Trizol Reagent. RNA was extracted after vigorous pipetting.[248] 200 µL chloroform was added to this solution followed by centrifugation (13,000 g) for 15 minutes. Aqueous phase containing RNA was separated and mixed with 500 µL isopropanol, followed by overnight storage at 20 °C. Then, the manufacturer's RNA clean-up protocol, RNeasy® Mini-Kit (Qiagen, Valencia, CA), with the optional On-column DNAse treatment was followed. RNA quality and concentration were checked using a Synergy™ NEO HTS Multi-Mode Microplate Reader (BioTek Instruments, Winooski, VT).

3.5.7 Quantitative Real-time PCR (qPCR) analysis

Total RNA was isolated from H9 hESC as described in the previous section. Purified RNA (2.5 µg in 20 µL reaction) was reverse transcribed using a SuperScript™ VILO™ Master Mix Kit. The synthesis of first-stranded cDNA was performed in the PCR tube after combining SuperScript VILO, RNA, and DEPC-treated water. The following conditions were used for qPCR experiments: 10 min at 25 °C in the first cycle, followed by incubating for 60 min at 42 °C, and terminating the

reaction at 85 °C for 5 min. The 7900HT Fast Real-Time PCR System (Applied Biosystems) with TaqMan Universal PCR Master Mix were used to conduct real-time PCR in triplicate for each sample using TaqMan probes (Applied Biosystems). Primer sequences used for qPCR are listed in Table 3.1.

Table 3.1: List of primers used in qPCR

Gene Symbol	Assay ID	UniGene ID
NANOG	Hs02387400_g1	Hs.635882
POU5F1 (OCT3/4)	Hs03005111_g1 (FAM-MGB)	Hs.249184
SOX2	Hs01053049 (FAM-MGB)	Hs.518438
GAPDH	Hs02786624_g1	Hs.544577

The comparative C_T method was used to calculate the relative quantity of NANOG, OCT4, KLF4 and SOX2 gene expression, normalized to Glyceraldehyde 3-phosphate (GAPDH), and was expressed as the fold change = $2^{-\Delta\Delta C_T}$.[248,251]

3.5.8 Alkaline Phosphatase Assay (ALP)

ALP assay was done by Dr. Xu Qian. An ALP detection kit from Millipore (#SCR004) was used for the phenotypic assessment of undifferentiated hESC colonies at day 7.[103] The recommended protocol was followed. Cells were fixed and rinsed with PBS, incubated in staining solution in the dark at room temperature for 15 min and prepared for imaging.

3.5.9 Statistical Analysis

Results are the mean values ± standard error of the mean (SEM) or mean values ± standard deviation (SD) and are adjusted for outliers. Microsoft Office Excel (Microsoft, USA) was used for processing the data.

CHAPTER 4 RESULTS AND DISCUSSION

Long term propagation of human pluripotent stem cells (hPSC) is important as they can serve as a virtually unlimited supply of cells for applications ranging from drug screening to cell therapies to understanding human developmental processes.[252] Several studies have shown that the complex microenvironment of the stem cell niche plays a major role in regulating cellular properties.[253] From a biomaterials' standpoint, it would be highly desirable to engineer alternatives that would mimic such a complex microenvironment. Interactions between biomaterial surfaces and cells alter cell behavior, resulting in beneficial or detrimental effects on their performance.[9,254] In reality, traditionally used feeder layer culture and Matrigel™ substrates have xenogeneic components, batch-to-batch variation, and processes that do not readily lend themselves to scale-up from an industrial research standpoint.[9,255]

The use of hydrogel materials would be beneficial in designing potential stem cell substrates because their properties can be tuned and altered systematically.[9,256] With burgeoning interest in translational research and regenerative medicine, synthetic cell culture systems are the hour of need. They are attractive due to their low costs, ease of use and bottom-up or top-down design.[30] Additionally, a defined biomaterial is needed to comply with good manufacturing practice (GMP) standards and eliminate the presence of animal-derived products.[257] Although several systems have been investigated, very few synthetic coatings have been commercially manufactured and sold.

Villa-Diaz *et al.* developed a fully defined synthetic zwitterionic polymer system, poly[2-(methacryloyloxy)ethyl dimethyl-(3-sulfopropyl) ammonium hydroxide] (PMEDSAH), by ultraviolet/ozone (UVO)-initiated free radical polymerization, which sustained the undifferentiated growth of human embryonic stem cell (hESC) and induced pluripotent stem cell (hiPSC) in several different culture media, including commercially available defined media for more than 25 passages.[13,14] PMEDSAH is a biomimetic polymeric hydrogel and it is hypothesized that a layer of proteins/lipids/growth factors is adsorbed on the polymeric material to facilitate hESC and iPSC proliferation. Section 4.1 describes the efficient functionalization of surfaces via

UVO-initiated free radical polymerization of MEDSAH onto vapor-deposited polymer coatings and tissue culture polystyrene dishes.

4.1 Ultraviolet/Ozone-Initiated Free Radical Polymerization

PMEDSAH polymer coatings were prepared using UVO-initiated free radical polymerization (UVO-grafting).[13] It was used as a control to compare the reversible deactivation radical polymerization (RDRP) techniques in the subsequent sections. Silicon and gold substrates were coated with poly-*p*-xylylene (PPX-N) via chemical vapor deposition polymerization. PMEDSAH polymer coatings were then grown from these substrates using UVO-initiated free radical polymerization. Physico-chemical characterization of these coatings was accomplished by measuring film thickness. The thickness of the films generated through UVO-grafting was 22 ± 11.1 nm, analyzed from 500 samples. The film thickness which correlates to molecular weight and grafting density of the UVO-grafted polymer could not be controlled, resulting in the large variance in the thickness.[173] This result showed that the film thickness varied with fixed monomer concentration and reaction time and supported the conclusion that UVO-grafting does not have the ability to control film thickness.

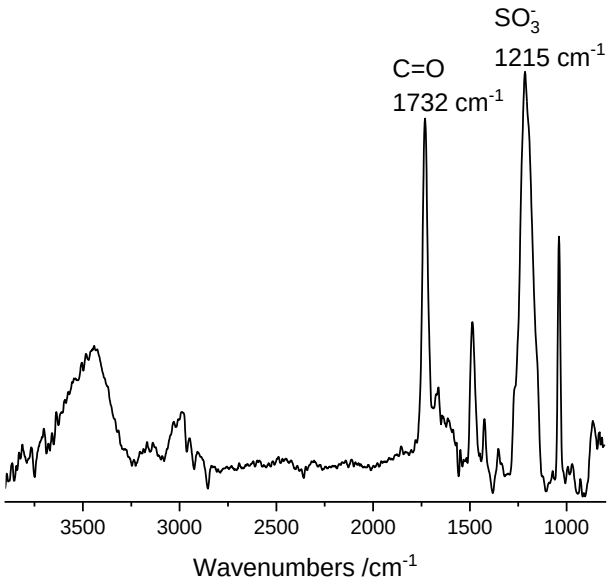

Figure 4.1: Fourier transform infrared (FTIR) spectrum of PMEDSAH coating showing distinct bands at 1732 cm^{-1} and 1215 $cm^{-1,}$ which indicate the presence of carbonyl and sulfonate groups, respectively.

The contact angle of UVO-grafted PMEDSAH was found to be 20° ± 3° and was consistent with the findings in our lab.[103] The Fourier transform infrared (FTIR) spectrum of PMEDSAH coated substrates, stored under ambient conditions, showed characteristic bands at 1732 cm^{-1} and 1215 cm^{-1} that correspond to the carbonyl and sulfonate groups respectively (Figure 4.1). This was consistent with previously reported FTIR spectra of grafted PMEDSAH brushes.[13] The result verified the grafting of PMEDSAH brushes on the surface. hMSC, hESC and HSC were cultured from UVO-grafted PMEDSAH coatings. The results of this study will be presented in Section 4.6.

4.2 SI-ATRP of Polymer Brushes on Chemical Vapor Deposition-based Initiator Films

Though UVO-grafted PMEDSAH coatings could maintain long-term self-renewal of hESC and hiPSC, and the prospect of commercially using these substrates were promising, the cells cultured on these substrates cannot be clinically translated without clearly understanding the underlying mechanism that support hESC self-renewal. Therefore, it was important to understand the key structural features and functions of the coatings that control pluripotency. The physico-chemical properties, such as hydrophilicity[15], surface topography, surface charge, surface roughness[258] and stiffness[259], of the biomaterials has been known to influence hESC expansion.[29] Therefore, the testing of the material properties of PMEDSAH coatings, like thickness, wettability and surface roughness was undertaken. RDRP techniques, such as surface-initiated atom transfer radical polymerization (SI-ATRP)[260] has enabled to synthesize well defined, tunable polymer brushes with controlled grafting densities and molecular weight distributions.[261] SI-ATRP provides exquisite control of polymer brush growth kinetics, which could be used to modify the interfacial properties of the polymer substrates.

With the goal of identifying the causes and mechanism behind the hESC propagation rates on PMEDSAH brushes, and to provide a framework for the desired biomaterial design criteria for hPSC culture systems, PMEDSAH brushes were generated by SI-ATRP using CVD based initiator coatings. The effect of the variations in the zwitterionic charge distance between the quaternary ammonium cation and the negatively charged sulfonate ion on the polymerization kinetics, was also examined. For this, poly[{2-(methacryloyloxy)ethyl}dimethyl-(3-sulfobutyl) ammonium hydroxide] P(M-2.4-S), a polymer with 4 methylene groups between the positive and the negative

ions; and poly[{2-(methacryloyloxy)ethyl}dimethyl-(3-sulfohexyl) ammonium hydroxide] P(M-2.6-S), a polymer with 6 methylene groups between the positive and the negative ions; were also grown from ATRP initiator coatings and the properties of these brushes as a function of thickness and wettability were measured. SI-ATRP of zwitterionic monomers is achieved on vapor-based polymer coatings at room temperature by using a catalytic system of CuBr/$CuBr_2$/bpy (Scheme 4.1).

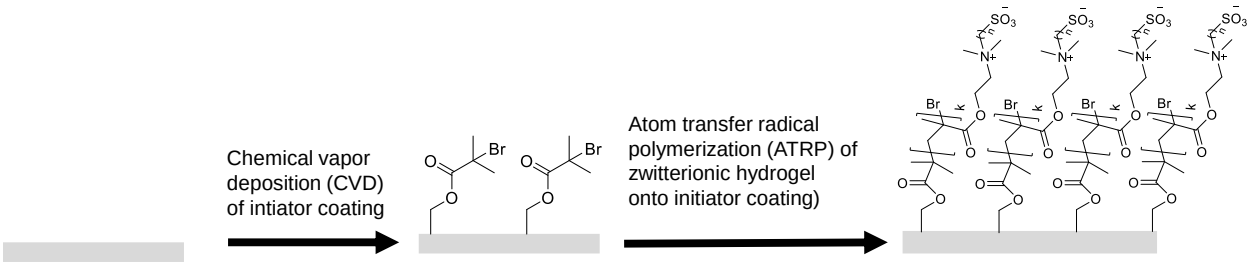

Scheme 4.1: Schematic of ATRP coatings on CVD initiator coatings. N = 3 for PMEDSAH, n = 4 for P(M-2.4-S) and n = 6 for P(M-2.6-S)).

First, the ATRP initiator coating was synthesized through the chemical vapor deposition (CVD) polymerization of [2.2]paracyclophane-4-methyl-2-bromoisobutyrate precursor, to form poly(*p*-xylylene-4-methyl-2-bromoisobutyrate)-*co*-(*p*-xylylene) (PPX-EB).[166] The thickness of the synthesized PPX-EB coatings were determined using ellipsometry and confirmed the formation of the coating. Additionally, the presence of ATRP-initiating ester bromide functional groups was confirmed by means of X-ray photoelectron spectroscopy (XPS) and Fourier-transform infrared (FTIR) spectroscopy. Next, PPX-EB coated substrates were used to grow PMEDSAH polymer brushes. Kinetic studies were conducted to better understand the polymerization process. The kinetic plot in Figure 4.2 showed that the propagation rate of the reaction is linear and provides good control over polymerization. By increasing the ATRP reaction time, the PMEDSAH thickness increased. Xiao *et al.* have successfully employed a kinetic model to predict polymer film thickness as a function of time.[193]

$$Thickness = \frac{[M]_0 k_p [P_n^\bullet]_0 t}{1 + [P_n^\bullet]_0 k_t t} \quad (17)$$

where $[M]_0$ is the initial monomer concentration, k_p is the rate constant of propagation, $[P_n^\bullet]_0$ is the concentration of propagation radical, and k_t is the rate constant of termination. Figure 4.2 indicates that this model describes the data well. The thickness of polymer film increases with reaction time almost linearly, which is typical of an RDRP process. The nonlinearity in the time dependence indicates termination.

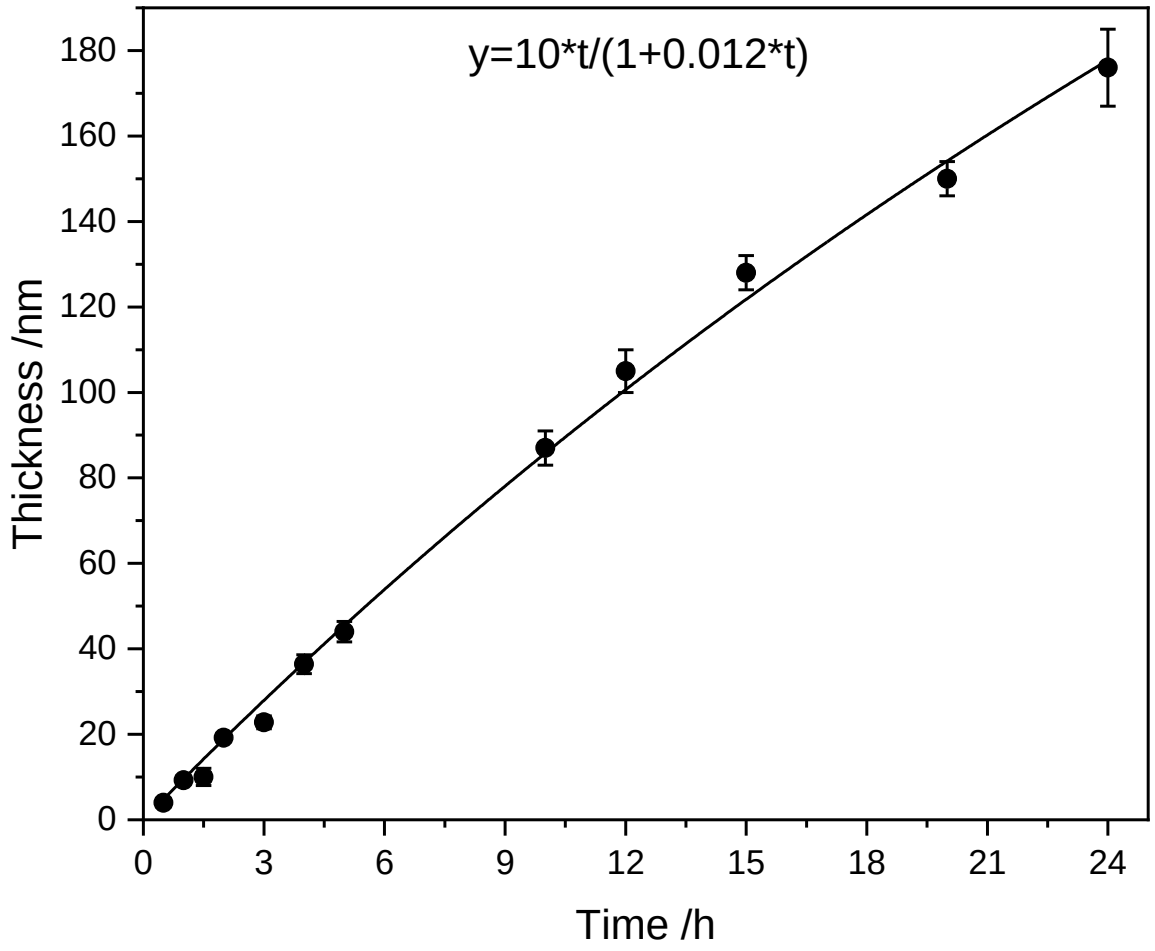

Figure 4.2: ATRP PMEDSAH film thickness vs time on vapor-based coatings at room temperature measured by ellipsometry. The data are indicated by the points and the curve shows the best fit to eq 17.

Furthermore, the wettability of the hydrogels was increased as a result of reaction time, leading to more hydrophobic brushes (Figure 4.3).

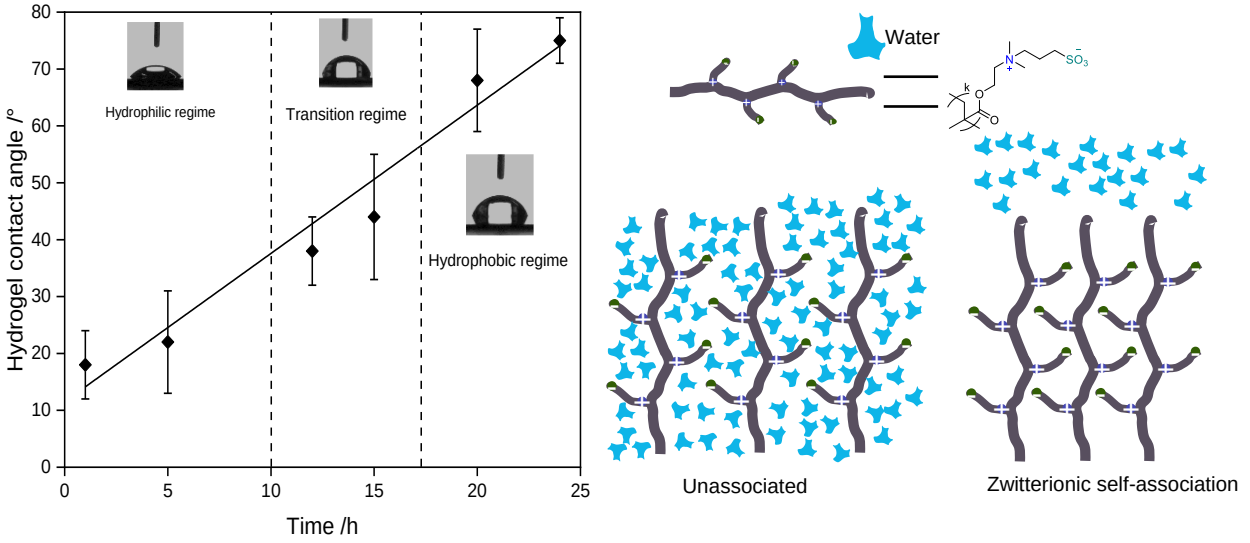

Figure 4.3: Hydrogel wettability as a function of reaction time for PMEDSAH ATRP modified surfaces. The schematic represents the architecture of a PMEDSAH brush and its interaction with water. It is unassociated in the hydrophilic regime. The PMEDSAH brushes switched from hydrophilic to hydrophobic due to zwitterionic self-association following a transition thickness regime. Images of representative water droplets illustrate the wettability differences. Schematic adapted from Qian *et al.*[103]

In particular, the static water contact angle ranged from 18° for ~20 nm brushes to 75° for ~175 nm brushes. Between these thicknesses, a broad transition regime was observed. The polymer conformation changes with increasing thickness and ATRP propagation rate.[80] Hence the polymer brush regime changes from hydrophilic when the brushes are unassociated to hydrophobic due to zwitterionic self-association.[80,96] Water is excluded from the brush due to the formation of inter-chain and intra-chain associations between quaternary ammonium cation and sulfonate anion of adjacent side chains[80] (Figure 4.3). The result strongly indicated that the length of the polymer brushes is a determining factor for the hydrophobic transition. Longer polymer brushes are likely to have increased chain association and thus exclude more water from the brush, explaining the increase of contact angle with reaction time. Thus, the interfacial properties of the polymer brush can be tuned through grafting thickness. Then, the zwitterionic charge distance between the quaternary ammonium cation and the sulfonate anion in the monomer subunit should influence the chain associations.

To investigate this hypothesis, Kratzer *et al.*[262] have developed a library of zwitterionic sulfobetaine methacrylates varying the number of methylene groups between quaternary ammonium and sulfonate charge centers. Two monomers from the library, M-2.4.S (4 methylene

groups between the charges) and M-2.6-S (6 methylene groups between the charges), were polymerized by SI-ATRP using the same conditions used for the polymerization of PMEDSAH brushes.

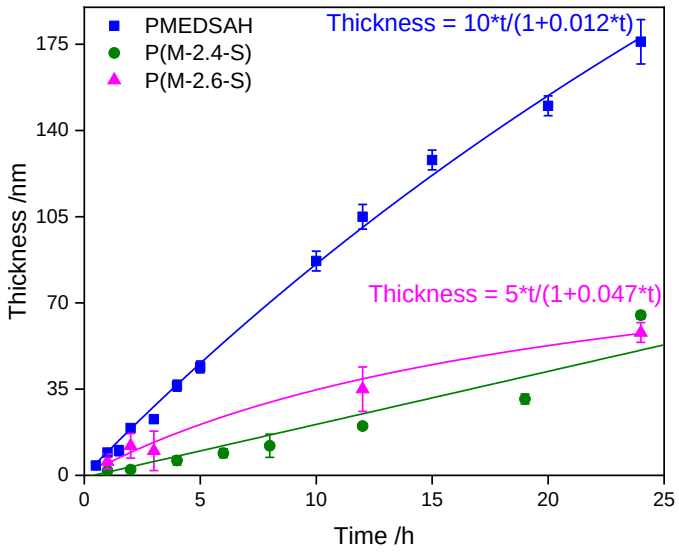

Figure 4.4: Kinetics of PMEDSAH, (P(M-2.4-S)) and P(M-2.6-S) brush growth from vapor based coatings.

Kinetic study with ellipsometry showed that P(M-2.6-S) followed similar reaction kinetics as PMEDSAH brushes (Figure 4.4). But thickness was considerably lower compared to the PMEDSAH brushes for similar reaction time. Contact angle measurements of P(M-2.6-S) after 24 h reaction time was 31±5°, which falls in the hydrophilic regime. Hence, it can be concluded that the P(M-2.6-S) polymer brushes are unassociated and in the dilute region, which is comparable to the PMEDSAH brushes of similar thickness.

P(M-2.4-S) did not show ATRP growth kinetics. However, the thickness of P(M-2.4-S) at 24 h was like the P(M-2.6-S) thickness at 24 h. Contact angle measurements of P(M-2.4-S) after 24 h reaction time was 67±2° which falls in the hydrophobic regime. Hence, it can be concluded that the polymer brushes undergo zwitterionic self-association at 65 nm brush thickness. Despite having similar thicknesses, the gel architecture of P(M-2.4-S) and P(M-2.6-S) were different. One reason could be because the brush growth of P(M-2.4-S) was less controlled. Another reason could be that the molecular weight determines the gel architecture. If the length of the polymer chains would be the only deciding factor, then 65 nm P(M-2.4-S) brushes should be hydrophilic, as observed with the other two polymeric materials. Therefore, the gel architecture must also be associated with the zwitterionic charge distance, that would alter the specific intrachain and

interchain interactions between neighboring chains. However, further studies need to be performed to optimize the propagation kinetics of P(M-2.4-S) by changing the monomer concentration, catalyst ratio and reaction time so that the polymerization is better controlled. Until then, we cannot establish with conviction, the correlation between zwitterionic charge distance and the gel architecture.

4.3 PMEDSAH Polymer Brushes based on Reversible Addition-Fragmentation Chain Transfer Polymerization from Chemical Vapor Deposition Films

The material in this section has been adapted with minor modifications from the following manuscript.

Gowthamy Venkidasubramonian, Domenic Kratzer, Vanessa Trouillet, Nicolas Zydziak, Matthias Franzreb, Leonie Barner, Joerg Lahann, "Surface-initiated RAFT polymerization from vapor-based polymer coatings"

In this section, interfaces were designed using S-RAFT polymerization. RAFT polymerization is advantageous for the preparation of water-soluble polymer brushes unlike ATRP, which requires an organic solvent to reduce the rate of propagation for better control of the polymer brushes. The direct polymerization of MEDSAH on surfaces using RAFT polymerization had previously proven problematic, even though several research groups have detailed the successful SI-ATRP of zwitterionic polymer brushes.[80,263,264] Here, polymer brushes were engineered on vapor-based coatings presenting reactive alkyne groups (PPX-alkyne) that can be further functionalized with RAFT agents via "click reactions". To this end, polymer brushes composed of zwitterionic monomer MEDSAH from RAFT agent decorated surfaces were prepared in a controlled manner by S-RAFT polymerization (Scheme 4.2).

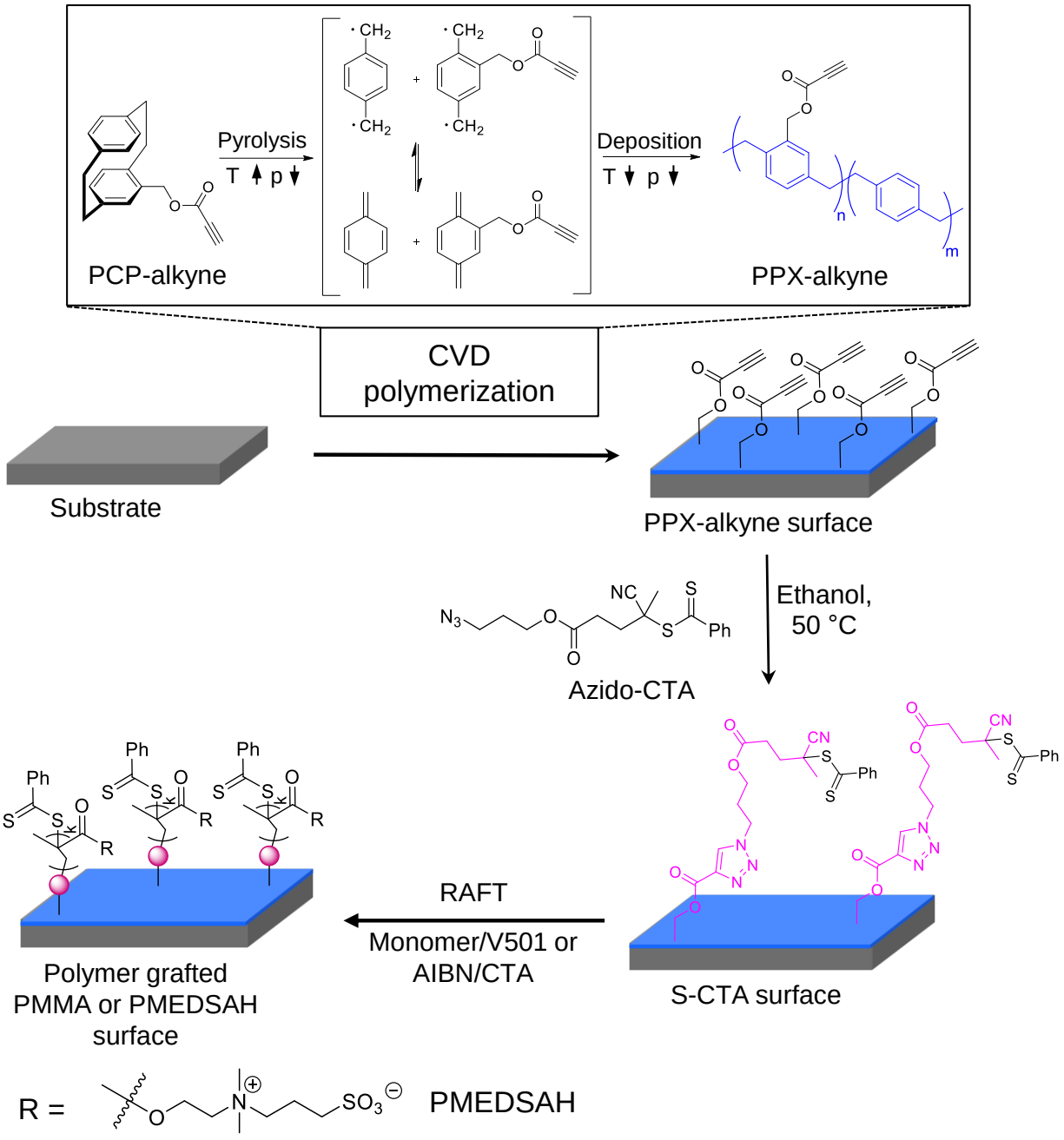

Scheme 4.2: Schematic illustration of the processes of CVD polymerization and the immobilization of the azide- functionalized CTA (azido-CTA) by copper-free click reaction on the alkyne-functionalized reactive polymer coatings (PPX-alkyne surface). During the CVD polymerization process, sublimation occurred for PCP-alkyne at approximately 100–120 °C. The sublimed paracyclophane was transferred from the source to the pyrolysis zone and exposed to elevated temperatures of 510 °C to thermally convert them into quinodimethanes. Finally, the quinodimethanes spontaneously polymerized upon condensation on a cooled (approximately 15 °C) substrate to generate PPX-alkyne surfaces. The surface-initiated RAFT polymerization of the MEDSAH monomer from the RAFT agent-decorated surface (S-CTA) followed.

4.3.1 Characterization of Vapor-Deposited Substrates

First, the PPX-alkyne was prepared by vaporization and pyrolysis of PCP-alkyne at 510° in the CVD apparatus. The 1,4-quinodimethanes that were obtained from the pyrolysis of PCP-alkyne were vapor deposited on substrates at 15 °C forming PPX-alkyne. Approximately 25-30 nm polymeric coatings of PPX-alkyne were generated and served as the base for subsequent surface modifications.

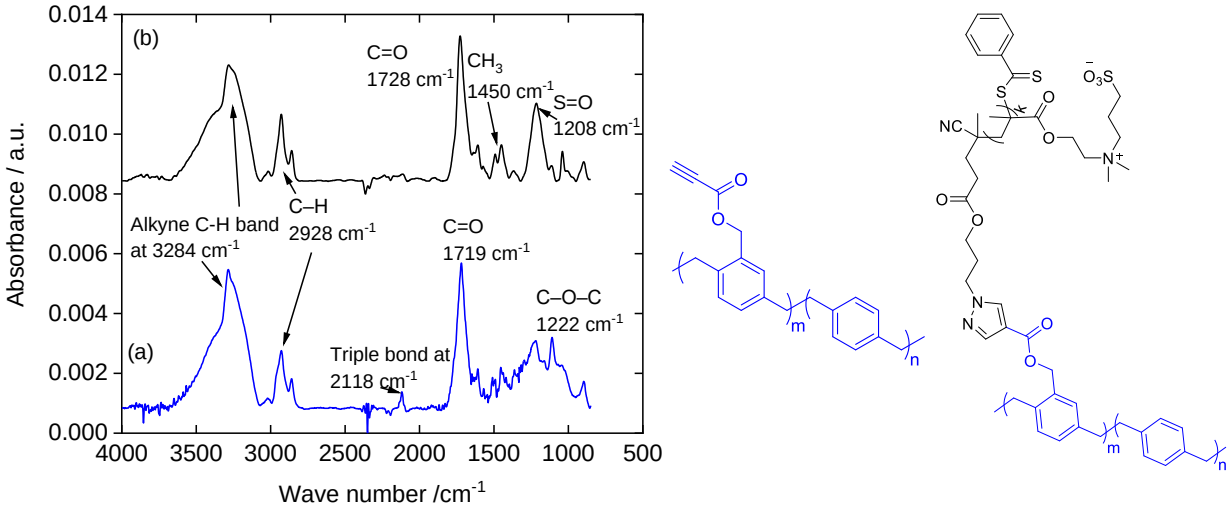

Figure 4.5: IRRAS confirms the presence of (a) PPX-alkyne, (b) PMEDSAH brushes.

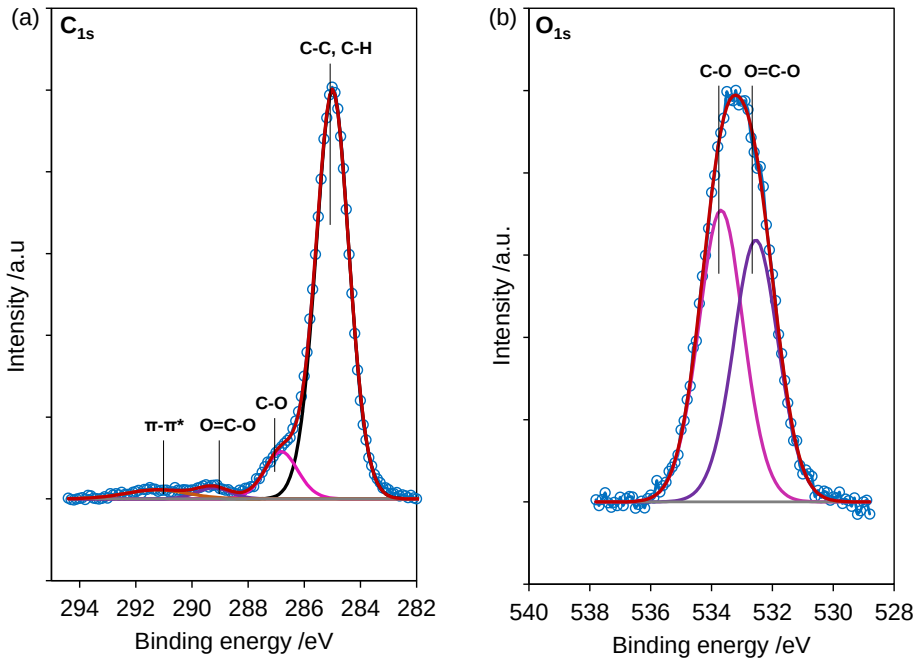

Figure 4.6: XPS measurements of carbon and oxygen content indicate the presence of PPX-alkyne coating.

This thickness was chosen to ensure relatively good pinhole-free surface coverage and compatible with XPS analysis (information depth 10-20 nm).[265] Using IRRAS spectroscopy (Figure 4.5(a)), the alkyne groups (at 3284 and 2118 cm^{-1}) as well as the carbonyl group (at 1719 cm^{-1}) were verified to be present on the substrate. Next, XPS was used to quantitatively analyze the carbon and oxygen content of the coatings (Figure 4.6). The C_{1s} spectrum confirmed the presence of aliphatic and aromatic carbons around 285.0 eV (a weak π-π^* transition at ~291 eV) and C–O and O–C=O components at 286.7 eV and 289.2 eV, respectively. The analysis indicated a composition of 88 ± 5 atomic percent (at%) carbon and 12 ± 2 at% oxygen which were in close agreement with theoretical values.

4.3.2 Surface modification: RAFT agent immobilization and Reversible Addition-Fragmentation Chain Transfer Polymerization

We hypothesized that the surface modification of PPX-alkyne coated substrates with azido-CTA will create active sites at the interface that promote S-RAFT polymerization and ultimately the coating of biomimetic zwitterionic polymer brushes on the surface. To this end, we prepared surfaces functionalized with PPX-alkyne coatings, then azido-CTA was formed as monolayers on the surface through a copper-free click reaction (Scheme 4.2).

In order to prepare monolayers of the azido-CTA, we employed the Cu-free 1,3-dipolar cycloaddition (Scheme 4.2)) to conjugate the azido-CTA to PPX-alkyne, which displays highly reactive alkyne functional groups.[11] XPS was used to confirm the RAFT agent immobilization. High-resolution N_{1s} and S_{2p} XPS spectra of PPX-alkyne coating before and after the reaction of the alkyne groups with azido-CTA confirm the successful click chemistry. From the XPS N_{1s} spectra in Figure 4.7, it is evident that after the reaction with azido-CTA, the N_{1s} peak can be fitted with two components attributed to the triazole species. The signal at 401.8 and 400.2 eV correspond to the single bond and double bond nitrogen of the N=N–*N* respectively. Elemental ratios for the three nitrogen atoms are 1.3:2, compared to calculated value of 1:2. Furthermore, the absence of an azide signal at ~405 eV indicates the absence of nonspecific adsorption of azides during the reaction. Additionally, no S_{2p} signal was detected on the PPX-alkyne surface before the reaction in the high-resolution S_{2p} spectrum.

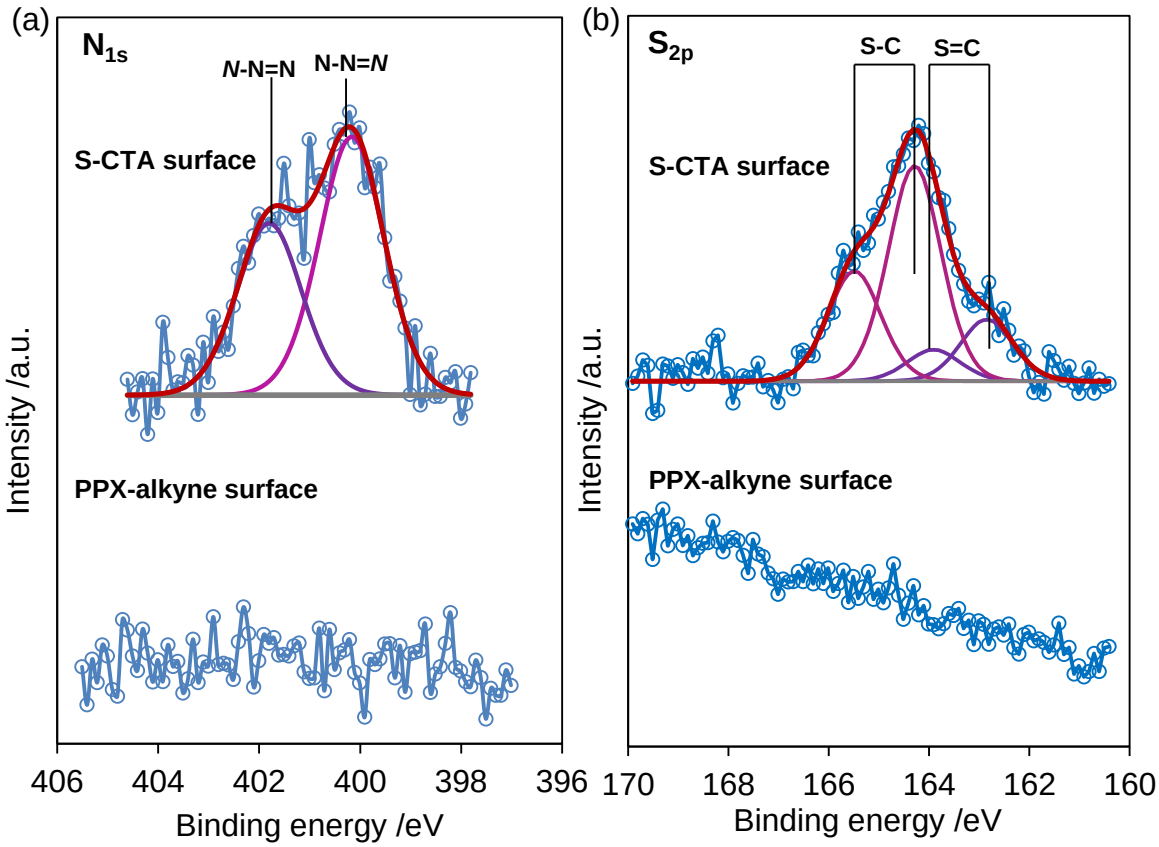

Figure 4.7: (a) N_{1s} and (b) S_{2p} high-resolution X-ray photoelectron spectroscopy of the PPX-alkyne coating and the S-CTA.

After the click reaction, the spectra can be deconvoluted into two main signals. The S_{2p} core-level spectrum consists of a spin-orbit doublet with $S_{2p3/2}$ and $S_{2p1/2}$. The $S_{2p3/2}$ at 162.8 eV corresponds to covalently bonded C=*S* sulfur group, and the peak at 164.2 eV which corresponds to the covalently bonded C–*S* sulfur group. These findings confirmed that CVD coatings can be a platform for "click chemistries" that are not copper-catalyzed.

Next, RAFT polymerization was performed on these CVD coatings. A design of experiment was applied to tune the parameters such as the solvent and $[CTA]_0/[Initiator]_0$ to establish the optimum polymerization conditions on surfaces. 16 experiments were included out of the total $3 \times 4 \times 4 = 48$ possible experiments of a full factorial design (Table 4.1). The parameters, RAFT agent/initiator ratio, solvent and salt concentration are known to have a significant influence on RAFT polymerization and were chosen as experimental factors. The highlighted experiments were

performed. The RAFT agent decorated substrates were immersed in the monomer solution, which contains not only the initiator, but also a free RAFT agent. The added RAFT agent was essential to suppress termination reactions in solution, hence stabilizing the controlled nature of the system.[266] Each experiment was started after the complete dissolution of the RAFT agent. All experiments were carried out at 70 °C. During polymerization the radicals are generated in the solution. The growing macroradical either diffuse to the RAFT agent immobilized on the surface or it undergoes chain transfer with free RAFT agent in solution.

Table 4.1: Design matrix for the variation of reaction conditions (TFE/H_2O solvent ratio; NaBr concentration; $[Monomer]_0/[CTA]_0/[I]_0$).

Run	TFE (v/v)	H_2O (v/v)	NaBr (M)	$[CTA]_0$	$[I]_0$	$[Monomer]_0$
1	1	99	0	0.8	1	1200
2	1	99	0.01	0.8	1	1200
3	1	99	0.5	0.8	1	1200
4	1	99	2	0.8	1	1200
5	10	90	0	0.8	1	1200
6	10	90	0.01	0.8	1	1200
7	10	90	0.5	0.8	1	1200
8	10	90	2	0.8	1	1200
9	50	50	0	0.8	1	1200
10	50	50	0.01	0.8	1	1200
11	50	50	0.5	0.8	1	1200
12	50	50	2	0.8	1	1200
13	100	0	0	0.8	1	1200
14	100	0	0.01	0.8	1	1200
15	100	0	0.5	0.8	1	1200
16	100	0	2	0.8	1	1200
17	1	99	0	2	1	3000
18	1	99	0.01	2	1	3000
19	1	99	0.5	2	1	3000
20	1	99	2	2	1	3000
21	10	90	0	2	1	3000
22	10	90	0.01	2	1	3000
23	10	90	0.5	2	1	3000
24	10	90	2	2	1	3000
25	50	50	0	2	1	3000

Run	TFE (v/v)	H_2O (v/v)	NaBr (M)	$[CTA]_0$	$[I]_0$	$[Monomer]_0$
26	50	50	0.01	2	1	3000
27	50	50	0.5	2	1	3000
28	50	50	2	2	1	3000
29	100	0	0	2	1	3000
30	100	0	0.01	2	1	3000
31	100	0	0.5	2	1	3000
32	100	0	2	2	1	3000
33	1	99	0	0.4	1	600
34	1	99	0.01	0.4	1	600
35	1	99	0.5	0.4	1	600
36	1	99	2	0.4	1	600
37	10	90	0	0.4	1	600
38	10	90	0.01	0.4	1	600
39	10	90	0.5	0.4	1	600
40	10	90	2	0.4	1	600
41	50	50	0	0.4	1	600
42	50	50	0.01	0.4	1	600
43	50	50	0.5	0.4	1	600
44	50	50	2	0.4	1	600
45	100	0	0	0.4	1	600
46	100	0	0.01	0.4	1	600
47	100	0	0.5	0.4	1	600
48	100	0	2	0.4	1	600

Table 4.2: Study of the impact of design variables on contact angle and thickness

Run	Thickness (nm)	Static contact angle (°)
1	21 ± 0.16	21 ± 1.6
2	22 ± 0.12	16.6 ± 2
3	20 ± 5.13	17 ± 2
4	15 ± 2.46	44 ± 11
5	13 ± 0.56	43 ± 10.8
6	19 ± 0.11	21.8 ± 5
7	13 ± 5.11	42 ± 2
8	12 ± 2.86	45 ± 2

Run	Thickness (nm)	Static contact angle (°)
25	18 ± 0.26	22 ± 1
26	19 ± 0.5	22 ± 9.4
27	13 ± 5.5	40 ± 2
28	24 ± 2.3	21.9 ± 10
45	2 ± 0.5	62 ± 3
46	2 ± 0.1	62 ± 3
47	4 ± 5.1	53 ± 2
48	6 ± 2.5	53 ± 2

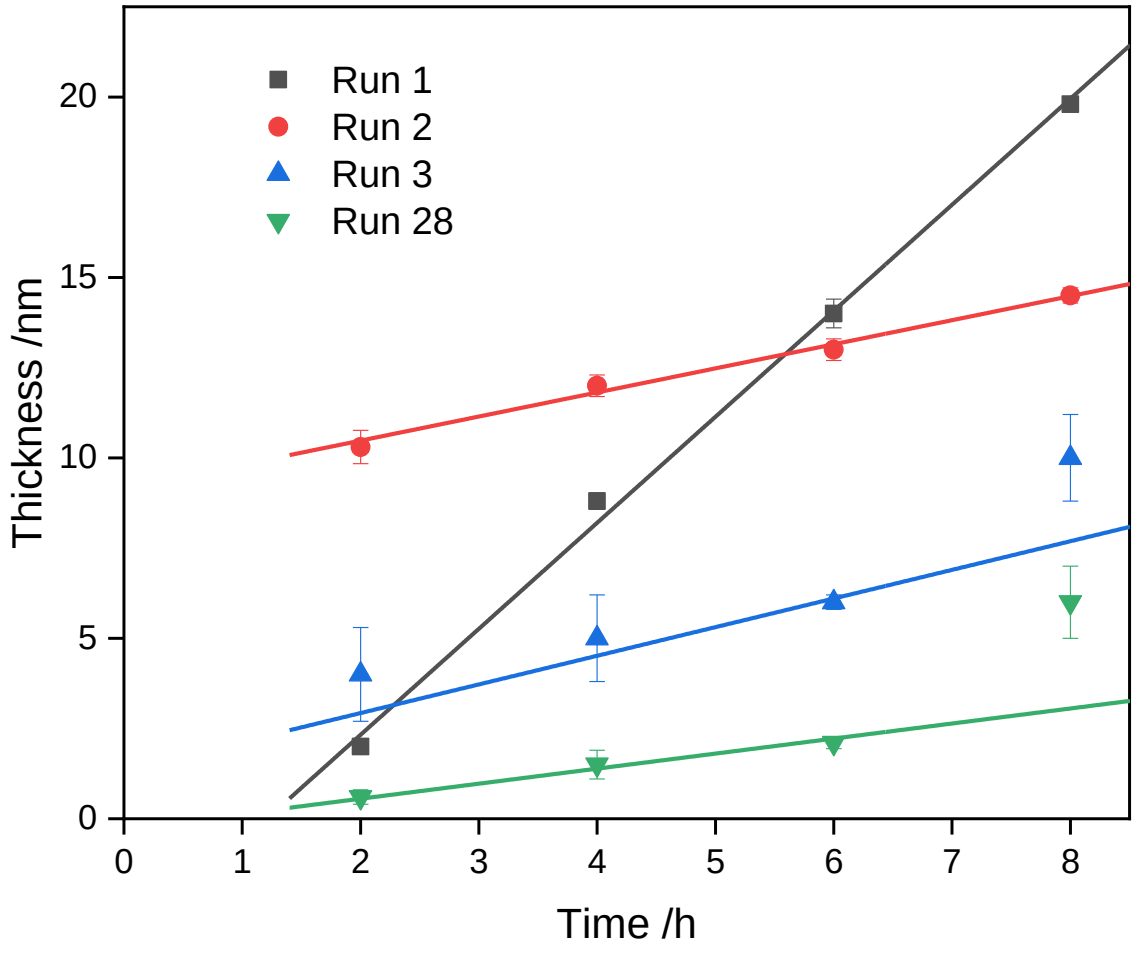

Figure 4.8: Brush thickness of runs 1, 2, 3 and 28 with time. Run 1: $[Monomer]_0/[CTA]_0/[Initiator]_0$ = 1200/0.8/1 in water/TFE (99:1 v/v); Run 2: $[Monomer]_0/[CTA]_0/[Initiator]_0$ = 1200/0.8/1 in water/TFE (99:1 v/v) and 0.01 M NaBr; Run 3: $[Monomer]_0/[CTA]_0/[Initiator]_0$ = 1200/0.8/1 in water/TFE (99:1 v/v) and 0.5 M NaBr; Run 28: $[Monomer]_0/[CTA]_0/[Initiator]_0$ = 3000/2/1 in water/TFE (1:1 v/v) and 2 M NaBr.

Ellipsometry was used to demonstrate the RAFT polymerization of PMEDSAH on the S-CTA surfaces. PMEDSAH layer was fitted with an n_k fix model assuming an n of 1.58. The thickness and contact angle of the resulting polymer brush surfaces are listed in table 4.2. Runs 1, 2, 3 and 28 were chosen to further investigate the kinetics of RAFT polymerization on surfaces. Run 1 proceeded with a pseudo-first order kinetic plot indicating a constant radical concentration while the others did not as can be seen from Figure 4.8.

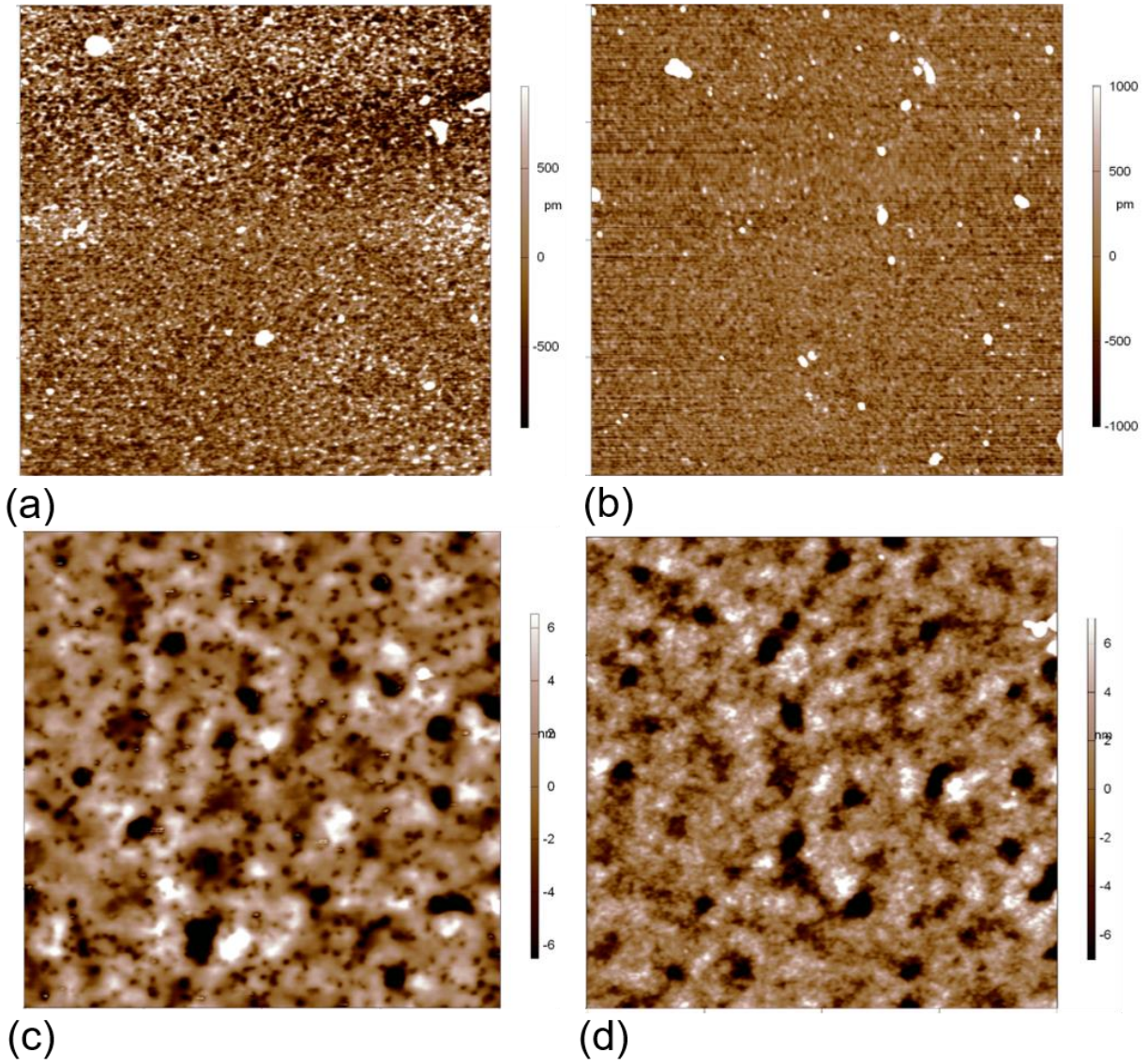

Figure 4.9: Atomic Force Microscopy (AFM) was used to visualize the topography of PMEDSAH brushes. (a) 2 h; thickness = 2 nm, R_q = 0.2 nm; (b) 4 h, thickness = 9 nm, R_q = 1.6 nm; (c) 6 h, thickness = 14 nm, R_q=3.1 nm; (d) 8 h, thickness = 20 nm, R_q = 0.6 nm.

AFM was used to visualize the topography of grafted PMEDSAH brushes from run 1 (Figure 4.9). Structural features were seen on the substrate with thickness of around 9 nm at 6 h reaction time with a root mean square (R_q) of the surface roughness of the PMEDSAH brushes of 3.1 nm. This indicated a mushroom regime of the polymer brushes. At 8h, R_q decreases to 0.6 nm indicating a brush-like regime. Reaction conditions were further tuned to increase the thickness of the polymer brushes. We chose the reactions of run 41 and investigated whether the polymerization follows a first order process. However, no polymerization occurred on surfaces. So, another set of parameters were taken: -the $[CTA]_0/[I]_0$ ratio was increased to 10/1, and the polymerization data was collected. However, the brush thickness increased to merely 2 nm after 8 h. Very high concentration of radicals were generated in solution.

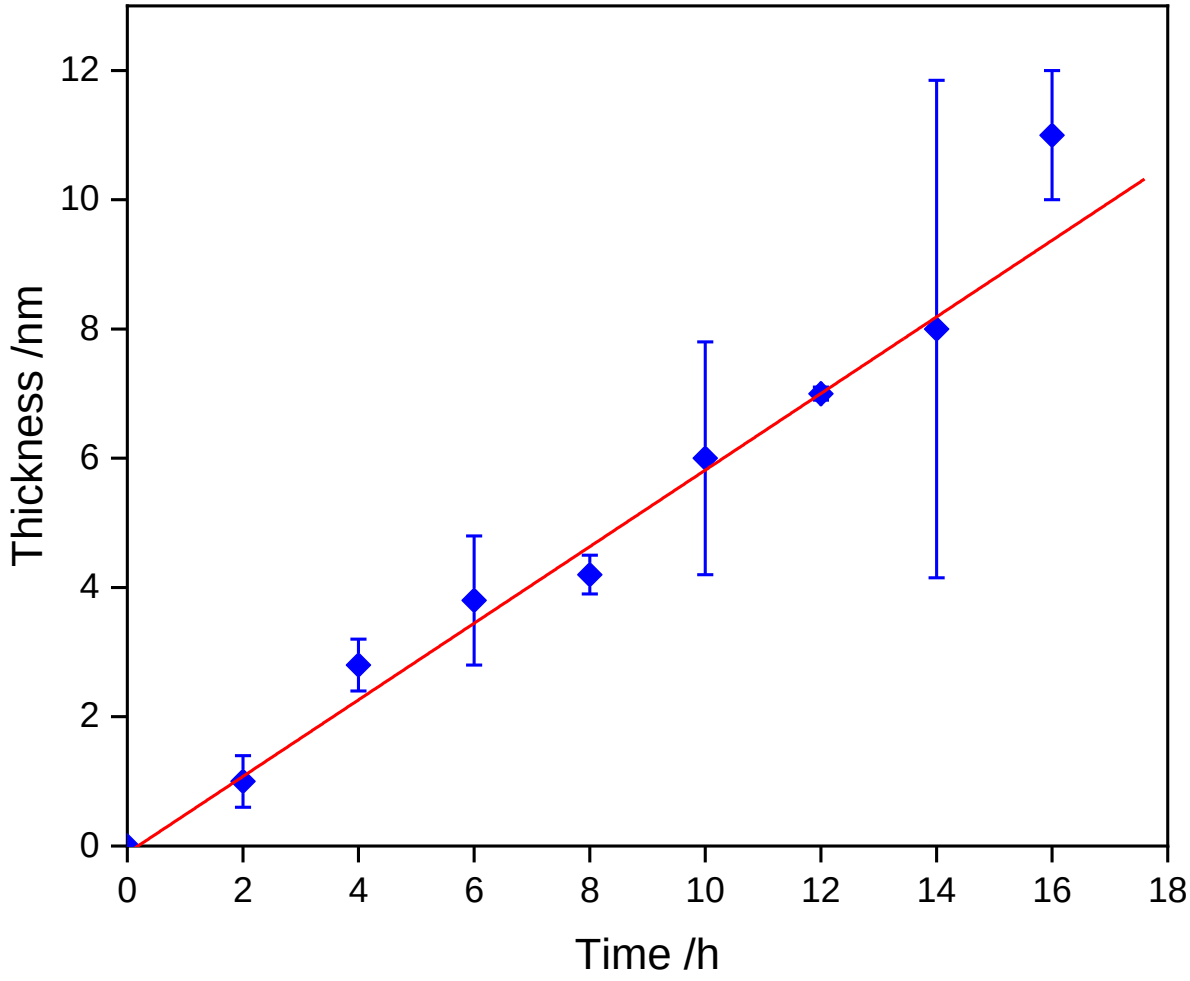

Figure 4.10: Dry brush thickness grown from RAFT agent modified reactive polymer coatings by RAFT polymerization. $[Monomer]_0/[CTA]_0/[Initiator]_0$ = 7500/10/1, temperature = 70 °C.

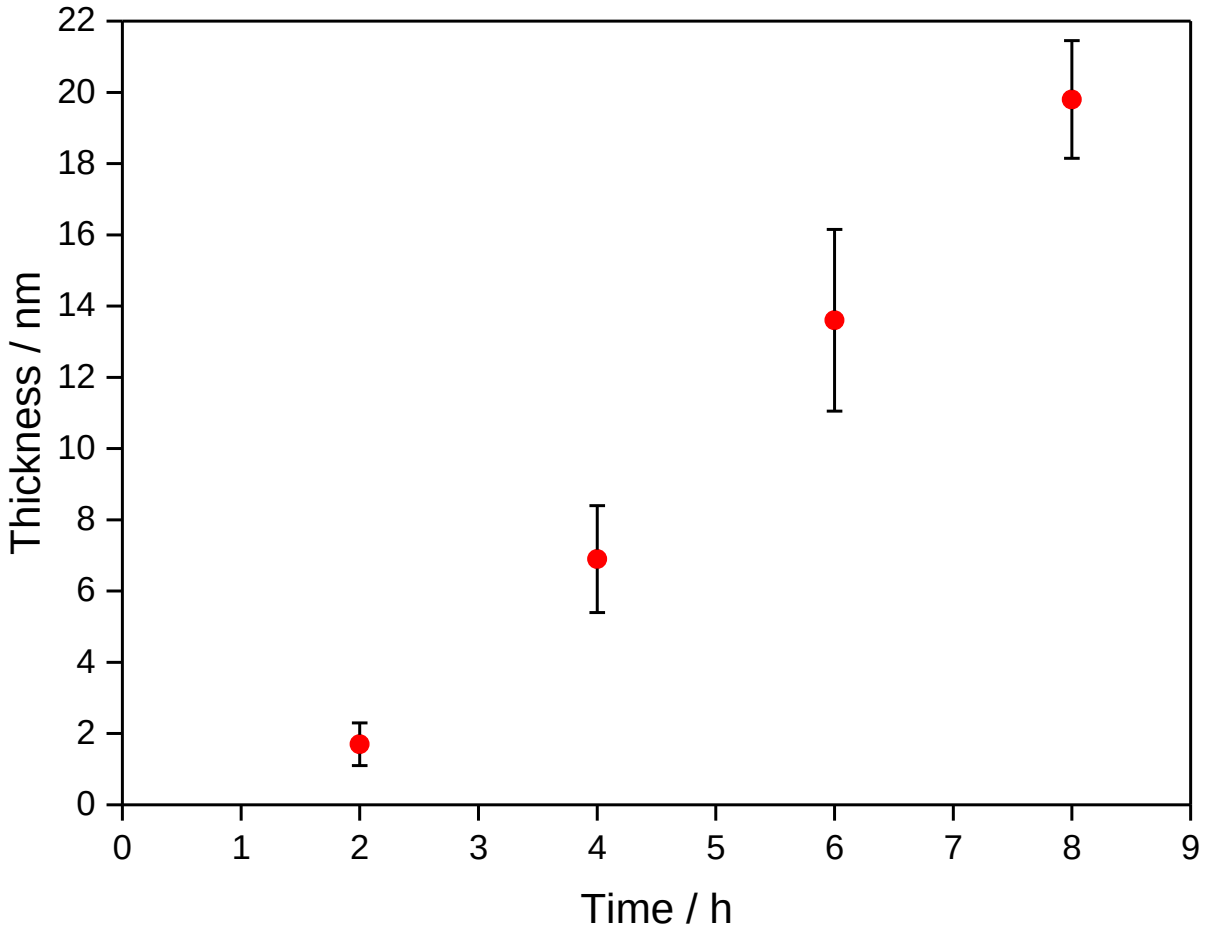

Figure 4.11: Change in brush thicknesses with time, measured by ellipsometry, for the polymerization of MEDSAH from silicon and gold surfaces at 80°C. Reaction conditions = MEDSAH/CTA/V501 = 7500/10/1.0.

The simultaneous solution polymerization yielded high molecular weight polymers, so it was not unexpected that the surface had a thin film. To get thicker polymer brushes, the $[Monomer]_0/[CTA]_0$ ratio was increased from 600 to 750. Increasing the temperature by 10 °C increased the rate of the reaction enabling control over polymerization kinetics and giving a film thickness of about 20 nm after an 8 h reaction (Figure 4.11). We concluded that the conditions described in Figure 4.11 were the most optimum reaction conditions for the polymerization. IRRAS measurement showed PMEDSAH brushes on the surface (Figure 4.5) as the C≡C stretch around 2118 cm^{-1} disappear, and there was a shift in the C=O stretch around 1719 cm^{-1} and the S=O stretch around 1208 cm^{-1} which also aligned well with previously reported data.[9]

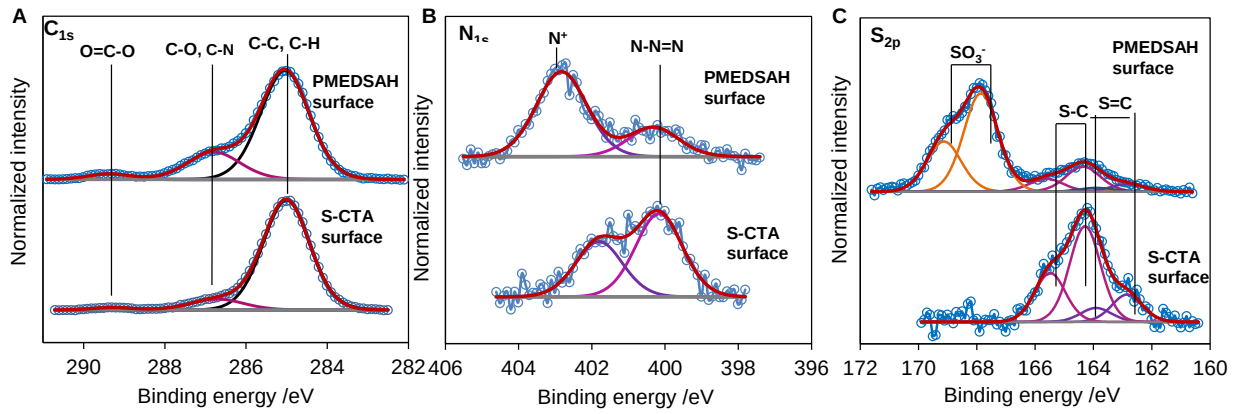

Figure 4.12: X-ray photoelectron spectroscopy of C_{1s} (a) N_{1s} (b) and S_{2p} (c) for PMEDSAH film with a thickness of 20 nm grafted onto the RAFT agent-decorated surface via SI-RAFT polymerization.

The XPS high-resolution C_{1s} scan (Figure 4.12) showed an increase in the signal intensity at 289.2 eV corresponding to the O–C=O group of PMEDSAH. In addition, the signal at 286.7 eV is indicative of the C–O signal of the carboxyl group of PMEDSAH. From the N_{1s} spectrum, it is apparent that there is a quaternary ammonium $–N(CH_3)_2^+$ signal (402.8 eV) on the S-CTA surface after grafting of the PMEDSAH.[267] Further, doublets are discernible in the spectrum of the PMEDSAH surface. The most intensive S_{2p} doublet with $S_{2p3/2}$ at 168.0 eV corresponds to sulfonate $C–SO_3^-$ group in the side chains of PMEDSAH. The other two weaker S_{2p} doublets with $S_{2p3/2}$ at 164.2 eV and 163.0 eV are associated with the C–S and the C=S bonds of the dithioester end-group.[268] The N^+/SO_3^-/O–C=O ratio was ~ 1:1:1.

Roughness is a potent physical signal in the cellular microenvironment to regulate a diverse array of hESC behaviors, including their morphology, cell adhesion, self-renewal and pluripotency.[269] The surface roughness of PPX-alkyne coatings characterized by AFM. Roughness R_q was 1.1 nm (Figure 4.13). The PMEDSAH brushes grown on the PPX-alkyne coatings had an R_q of 3.6 nm. The change in surface roughness was not statistically significant. Hence, PMEDSAH coatings synthesized by S-RAFT polymerization can be categorized as smooth. Smooth surfaces has been shown to support hESC growth better than nano-rough surfaces with an R_q of 75-150 nm.[258]

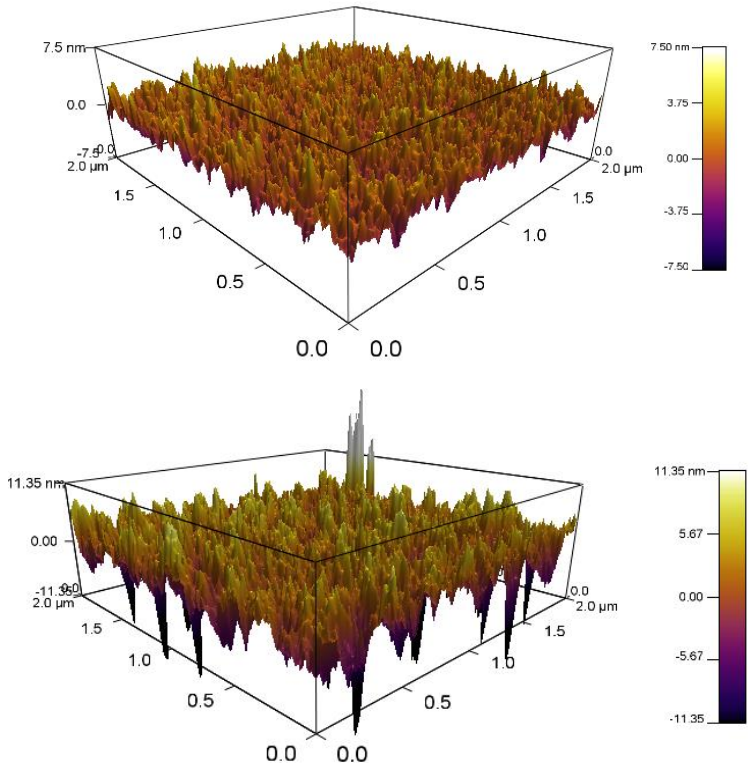

(a)
PPX-alkyne surface
R_q = 1.1 nm

(b)
PMEDSAH surface
R_q = 3.6 nm

Figure 4.13: AFM was used to measure the surface roughness of (a) PPX-alkyne coating and (b) PMEDSAH brushes. Three-dimensional projections of the surfaces obtained from AFM imaging of dry substrates. PPX-alkyne thickness = 20 nm. PMEDSAH brush thickness = 20 nm.

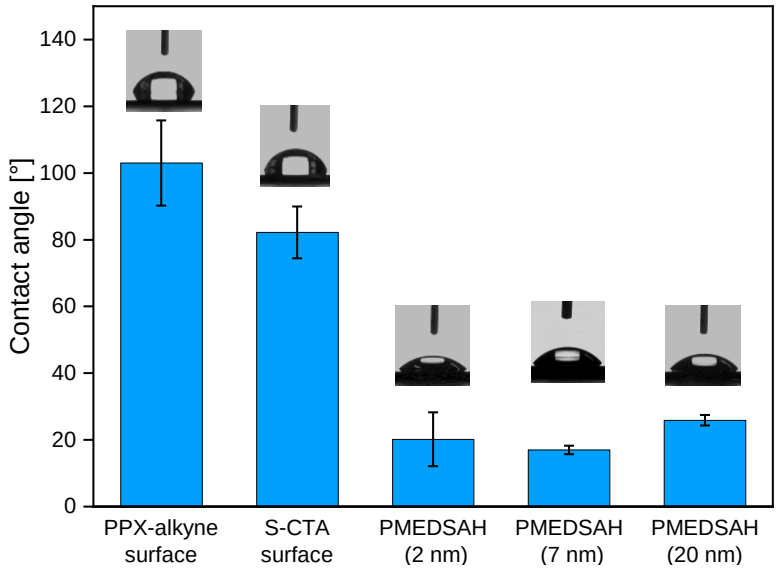

Figure 4.14: Water contact angle. Vertical error bars represent standard deviation of experimental measurement.

Contact angle was measured as a function of brush thickness to determine the wettability of the PMEDSAH substrates (Figure 4.14). The PPX-alkyne surface and the S-CTA surface exhibited average contact angles of 103° and 82°, respectively. The PMEDSAH layer had an average contact angle of 21°, which were comparable to the thin, unassociated PMEDSAH brushes synthesized by SI-ATRP. In the unassociated state, the sulfonate and ammonium groups in the side chains interact with water molecules, and not with each other, allowing the polymer to be fully hydrated, resulting in surfaces with low water contact angle.[96] No significant differences in the contact angle was observed upon increasing the brush thickness to 20 nm.

In conclusion, SI-RAFT polymerization protocol for the synthesis of PMEDSAH brushes were successfully established. PMEDSAH was in the thin, unassociated state at the highest well-controlled brush thickness we could obtain by this method. The film thickness was comparable to the UVO-grafted PMEDSAH films and 1 h ATRP PMEDSAH films. It has already been established that hESC adhesion is favored on the latter two substrates. Hence, SI-RAFT method could offset the copper catalyst requiring SI-ATRP and allow us to tune the material properties on brush surfaces.

However, the grafting-from process is still quite cumbersome, expensive and time consuming. It requires air-sensitive techniques and instruments like glove box which require specialized skill to operate. Our goal is to identify design parameters of PMEDSAH coatings that would eventually lead to a streamlined, established and facile scale-up process that is commercially viable. To this end, we attempted to develop a "grafting-to" approach to synthesize polymer brushes on substrates. Interfacial Gemini transporter (IGT) is a novel system with a small hydrophobic functional segment at the center and two flanking zwitterionic polymer segments. Such a system can be universally adapted for surface modification, not only on flat substrates, but also on particles, and complex 3D geometries. In this method, the small hydrophobic segment in the center drives the immobilization of the polymer in a thermodynamically good solvent, here, aqueous solutions.

The chemical composition of the surfaces and thus the molecular weight of the IGT was tailored to investigate and optimize the influence of the length of the polymer chains on stem cell behavior. In section 4.4, IGT with varying molecular weights are utilized for their immobilization on reactive polymer coatings containing aldehyde groups. Cell adhesion to the IGT-modified biomaterial surfaces is demonstrated in section 4.6.

4.4 Preparation of Brushes by Grafting-to Approach

The "grafting-from" approach discussed in Section 4.2 could produce dense, tunable and functional polymer brushes. However, the "grafting-to" approach is more advantageous for biomaterials design for hPSC culture platforms because it can be scaled up easily.[270] Thin polymer films can be produced by the grafting-to approach using a variety of solution-phase processes such as spin coating, spray coating, and dip coating from a polymer solution. The self-assembly of block copolymers with various charged blocks relying on hydrophobic or electrostatic interactions to physically adsorb to the interface is also a very useful method.[271] But these coatings are unlikely to be mechanically and chemically robust in the absence of covalent bonds between the substrate and the polymer film.[272] It was found that these coatings do not possess long-term stability in physiological buffers, or conditions where high shear forces are involved. Further chemical modification of the polymer films on the surface might be hampered by the requirements for the physisorption to the surface.[272] Covalent anchoring strategies of polymers to surfaces are a powerful alternative to control the ordering, orientation and functionality of the coated polymer with molecular precision. In this section, a top-down surface engineering approach toward developing biointerfaces using a grafting-to approach is discussed. The development of a standardized, controllable and sustainable hPSC culture platforms is an essential first step for large-scale cell culture in the future.

Scheme 4.3 outlines the steps of the research strategy involving the top-down surface engineering approach. The substrates were first coated with poly[(4-formyl-*p*-xylylene)-*co*-(*p*-xylylene)] (PPX-aldehyde) through CVD polymerization of the precursor 4-formyl[2.2]paracyclophane (PCP-aldehyde). The thickness of these PPX-aldehyde coatings was determined using ellipsometry and confirmed the formation of the coating. Additionally, XPS and IRRAS were performed in order to ascertain that the reactive formyl functional groups were present.

Next, a zwitterionic sulfobetaine block copolymer consisting of PMEDSAH called "interfacial Gemini transformer" (IGT) was synthesized. ATRP has enabled the synthesis of polymer brushes with diverse architectures and functionalities.[175,195] IGT was synthesized using ATRP of MEDSAH using a novel difunctional benzaldehyde ATRP initiator in a mixture of methanol and deionized water (4/1 v/v) at room temperature for different reaction times.

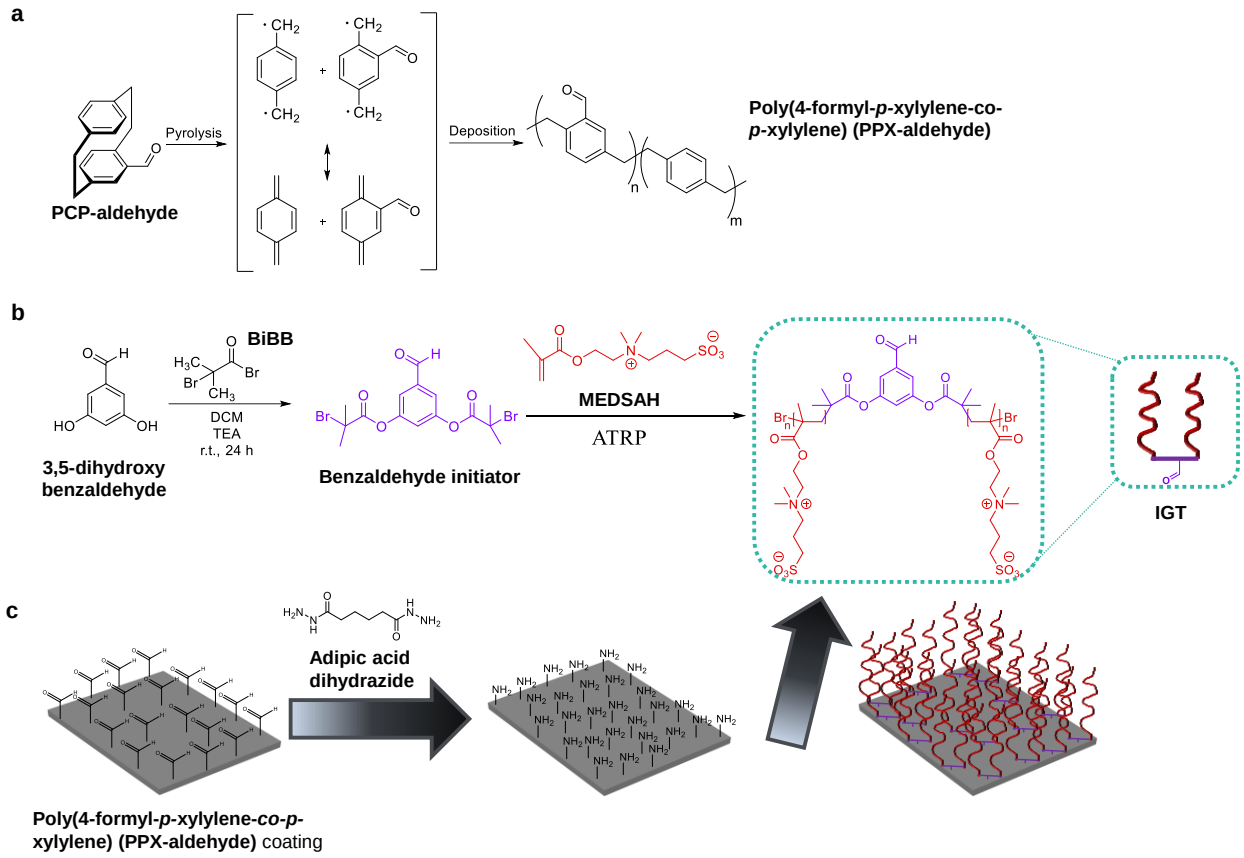

Scheme 4.3: Research strategy for coating substrates with the interfacial Gemini transformer (IGT). (a) CVD polymerization of 4-formyl[2.2]paracyclophane (PCP-aldehyde) to yield poly[(4-formyl-*p*-xylylene)-*co*-(*p*-xylylene)]. In Step 1, PCP-aldehyde is pyrolyzed (660°C, 0.16 mbar). In step 2, PCP-aldehyde is polymerized to [(4-formyl-*p*-xylylene)-*co*-(*p*-xylylene)] (PPX-aldehyde) (14°C, 0.16 mbar). (c) Immobilization of PMEDSAH IGT using a PPX-aldehyde coating.

Then using a bivalent spacer, chemically coupled the IGT onto the CVD coated surfaces using hydrazide chemistry.[227] The marriage of the hydrophilic sulfobetaine and hydrophobic benzaldehyde moieties produced a surfactant, which, when in aqueous environments, drove the interaction of the benzaldehyde to the surfaces of the hydrophobic CVD films. To confirm the successful coating of IGT on the substrates, we employed XPS and Tof-SIMS. As a proof-of-principle, microcontact printing (μCP) was used to show the straightforward linkage of IGT to the CVD surface. This evaluation was done by XPS mapping, ToF-SIMS and fluorescein-conjugated bovine serum albumin.

4.4.1 Design of the interfacial Gemini transformer with tailored chain lengths

The aldehyde-functionalized benzaldehyde initiator 2-bromo-2-methylpropionic acid 3-(2-bromo-2-methylpropionyloxy)-5-formyl-phenyl ester was prepared according to a procedure outlined in scheme 4.3(b). While free radical polymerization of PMEDSAH is generally effective, the length of the polymer chains could not have been controlled. Subsequently, the aldehyde functional group in the initiator would not have been available for further functionalization, as it would have been buried under the polymer chains. Thus, ATRP was used. Here, IGT was synthesized by ATRP of the MEDSAH monomer with 2,2´-bipyridyl (bpy) ligands and benzaldehyde initiator in methanol/water (4/1 v/v) solution. (Scheme 4.4b). The concentration of the MEDSAH was 1 M and the target DP was 100. These conditions gave nearly quantitative monomer conversion in 2 h. The polymer product was purified by elution through a short plug of neutral alumina to remove the copper impurities. Then, the polymer product was dialyzed against water and subsequently freeze-dried to obtain a white solid.

Monomer conversion was analyzed using ^{1}H NMR spectroscopy to confirm the formation of the polymer. The monomer alkene signal at 5.67 and 6.12 ppm disappeared, and the broad signals centered around 1 ppm for the methylene groups of the polymer backbone appeared. The signal at 10 ppm, arising from the aldehyde group, was used for the number-average molecular weight estimation by NMR (Figure 4.15).

The semi-logarithmic plot of monomer concentration vs. time for the polymerization of MEDSAH is shown in Figure 4.16. A linear plot of $Ln([M]_0/[M]_t)$ vs time was obtained, indicating that the number of propagating species remained constant. The rate of polymerization is fast, a monomer conversion of 75% was reached after 3 h at room temperature. The conversion leveled off after that timepoint. Proper control of the polymerization reaction is important for controlling the properties of the product. Therefore, different reaction conditions of the polymerization were investigated to optimize IGT polymerization to be able to prepare desired sizes of IGT molecules based on the biomaterials design.

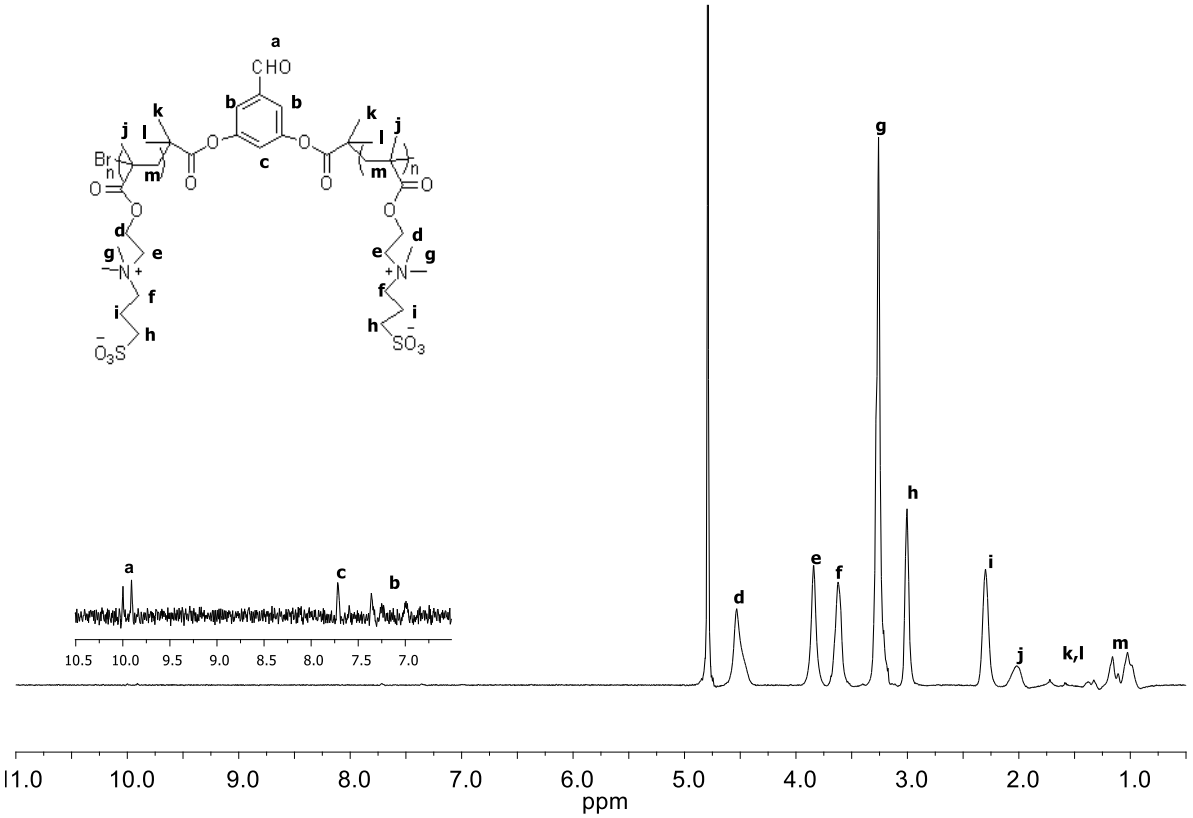

Figure 4.15: ^{1}H NMR spectrum of interfacial Gemini transformer in D_2O.

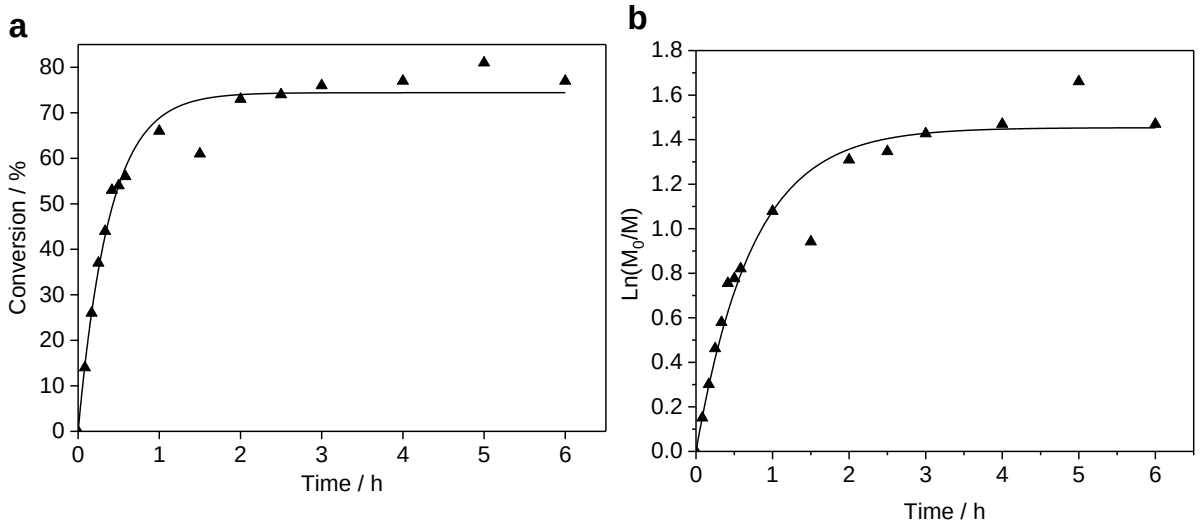

Figure 4.16: ATRP polymerization kinetics of IGT synthesized using benzaldehyde initiator. (a) Monomer conversion (▲) vs time and (b) $\ln([M]_0/[M])$ (▲) vs time. Reaction conditions: $[M]_0$:[benzaldehyde initiator]:$[bpy]_0$:$[Cu(I)]_0$ = 100:1:3:1 in methanol/water (4/1 v/v) at room temperature.

Table 4.3 lists IGT prepared using different reaction conditions, with molecular weights estimated by aqueous size exclusion chromatography (SEC) and ^{1}H NMR analysis (integrating the signals of 10 and 3.84 ppm).

Table 4.3: MEDSAH polymerization using benzaldehyde initiator

Sample	$[M]_0/[I]_0/[CuBr]_0/[bpy]_0$	Time (min)	Conv (%)	$M_{n,th}$ (gmol^{-1})	M_n (^{1}H NMR) (gmol^{-1})	M_n (SEC) (gmol^{-1})	$Đ$ (M_w/M_n)
1	25:1:2:3	300	80	5600	5500	2300	1.2
2	100:1:2:5	300	63	17900	17800	9500	1.4
3	100:1:1:2	60	64	17900	20600	6700	1.2
4	100:1:1:2	25	21	5900	4600	5600	1.2

Differential scanning calorimetry (DSC) was used to determine the glass transition temperature of the IGT. IGT exhibited a melting point close to 250 °C. DLS measurements showed an average hydrodynamic diameter of 44 nm with PDI 0.326 (Figure 4.17). The electrical double layer surrounding the polymer in DI water will have long-distance interactions. Hence, the size obtained is always 2-10 nm larger than the actual size.[273]

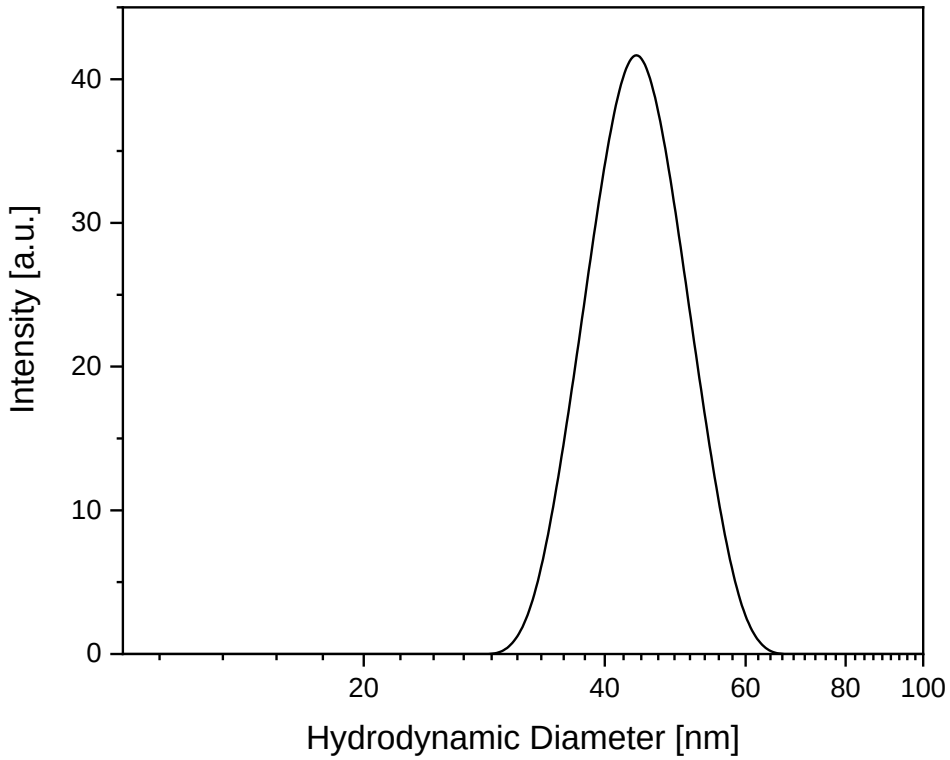

Figure 4.17: Representative hydrodynamic diameter measurement by DLS of interfacial Gemini transformer in water.

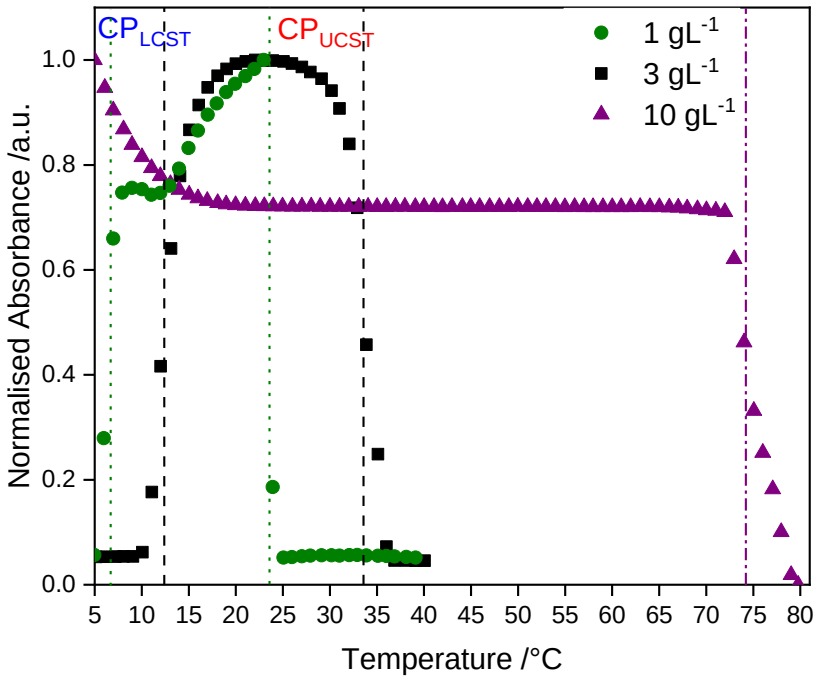

Figure 4.18: Light absorbance of a 1 gL^{-1}, 3 gL^{-1} and 10 gL^{-1} solution of $IGT_{3.57kgmol^{-1}}$ in H_2O. The lines show CP_{UCST} and CP_{LCST}; (green ··) for 1 gL^{-1}, (black --) for 3 gL^{-1} and (purple- - -). The lines are guides to the eye. Cooling runs not shown.

We investigated the temperature-dependent phase behavior of IGT in water by turbidimetry (Figure 4.18). Two heating/cooling scans were used in every measurement to offset the effects of sample preparation.

CP_{UCST}(3.57 kgmol^{-1}, 1 gL^{-1}) = 23.5 ± 0.5 °C and CP_{LCST}(3.57 kgmol^{-1}, 1 gL^{-1}) = 6.7 ± 0.5 °C.

CP_{UCST}(3.57 kgmol^{-1}, 3 gL^{-1}) = 33.5 ± 0.5 °C and CP_{LCST}(3.57 kgmol^{-1}, 3 gL^{-1}) = 12.4 ± 0.5 °C.
CP_{UCST}(3.57 kgmol^{-1}, 10 gL^{-1}) = 74.2 ± 0.5 °C.

The measured UCST cloud point for 3 gL^{-1} IGT was similar with the ones around 30 °C reported in the literature for PMEDSAH with molar masses 4.35 × 10^5 gmol^{-1}.[274] Three regimes were distinguished in the absorbance curve (Figure 4.19). In the middle regime, the solution was turbid indicating the formation of aggregates. The phase transition of 1 g L^{-1} IGT was broad. For 10 g L^{-1} IGT, the absorbance was 100% at the start of the measurement and the phase transition was broad. In leftmost and the rightmost regime, only a maximum of 45% of the light was absorbed, i.e., they were translucent. The absorbance changed sharply between the regimes. Increasing the polymer concentration 3 times increased both the CP_{LCST} by 5 °C and CP_{UCST} by 10 °C which is a significant difference. Polymer solution at 10 g L^{-1} did not exhibit a CP_{LCST} at the investigated temperature range. Thus, CP_{LCST} and CP_{UCST} of IGT were sensitive to the polymer concentration. Zwitterionic PMEDSAH brushes have not exhibited an LCST temperature before. The reasons for the findings seem complex, suggesting a certain extent of hydrophobic interactions between zwitterionic chains. The precise molecular structure of IGT combines the LCST and UCST behaviors between 0 and 100 °C in aqueous solutions which is interesting for applications in biomedical applications. In future, small-angle neutron scattering (SANS) could be used to determine the structure of IGT. Different structure formations at UCST and LCST transition would further elucidate the behavior of IGT. These findings would be important to generate well defined, tunable biomaterials for hPSC culture platforms.

4.4.2 Synthesis and characterization of reactive coatings and IGT-modified substrates

From Scheme 4.4(c) shown above, IGT was assumed to be immobilized on vapor-based polymer coatings. To verify this hypothesis, the “grafting-to” process was done in three steps:

- Reactive coatings consisting of aldehyde groups were synthesized by CVD polymerization.

- Immobilization of the dihydrazide linker adipic acid dihydrazide (ADH)
- IGT was "grafted to" ADH decorated substrate by an aldehyde-hydrazide reaction

4-Formyl[2.2]paracyclophane (PCP-aldehyde) functional precursor was synthesized via "Rieche" formylation of [2.2]paracyclophane.[227] CVD polymerization of the resulting dimer yielded PPX-aldehyde polymer (Scheme 4.4(a)). XPS analysis of the PPX-aldehyde reactive coating revealed that the elemental composition was in close agreement with the theoretical values derived from the molecular structure. Table 4.4 summarizes the elemental composition of the PPX-aldehyde reactive coating.

Table 4.4: XPS analysis of PPX-aldehyde coated on silicon substrates. Silicon contamination probably from the vacuum grease constituted 1.4 at% , which accounts for the discrepancy in the theoretical and experimental values. The theoretical values agree well with literature[227].

Elements	**C (1s)**				**O (1s)**
(Chemical states)	**C–C/C–H**	**C–C=O**	**C=O**	**$\pi \rightarrow \pi^*$**	
BE [eV]	285	286.7	287.8	291.3	532.4
Calculated [at%]	83.2	5.6	5.6	-	5.6
Experimental [at%]	79.9	1.9	3.1	3.2	10.5

High resolution scans of the C_{1s} region were performed in order to quantify signals from the aliphatic C–C bonds, C–C=O bonds and the C=O from the aldehyde as shown in Figure 4.20(c). The distribution of areas under each of the fitted peaks matches the theoretical contribution from each component, which provides additional validation that the PPX-aldehyde reactive coating was synthesized successfully.

Figure 4.19 displays IRRAS spectrum of PPX-aldehyde coatings.

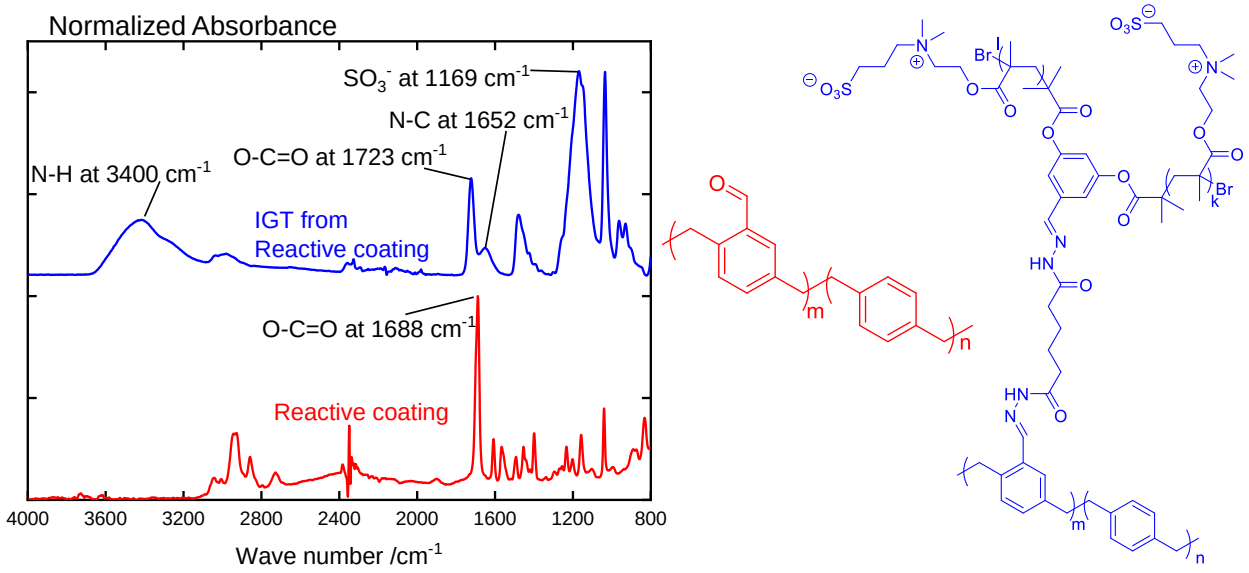

Figure 4.19: IRRAS confirms the chemical structures of PPX-aldehyde reactive coating and IGT-modified substrates**.**

PPX-aldehyde and "reactive coating" is mentioned interchangeably as it provides an aldehyde reactive group on the substrate. PPX-aldehyde coatings require an additional activation step for linkage of polymers.

Typically, bivalent spacers containing hydrazide groups are used for aldehyde-functionalized polymers.[227,275] Specificity of hydrazides towards aldehydes makes them superb binding agents for immobilization of IGT.[276] Modification of carbonyl-containing surfaces by dihydrazide homodifunctionalized linkers form hydrazine bonds on one side while yielding alkyl hydrazide spacers on the other side, making it suitable for subsequent reaction with formyl-containing groups available in IGT.[276] Adipic acid dihydrazide linker was first immobilized on PPX-aldehyde by reacting it to the aldehyde groups on the coating via aldehyde-hydrazide coupling. Adipic acid dihydrazide was chosen as the linker due to its intermediate-length spacer arm, which leads to accessible reactive sites for further reaction to IGT.[275] Hydrazide-modified surface was further reacted with IGT.

IGT (1% w/v) with different molecular weights (5-10 kg mol^{-1}, 24 kg mol^{-1}) were immobilized on the substrates. Brushes were generated with a thickness of 2.1 ± 1.3 nm, for molecular weights from 5 kg mol^{-1}–10 kg mol^{-1}. The thickness of the IGT film of molecular weight 24 kg mol^{-1} was

8 ± 2.8 nm. The surface coverage, Γ (mgm^{-2}), was calculated from the ellipsometry thickness of the layer, *h* (nm), by

$$\Gamma = h\rho \tag{18}$$

where ρ is the bulk polymer density (1.34 g cm^{-3})[277].Therefore, Γ of IGT (5 kgmol^{-1}-10 kg mol^{-1}) was 2.81 mg m^{-2}. Γ of IGT (24 kg mol^{-1}) was 10.72 mg m^{-2}. The chain density, Σ (chains nm^{-2}), i.e., the inverse of the average area of the attached chain, was determined by

$$\Sigma = \frac{\Gamma N_{\mathrm{A}}(10^{-21})}{M_{\mathrm{n}}} = (6.023\Gamma \times 100)/M_{\mathrm{n}} \tag{19}$$

where N_{A} is the Avogadro's number and M_{n} (g mol^{-1}) is the number average molar mass of the grafted polymer. Chain density values are shown in Table 4.5. The value represents the upper bound value for the grafting density of the IGT layer.

Table 4.5: Chain Density

M_{n} (gmol^{-1})	Thickness (nm)	Γ (24 kgmol^{-1})	Σ (chains/nm^{-2})
5000	2.1 ± 1.3	2.81	0.34
6453	2.1 ± 1.3	2.81	0.26
7000	2.1 ± 1.3	2.81	0.24
8089	2.1 ± 1.3	2.81	0.21
9000	2.1 ± 1.3	2.81	0.19
10810	2.1 ± 1.3	2.81	0.16
24180	8 ± 2.8	10.72	0.27

The IRRAS spectra (Figure 4.19) of IGT surfaces showed the presence of bands at 1492 cm^{-1} for CH_2 bending and 1723 cm^{-1} for C=O stretching. The C–N^+ stretching band (1652 cm^{-1}) is characteristic of quaternary ammonium group.[278] The band at 1169 cm^{-1} is characteristic of

sulfonate asymmetric stretching.[279] Again, this confirmed that the IGT polymer was successfully grafted to the surface.

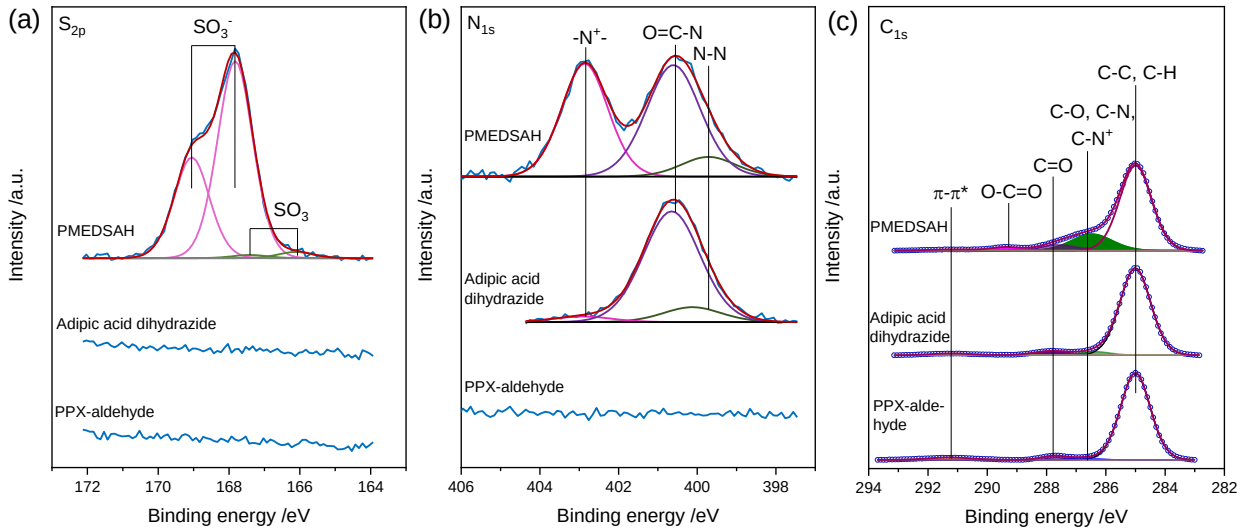

Figure 4.20: XPS characterization of IGT. (a) S_{2p}, (b) N_{1s} and (c) C_{1s} XPS spectra.

XPS data showed peaks at 167.8 ± 0.1 eV for $S_{2p3/2}$, and 402.9 ± 0.2 eV for N_{1s} quaternized amine of PMEDSAH and were consistent with the structure of the resulting brushes. The ratio of N/S measured by XPS was found to be 1.1 instead of 1.0, an observation consistent with other reports[93,280] (Figure 4.20).

The surface charge of PMEDSAH brushes was investigated *via* ζ-potential (Figure 4.21). The ζ-potential of IGT-4 kgmol^{-1} was less negative than surface-initiated ATRP 93 nm thick coating. In addition, IGT-8 kgmol^{-1} and IGT-14 kgmol^{-1} coatings exhibited more negative charge than the 105 nm thick coating in the neutral range of pH values. Lower isoelectric pH is the consequence of higher density of exposed sulfonate groups on dilutely grafted polymer chains. IGT-6 kgmol^{-1} coatings are the closest to the surface-initiated ATRP 93 nm thick brushes. The water contact angle of IGT-6 kgmol^{-1} was 52 ± 12.8°, like the moderately associated SI-ATRP PMEDSAH brush that had a contact angle of 45°. The negative surface charge may be related to the slight N/S imbalance of 1.1 measured in these brushes *via* XPS. The unreacted MEDSAH monomer has also known to show an N/S imbalance when measured by XPS.[280] The IGT coating was chemically stable in a dry-air environment.

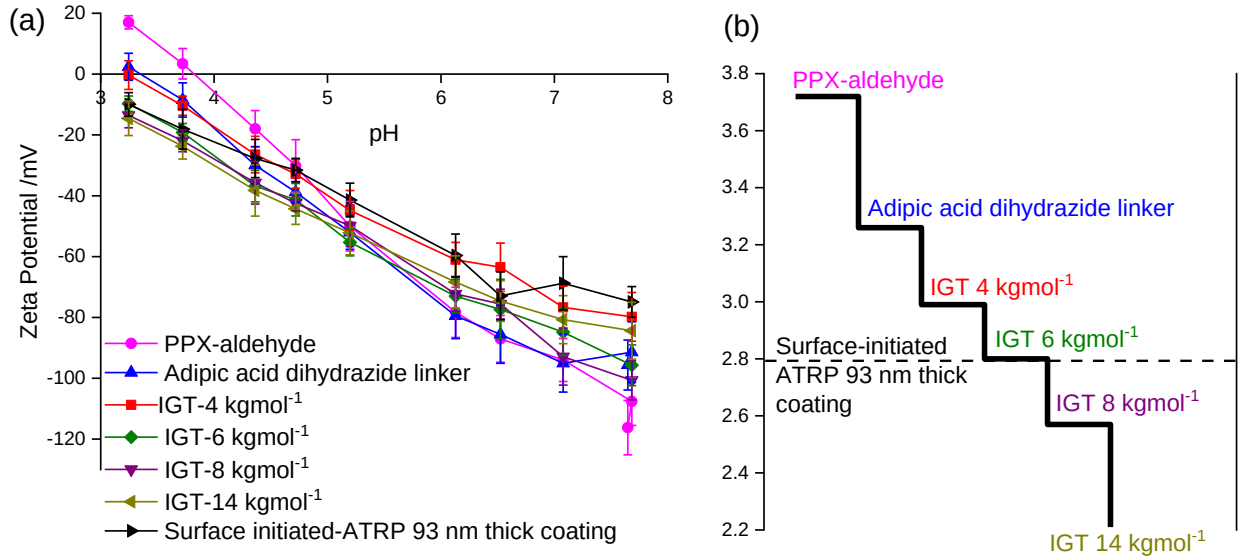

Figure 4.21: (a) Zeta potential values of IGT-modified coatings and PMEDSAH coatings polymerized through surface-initiated ATRP. (b) Evolution of isoelectric pH of different substrates.

Samples could be stored for several weeks under dry air without losing its functionality, as proved by using stored samples for cell culture experiments. The cells adhered equally well to freshly prepared samples and stored samples.

Control on localization of biomaterials in specific zones can assist in precise engineering of the cellular microenvironment. To demonstrate the controlled deposition of IGT molecules on surfaces, IGT was patterned on reactive coatings using microcontact printing (µCP) with lines and square island patterns µCP is a widely used soft lithographic technique that has been used to modify CVD coatings.[150,281,282] For example, Nandivada *et al.*, used µCP to pattern hydrazide linkers to PPX-aldehyde films.[227] The patterned hydrazide moieties served as binding partners for the subsequent immobilization of a polysaccharide, 2-α-mannobiose, via an alkyl-hydrazide linkage which further reacted with formyl groups on the disaccharide.. For patterning IGT, elastomeric stamps comprised of PDMS were inked with the IGT polymer following a protocol established by Schmid *et al.*.[283] The hydrazide moieties on the substrate reacted to the aldehyde functional group in the IGT.

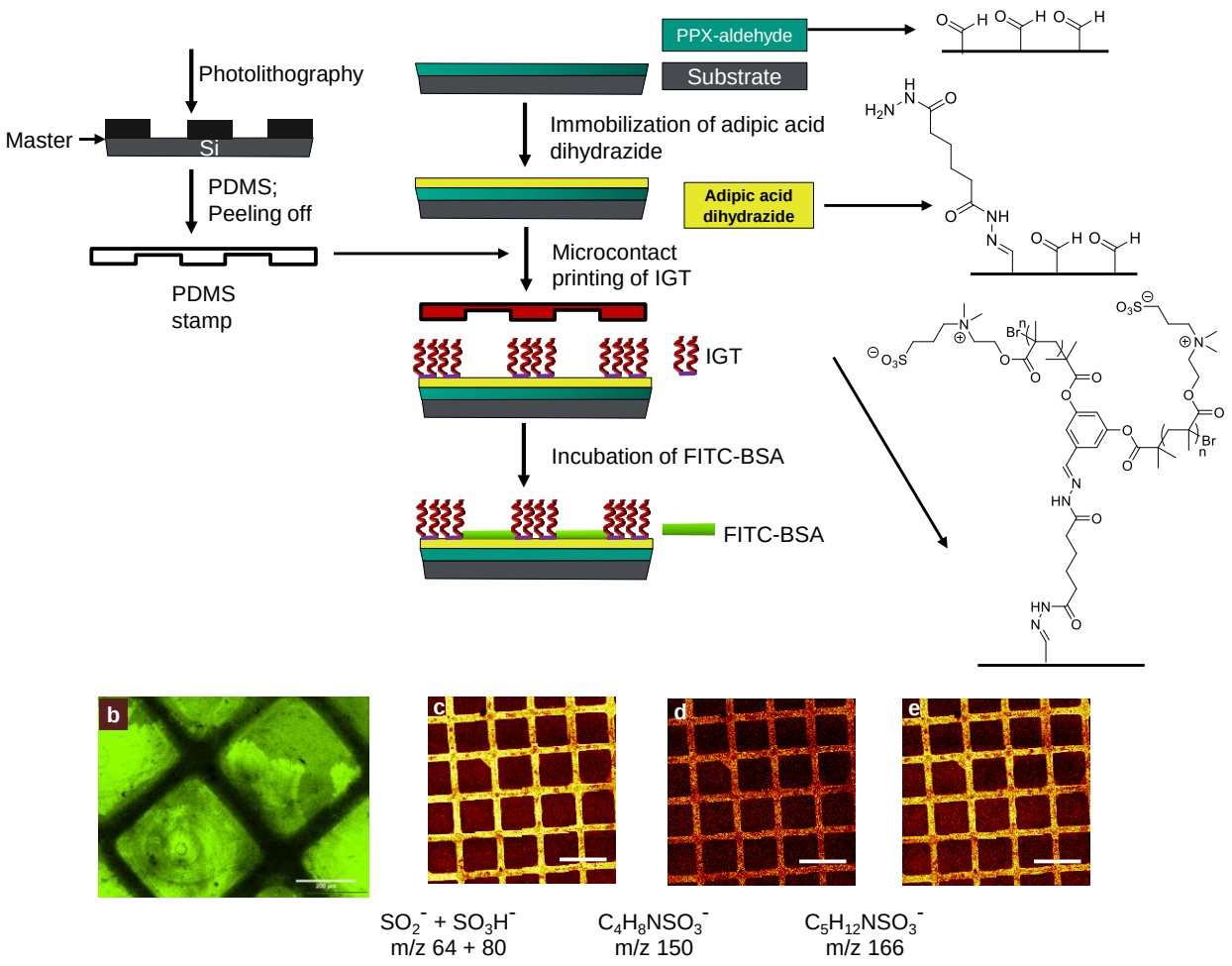

Figure 4.22: (a) Controlled deposition of fluorescent-labeled bovine serum albumin (BSA) occurs in areas where zwitterionic interfacial Gemini transformer (IGT) are absent. No protein adsorption occurs in domains where the IGT are grafted. (b) Fluorescence-labeled bovine serum albumin only adheres to regions where IGT is absent. Scale bar is 200 μm. (b), (c), (d) ToF-SIMS snapshot of SO_2^- and SO_3H^- fragments reveal high sulfonate intensity where IGT is present but very weak signals where IGT is absent. Scale bar = 500 μm.

The patterned IGT was characterized using time of flight-secondary ion mass spectroscopy (ToF-SIMS) as shown in Figure 4.22, where SO_2^- and SO_3H^- fragments were focused on. A strong contrast in these signals was observed owing to the high thickness and density of the IGT in the patterned areas compared to the linker present in the untreated regions. High molecular weight fragments, *m/z* 150, $C_4H_8NSO_3^-$; *m/z* 166, $C_5H_{12}NSO_3^-$, were also observed that were characteristic to the PMEDSAH fragments in the patterned areas, confirming that patterned IGT is controlled to

the regions where IGT was grafted. Zwitterionic sulfobetaine brushes have exceptional resistance to non-specific adsorption.[284–286] It was hypothesized that IGT should lead to the selective deposition of proteins such as bovine serum albumin (BSA) on domains where the IGT was not grafted. BSA was chosen since serum albumins are the most abundant proteins in blood and they are known to show non-specific adsorption on surfaces. Figure 4.22(b) shows a fluorescence image of this substrate after incubation. IGT prevents adsorption of BSA in regions where it is present (lines). BSA was spatially restricted to the square islands of the substrate surface where IGT was not coated.

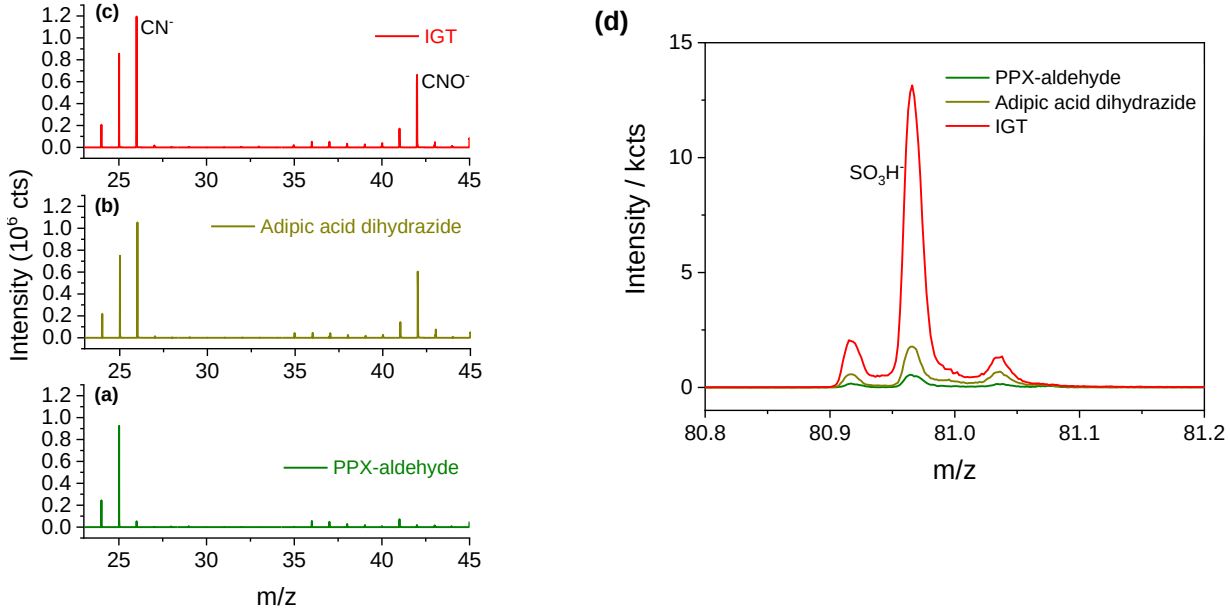

Figure 4.23: Negative ToF-SIMS spectrum of IGT bound to reactive polymer via adipic acid dihydrazide spacer: (a) reactive polymer coating, (b) adipic acid dihydrazide spacer, (c) IGT. Characteristic peaks are mentioned here. (d) Negative ToF-SIMS spectra of the PPX-aldehyde, adipic acid dihydrazide surface and immobilized IGT. SO_3H^- ion peak is found only in IGT.

Characteristic peaks of functionalization of PPX-aldehyde with adipic acid dihydrazide spacer in the negative ion ToF-SIMS mode are observed at *m/z* 26 (CN^-) and 42 (CNO^-) (Figure 4.23(b)). The positive ion spectrum also has peaks characteristic to the spacer at *m/z* 18 (NH_4^+) and 32 ($N_2H_4^+$).[287] In comparison, the negative spectrum of IGT bound to PPX-aldehyde showed

characteristic PMEDSAH fragments, at *m/z* 32 (S^-), 64 (SO_2^-), 80 (SO_3^-), 79 (Br^-), and higher fragments at *m/z* 166 ($C_5H_{12}NSO_3^-$) and 150 ($C_4H_8NSO_3^-$). These fragments clearly confirmed that IGT was immobilized on the substrate.

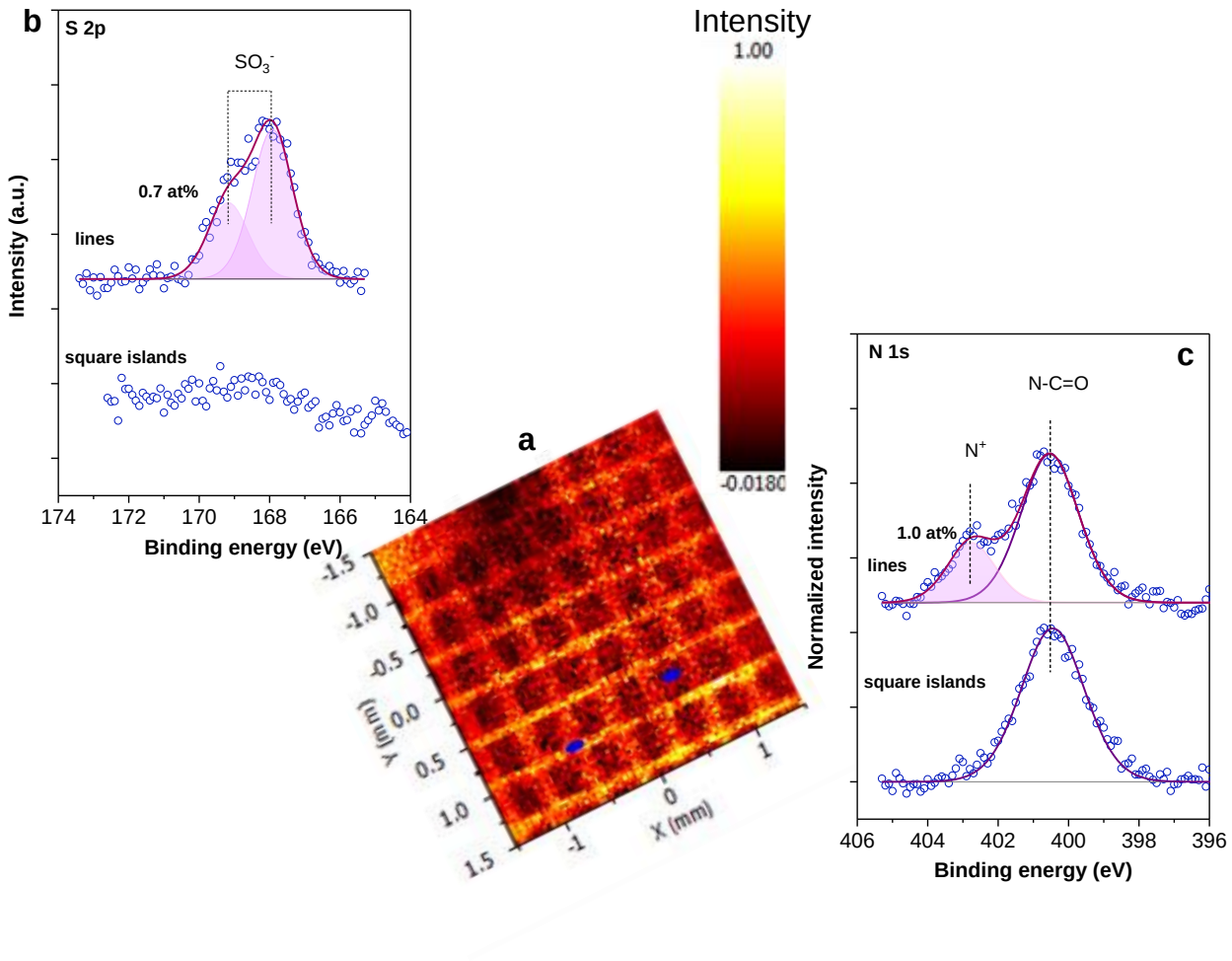

Figure 4.24: (a) XPS mapping of lines and square island pattern of IGT. (b), (c) Principal component analysis of all S_{2p} and N_{1s} spectra from the 1.5 × 1.5 mm^2 area.

Finally, XPS measurements of the patterned substrates were conducted to understand its elemental composition. As seen in Figure 4.24(a), the intensity map of the S_{2p} signals recorded in the snap-shot mode shows the spatial location of SO_3^- content. The intensity variations of the SO_3^- signal between the lines where IGT was present and the square islands where IGT was absent demonstrate the successful patterning of the substrate. The measured binding energies of N_{1s} and

S_{2p} signals on the lines consistently indicate the characteristic signals of PMEDSAH (N^+ and SO_3^-) and the square islands exhibit different binding energy shifts. The XPS mapping agreed well with the conclusions from the chemical maps generated by ToF-SIMS, where there were strong contrasts in sulfonate content between patterned and non-patterned areas. The XPS mapping, fluorescent protein patterns and ToF-SIMS together suggest that the patterning strategy was successful and the micro-structured polymer brushes could be prepared with the "grafting-to" approach using IGT. Patterned polymer brushes could be used to prepare biosensors and surfaces to control specific deposition of proteins.

Next, to verify that the IGT-modified substrates could be used as cell culture substrates, human embryonic stem cells were cultured on them. The results of these experiments are described in Section 4.6.4. In summary, a modular molecular system was developed with zwitterionic polymer brushes that could modify any substrate containing a complimentary reactive group to that present on the IGT. By allowing the zwitterionic bushes to attain a brush thickness of 2-8 nm on surfaces, these IGT-modified substrates could be used to adhere and expand human embryonic stem cells, even when the grafting density was low.

The disadvantage of synthesizing IGT by ATRP is the additional step required to remove the copper catalyst residues from IGT molecules before use. Metal catalyst residues make ATRP ineffective for biomedical applications.[288] RAFT polymerization represents a powerful toolbox to synthesize a wide variety of polymers with controlled architectures, defined end group functionalities, controlled molecular weights, and narrow dispersity using mild conditions (such as aqueous solutions and room temperatures). RAFT is one of the most useful and amenable fabrication strategies for generating polymer brushes for potential biotechnology and biomedical applications. RAFT polymerization achieves good control over hydrophilic polymer synthesis with polar functional groups.[289] Given the prominent utility of RAFT polymerization, it was hypothesized that this process would provide an easier way to synthesize zwitterionic polymers in solution, by avoiding the use of copper during the reaction.

4.5 RAFT Polymerization in Solution

Though RAFT polymerization holds the promise of facile synthesis of zwitterionic polymers in solution, the reaction parameters need to be optimized to develop biomaterials that ensure successful cell culture. In this section, the synthesis and characterization of zwitterionic sulfobetaine methacrylate polymers with varying charge distance were investigated. These polymer brushes can be easily grafted to the surface for the development of cell culture substrates. Donovan *et al.* had synthesized PMEDSAH by RAFT-mediated polymerization in solution[290] using 4-cyano-4-(phenylcarbonothioylthio) pentanoic acid (CPA) in 0.5 M NaBr aqueous solution at 70 °C, which gave successfully controlled molecular weight and narrow *Đ* (<1.1).

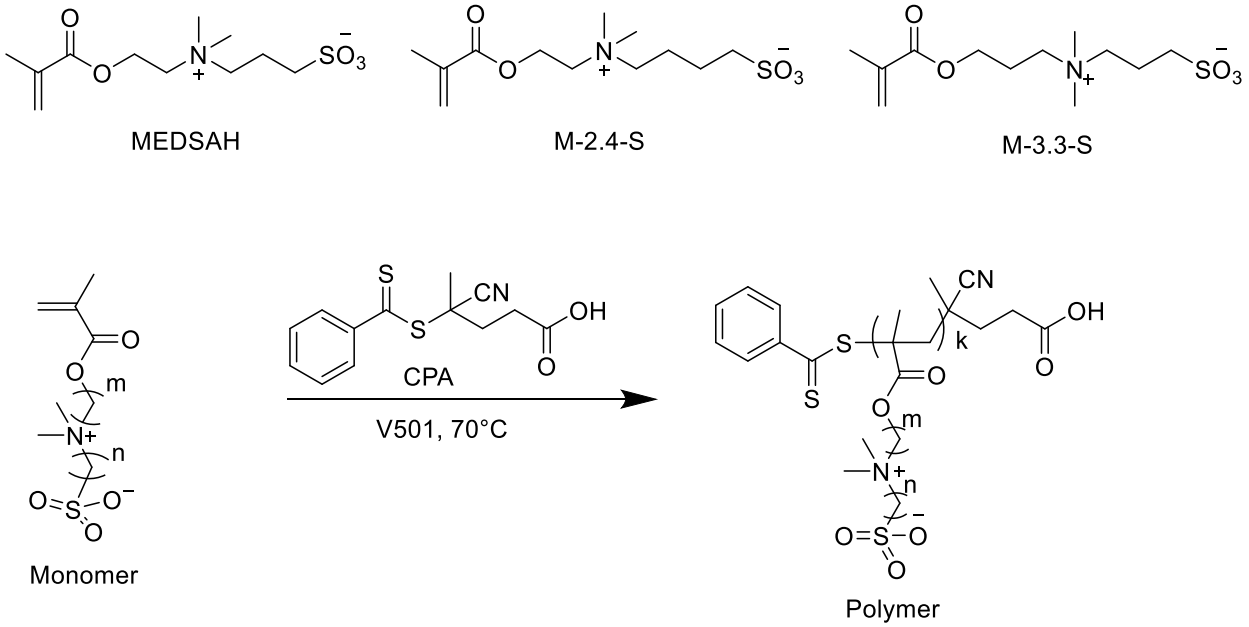

Scheme 4.4 RAFT-mediated polymerization of [2-(methacryloyloxy) ethyl] dimethyl-(3-sulfopropyl) ammonium hydroxide (MEDSAH), [2-(methacryloyloxy) ethyl] dimethyl-(3-sulfobutyl) ammonium hydroxide (M-2.4-S), and [2-(methacryloyloxy) propyl] dimethyl-(3-sulfopropyl) ammonium hydroxide (M-2.6-S) in 0.5 M NaBr solution at 70°C, using 4,4´-azobis(4-cyanopentanoic acid) **(**V501) as the thermally degradable initiator and 4-cyano-4-(phenylcarbonothioylthio) pentanoic acid (CPA) as the chain transfer agent.

Using the same reaction conditions as starting point, three zwitterionic monomers were chosen from the existing library in our lab to investigate and optimize the RAFT polymerization reaction conditions (Scheme 4.4). Specifically, three process parameters were considered: a) an optimal

RAFT agent, b) RAFT agent/initiator ratio, c) solvent. The first important process parameter was the chemical structure of the RAFT agent. Dithiobenzoates are typically selected to control methacrylate polymerization because they have a Z-group that will help stabilize the intermediate radical.[172] 4-Cyano-4-(phenylcarbonothioylthio)pentanoic acid (CPA) provides a good control of zwitterionic polymers.[291] Hence, it was chosen as the RAFT agent. 4,4´-azobis(4-cyanopentanoic acid) (V501) was used as the initiator. All polymerizations proceeded with a monomer concentration of 1 mol L^{-1}. The second important process parameter was the ratio of CTA to initiator. The rate of the polymerization is usually controlled by maintaining the CTA:initiator ratio in the range of 5-10.[172] The initiator concentration is key to process control since the number of radicals generated by the initiator is directly related to the polymerization rate of the system. The third important process parameter is the solvent. An optimal solvent would dissolve all the components in the reaction system giving a homogenous mixture. It would not react and deactivate the components in the system. It would give a higher polymerization rate. A higher polymerization rate would shorten the polymerization time to reach full conversion. Polar solvents are known to stabilize the transition state of propagating radicals, thus achieving kinetic control of the polymerization.[292] Hence, aqueous solvent and trifluoroethanol (TFE) were investigated.

The applicability of the same conditions for all three monomers were tested. Here, we aimed to evaluate the relationship between molecular weight of the polymers and reaction time. The molar ratio of the parameters is monomer/CTA/initiator ($[M]_0/[CTA]_0/[I]_0$) = 1500/5/1. As they have not been extensively studied, the aim was to investigate whether the three monomers form polymers that increase in molecular weight with reaction time and have narrow molecular weight distributions, which is typical of RDRP techniques.

Figure 4.25 illustrates the kinetics of MEDSAH polymerization at the conditions described above. In the SEC trace (Figure 4.25(b)), the shifts in peaks towards a higher retention volume with reaction time indicated a gradual increase in the molar mass of the polymer with reaction time. Figure 4.25(a),(c) showed the increase in conversion with time and linear increase in molecular weight with conversion, respectively.

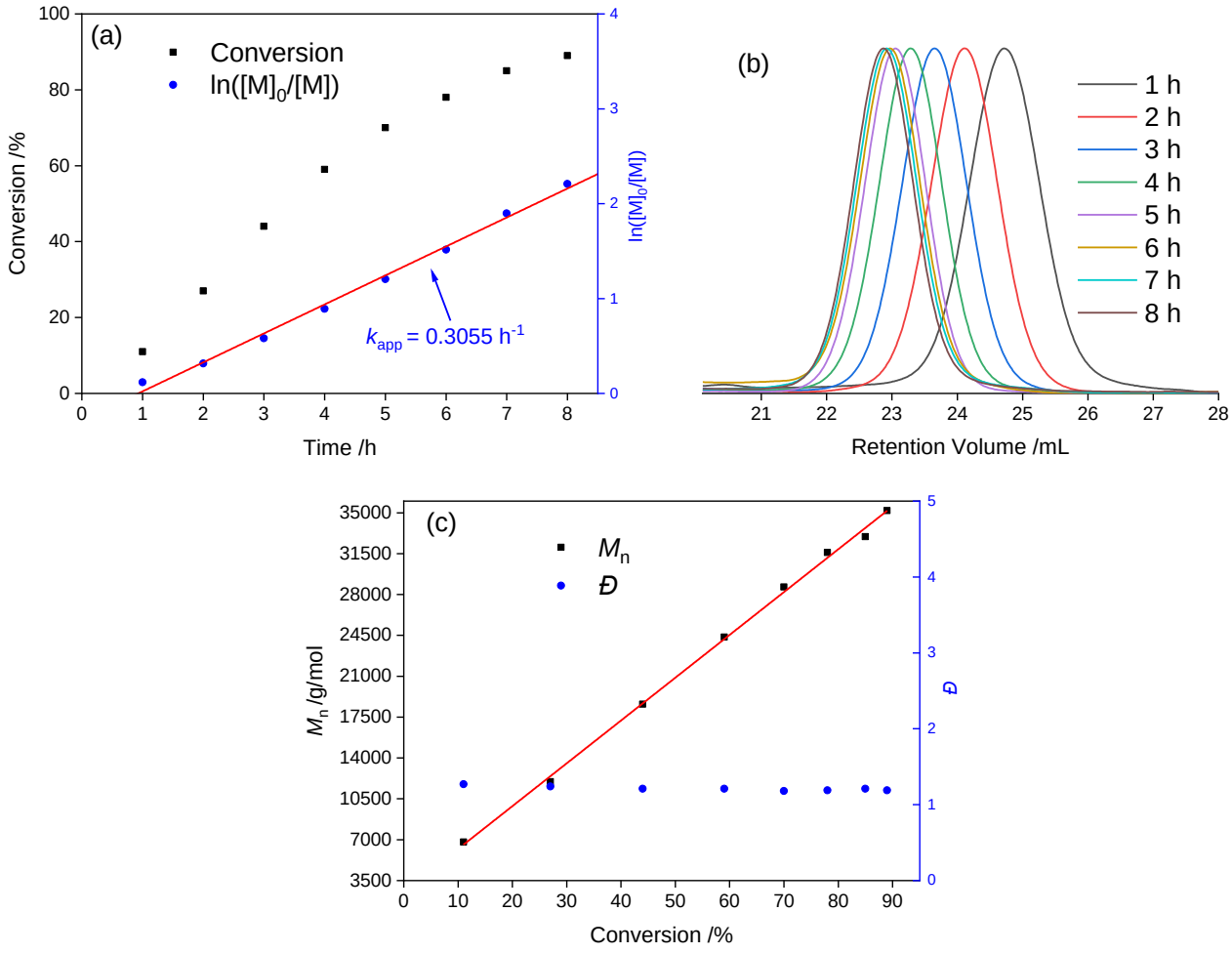

Figure 4.25: (a) Semi-logarithmic and conversion vs. time plots demonstrating MEDSAH polymerization, (b) Shifts in SEC peaks with the MEDSAH RAFT polymerization, (c) evolution of PMEDSAH molecular weight and dispersity (*Đ*) with conversion, in 0.5 M NaBr solution using V501 as initiator and CPA as the chain transfer agent at 70°C and $[M]_0/[CTA]_0/[I]_0$ = 1500:5:1

Ln ($[M]_0/[M]$) *vs.* reaction time was linear indicating a pseudo-first order reaction with respect to the monomer concentration with an apparent propagation rate constant (k_{app}) of 0.306 min^{-1}. This indicated a well-controlled PMEDSAH polymerization under the given conditions. Low dispersity (*Đ*) were also observed even for higher molecular weight polymers. A summary of the polymerization kinetics is shown in Table 4.6.

Table 4.6: Evolution of molecular weight and *Đ* for MEDSAH polymerization using $[M]_0/[CTA]_0/[I]_0$ = 1500:5:1

Reaction time/h	**Conv./% (NMR)**	**M_n (theory) (x 10^4)/g mol^{-1}**	**M_n (SEC) (x 10^4)/g mol^{-1}**	**M_w (SEC) x (10^4)/g mol^{-1}**	***Đ***
1	11	0.94	0.68	0.87	1.27
2	27	2.26	1.2	1.48	1.24
3	44	3.67	1.86	2.16	1.21
4	59	4.91	2.44	2.94	1.21
5	70	5.82	2.86	3.55	1.18
6	78	6.48	3.16	3.78	1.19
7	85	7.06	3.3	4	1.21
8	89	7.39	3.52	4.08	1.19

Next, the solution properties of PMEDSAH were investigated. Temperature-dependent measurements by DLS showed that PMEDSAH of M_n = 60,700 gmol^{-1} with a *Đ* of 1.22 decreased from 44.14 ± 5.3 nm at 10 °C to 5.2 ± 1.94 nm at 60 °C, indicating that the UCST value was within the temperature range 10-100 °C, and hence is desirable for therapeutics and biosensors.

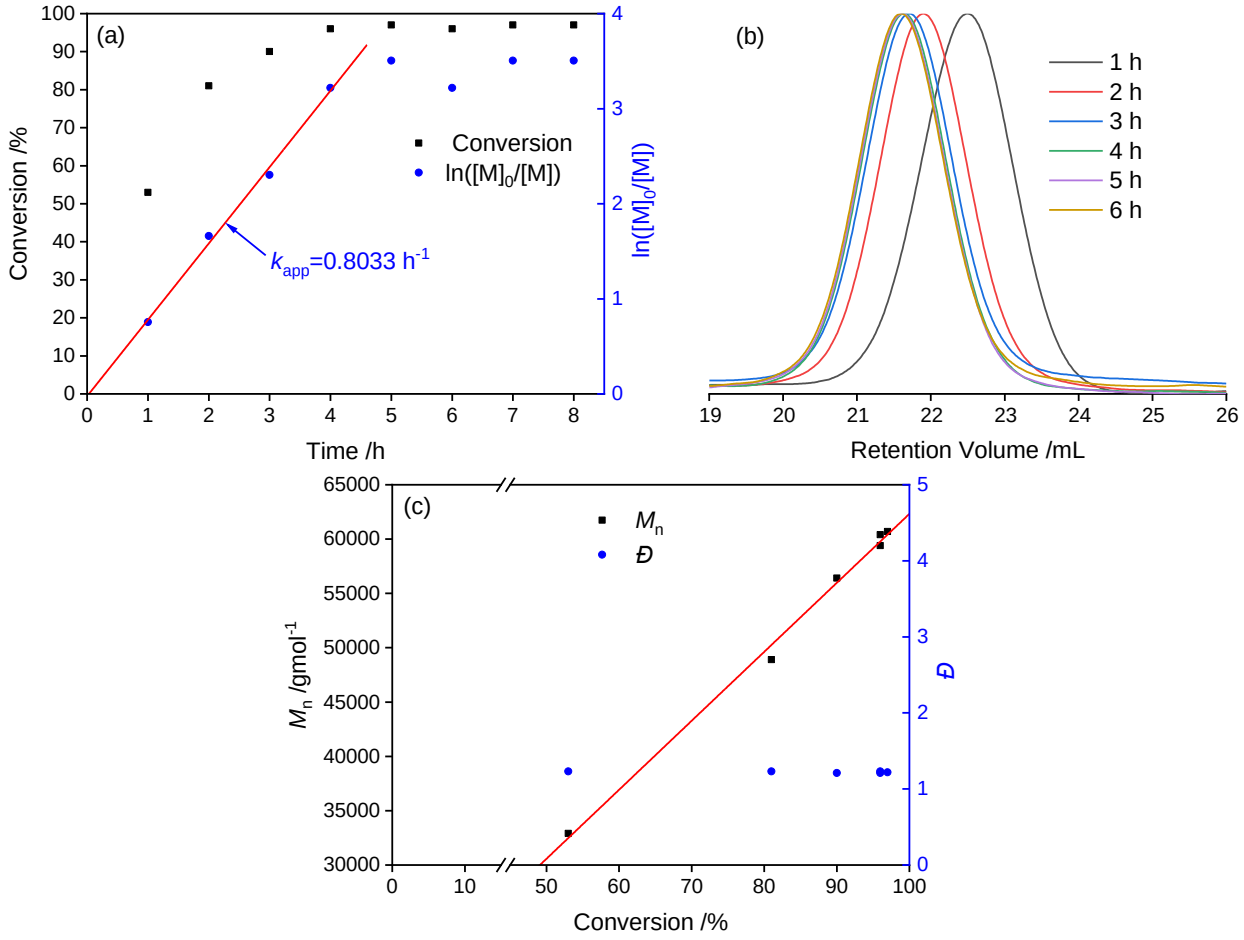

Figure 4.26: (a) Semi-logarithmic and conversion plot *vs.* reaction time; (b) shifts in SEC peaks; (c) evolution of PMEDSAH molecular weight and dispersity ($Đ$) with conversion, with MEDSAH RAFT polymerization in 0.5 M NaBr, using the initiator V501 and chain transfer agent CPA at 70°C with a target DP of 600 and $[CTA]_0/[I]_0$ = 2.5.

Kinetic studies under the condition of $[M]_0/[CTA]_0/[I]_0$ = 1500:2.5:1, and the results showed a conversion of around 53% in the first hour (Figure 4.26(a)). Higher amount of initiator with respect to CTA generated more radicals and hence termination reactions set in at around 5 h. It turns out, using more initiator increased the polymerization reaction rate. A linear plot of $\ln([M]_0/[M])$ vs time appeared up to monomer conversion of 96%, indicating the first order kinetics with respect to monomer concentration. The linear relationship between M_n and conversion as well as the relatively low $Đ$ ($\leq$ 1.23) further demonstrated the good polymerization control (Figure 4.26(c)). SEC curves (Figure 4.26(b)) showed unimodal and narrow distribution. The MEDSAH polymerization in water was found to be very fast. Another factor is that the

dissolution of solid phase V501 and CPA in pure water was difficult. Addition of 50 mM NaOH improved the dissolution. However, at least 3 h stirring was still required. Considering the above reasons, MEDSAH RAFT polymerization was carried out in TFE. TFE was shown to be a thermodynamically better solvent than aqueous salt solution for PMEDSAH.[293] TFE readily dissolved V501, CPA and MEDSAH and a homogenous mixture was obtained. MEDSAH RAFT polymerization in TFE proceeded quickly but in a poorly controlled manner, leading to a high molecular weight distribution higher than $Đ$ = 1.4 (Figure 4.27).

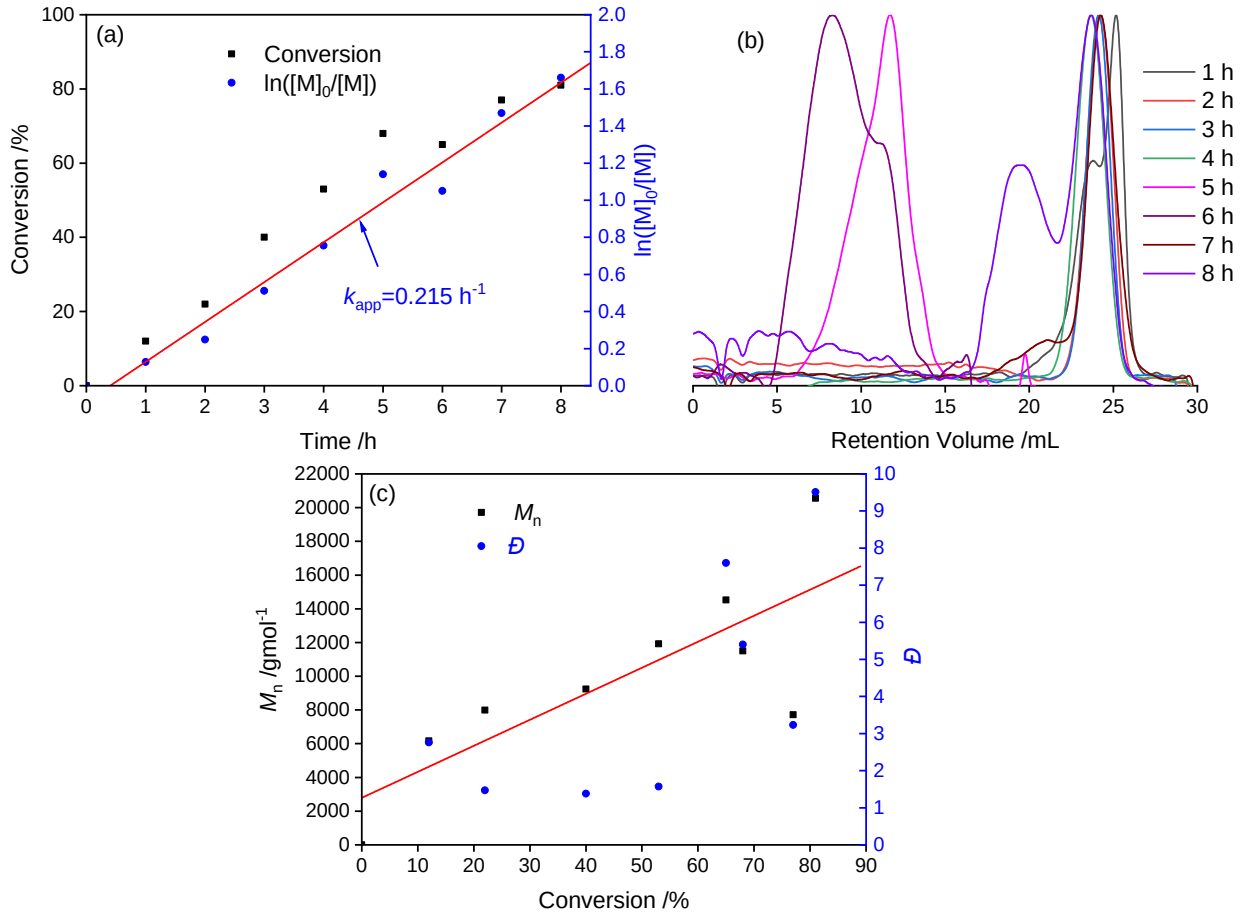

Figure 4.27: (a) Semi-logarithmic and conversion plot *vs.* reaction time; (b) shifts in SEC peaks; (c) evolution of PMEDSAH molecular weight and dispersity ($Đ$) with conversion, with MEDSAH RAFT polymerization in TFE, using the initiator V501 and chain transfer agent CPA at 70°C with a target DP of 300 and $[CTA]_0/[I]_0$ = 5.

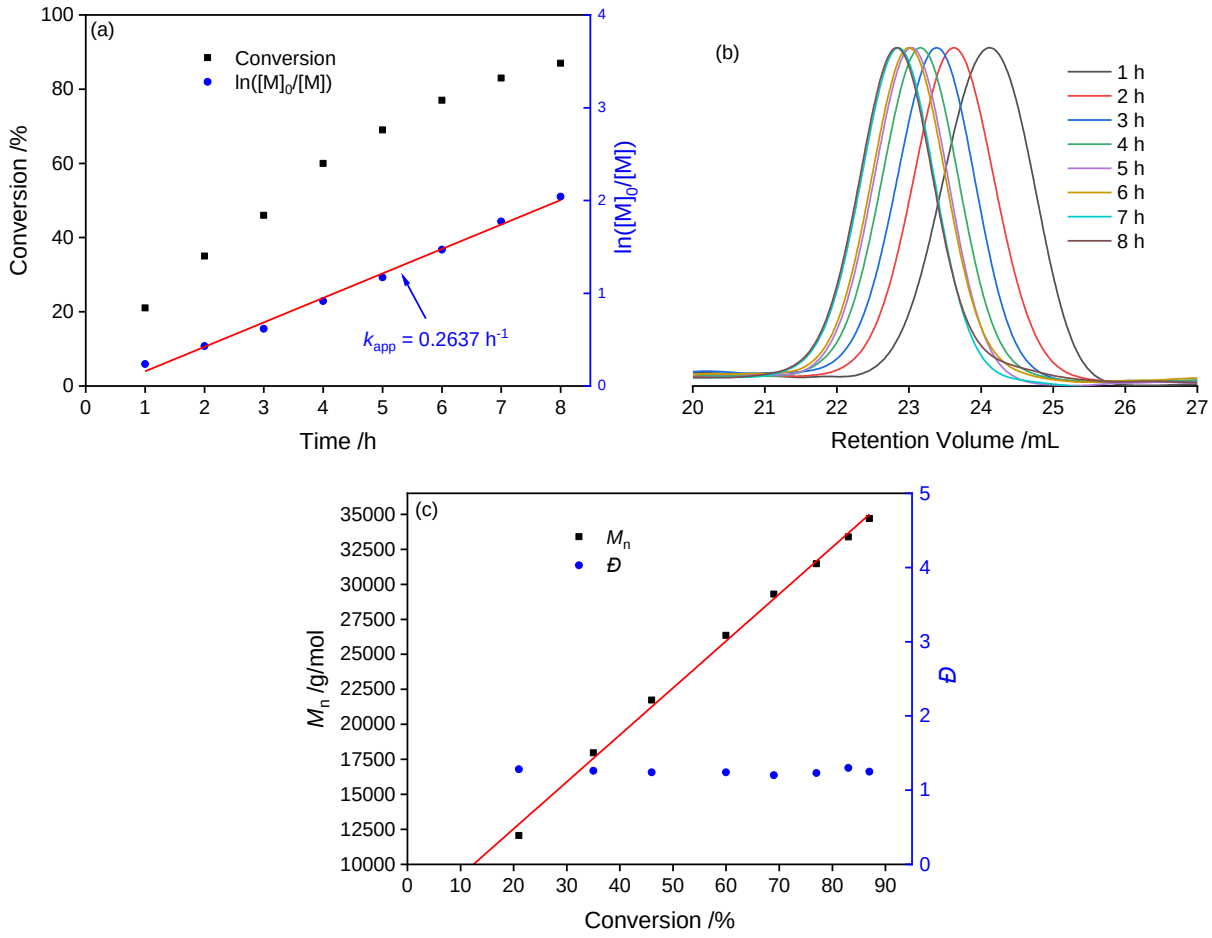

Figure 4.28: Polymerization of M-2.4-S in water: (a) plot of conversion and ln($[M]_0/[M]$) as a function of polymerization time; (b) SEC trace; (c) evolution of molecular weight and *Đ* with monomer conversion in 0.5 M NaBr solution at 70°C using $[M]_0/[CTA]_0/[I]_0$ = 1500:5:1.

Table 4.7: Data for M-2.4-S polymerization in water using $[M]_0/[CTA]_0/[I]_0$ = 1500:5:1.

Reaction time/h	Conv./% (NMR)	M_n (theory) (x 10^4)/g mol^{-1}	M_n (SEC) (x 10^4)/g mol^{-1}	M_w (SEC) (x 10^4)/g mol^{-1}	$Đ$
1	21	1.88	1.21	1.56	1.28
2	35	3.11	1.8	2.27	1.26
3	46	4.09	2.17	2.82	1.24
4	60	5.32	2.63	3.34	1.24
5	69	6.11	2.93	3.69	1.2
6	77	6.82	3.15	3.76	1.23
7	83	7.35	3.34	4.35	1.25
8	87	7.7	3.47	4.34	1.3

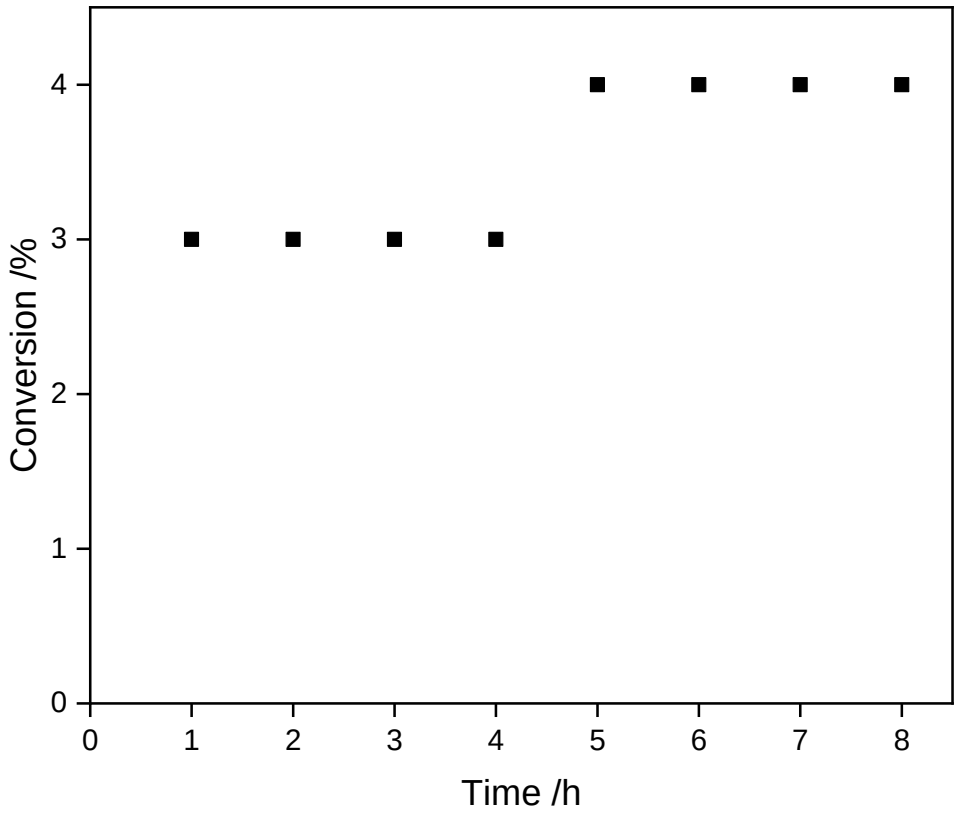

Figure 4.29: M-2.4-S polymerization in TFE using initiator V501 and RAFT agent CPA at 70 °C $[CTA]_0/[I]_0$ = 5. Conversion determined by NMR vs time.

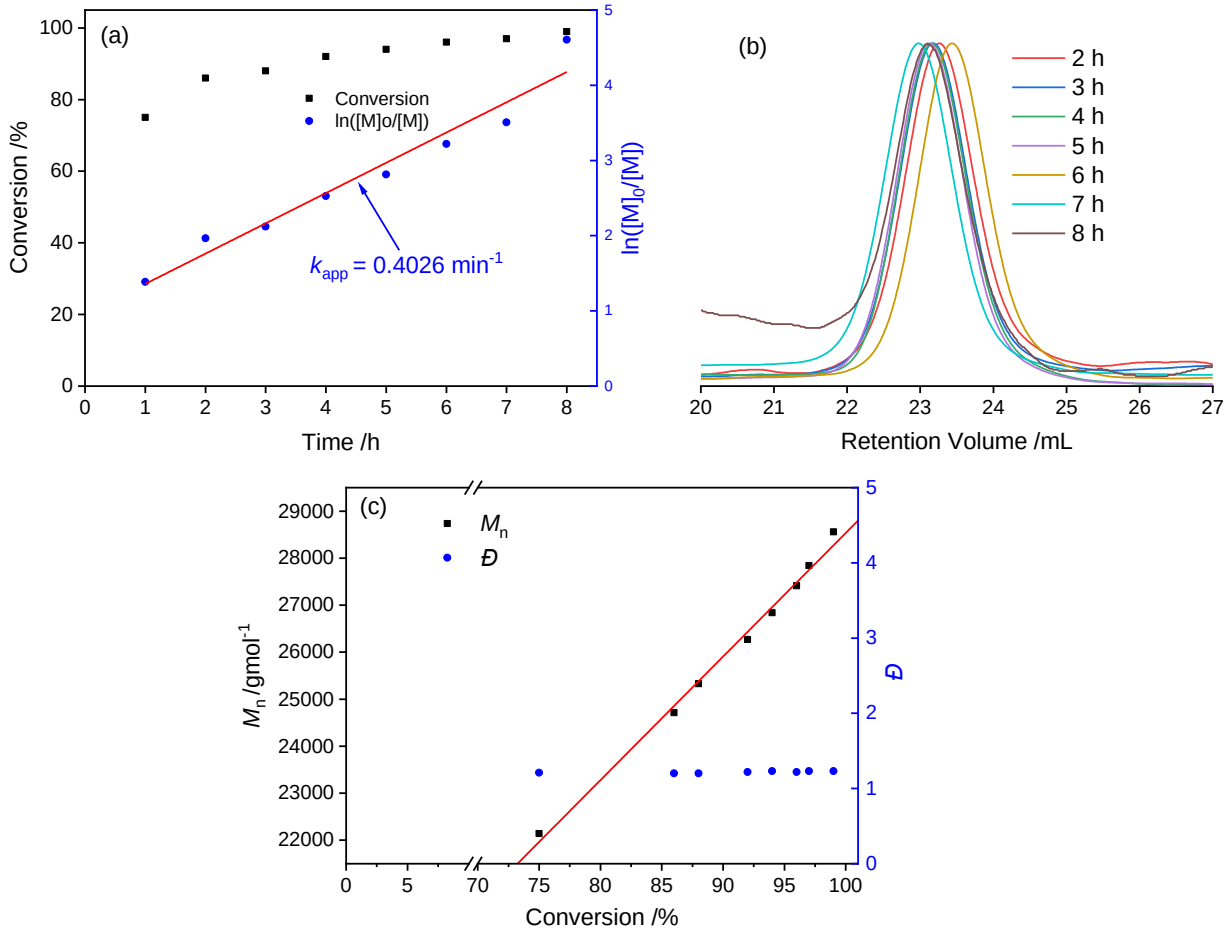

Figure 4.30: Polymerization of M-3.3-S: (a) plot of conversion and ln([M]$_0$/[M]) as a function of polymerization time; (b) SEC trace; (c) evolution of molecular weight and *Đ* of M-3.3-S with monomer conversion in 0.5 M NaBr solution at 70°C using [M]$_0$/[CTA]$_0$/[I]$_0$ = 1500:5:1, confirming controlled polymerization.

Polymerizations with M-2.4-S and M-3.3-S were conducted, and the corresponding results are summarized in Figure 4.28-4.30. P(M-2.4-S) was soluble in water and possessed low *Đ* characteristic of optimal RAFT polymerizations (Figure 4.28). M-2.4-S was polymerized in TFE. Figure 4.29 shows that the M-2.4-S polymerization at 70 °C only achieved 4% conversion until 8 h. The polymerization of M-2.4-S in TFE was not carried out in a controlled manner. Hence, TFE was not an appropriate solvent for M-2.4-S RAFT-mediated polymerization. Results for the polymerization of M-3.3-S showed that the polymerization rate was fast. A high monomer conversion of 75% was achieved after 10 h of reaction (Figure 4.30). The molecular weight distribution was narrow.

To conclude, we examined the differences in the polymerization kinetics of three zwitterionic monomers with varying charge distance. The objective was to find the optimum RAFT conditions for MEDSAH polymerization in solution and whether the effects of varying the zwitterionic charge distance on the polymerization kinetics. The controlled nature of MEDSAH polymerization was demonstrated by the kinetic study with the following conditions: $[M]_0/[CTA]_0/[I]_0$ = 1500:5:1 at 70 °C in an aqueous 0.5 M NaBr solvent. PMEDSAH showed low dispersities ($Đ$<1.3). Using MEDSAH polymerization as a model, we examined the polymerization kinetics of M-2.4-S and M-3.3-S under similar reaction conditions. In M-2.4-S polymerization, the propagation rate or k_{app} is around 0.26 h^{-1}, which indicated a comparable propagation rate to PMEDSAH (k_{app} = 0.3 h^{-1}). In M-3.3-S polymerization, the propagation rate constant was around 0.4 h^{-1}, indicating a faster polymerization rate than PMEDSAH and P(M-2.4-S). Additionally, $Đ$ the of the resulting polymers were narrow. Thus, the optimum process parameters for the RAFT polymerization of zwitterionic monomers in solution are a) using a dithiobenzoate RAFT agent, b) a CTA/initiator ratio of 5/1, and c) an aqueous 0.5 M NaBr solvent. In addition, the zwitterionic charge distance varied the propagation rate of the polymerization, reiterating the role of zwitterionic charge distance in the material properties of PMEDSAH. A recommendation to future investigators is to modify the polymers by post-translational modification to introduce clickable azide groups that can then be clicked to the alkyne group presenting CVD coatings, in a “grafting-to” approach.

4.6 Investigation of Human Stem Cell Growth on Various Substrates

After the surfaces were generated and fully characterized, cellular response could be assessed. Since it would be beneficial for a synthetic culture substrate to be compatible with multiple stem cell lines/types, the behavior of hMSC, hESC and HSC on the synthetic surfaces was evaluated. hMSC were evaluated in terms of cell attachment and morphology after 7 days of culture. hESC were evaluated based on cell attachment, morphology and differentiation after 5 weeks of passage. HSC were evaluated at the end of a 7-day culture.

4.6.1 Propagation of hematopoietic stem cells on UVO-grafted PMEDSAH coatings

In Villa-Diaz *et al.*[13], UVO-grafted PMEDSAH polymer coatings were used for long-term maintenance of hESC in an undifferentiated state. UVO-grafted PMEDSAH coatings have also been used for long-term culture of iPSC.[294] However, this platform had not been explored for the culture of HSC. HSC play a crucial role in the generation of blood and immune cells. The ability to expand clinically relevant HSC populations in vitro is still lacking.

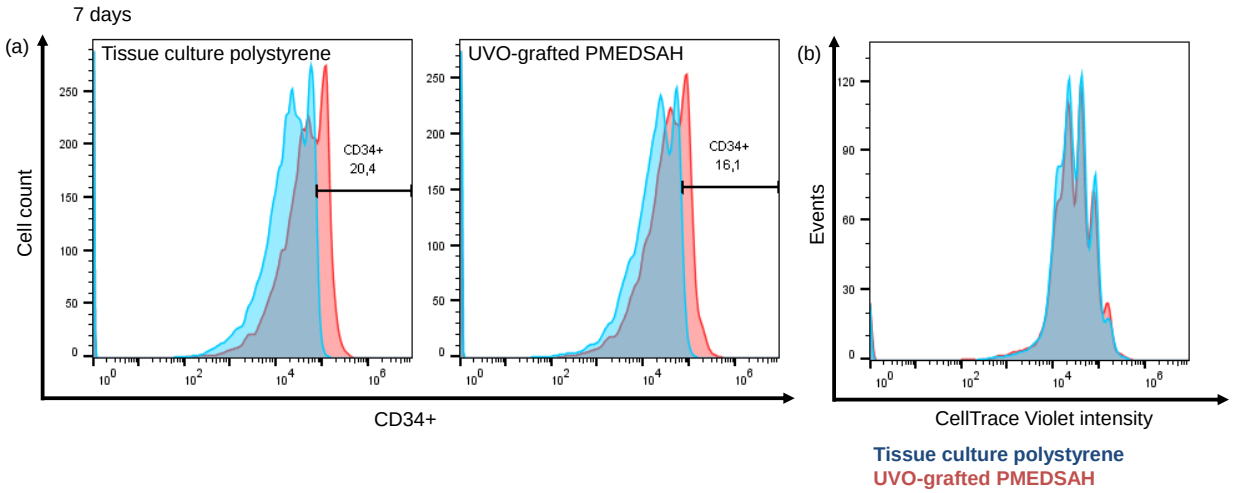

Figure 4.31: HSC proliferation assays were performed by Dr. Lisa Rodling at Karlsruhe Institute of Technology. (a) The percentage of CD34 positive cells was determined after HSC culture for 7 days on tissue culture polystyrene and UVO-grafted PMEDSAH surfaces. The CD34 isotype control is shown in red. (b) The proliferation of the cells is visualized by plotting the number of events against the CellTrace Violet fluorescence intensity. Each peak indicates a subpopulation of cells that has undergone a certain number of cell divisions. The lower the fluorescence intensity the more the dye was diluted in cell division events and thus more cell divisions have taken place.

The aim was to investigate the influence of UVO-grafted PMEDSAH coatings on HSC adhesion and proliferation. Umbilical cord blood cell cultures were cultured on UVO-grafted PMEDSAH coatings and compared to tissue culture polystyrene surfaces. Flow cytometry was used after 7 days of culture on the two different surfaces to determine the expression amount of retained CD34. Similar results were obtained from both surfaces regarding CD34 expression (Figure 4.31). Cell proliferation assay was performed after 7 days of culture on the two surfaces to test the influence of PMEDSAH on HSC differentiation. No significant differences in the

number or type of colonies were found (Figure 4.31(b)), indicating that the UVO-grafted PMEDSAH coatings had no impact on HSC differentiation.

The total number of cells in culture at the end of 7 days on UVO-grafted plates was found to be like the number of cells cultured on the control TCPS plates. In summary, these findings showed that UVO-grafted PMEDSAH coatings does not affect cell viability, proliferation and differentiation. These results were also a propelling factor to control the material properties of the PMEDSAH coatings to investigate whether changing the physico-chemical properties would improve the proliferation of the HSC with reduced differentiation. Hence, RDRP techniques were employed to fabricate substrates with tunable material properties.

4.6.2 Propagation of human mesenchymal stem cells on ATRP PMEDSAH coatings

The experiments in this section was done together with Dr. Thomas Eyster. Cells were assessed on the various ATRP surfaces and UVO-grafted surfaces. Concerning cell attachment, more hMSC were found on ATRP modified surfaces than on the UVO grafted surfaces (Figure 4.32). After 7 days of culture, differences in cell morphology were apparent for the different surface treatments. HMSC cultured on the UVO-grafted surfaces were larger than those on the ATRP modified surfaces. This may occur as a result of there being fewer cells adhered on the UVO-grafted surface which affords more area for spreading and thus larger cell areas on average. However, the cell sizes on the various ATRP surfaces were comparable indicating that the thickness and thus the corresponding wettability differences have little influence on cell morphology (Figure 4.33). Additionally, the cell count on the different ATRP surfaces increased compared to the UVO-grafted PMEDSAH surfaces (Figure 4.33).

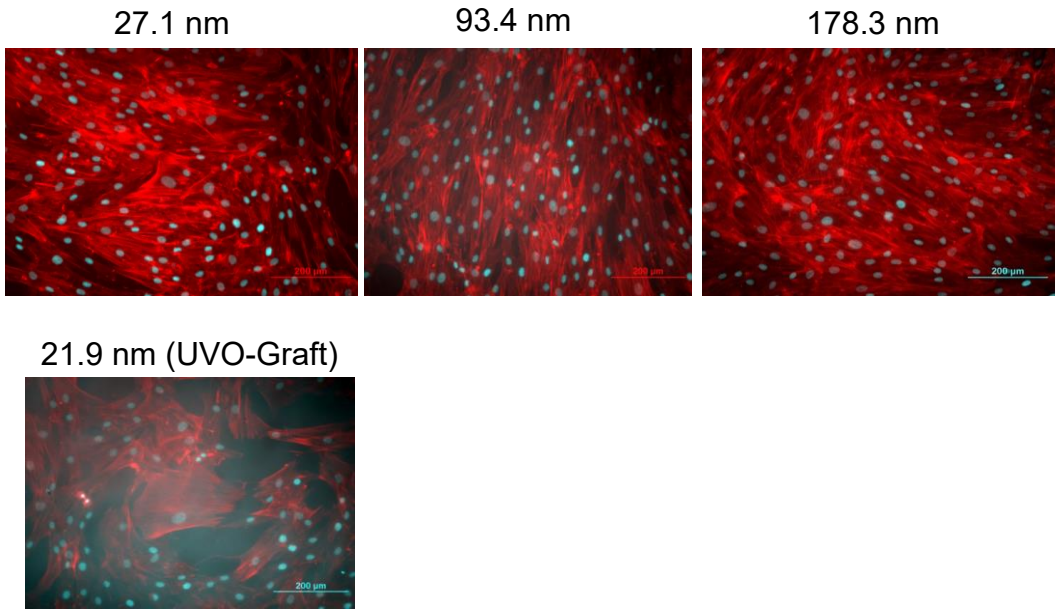

Figure 4.32: Characterization of hMSC on PMEDSAH UVO-grafted surfaces, 1 h, and 12 h and 24 h ATRP surfaces. Fluorescence micrographs of colonies stained with phalloidin and DAPI nucleic acid stains. Scale bar = 200 µm.

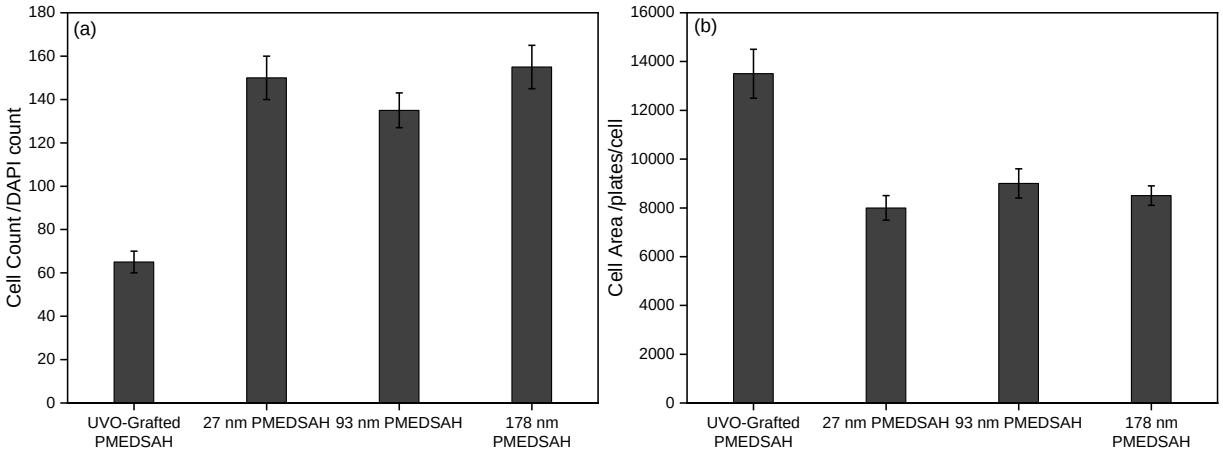

Figure 4.33: (a) Average number hMSC counted on different surfaces after 1 week of growth, (b) Average cell area (pixels) of hMSC grown on different surfaces as observed after 1 week of growth.

Since very little difference was noted in the morphology between the ATRP modified surfaces, subsequent experiments with hMSC were done on the 1h ATRP coated surface with ~27 nm thick hydrogel. This work was done together with Dr. Aftin Ross[295] and Dr. Thomas Eyster, University of Michigan. It was used to quantify the extent of cell differentiation as the cells were stained with fluorescent dyes for the pluripotency markers of interest.

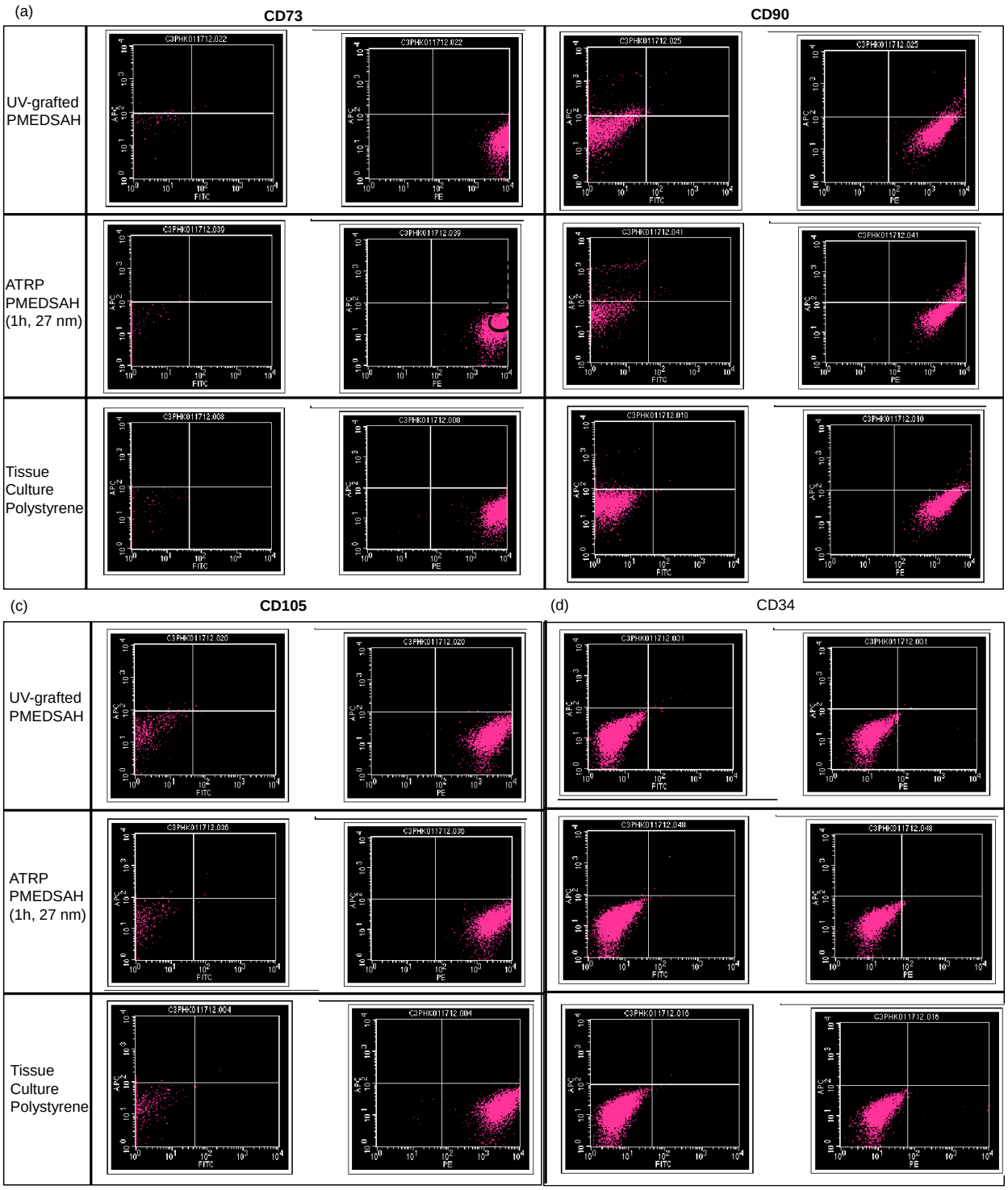
(a)
CD73
CD90
UV-grafted PMEDSAH
ATRP PMEDSAH (1h, 27 nm)
Tissue Culture Polystyrene
(c)
CD105
(d)
CD34
UV-grafted PMEDSAH
ATRP PMEDSAH (1h, 27 nm)
Tissue Culture Polystyrene

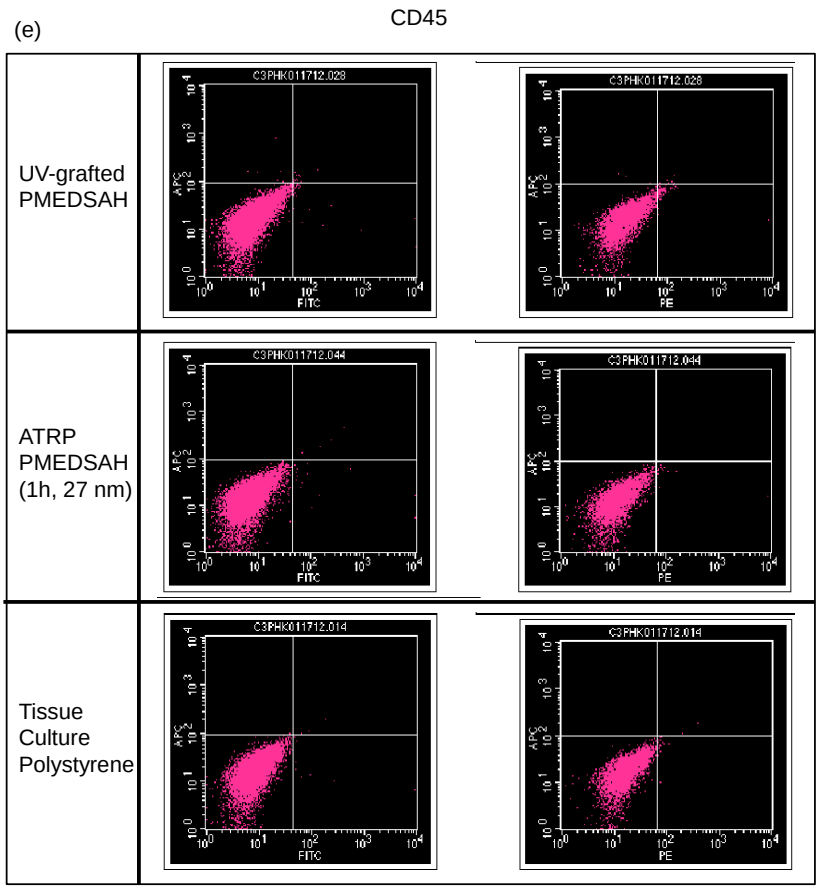

Figure 4.34: Flow cytometry was performed to measure the expression of (a) CD 73 (b) CD 90 (c) CD 105 (d) CD 34 and (e) CD 45 on hMSC cultured on ATRP substrates after 1 week to determine the percentage of cells expressing each marker.

CD73 is an enzyme in humans that commonly serves to convert AMP to adenosine. It is expressed in mesenchymal stem cells. Hence it is used as typical positive pluripotent markers for hMSC (Figure 4.34(a)). Characterization of CD73 suggested that the surfaces consisted of a significant number of pluripotent cells and showed differentiation potential. CD90 is a 25-37 kDa heavily N-glycosylated, glycophosphatidylinositol anchored conserved cell surface protein with a single V-like immunoglobulin domain. It is used as a positive marker for hMSC. The cultures grown on UVO-grafted PMEDSAH and ATRP PMEDSAH showed positive expression for CD90 (Figure 4.34(b)). The high levels of CD90 expression in UVO-grafted PMEDSAH and ATRP PMEDSAH cultures suggested that hMSC are undifferentiated in culture.

CD105 is a transmembrane glycoprotein located on cell surfaces and is a part of the TGF beta-receptor complex.[296] It is highly expressed in undifferentiated hMSC. The expression of CD105 surface markers (Figure 4.34(c)) suggested that the hMSC have retained their pluripotency on UVO-grafted and ATRP PMEDSAH surfaces. CD34 protein expression is used as a negative marker for hMSC. CD34 negative cells represented ~2% of the human mesenchymal stem cell population on all surfaces. CD45 antigen (Leukocyte Common Antigen) is expressed on almost all hematopoietic cells except for mature erythrocytes.[297] It is also used as a negative marker for the characterization of pluripotent hMSC. Negative expression of CD45 on cells grown on the ATRP surface indicated that ATRP PMEDSAH surfaces maintained hMSC in their pluripotent state. Based on the dot-plots, these cells had low levels of CD45 (~ 9%) on their surface. The results did not reveal any significant difference between UVO-grafted PMEDSAH and among ATRP PMEDSAH substrates. This showed that the interfacial properties of the substrate do not influence the culture of hMSC. ATRP PMEDSAH coatings were able to maintain mesenchymal stem cell markers for 7 days. In conclusion, ATRP PMEDSAH-based coatings support hMSC culture and the cells were viable.

4.6.3 Propagation of undifferentiated hESC on ATRP PMEDSAH coatings

Influence of thickness material property of ATRP PMEDSAH brushes on stem cell function was investigated. UVO-grafted PMEDSAH coatings were used as control in this study. 20,000 of hESC, cultured initially as single cells, were incubated on UVO-grafted PMEDSAH and ATRP PMEDSAH brush coatings with three different thicknesses. Cell adhesion was found by counting the number of cells present on the surface after 7 days of culture. The total cell number ratio compared to the UVO-grafted PMEDSAH coatings was quantified prior to each passage to new dishes. They were passaged weekly for five weeks. hESC colony growth was monitored for these five weeks and optic al images were acquired after 5 passages of proliferation on day 7 of culture.

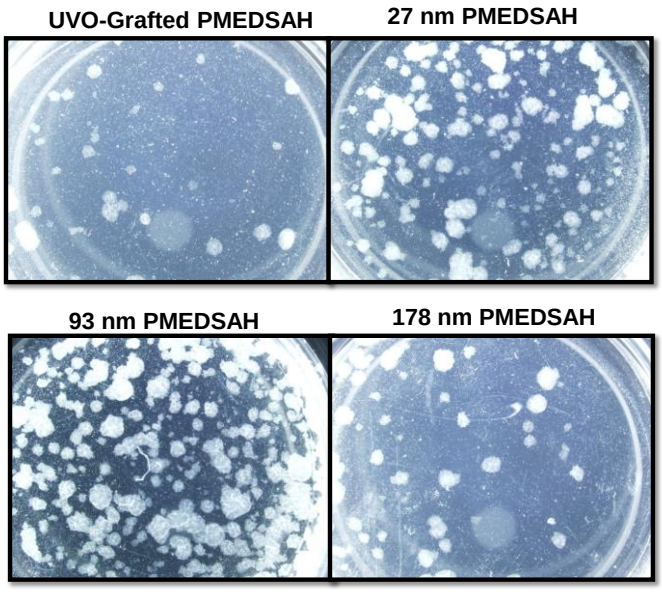

Figure 4.35: The representative optical images were acquired (10x) for different substrates after 5 passages on day 7 of culture.

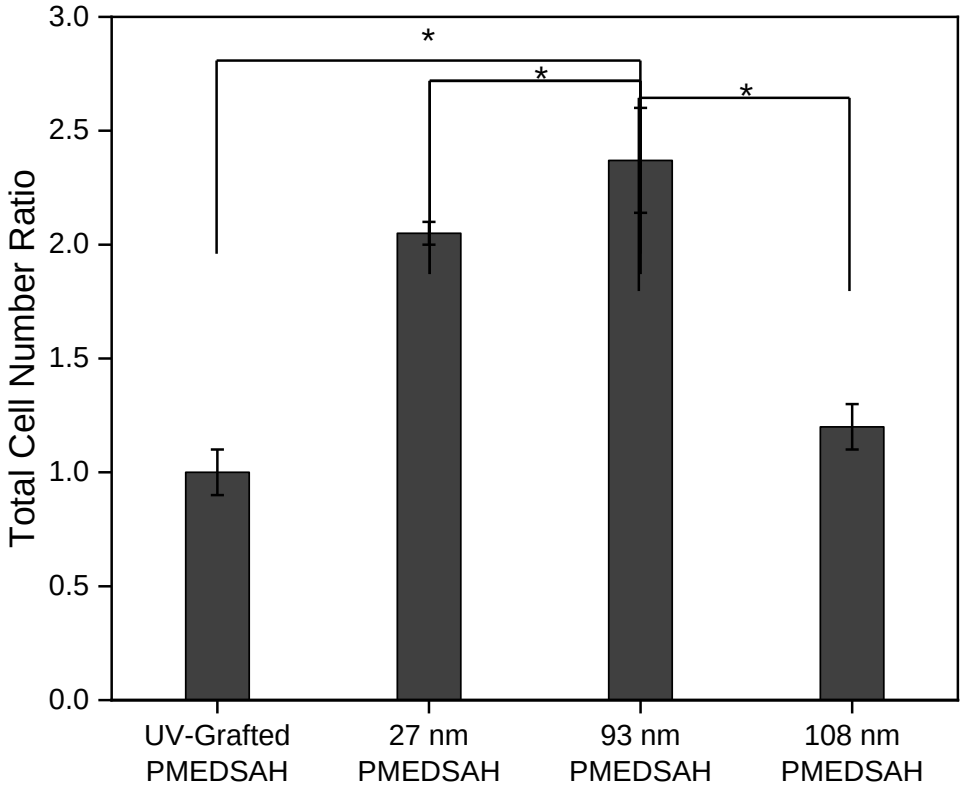

Figure 4.36: Plot of total cell number ratio compared to UVO-grafted PMEDSAH coatings used as control after 5 weeks, indicated ATRP PMEDSAH brushes with 93 nm hydrogel thickness lead to a higher total cell number compared to other experimental groups. n = 3; *$p < 0.05$; data presented as mean ± standard deviation (SD).

Alkaline phosphatase provides supportive evidence that cells are in the pluripotent state.[298] ALP was used to determine the colony size and density differences of cells on the different surfaces. Colony sizes were different between the different coatings, after 5 passages (Figure 4.35). Enhanced cell adhesion was observed on 93 nm ATRP PMEDSAH substrates compared to the other substrates. The yield of hESC after 5 passages on each substrate was calculated assuming all cells obtained at each passage were sub-cultured, instead of the 20,000 cells that were propagated.[103] The theoretical yield of cells was determined from the formula

$$CN_{(n+1)} = \frac{CN_{\mathrm{n}} \times TN_{n+1}}{20{,}000} \tag{20}$$

where CN was the calculated total cell number, TN was the total cell number in the determined week and n represented the culture week.

The hESC cultures grown on the 93 nm thick brush plates that have moderately self-associated PMEDSAH coatings had 2.3-fold more cells compared to hESC cultures grown on UVO-grafted PMEDSAH plates (Figure 4.36). Using eq 20, it was estimated that 20,000 hESC cultured on the moderately self-associated PMEDSAH brush coating, expanded over a period of five weeks to yield up to 4.7 billion undifferentiated cells.[103] Additionally, there is a significant difference in the propagation rate of hESC expanded on the brushes with unassociated (27 nm) and highly associated (178 nm) polymer brush coatings. Thus, moderately self-associated PMEDSAH polymer brushes significantly facilitated the expansion of hESC. These studies determined that thickness, and in turn, wettability material properties strongly influence the proliferation of undifferentiated hESC on PMEDSAH substrates, thus contributing to the design of PMEDSAH polymer brush cell culture platforms

We assessed hESC cultures after the 5th passage for SSEA-4, a key marker of pluripotency. It is a regulatory transcription factor necessary for the maintenance of the hESC pluripotent state. Flow cytometry was used to quantitatively assess the expression of SSEA-4 in hESC (Figure 4.37).

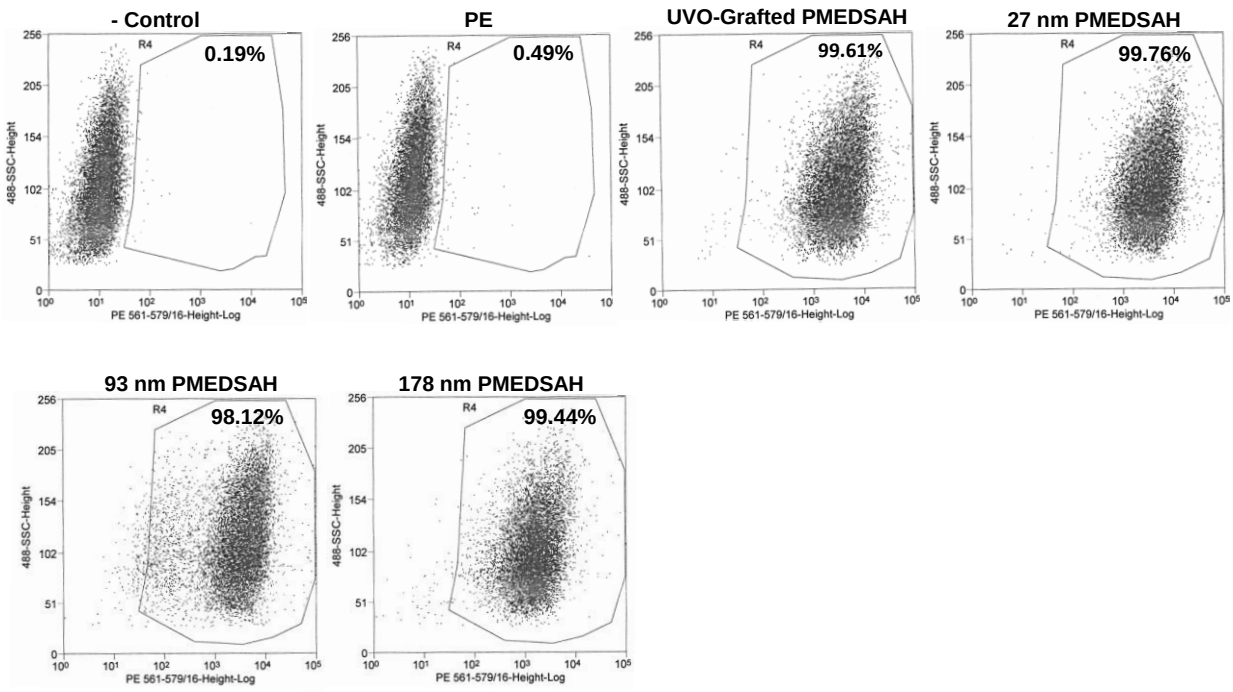

Figure 4.37: Flow cytometry analysis performed by Dr. Xu Qian, University of Michigan. hESC cultured on different substrates after the 5th passage was analyzed by flow cytometry to determine the percentage of SSEA-4 expressing cells. Background fluorescence and autofluorescence were determined using cells without treatment (-Control) and treated with Mouse IgG1 Phycoerythrin Isotype Control (PE).

As expected, flow cytometric analysis revealed that the percentage of SSEA-4$^+$ cells were ~99% in all substrates.[103] The results were not significantly different ($p>0.05$) between the ATRP-modified coatings and UVO-grafted coating. We found that hESC were strongly positive for SSEA-4 as compared to control cells stained with non-specific IgG. The results revealed that the cells were pluripotent on all the PMEDSAH coatings, and that the different gel architectures influence the number of cells grown on the brushes but maintain pluripotency of the cells regardless. Thus, modifying the extent of zwitterionic self-association of PMEDSAH coatings enhance the propagation rate of hESC.

4.6.4 Screening IGT-modified polymer coatings for hESC colony adhesion

Before conducting experiments to examine the long-term maintenance of hESC on IGT-modified surfaces, we needed to establish the optimum chain length of IGT molecules to be grafted to the surfaces that would maintain the pluripotency of the cells. Adhesion of 20,000 hESC/plate plated on substrates modified with IGT of six different molecular weights (5-10 $kgmol^{-1}$) was examined to investigate and find an optimum polymer chain length of IGT that will help in the adhesion of hESC. We wished to verify whether a trend in hESC adhesion is observed with increasing molecular weights of IGT molecule.

Throughout the two passages, H9 hESC were observed to adhere to five of the six different coatings, albeit at different rates. Plates coated with IGT with a M_n of 6 $kgmol^{-1}$ were observed to have higher cell adhesion than the plates that had been modified with the other molecular weight polymers. No attachment was observed on IGT modified substrates with a M_n of 8 $kgmol^{-1}$. At the center of the self-renewal of hESC are the transcription factors Sox2, oct4 and NANOG, whose expression is precisely and tightly regulated in hESC. Immunofluorescent staining of *OCT4*, *NANOG* and *SOX2* after each passage was strong when cultured on the five different coatings. Thus, hESC remained pluripotent on all the substrates investigated for 2 passages except for IGT modified substrates with M_n of 8 $kgmol^{-1}$ (Figure 4.38). 6 $kgmol^{-1}$ and 9 $kgmol^{-1}$ IGT-modified substrates had more cell spreading than the other substrates. Though there were differences visually on how the cells adhere to the different IGT-modified substrates as observed in Figure 4.38, no trend could be observed in hESC adhesion with increasing molecular weight IGT modified substrates.

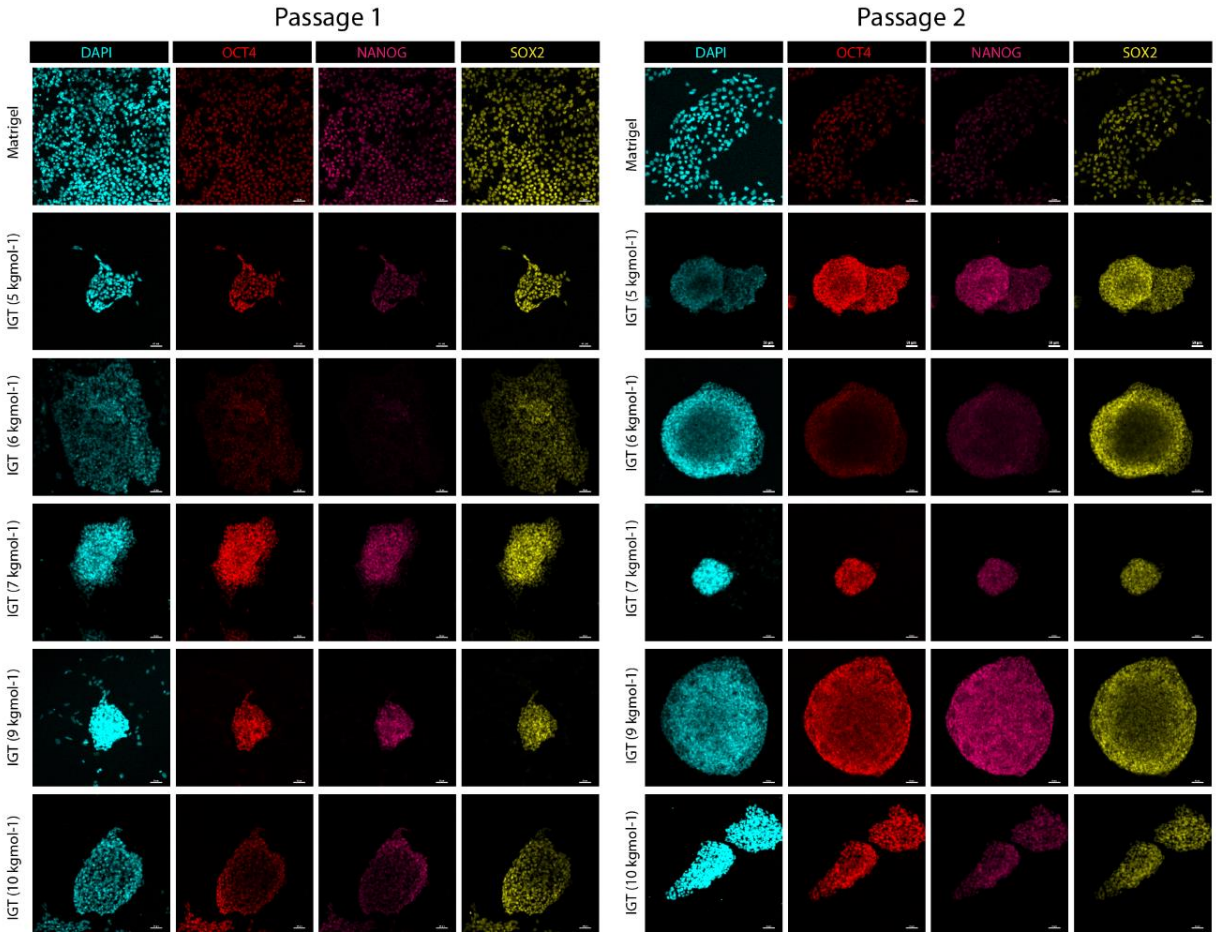

Figure 4.38: Cell culture and analysis performed by Dr. Tugba Topal at University of Michigan. Fluorescence micrographs of colonies of H9 cells cultured on IGT-modified substrates and Matrigel with different molecular weights for 2 passages in human cell-conditioned medium showing expression of hESC markers: DAPI, OCT4, NANOG and SOX2. Scale bars, 50 µm.

In addition to immunofluorescence staining, the cells were examined for the expression of pluripotency markers for the two passages using quantitative reverse transcription PCR (RT-PCR) analysis[299] (Figure 4.39). Results demonstrated that the RNA expression levels of hESC markers *OCT4* for IGT-5 kgmol^{-1} (0.8 fold change), IGT-6 kgmol^{-1} (0.9 fold change), IGT-7 kgmol^{-1} (0.9 fold change), IGT-9 kgmol^{-1} (1 fold change) and IGT-10 kgmol^{-1} (1.1 fold change); *KLF 4* for IGT-5 kgmol^{-1} (0.9 fold change), IGT-6 kgmol^{-1} (0.9 fold change), IGT 7 kgmol^{-1} (1.2 fold change), IGT-9 kgmol^{-1} (0.9 fold change) and IGT-10 kgmol^{-1} (1.7 fold change); and *SOX2* for IGT-5 kgmol^{-1} (0.4 fold change), IGT-6 kgmol^{-1} (0.3 fold change), IGT-7 kgmol^{-1} (0.4 fold change), IGT-9 kgmol^{-1} (0.6 fold change) and IGT-10 kgmol^{-1} (0.5 fold change); compared to

levels expressed by cells cultured on Matrigel (Figure 4.39). The results revealed comparable RNA expression levels of KLF 4, OCT4 and SOX2. Though, from the figure, the fold change RNA expression levels look different qualitatively, no significant differences were found between hESC cells cultured on the different IGT-modified substrates and Matrigel.

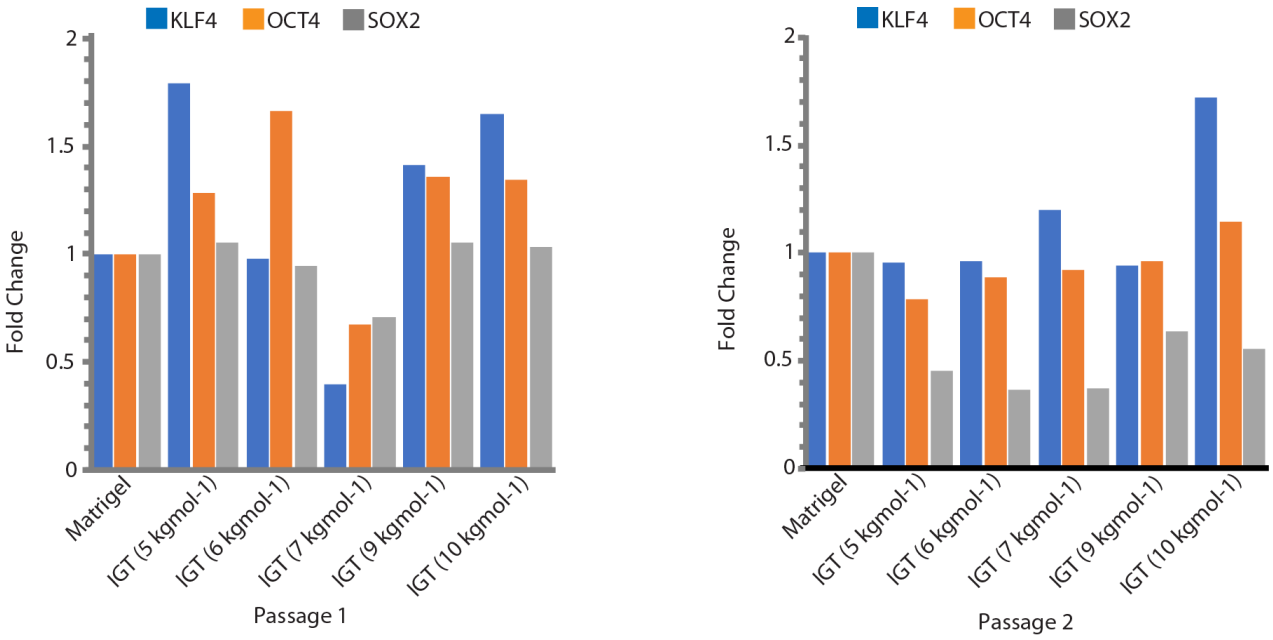

Figure 4.39: Analysis performed by Dr. Tugba Topal at University of Michigan. Relative transcript levels of KLF4, OCT4 and SOX2 from hESC cultured on different IGT-modified substrates and Matrigel at passages 1 and 2 after analysis in RT-qPCR.

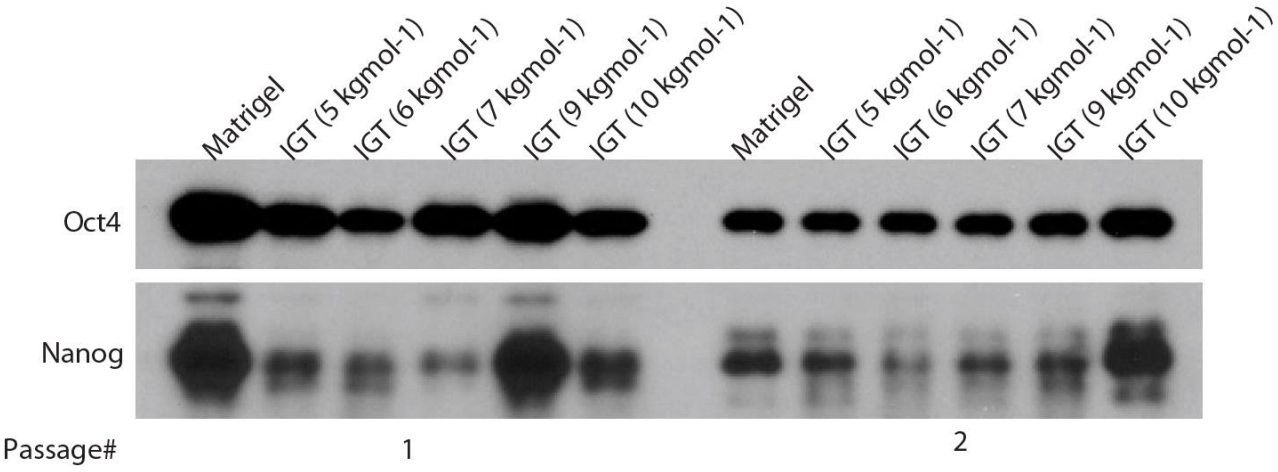

Figure 4.40: Western blot analysis of OCT4 and NANOG markers expression of hESC cultured on Matrigel and the different IGT-modified substrates after the first (left) and second (right) passage of culture.

Further, Western blotting was utilized to investigate the expression of *OCT4* and *NANOG* in hESC cultured on Matrigel and the different surfaces of IGT-modified substrates (Figure 4.40). A protein band of approximately 37 kDa corresponding to the predicted size of *NANOG* was detected in cells cultured on all IGT-modified substrates. The result suggested that *OCT4* expression in hESC cultured on the different IGT-modified substrates and Matrigel did not change. However, the expression of *NANOG* was clearly downregulated for hESC cultured on the different IGT-modified substrates except for IGT-9 kgmol^{-1} compared to cells on Matrigel substrates.

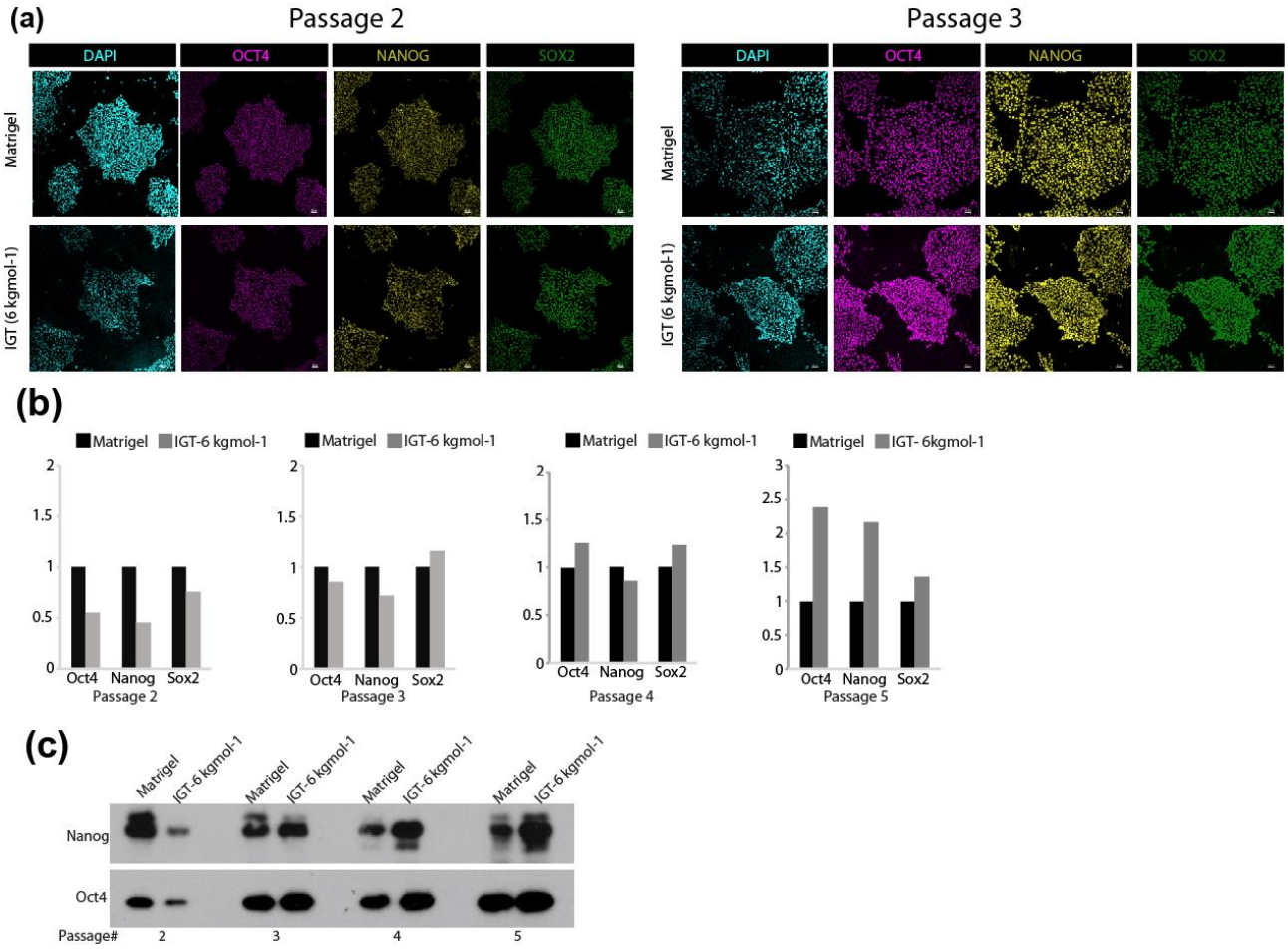

Figure 4.41: IGT-6 kgmol^{-1} supports hESC stemness. (a) Fluorescence image of hESC colonies cultured on IGT-6 kg mol^{-1} modified substrates and Matrigel showing expression of pluripotent markers after the second and the third passage. Primary antibodies OCT4, NANOG and SOX2 were used to detect the expression of these markers from hESC cultured on IGT-6 kg mol^{-1} and Matrigel substrates. (b) Relative transcript levels of OCT4, NANOG and SOX2 from hESC cultured on IGT-6 kg mol^{-1} substrates for passages 2-5 had no significant differences compared to hESC cultured on Matrigel substrates. (c) Western blotting of OCT4 and NANOG markers expression of hESC cultured on Matrigel and the IGT-6 kg mol^{-1} modified substrates after 2-5 passages.

Since all the substrates showed pluripotency markers of hESC, IGT-6 kgmol^{-1} modified substrates were selected for long-term hESC. This is because these coatings had the closest ξ-potential to the grafting-from ATRP 93 nm-thick PMEDSAH brush coating that showed a significant increase in the expansion rate of hESC as described in Section 4.6.2. For "grafting-to" polymer brushes, the thickness of the brushes does not considerably increase based on the polymer chain length when compared to the "grafting-from" polymer brushes. Hence, the surface charge and the contact angle were compared with the SI-ATRP PMEDSAH brushes. IGT-6 kgmol^{-1} modified substrates had a similar surface charge and contact angle (52°) compared to the SI-ATRP PMEDSAH brushes (45°).

Cells grown on IGT-6 kgmol^{-1} modified substrates with HCCM, was able to support the propagation of undifferentiated hESC colonies for five passages. When H9 hESC were cultured as single cells on IGT-6 kgmol^{-1} modified substrates, the number of undifferentiated colonies were comparable to the Matrigel control group. Throughout the five passages in HCCM, expression of characteristic pluripotent hESC markers were confirmed by immunofluorescent staining of *OCT4*, *SOX2* and *NANOG*, which are associated with the undifferentiated state of hESC (Figure 4.41(a)). No significant differences in the relative transcript levels were observed among the IGT-modified substrates and the Matrigel control group (Figure 4.41(b)). Taken together, these results established that the IGT-modified substrates support hESC colony formation and expansion.

In summary, a commercially viable method to functionalize substrates for use in hESC culture was demonstrated. The IGT-modified substrates were found to support self-renewal of undifferentiated hESC in *in vitro* cell culture conditions tested here; that is culture using HCCM. This type of process method utilizes CVD polymerization of modified parylenes, which is a commercially available technique. To gain valuable insight into the role of IGT molecules in maintaining self-renewal of hESC, different molecular weights of IGT were synthesized and immobilized on PPX-aldehyde coatings. Then, H9 hESC were cultured on these substrates. Matrigel is the most widely used substrate for feeder-free hESC culture.[23] Therefore, it was used as a control in the experiments. Though initial cell attachment to the different substrates happened at different rates, and in some cases, the rate of growth of cells were slower when compared to other molecular weight substrates, no significant differences in the growth of hESC were observed after two passages from the different molecular weight IGT-modified substrates. However, in the

end, the cells grown on the different molecular weight substrates proliferated and expressed pluripotency markers.

IGT-6 $kgmol^{-1}$ modified substrates were chosen to investigate five-week hESC expansion. This substrate was chosen because its surface charge was the closest to the "grafting from" ATRP 98 nm thick coating that was shown to significantly higher total hESC cell number than the other experimental groups in Section 4.6.2. In addition, hESC retained their pluripotency after five passages during culture on IGT-6 $kgmol^{-1}$, which indicated that IGT-modified surfaces would be a potential cell culture platform.

These findings are well aligned with the long-term goal of large-scale production of clinical grade hESC. PMEDSAH is a synthetic polymer coating that does not contain motifs that would likely mimic ECM proteins like laminin or RGD.[13] However, α6β1 integrin has been identified as the dominant integrin present in hESC growing on PMEDSAH grafted plates by Villa-Diaz *et al.*.[300] They also demonstrated that the cells express laminin α5. This suggests that hPSC also contributes to remodeling the substrate in which they are cultured by secreting and depositing new ECM.[300]

CHAPTER 5 CONCLUSIONS & FUTURE DIRECTIONS

5.1 Conclusions

The main objective of this dissertation was to develop a method for growing embryonic stem cells in an undifferentiated state without the need for xenogeneic components and further decouple the physicochemical properties and cues that determines the embryonic stem cell fate. The engineering approach we proposed was the use of reversible deactivation radical process, in which the zwitterionic polymer brushes can be prepared on surfaces by RAFT polymerization or ATRP.

In summary, zwitterionic polymer brushes were extensively used to tailor the interactions of biomaterial surfaces with cells and biomolecules. By borrowing these powerful chemical motifs from nature, and amplifying them in the form of polymer brushes, we established a modular functional materials platform wherein architecture and spatial presentation can be independently controlled. Synergies with chemical vapor deposition (CVD) polymerization were identified and exploited to discover optimal polymer brush design parameters for several biomedical applications.

In **Section 4.1**, free radical polymerization of a zwitterionic hydrogel, poly[2-(methacryloyloxy)ethyl dimethyl-(3-sulfopropyl)ammonium hydroxide] (PMEDSAH), developed in our lab is presented. PMEDSAH coatings have been shown to be stable and robust after a prolonged storage period.[9] Here, the variability of the PMEDSAH coating process is proved, supporting the need for biomaterials design with tunable material properties for pluripotent stem cell culture systems. Next, the PMEDSAH coatings were investigated for the proliferation of hematopoietic stem cells (HSC). In the first investigative trial, it was found that PMEDSAH coatings have little impact on the proliferation of HSC compared to tissue culture polystyrene plates. Controlling the physicochemical properties of the material might lead to higher proliferation.

In **Section 4.2,** reactive CVD coatings of [2.2]paracylophane-4-methyl 2-bromoisobutyrate (PPX-EB) were used as ATRP initiator coatings to grow three zwitterionic hydrogels, PMEDSAH, P(M-2.4-S) and P(M-2.6-S) polymer brushes from the surface using surface-initiated atom transfer radical polymerization (SI-ATRP). The thickness of the polymer brushes was measured by ellipsometry. The thickness of the PMEDSAH and P(M-2.6-S) brushes linearly increased with reaction time, showing that the polymerizations followed the typical ATRP kinetics. However, the thickness of P(M-2.6-S) brushes was considerably lower (58 ± 4 nm) compared to PMEDSAH brushes (176 ± 9 nm) for similar reaction time (24 h). Contact angle measurements of P(M-2.6-S) after 24 h reaction time was 31±5°, which falls in the hydrophilic regime. Hence, it can be concluded that the P(M-2.6-S) polymer brushes are unassociated and in the dilute region, which is comparable to the PMEDSAH brushes of similar thickness. P(M-2.4-S) polymer brushes did not show ATRP growth kinetics.

In **Section 4.3**, for the first time, alkyne-functionalized CVD films were used as a new platform for "click reactions" which were not copper catalyzed and that utilize azide-functionalized RAFT agent was demonstrated, thereby expanding the CVD based coatings to RAFT polymerization. Reactivity of the alkyne functional groups to the RAFT agent and the subsequent polymerization of MEDSAH on these surfaces was clearly demonstrated via IRRAS, XPS, AFM, ellipsometry and contact angle measurements. This platform provided a means of generating zwitterionic polymer brushes using a grafting-from approach and devoid of any toxic ligands. Other zwitterionic monomers could also be polymerized in this fashion.

In **Section 4.4**, a "grafting–to" approach that negate the need for glove box facilities was investigated. The benefits of "grafting–to" approach for polymer brush generation include working under ambient conditions, precise control of molecular weight, and control of dispersity. The facile surface modification compensates for the low grafting density typically achieved. Interfacial Gemini transformers (IGT) are a novel system developed based on covalent attachment of the polymer brushes to the surface. It consists of a zwitterionic polysulfobetaine flanking on either side of a small hydrophobic benzaldehyde moiety and is prepared by ATRP. This method can be potentially used for any geometry and requires only a minimum of polymer solution. The surfaces were characterized by ellipsometry, water contact angle, ξ–potential measurements, XPS and ToF–SIMS. From these characterization methods, it was observed that a uniform brush layer was obtained by the "grafting–to" approach. In addition, one fabrication cycle required approximately

48 h to complete, and potential scaling up the production of IGT-modified substrates is possible with the right manufacturing, process and infrastructure support.

Patterned IGT-modified substrates were generated via microcontact printing (μCP) on a hydrazide moiety expressing surface via aldehyde-hydrazide coupling. Subsequent immobilization with a fluorescently labelled protein proved controlled immobilization of the protein. Moreover, IGT displayed both the upper and lower critical solution temperature (UCST and LCST) behaviors, respectively. This striking phenomenon can be attributed to the hydrophobic and ionic interactions, dominating in the different regimes. Additionally, CP_{LCST} was lower than CP_{UCST}, so that the polymer is hydrophobic at intermediate temperatures. The integration of design elements that enable stimuli-responsive properties such as change in temperature, change in ionic strength as shown by the swelling studies and change in surface charge with pH as shown by ξ-potential measurements would facilitate application of these structured materials in therapeutic applications.

In **Section 4.5**, RAFT polymerization was employed to create zwitterionic polymer brushes with defined molar mass in solution. The polymers investigated are PMEDSAH, poly[2–(methacryloyloxy)ethyl dimethyl-(3-sulfobutyl)ammonium hydroxide] (P(M–2.4–S)), and poly[2–(methacryloyloxy)propyl dimethyl-(3-sulfopropyl)ammonium hydroxide] (P(M–3.3–S)). Varying the charge distance between the positive and negative ions in the monomeric side chain influences the polymerization kinetics under the same conditions. The growth kinetics of the three polymers were investigated in detail. These polymers, prepared in water, could be further modified to graft to the surfaces.

In **Section 4.6**, hMSC and hESC expansion on different PMEDSAH surfaces were investigated. hMSC were cultured on ATRP PMEDSAH coatings of three different thickness. The cells proliferated at the same rate on all the substrates, and retained their multipotent state, as confirmed by MSC markers (CD73+, CD105+, CD90+, CD34–, and CD45–). PMEDSAH substrates prepared by both UVO-grafting and SI-ATRP were able to support hESC adhesion, expansion and self-renewal. In particular, the 98 nm thick PMEDSAH brushes led to the successful proliferation of undifferentiated hESC throughout 5 passages. In addition, because the molecular weight of IGT-modified substrates could be tuned and altered systematically, the impact of hESC expansion on the different molecular weight IGT–modified substrates were determined. hESC retained their pluripotency after five passages during culture on IGT 6 $kgmol^{-1}$ substrate. These

results indicated that IGT-modified substrates provide a defined environment for hESC propagation and pluripotency.

The different coatings tested in this dissertation affected the physicochemical and biological properties of the substrates. Changes in the method of surface preparation changed primarily the thickness, which is linked to the wettability of the substrate. It also affected the grafting density and nano-scale roughness of the substrates. Thirdly, the substrate rigidity of two-dimensional cell cultures impacted the differentiation potential of hESC.[301,302] "Grafting-from" methods gave a denser, thicker brush architecture whereas the "grafting-to" method could not achieve a similar grafting density or thickness. But despite that, the IGT-modified substrates promoted hESC adhesion. It could be hypothesized that since the grafting-to method produces less dense brushes, a thicker CVD coating underneath augments the stiffness of the substrate overall.

5.2Future Directions

The fibrous nature of the ECM creates a unique microenvironment that enables long range mechanical cell-cell communication via cell-induced remodeling of the network.[112] Zwitterionic polymers are not only reminiscent of chemical structures found in abundance with organisms, but can elicit well-defined predictable response from cells and other biomolecules. In this dissertation, 2D zwitterionic polymer brush surfaces were explored. The next step would be to investigate 3D scaffolds for tissue engineering. One way to prepare 3D scaffolds is to introduce the zwitterionic polymer brushes on scaffolds by incorporating ATRP initiators on the scaffolds and growing the zwitterionic polymer from the scaffold surface. SI-ATRP from electrospun fibers[303,304] and 3D printed constructs[305] have been reported. However, the solvents used for polymerization may not be optimal for the fibers. In view of this, the IGTs developed in this dissertation could be directly employed in the preparation of cell-compatible polymer scaffolds for tissue engineering. IGT hydrogels can be directly used for creating fibers using electrohydrodynamic (EHD) jetting. As a proof of concept, IGT fibers from a 33 wt% water solution of IGT was prepared (Figure 5.1(a)). In the future, 3D jet writing,[306] a modified electrospinning process, could be used to generate 3D structures consisting of IGT. The full exploration of IGT in its ability to form scaffolds could lead to a range of biomedical applications including 3D cell culture platform, cancer biology, and stem cell biotechnology.

(a) 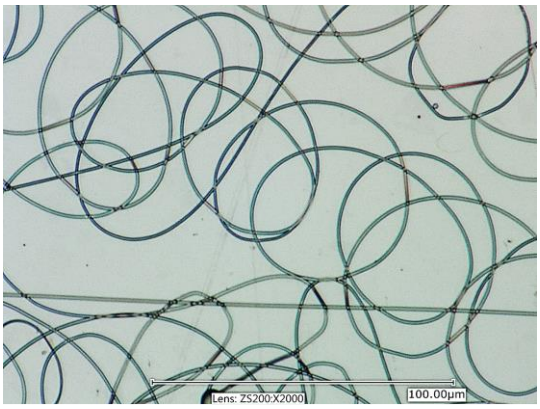

(b) 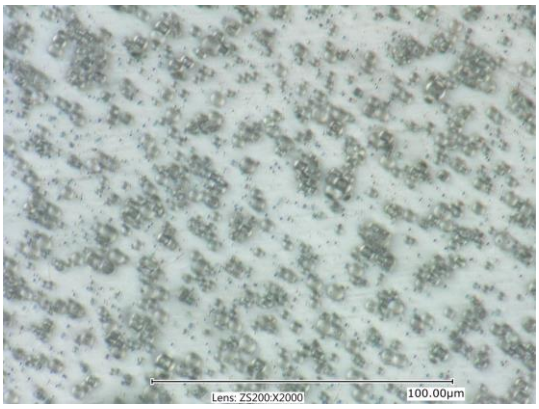

Figure 5.1: Optical images of the (a) as-jetted IGT fibers and (b) as-jetted IGT particles

In yet another perspective, the IGTs could also be jetted as microparticles (Figure 5.1(b)). The use of zwitterionic microparticles holds great therapeutic potential as drug carriers.[307] The drug could be covalently bound to functional group present in IGT through a pH sensitive linkage.

Currently, the physical and thermodynamic behavior of the tethered IGT chains is being investigated by molecular dynamics (MD) simulations to understand the molecular conformation of the polymer at the molecular level. MD simulations have been used to investigate the behavior of zwitterionic surfactants in aqueous solutions.[308] Hence, MD simulations could shed light on the relationship between IGT brush parameters and the surrounding environment. Simulating the physiological environment could show the gel architectures that the brushes would assume in that environment. This could lead to a better understanding of how the brushes influence the adhesion and proliferation of hPSC.

IGT also could be conjugated to complex architectures found in nature, as in proteins (Figure 5.2). Polymer-protein conjugates are crucial in therapeutic protein formulation design including vaccine formulations, antibody-drug conjugates, etc.[309,310] The central benzaldehyde aldehyde moiety can be replaced with more reactive biocompatible groups such as N-hydroxysuccinimide (NHS), pentafluorophenyl (PFP) esters, or maleimide groups for more efficient protein conjugation.[311] Alternatively, IGT could serve as zwitterionic coatings on nanoparticles (Figure 5.2). Nanoparticles represent highly promising platforms for the development of diagnostic and therapeutic agents, including multi-modal imaging agents or theranostics.[312]

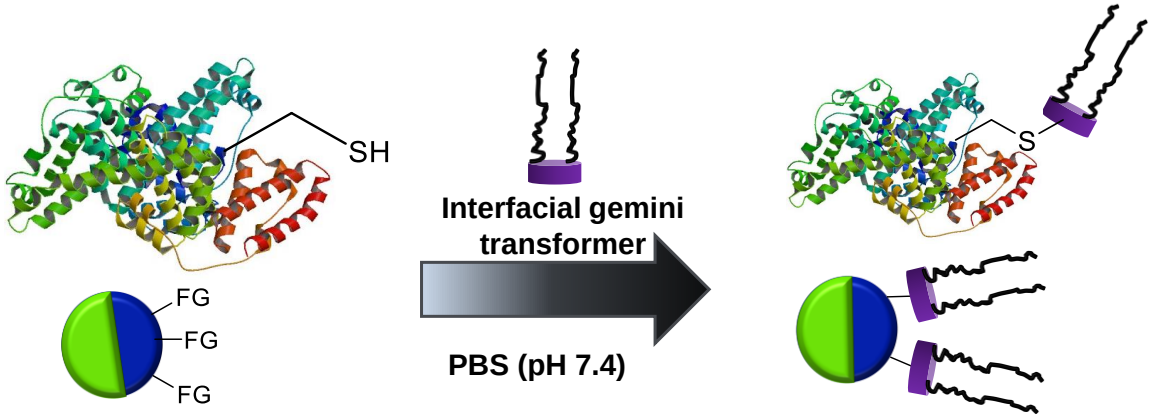

Figure 5.2: Schematic representing the potential conjugation of interfacial gemini transformer to the free cysteine (CYS-34) residue of bovine serum albumin (BSA) and surface functionalized particles. FG = Functional group.

A major challenge to their development and clinical translation, however, is the fact that many opsonized nanoparticles accumulate in the liver and spleen as a result of phagocytic cell scavenging system.[313] Zwitterionic IGT could be conjugated to bicompartmental anisotropic particles generated by EHD co-jetting which could make them more viable for biological applications and reduce the rate of non-specific adsorption of proteins and lipids to the particle surface. Moreover, *in vivo* studies have demonstrated that particles with zwitterionic coating have extended circulatory lifetimes. The anisotropic particles in itself allows the possible incorporation of multiple therapeutics – and polymers – in selected compartments and can result in distinct release profiles for each therapeutic.[314] IGT coatings on such particles could be a potential carrier system for drug delivery.

One unique feature of polymers synthesized by RAFT polymerization is the presence of a thiocarbonylthio group at the end of the polymer chain, which can be modified to an alkene, thiol, or a dienophile.[315] The RAFT end group of the zwitterionic polymers synthesized by RAFT polymerization in solution as discussed in Section 4.5, could be modified and further used to orthogonally immobilize them on vapor-based reactive coatings. This would be an alternative to circumvent the use of organic solvents and initiators for the preparation of IGT-type polymers as described in Section 4.4. In addition, as RAFT polymerization is performed in water and does not require toxic components, this approach is relevant for applications in the biological regime.

LIST OF TABLES

LIST OF FIGURES

LIST OF SCHEMES

LIST OF ABBREVIATIONS

2D	2-dimensional
3D	Three-dimensional
ξ	Zeta
APMAAm	Aminopropylmethacrylamide
a.u.	Arbitrary unit
AFM	Atomic force microscopy
ATRP	Atom transfer radical polymerization
ATR	Attenuated total reflection
bFGF	Basic fibroblast growth factor
Bpy	2,2´-Bipyridine
BSA	Bovine serum albumin
C_P	Cloud point
CTA	Chain transfer agent
CVD	Chemical vapor deposition
Đ	Dispersity
D_2O	Deuterium oxide
DAPI	4´,6-diamidino-2-phenylindole
DP	Degree of polymerization
D-PBS	Dulbecco's phosphate buffered saline
DCM	Dichloromethane

DEPT	Distortionless enhancement by polarization transfer
E	Elasticity
EB	Embryoid body
EBiB	Ethyl 2-bromoisobutyrate
ECM	Extracellular matrix
EDTA	Ethylenediaminetetraacetic acid
EHD	Electrohydrodynamic
EtOAc	Ethyl acetate
Eq.	Equation
GMP	Good manufacturing practice
FBS	Fetal bovine serum
F_e	External force
FGF	Fibroblast growth factor
F_i	Internal force
FITC	Fluorescein-5-isothiocyanate
^{1}H NMR	Proton nuclear magnetic spectroscopy
HCCM	Human-cell-conditioned medium
Hz	Hertz
HEMA	2-hydroxymethacrylate
hESC	Human embryonic stem cell
hMSC	Human mesenchymal stem cell
hPSC	Human pluripotent stem cell
HSC	Hematopoietic stem cell
IGT	Interfacial Gemini transformer
iPSC	Induced pluripotent stem cell

IRRAS	Infrared refection-absorption spectroscopy
K_{ATRP}	ATRP equilibrium constant
k_{act}	Activation rate constant
k_{deact}	Deactivation rate constant
k_p	Propagation rate constant
k_t	Termination rate constant
KE	Kinetic energy
L	End-to-end distance
LB	Langmuir-Blodgett
LbL	Layer-by-layer
LCST	Lower critical solution temperature
LN	Laminin
M	Monomer (unless it is a unit)
Mbar	Millibar
MEF	Mouse embryonic feeder cells
MEDSAH	[2-(Methacryloyloxy)ethyl]dimethyl-(3-sulfopropyl)ammonium hydroxide
MEM	Minimal essential medium
µCP	Microcontact printing
mg	milligram
MHz	megahertz
mL	Millilter
MD	Molecular dynamics
mmol	Millimol
min	minutes
M_n	Number average molecular weight

$M_{n,th}$	Theoretical molecular weight
M_w	Weight average molecular weight
Me_6TREN	Tris[2-(dimethylamino)-ethyl]amine
NaCl	Sodium chloride
NHS	N-hydroxysuccinimide
NMP	Nitroxide-mediated radical polymerization
NMR	Nuclear Magnetic Resonance Spectroscopy
Oct4	Octamer-binding transcription factor 4
PBS	Phosphate buffered saline
PCP	[2.2]paracyclophane
PDMS	Polydimethylsiloxane
PE	Phycoerythrin
PEG	Poly(ethylene glycol)
PEGMA	Poly(ethylene glycol) methacrylate
PEO	Poly(ethylene oxide)
PFP	Pentafluorophenyl
PMEDSAH	Poly[2-(methacryloyloxy)ethyl dimethyl-(3-sulfopropyl)ammonium hydroxide]
P_n•	Polymeric radical
ppm	Parts per million
R_G	Radius of gyration
RAFT	Reversible addition-fragmentation chain transfer
RDRP	Reversible deactivation radical process
RGD	Arginylglycylaspartic acid
R_h	Hydrodynamic radius
RMS	root-mean-square

SEC	Size exclusion chromatography
SEM	Standard error mean
SD	Standard deviation
SDS-PAGE	Sodium dodecyl sulfate polyacrylamide gel electrophoresis
TCPS	Tissue culture polystyrene
TGF-ß	Tissue Growth Factor-ß
TLC	Thin layer chromatography
TMS	Tetramethylsilane
ToF-SIMS	Time-of-flight secondary ion mass spectrometry
UCB	Umbilical cord blood
UCST	Upper critical solution temperature
VDP	Vapor deposition polymerization
WCA	Water contact angle
XPS	X-ray photoelectron spectroscopy

BIBLIOGRAPHY

1. Thomson, J. A. *et al.* Embryonic Stem Cell Lines Derived from Human Blastocysts. *Science* **282**, 1145–1147 (1998).
2. Reubinoff, B. E., Pera, M. F., Fong, C. Y., Trounson, A. & Bongso, A. Embryonic stem cell lines from human blastocysts: somatic differentiation in vitro. *Nat. Biotechnol.* **18**, 399–404 (2000).
3. Takahashi, K. *et al.* Induction of Pluripotent Stem Cells from Adult Human Fibroblasts by Defined Factors. *Cell* **131**, 861–872 (2007).
4. Lindvall, O., Kokaia, Z. & Martinez-Serrano, A. Stem cell therapy for human neurodegenerative disorders-how to make it work. *Nat. Med.* **10**, S42–S50 (2004).
5. Schulz, T. C. *et al.* A scalable system for production of functional pancreatic progenitors from human embryonic stem cells. *PLoS One* **7**, (2012).
6. *Global Stem Cells Market Size, Market Share, Application Analysis, Regional Outlook, Growth Trends, Key Players, Competitive Strategies and Forecasts, 2017 to 2025*. (2017).
7. Serra, M., Brito, C., Correia, C. & Alves, P. M. Process engineering of human pluripotent stem cells for clinical application. *Trends Biotechnol.* **30**, 350–359 (2012).
8. Kirkeby, A. *et al.* Predictive Markers Guide Differentiation to Improve Graft Outcome in Clinical Translation of hESC-Based Therapy for Parkinson's Disease. *Cell Stem Cell* **20**, 135–148 (2017).
9. Ross, A. M., Nandivada, H., Ryan, A. L. & Lahann, J. Synthetic substrates for long-term stem cell culture. *Polymer* **53**, 2533–2539 (2012).
10. Chen, W. L., Cordero, R., Tran, H. & Ober, C. K. 50th Anniversary Perspective: Polymer Brushes: Novel Surfaces for Future Materials. *Macromolecules* **50**, 4089–4113 (2017).

11. Deng, X., Friedmann, C. & Lahann, J. Bio-orthogonal 'double-click' chemistry based on multifunctional coatings. *Angew. Chemie - Int. Ed.* **50**, 6522–6526 (2011).

12. Sumerlin, B. S. & Vogt, A. P. Macromolecular engineering through click chemistry and other efficient transformations. *Macromolecules* **43**, 1–13 (2010).

13. Villa-Diaz, L. G. *et al.* Synthetic polymer coatings for long-term growth of human embryonic stem cells. *Nat. Biotechnol.* **28**, 581–3 (2010).

14. Villa-Diaz, L. G. *et al.* Derivation of mesenchymal stem cells from human induced pluripotent stem cells cultured on synthetic substrates. *Stem Cells* **30**, 1174–1181 (2012).

15. Mei, Y. *et al.* Combinatorial development of biomaterials for clonal growth of human pluripotent stem cells. *Nat Mat* **9**, 768–778 (2010).

16. Biehl, J. K. & Russell, B. Introduction to Stem Cell Therapy. *J. Cardiovasc. Nurs.* **24**, 98–103 (2009).

17. Lutolf, M. P., Gilbert, P. M. & Blau, H. M. Designing materials to direct stem-cell fate. *Nature* **462**, 433–441 (2009).

18. Bryder, D., Rossi, D. J. & Weissman, I. L. Hematopoietic stem cells: The paradigmatic tissue-specific stem cell. *Am. J. Pathol.* **169**, 338–346 (2006).

19. Broxmeyer, H. E. *et al.* Growth characteristics and expansion of human umbilical cord blood and estimation of its potential for transplantation in adults. *Proc. Natl. Acad. Sci. USA* **89**, 4109–13 (1992).

20. Ertl, P., Sticker, D., Charwat, V., Kasper, C. & Lepperdinger, G. Lab-on-a-chip technologies for stem cell analysis. *Trends Biotechnol.* **32**, 245–253 (2014).

21. Villa-Diaz, L. G. *et al.* Analysis of the Factors that Limit the Ability of Feeder Cells to Maintain the Undifferentiated State of Human Embryonic Stem Cells. *Stem Cells Dev.* **18**, 641–651 (2009).

22. Chen, K. G., Mallon, B. S., McKay, R. D. G. & Robey, P. G. Human Pluripotent Stem Cell Culture: Considerations for Maintenance, Expansion, and Therapeutics. *Cell Stem Cell* **14**, 13–26 (2014).

23. Xu, C. *et al.* Feeder-free growth of undifferentiated human embryonic stem cells. *Nat.*

Biotechnol. **19**, 971–974 (2001).

24. McDevitt, T. & Palecek, S. Innovation in the Culture and Derivation of Pluirpotent Human Stem Cells. *Curr Opin Biotechnlol* **19**, 527–533 (2008).

25. Hovatta, O. *et al.* A culture system using human foreskin fibroblasts as feeder cells allows production of human embryonic stem cells. *Hum. Reprod.* **18**, 1404–1409 (2003).

26. Ma, X., Li, H., Xin, S., Ma, Y. & Ouyang, T. Human amniotic fluid stem cells support undifferentiated propagation and pluripotency of human embryonic stem cell without b-FGF in a density dependent manner. *Int. J. Clin. Exp. Pathol.* **7**, 4661–4673 (2014).

27. Hwang, S. T. *et al.* The expansion of human ES and iPS cells on porous membranes and proliferating human adipose-derived feeder cells. *Biomaterials* **31**, 8012–8021 (2010).

28. Martin, M. J., Muotri, A., Gage, F. & Varki, A. Human embryonic stem cells express an immunogenic nonhuman sialic acid. *Nat. Med.* **11**, 228–232 (2005).

29. Villa-Diaz, L. G., Ross, A. M., Lahann, J. & Krebsbach, P. H. Concise review: The evolution of human pluripotent stem cell culture: From feeder cells to synthetic coatings. *Stem Cells* **31**, 1–7 (2013).

30. Azarin, S. M. & Palecek, S. P. Development of scalable culture systems for human embryonic stem cells. *Biochem. Eng. J.* **48**, 378–384 (2010).

31. Vining, K. H. & Mooney, D. J. Mechanical forces direct stem cell behaviour in development and regeneration. *Nat. Rev. Mol. Cell Biol.* **18**, 728–742 (2017).

32. Higuchi, A. *et al.* Polymeric design of cell culture materials that guide the differentiation of human pluripotent stem cells. *Prog. Polym. Sci.* **65**, 83–126 (2017).

33. Jarvelainen, H., Sainio, A., Koulu, M., Wight, T. N. & Penttinen, R. Extracellular Matrix Molecules: Potential Targets in Pharmacotherapy. *Pharmacol. Rev.* **61**, 198–223 (2009).

34. Morrison, S. J. & Spradling, A. C. Stem cells and niches : mechanisms that promote stem cell maintenance throughout life. *Cell* **132**, 598–611 (2008).

35. Frantz, C., Stewart, K. M. & Weaver, V. M. The extracellular matrix at a glance. *J. Cell Sci.* **123**, 4195–4200 (2010).

36. Capozza, R. *et al.* Cell Membrane Disruption by Vertical Micro-/Nanopillars: Role of Membrane Bending and Traction Forces. *ACS Appl. Mater. Interfaces* **10**, 29107–29114 (2018).

37. Dalby, M. J. *et al.* The control of human mesenchymal cell differentiation using nanoscale symmetry and disorder. *Nat. Mater.* **6**, 997–1003 (2007).

38. Ross, A. M., Jiang, Z., Bastmeyer, M. & Lahann, J. Physical aspects of cell culture substrates: Topography, roughness, and elasticity. *Small* **8**, 336–355 (2012).

39. Hynes, R. O. Integrins: Bidirectional, allosteric signaling machines. *Cell* **110**, 673–687 (2002).

40. Dalby, M. J. *et al.* Nanomechanotransduction and interphase nuclear organization influence on genomic control. *J. Cell. Biochem.* **102**, 1234–1244 (2007).

41. Moore, S. W., Keller, R. E. & Koehl, M. A. R. The dorsal involuting marginal zone stiffens anisotropically during its convergent extension in the gastrula of Xenopus laevis. *Development* **121**, 3131–3140 (1995).

42. Yeung, T. *et al.* Effects of substrate stiffness on cell morphology, cytoskeletal structure, and adhesion. *Cell Motil. Cytoskeleton* **60**, 24–34 (2005).

43. Goetzke, R., Sechi, A., De Laporte, L., Neuss, S. & Wagner, W. Why the impact of mechanical stimuli on stem cells remains a challenge. *Cell. Mol. Life Sci.* **75**, 3297–3312 (2018).

44. Trappmann, B. *et al.* Extracellular-matrix tethering regulates stem-cell fate. *Nat. Mater.* **11**, 642–649 (2012).

45. Gerecht, S. *et al.* The effect of actin disrupting agents on contact guidance of human embryonic stem cells. *Biomaterials* **28**, 4068–4077 (2007).

46. Underwood, P. A., Steele, J. G. & Dalton, B. A. Effects of polystyrene surface-chemistry on the biological-activity of solid-phase fibronectin and vitronectin, analyzed with monoclonal-antibodies. *J. Cell Sci.* **104**, 793–803 (1993).

47. Anderson, D. G., Levenberg, S. & Langer, R. Nanoliter-scale synthesis of arrayed biomaterials and application to human embryonic stem cells. *Nat. Biotechnol.* **22**, 863–866

(2004).

48. Takebe, J., Champagne, C. M., Offenbacher, S., Ishibashi, K. & Cooper, L. F. Titanium surface topography alters cell shape and modulates bone morphogenetic protein 2 expression in the J774A.1 macrophage cell line. *J. Biomed. Mater. Res.* **64A**, 207–216 (2003).

49. Refai, A. K., Textor, M., Brunette, D. M. & Waterfield, J. D. Effect of titanium surface topography on macrophage activation and secretion of proinflammatory cytokines and chemokines. *J. Biomed. Mater. Res. - Part A* **70**, 194–205 (2004).

50. Huang, S. & Ingber, D. E. The structural and mechanical complexity of cell-growth control. *Nat. Cell Biol.* **1**, E131–E138 (1999).

51. Xu, R. H. *et al.* Basic FGF and suppression of BMP signaling sustain undifferentiated proliferation of human ES cells. *Nat. Methods* **2**, 185–190 (2005).

52. Chadwick, K. *et al.* Cytokines and BMP-4 promote hematopoietic differentiation of human embryonic stem cells. *Blood* **102**, 906–915 (2003).

53. Park, K. S. TGF-beta family signaling in embryonic stem cells. *Int. J. Stem Cells* **4**, 18–23 (2011).

54. Li, Y., Powell, S., Brunette, E., Lebkowski, J. & Mandalam, R. Expansion of human embryonic stem cells in defined serum-free medium devoid of animal-derived products. *Biotechnol. Bioeng.* **91**, 688–698 (2005).

55. Yao, S. *et al.* Long-term self-renewal and directed differentiation of human embryonic stem cells in chemically defined conditions. *Proc. Natl. Acad. Sci. USA* **103**, 6907–12 (2006).

56. Lu, J., Hou, R., Booth, C. J., Yang, S.-H. & Snyder, M. Defined culture conditions of human embryonic stem cells. *Proc. Natl. Acad. Sci. USA* **103**, 5688–5693 (2006).

57. Hoss, M. *et al.* Integrin α 4 impacts on differential adhesion of preadipocytes and stem cells on synthetic polymers. *J. Tissue Eng. Regen. Med.* **7**, 312–323 (2013).

58. Kim, M. H. & Kino-oka, M. Switching between self-renewal and lineage commitment of human induced pluripotent stem cells via cell-substrate and cell-cell interactions on a dendrimer-immobilized surface. *Biomaterials* **35**, 5670–5678 (2014).

59. Meng, Y. *et al.* Characterization of integrin engagement during defined human embryonic stem cell culture. *FASEB J.* **24**, 1056–1065 (2010).

60. Ludwig, T. E. *et al.* Derivation of human embryonic stem cells in defined conditions. *Nat. Biotechnol.* **24**, 185–187 (2006).

61. Peppas, N. & Langer, R. New challenges in biomaterials. *Science* **263**, 1715–1720 (1994).

62. Lewis, A. L., Tolhurst, L. A. & Stratford, P. W. Analysis of a phosphorylcholine-based polymer coating on a coronary stent pre- and post-implantation. *Biomaterials* **23**, 1697–1706 (2002).

63. Ganet, F. *et al.* Development of a smart guide wire using an electrostrictive polymer: Option for steerable orientation and force feedback. *Sci. Rep.* **5**, 1–12 (2015).

64. Jiang, S. & Cao, Z. Ultralow-Fouling, Functionalizable, and Hydrolyzable Zwitterionic Materials and Their Derivatives for Biological Applications. *Adv. Mater.* **22**, 920–932 (2010).

65. Madl, C. M. & Heilshorn, S. C. Engineering Hydrogel Microenvironments to Recapitulate the Stem Cell Niche. *Annu. Rev. Biomed. Eng.* **20**, 21–47 (2018).

66. Hubbell, J. A. Biomaterials in tissue engineering. *Bio/technology* **13**, 565–576 (1995).

67. Ostuni, E., Chapman, R. G., Holmlin, R. E., Takayama, S. & Whitesides, G. M. A survey of structure-property relationships of surfaces that resist the adsorption of protein. *Langmuir* **17**, 5605–5620 (2001).

68. Jeon, S. I., Lee, J. H., Andrade, J. D. & De Gennes, P. G. Protein-surface interactions in the presence of polyethylene oxide. I. Simplified theory. *J. Colloid Interface Sci.* **142**, 149–158 (1991).

69. Hern, D. L. & Hubbell, J. A. Incorporation of adhesion peptides into nonadhesive hydrogels useful for tissue resurfacing. *J. Biomed. Mater. Res.* **39**, 266–276 (1997).

70. Hamburger, R., Azaz, E. & Donbrow, M. Autoxidation of polyoxyethylenic non-ionic surfactants and of polyethylene glycols. *Pharm. Acta Helv.* **50**, 10–7 (1975).

71. Lowe, S., O'Brien-Simpson, N. M. & Connal, L. A. Antibiofouling polymer interfaces: poly(ethylene glycol) and other promising candidates. *Polym. Chem.* **6**, 198–212 (2015).

72. Benhabbour, S. R., Sheardown, H. & Adronov, A. Protein Resistance of PEG-Functionalized Dendronized Surfaces: Effect of PEG Molecular Weight and Dendron Generation. *Macromolecules* **41**, 4817–4823 (2008).

73. Hlídková, H., Kotelnikov, I., Pop-Georgievski, O., Proks, V. & Horák, D. Antifouling Peptide Dendrimer Surface of Monodisperse Magnetic Poly(glycidyl methacrylate) Microspheres. *Macromolecules* **50**, 1302–1311 (2017).

74. Mrabet, B. *et al.* Anti-fouling poly(2-hydoxyethyl methacrylate) surface coatings with specific bacteria recognition capabilities. *Surf. Sci.* **603**, 2422–2429 (2009).

75. Zhang, Z., Chao, T., Chen, S. & Jiang, S. Superlow fouling sulfobetaine and carboxybetaine polymers on glass slides. *Langmuir* **22**, 10072–10077 (2006).

76. He, Y., Hower, J., Chen, S. & Bernards, M. Molecular simulation studies of protein interactions with zwitterionic phosphorylcholine self-assembled monolayers in the presence of water. *Langmuir* **22**, 10358–10364 (2008).

77. Higaki, Y. *et al.* Effect of Charged Group Spacer Length on Hydration State in Zwitterionic Poly(sulfobetaine) Brushes. *Langmuir* **33**, 8404–8412 (2017).

78. Georgiev, G. *et al.* Electrostimulated shift of the precipitation temperature of aqueous polyzwitterionic solutions. *Macromol. Symp.* **210**, 393–401 (2004).

79. Sin, M. C., Sun, Y. M. & Chang, Y. Zwitterionic-based stainless steel with well-defined polysulfobetaine brushes for general bioadhesive control. *ACS Appl. Mater. Interfaces* **6**, 861–873 (2014).

80. Cheng, N., Brown, A. A., Azzaroni, O. & Huck, W. T. S. Thickness-dependent properties of polyzwitterionic brushes. *Macromolecules* **41**, 6317–6321 (2008).

81. Sin, M.-C., Chen, S.-H. & Chang, Y. Hemocompatibility of zwitterionic interfaces and membranes. *Polym. J.* **46**, 436–443 (2014).

82. Moelbert, S. & De Los Rios, P. Hydrophobic interaction model for upper and lower critical solution temperatures. *Macromolecules* **36**, 5845–5853 (2003).

83. Chang, Y. *et al.* Dual-thermoresponsive phase behavior of blood compatible zwitterionic copolymers containing nonionic poly(N-isopropyl acrylamide). *Biomacromolecules* **10**,

2092–2100 (2009).

84. Milner, S., Witten, T. & Cates, M. Theory of the grafted polymer brush. *Macromolecules* **21**, 2610–2619 (1988).

85. Schmaljohann, D. Thermo- and pH-responsive polymers in drug delivery. *Adv. Drug Deliv. Rev.* **58**, 1655–1670 (2006).

86. Singh, N. K. & Lee, D. S. In situ gelling pH- and temperature-sensitive biodegradable block copolymer hydrogels for drug delivery. *J. Control. Release* **193**, 214–227 (2014).

87. Chang, Y., Chen, S., Zhang, Z. & Jiang, S. Highly protein-resistant coatings from well-defined diblock copolymers containing sulfobetaines. *Langmuir* **22**, 2222–2226 (2006).

88. Chen, S., Zheng, J., Li, L. & Jiang, S. Strong resistance of phosphorylcholine self-assembled monolayers to protein adsorption: Insights into nonfouling properties of zwitterionic materials. *J. Am. Chem. Soc.* **127**, 14473–14478 (2005).

89. Yancey, P. H., Clark, M. E., Hand, S. C., Bowlus, R. D. & Somero, G. N. Living with Water Stress : Evolution of Osmolyte Systems. *Science* **217**, 1214–1222 (1982).

90. Zhang, Z., Chen, S. & Jiang, S. Dual-functional biomimetic materials: Nonfouling poly(carboxybetaine) with active functional groups for protein immobilization. *Biomacromolecules* **7**, 3311–3315 (2006).

91. Ladd, J., Zhang, Z., Chen, S., Hower, J. C. & Jiang, S. Zwitterionic polymers exhibiting high resistance to nonspecific protein adsorption from human serum and plasma. *Biomacromolecules* **9**, 1357–1361 (2008).

92. Huxtable, R. J. Physiological actions of taurine. *Physiol. Rev.* **72**, 101–163 (1992).

93. Bernards, M. T., Cheng, G., Zhang, Z. & Chen, S. Nonfouling Polymer Brushes via Surface-Initiated, Two-Component Atom Transfer Radical Polymerization. *Macromolecules* **41**, 4216–4219 (2008).

94. Chang, Y. *et al.* A highly stable nonbiofouling surface with well-packed grafted zwitterionic polysulfobetaine for plasma protein repulsion. *Langmuir* **24**, 5453–5458 (2008).

95. Liaw, D., Lee, W. & Whung, Y. A. Aqueous Solution Properties of Poly[3-Dimethyl (Methacryloyloxyethyl) Ammonium Propane Sulfonate. *J. Appl. Polym. Sci.* **34**, 999–1011

(1987).

96. Azzaroni, O., Brown, A. A. & Huck, W. T. S. UCST Wetting Transitions of Polyzwitterionic Brushes Driven by Self-Association. *Angew. Chemie Int. Ed.* **45**, 1770–1774 (2006).

97. Zhu, Y., Noy, J.-M., Lowe, A. B. & Roth, P. J. The synthesis and aqueous solution properties of sulfobutylbetaine (co)polymers: comparison of synthetic routes and tuneable upper critical solution temperatures. *Polym. Chem.* **6**, 5705–5718 (2015).

98. Lowe, A. B., Billingham, N. C. & Armes, S. P. Synthesis and properties of low-polydispersity poly(sulfopropylbetaine)s and their block copolymers. *Macromolecules* **32**, 2141–2148 (1999).

99. Willcock, H. *et al.* One-pot synthesis of responsive sulfobetaine nanoparticles by RAFT polymerisation: the effect of branching on the UCST cloud point. *Polym. Chem.* **5**, 1023–1030 (2014).

100. Lee, W. F. & Chen, C. F. Poly(2-hydroxyethyl methacrylate-co-sulfobetaine) hydrogels. II. Synthesis and swelling behaviors of the [2-hydroxyethyl methacrylate-co-3-dimethyl (methacryloyloxyethyl) ammonium propane sulfonate] hydrogels. *J. Appl. Polym. Sci.* **69**, 2021–2034 (1998).

101. Han, D., Letteri, R., Chan-Seng, D., Emrick, T. & Tu, H. Examination of zwitterionic polymers and gels subjected to mechanical constraints. *Polymer* **54**, 2887–2894 (2013).

102. Kasák, P., Kroneková, Z., Krupa, I. & Lacík, I. Zwitterionic hydrogels crosslinked with novel zwitterionic crosslinkers: Synthesis and characterization. *Polymer* **52**, 3011–3020 (2011).

103. Qian, X., Villa-Diaz, L. G., Kumar, R., Lahann, J. & Krebsbach, P. H. Enhancement of the propagation of human embryonic stem cells by modifications in the gel architecture of PMEDSAH polymer coatings. *Biomaterials* **35**, 9581–90 (2014).

104. Kirouac, D. C. & Zandstra, P. W. The Systematic Production of Cells for Cell Therapies. *Cell Stem Cell* **3**, 369–381 (2008).

105. McKee, C. & Chaudhry, G. R. Advances and challenges in stem cell culture. *Colloids*

Surfaces B Biointerfaces **159**, 62–77 (2017).

106. Klim, J. R., Li, L., Wrighton, P. J., Piekarczyk, M. S. & Kiessling, L. L. A defined glycosaminoglycan-binding substratum for human pluripotent stem cells. *Nat. Methods* **7**, 989–994 (2010).

107. Rodin, S. *et al.* Clonal culturing of human embryonic stem cells on laminin-521/E-cadherin matrix in defined and xeno-free environment. *Nat. Commun.* **5**, 1–13 (2014).

108. Chen, A. K.-L., Chen, X., Lim, Y. M., Reuveny, S. & Oh, S. K. W. Inhibition of ROCK–Myosin II Signaling Pathway Enables Culturing of Human Pluripotent Stem Cells on Microcarriers Without Extracellular Matrix Coating. *Tissue Eng. Part C Methods* **20**, 227–238 (2014).

109. Chen, A. K. L., Chen, X., Choo, A. B. H., Reuveny, S. & Oh, S. K. W. Critical microcarrier properties affecting the expansion of undifferentiated human embryonic stem cells. *Stem Cell Res.* **7**, 97–111 (2011).

110. Leino, M. *et al.* Human embryonic stem cell dispersion in electrospun PCL fiber scaffolds by coating with laminin-521 and E-cadherin-Fc. *J. Biomed. Mater. Res. - Part B Appl. Biomater.* **106**, 1226–1236 (2018).

111. Gao, S. Y. *et al.* Modeling the adhesion of human embryonic stem cells to poly(lactic- co -glycolic acid) surfaces in a 3D environment. *J. Biomed. Mater. Res. Part A* **92A**, 683–692 (2010).

112. Kim, I. G. *et al.* Mechanotransduction of human pluripotent stem cells cultivated on tunable cell-derived extracellular matrix. *Biomaterials* **150**, 100–111 (2018).

113. Morris, A. H., Stamer, D. K. & Kyriakides, T. R. The host response to naturally-derived extracellular matrix biomaterials. *Semin. Immunol.* **29**, 72–91 (2017).

114. Derda, R. *et al.* Defined Substrates for Human Embryonic Stem Cell Growth Identified from Surface Arrays. *ACS Chem. Biol.* **2**, 347–355 (2007).

115. Klimanskaya, I. *et al.* Human embryonic stem cells derived without feeder cells. *Lancet* **365**, 1636–1641 (2005).

116. Gerecht, S. *et al.* Hyaluronic acid hydrogel for controlled self-renewal and differentiation

of human embryonic stem cells. *Proc. Natl. Acad. Sci.* **104**, 11298–11303 (2007).

117. Baker, B. M. & Chen, C. S. Deconstructing the third dimension – how 3D culture microenvironments alter cellular cues. *J. Cell Sci.* **125**, 3015–3024 (2012).

118. Khetan, S. *et al.* Degradation-mediated cellular traction directs stem cell fate in covalently crosslinked three-dimensional hydrogels. *Nat. Mater.* **12**, 458–465 (2013).

119. Hughes, C. S., Postovit, L. M. & Lajoie, G. A. Matrigel: a complex protein mixture required for optimal growth of cell culture. *Proteomics* **10**, 1886–1890 (2010).

120. Miyazaki, T. *et al.* Laminin E8 fragments support efficient adhesion and expansion of dissociated human pluripotent stem cells. *Nat. Commun.* **3**, 1210–1236 (2012).

121. Braam, S. R. *et al.* Recombinant Vitronectin Is a Functionally Defined Substrate That Supports Human Embryonic Stem Cell Self-Renewal via αVβ5 Integrin. *Stem Cells* **26**, 2257–2265 (2008).

122. Higuchi, A. *et al.* Long-term xeno-free culture of human pluripotent stem cells on hydrogels with optimal elasticity. *Sci. Rep.* **5**, 1–16 (2015).

123. Chang, C.-W. *et al.* Engineering cell–material interfaces for long-term expansion of human pluripotent stem cells. *Biomaterials* **34**, 912–921 (2013).

124. Amit, M., Shariki, C. & Margulets, V. Feeder Layer- and Serum-Free Culture of Human Embryonic Stem Cells. *Biol. Reprod.* **70**, 837–845 (2004).

125. Hughes, C. S., Radan, L., Betts, D., Postovit, L. M. & Lajoie, G. A. Proteomic analysis of extracellular matrices used in stem cell culture. *Proteomics* **11**, 3983–3991 (2011).

126. Brafman, D. *et al.* Long-term human pluripotent stem cell self-renewal on synthetic polymer surfaces. *Biomaterials* **31**, 9135–9144 (2010).

127. Irwin, E. F., Gupta, R., Dashti, D. C. & Healy, K. E. Engineered polymer-media interfaces for the long-term self-renewal of human embryonic stem cells. *Biomaterials* **32**, 6912–6919 (2011).

128. Mohr, J. C., de Pablo, J. J. & Palecek, S. P. 3-D microwell culture of human embryonic stem cells. *Biomaterials* **27**, 6032–6042 (2006).

129. Love, J. C., Estroff, L. a., Kriebel, J. K., Nuzzo, R. G. & Whitesides, G. M. Self-Assembled Monolayers of Thiolates on Methals as a Form of Nanotechnology. *Chem. Rev.* **105**, 1103–1169 (2005).

130. Arima, Y. & Iwata, H. Effect of wettability and surface functional groups on protein adsorption and cell adhesion using well-defined mixed self-assembled monolayers. *Biomaterials* **28**, 3074–3082 (2007).

131. Mahapatro, A. *et al.* Surface modification of functional self-assembled monolayers on 316L stainless steel via lipase catalysis. *Langmuir* **22**, 901–905 (2006).

132. Langmuir, I. & Schaefer, V. J. The Effect of Dissolved Salts on Insoluble Monolayers. *J. Am. Chem. Soc.* **59**, 2400–2414 (1937).

133. Blodgett, K. B. Films Built by Depositing Successive Monomolecular Layers on a Solid Surface. *J. Am. Chem. Soc.* **57**, 1007–1022 (1935).

134. Roberts, G. *Langmuir-Blodgett Films*. (Kluwer Academic, 1990).

135. Ulman, A. *An Introduction to Ultrathin Organic Films Academic*. (Academic Press, 1991).

136. Peterson, I. R. Langmuir-Blodgett films. *J. Phys. D. Appl. Phys.* **23**, 379–395 (1990).

137. Erokhin, V. *Handbook of Thin Film Materials*. (Academic, 2002).

138. Crawford, N. F. & Leblanc, R. M. Serum albumin in 2D: A Langmuir monolayer approach. *Adv. Colloid Interface Sci.* **207**, 131–138 (2014).

139. Tang, Z., Wang, Y., Podsiadlo, P. & Kotov, N. A. Biomedical applications of layer-by-layer assembly: From biomimetics to tissue engineering. *Adv. Mater.* **18**, 3203–3224 (2006).

140. Keeney, M. *et al.* Nanocoating for biomolecule delivery using layer-by-layer self-assembly. *J. Mater. Chem. B* **3**, 8757–8770 (2015).

141. Lvov, Y., Decher, G. & Sukhorukov, G. Assembly of thin films by means of successive deposition of alternate layers of DNA and poly(allylamine). *Macromolecules* **26**, 5396–5399 (1993).

142. Carlsson, J.-O. & Martin, P. M. *Handbook of Deposition Technologies for Films and Coatings*. (Elsevier, 2010).

143. Gleason, K. K. *CVD Polymers: Fabrication of Organic Surfaces and Devices*. (Wiley-VCH: Weinheim, Germany, 2015).

144. Coclite, A. M. *et al.* 25th Anniversary Article: CVD polymers: A new paradigm for surface modification and device fabrication. *Adv. Mater.* **25**, 5392–5423 (2013).

145. Alf, M. E. *et al.* Chemical vapor deposition of conformal, functional, and responsive polymer films. *Adv. Mater.* **22**, 1993–2027 (2010).

146. Vaddiraju, S., Seneca, K. & Gleason, K. K. Novel strategies for the deposition of -COOH functionalized conducting copolymer films and the assembly of inorganic nanoparticles on conducting polymer platforms. *Adv. Funct. Mater.* **18**, 1929–1938 (2008).

147. Kim, J., Kwon, S., Han, S. & Min, Y. Nanofilms based on vapor deposition of polymerized polypyrrole and its characteristics. *Jpn. J. Appl. Phys.* **43**, 5660 (2004).

148. Chen, H. Y. & Lahann, J. Designable biointerfaces using vapor-based reactive polymers. *Langmuir* **27**, 34–48 (2010).

149. Gorham, W. F. A New, General Synthetic Method for the Preparation of Linear Poly-p-xylylenes. *J. Polym. Sci. Part A-1 Polym. Chem.* **4**, 3027–3039 (1966).

150. Lahann, J., Choi, I. S., Lee, J., Jensen, K. F. & Langer, R. A new method toward microengineered surfaces based on reactive coating. *Angew. Chemie - Int. Ed.* **40**, 3166–3169 (2001).

151. Lahann, J., Höcker, H. & Langer, R. Synthesis of Amino[2.2]paracyclophanes - Beneficial Monomers for Bioactive Coating of Medical Implant Materials. *Angew. Chemie - Int. Ed.* **40**, 726–728 (2001).

152. Elkasabi, Y., Chen, H.-Y. & Lahann, J. Multipotent Polymer Coatings Based on Chemical Vapor Deposition Copolymerization. *Adv. Mater.* **18**, 1521–1526 (2006).

153. Lahann, J., Klee, D. & Hocker, H. Chemical vapour deposition polymerization of substituted [2.2]paracyclophanes. *Macromol. Rapid Commun.* **19**, 441–444 (1998).

154. Hopf, H. *et al.* Metal-Containing Poly(p-xylylene) Films by CVD: Poly(p-xylylene) with Germanium Crystals. *Chem. Vap. Depos.* **3**, 197–200 (1997).

155. Gerasimov, G. N. *et al.* Ge- and Sn-containing poly (p-xylylene): synthesis , structure and

thermal behavior. *Macromol. Chem. Phys.* **199**, 2179–2184 (1998).

156. Popova, E. *et al.* New monomers for organometallic poly-p-xylylenes: Synthesis of silyl-, germyl- and stannyl[2.2]paracyclophane derivatives. *Eur. J. Inorg. Chem.* 1733–1737 (1998).

157. Kratzer, D. Synthese neuer zwitterionischer Methacrylate und deren Anwendungen in oberflächeninitiierten Polymerisationen. (Karlsruhe Institute of Technology, 2015).

158. Chen, H. Y. *et al.* Substrate-independent dip-pen nanolithography based on reactive coatings. *J. Am. Chem. Soc.* **132**, 18023–18025 (2010).

159. Lahann, J. & Langer, R. Novel poly(p-xylylenes): Thin films with tailored chemical and optical properties. *Macromolecules* **35**, 4380–4386 (2002).

160. Lahann, J. Reactive polymer coatings for biomimetic surface engineering. *Chem. Eng. Commun.* **193**, 1457–1468 (2006).

161. Gołda, M., Brzychczy-Włoch, M., Faryna, M., Engvall, K. & Kotarba, A. Oxygen plasma functionalization of parylene C coating for implants surface: Nanotopography and active sites for drug anchoring. *Mater. Sci. Eng. C* **33**, 4221–4227 (2013).

162. Cieślik, M. *et al.* Parylene coatings on stainless steel 316L surface for medical applications - Mechanical and protective properties. *Mater. Sci. Eng. C* **32**, 31–35 (2012).

163. Dorozhkin, S. V. Calcium orthophosphate coatings on magnesium and its biodegradable alloys. *Acta Biomater.* **10**, 2919–2934 (2014).

164. Tan, C. P. & Craighead, H. G. Surface Engineering and Patterning Using Parylene for Biological Applications. *Materials* **3**, 1803–1832 (2010).

165. Stuart, M. A. C. *et al.* Emerging applications of stimuli-responsive polymer materials. *Nat. Mater.* **9**, 101–113 (2010).

166. Jiang, X., Chen, H. Y., Galvan, G., Yoshida, M. & Lahann, J. Vapor-based initiator coatings for atom transfer radical polymerization. *Adv. Funct. Mater.* **18**, 27–35 (2008).

167. Venkidasubramonian, G. *et al.* Surface-initiated RAFT polymerization from vapor-based polymer coatings. *Polymer* **150**, (2018).

168. Jenkins, A. D., Jones, R. G. & Moad, G. Terminology for reversible-deactivation radical polymerization previously called ‘controlled’ radical or ‘living’ radical polymerization (IUPAC Recommendations 2010). *Pure Appl. Chem.* **82**, 483–491 (2010).

169. Braunecker, W. A. & Matyjaszewski, K. Controlled/living radical polymerization: Features, developments, and perspectives. *Prog. Polym. Sci.* **32**, 93–146 (2007).

170. Greszta, D., Mardare, D. & Matyjaszewski, K. “Living” Radical Polymerization. 1. Possibilities and Limitations. *Macromolecules* **27**, 638–644 (1994).

171. Fischer, H. The Persistent Radical Effect: A Principle for Selective Radical Reactions and Living Radical Polymerizations. *Chem. Rev.* **101**, 3581–3610 (2001).

172. Perrier, S. 50th Anniversary Perspective: RAFT Polymerization - A User Guide. *Macromolecules* **50**, 7433–7447 (2017).

173. Huang, X. & Wirth, M. J. Surface-initiated radical polymerization on porous silica. *Anal. Chem.* **69**, 4577–4580 (1997).

174. Azzaroni, O. & Szleifer, I. *Polymer and Biopolymer Brushes : for Materials Science and Biotechnology*. (John Wiley and Sons, 2018).

175. Wang, J. S. & Matyjaszewski, K. Controlled/"Living" Radical Polymerization. Halogen Atom Transfer Radical Polymerization Promoted by a Cu(I)/Cu(II) Redox Process. *Macromolecules* **28**, 7901–7910 (1995).

176. Matyjaszewski, K. Atom Transfer Radical Polymerization (ATRP): Current status and future perspectives. *Macromolecules* **45**, 4015–4039 (2012).

177. Fairbanks, B. D., Gunatillake, P. A. & Meagher, L. Biomedical applications of polymers derived by reversible addition - fragmentation chain-transfer (RAFT). *Adv. Drug Deliv. Rev.* **91**, 141–152 (2015).

178. Rizzardo, E. & Solomon, D. H. On the origins of nitroxide mediated polymerization (NMP) and reversible addition fragmentation chain transfer (RAFT). *Aust. J. Chem.* **65**, 945–969 (2012).

179. Chiefari, J. *et al.* Living Free-Radical Polymerization by Reversible Addition−Fragmentation Chain Transfer: The RAFT Process. *Macromolecules* **31**, 5559–

5562 (1998).

180. Georges, M. K., Veregin, R. P. N., Kazmaier, P. M. & Hamer, G. K. Narrow Molecular Weight Resins by a Free-Radical Polymerization Process. *Macromolecules* **26**, 2987–2988 (1993).

181. Hawker, C. J., Bosman, A. W. & Harth, E. New Polymer Synthesis by Nitroxide Mediated Living Radical Polymerizations. *Chem. Rev.* **101**, 3661–3688 (2001).

182. Kocak, G., Tuncer, C. & Bütün, V. pH-Responsive polymers. *Polym. Chem.* **8**, 144–176 (2017).

183. Boyes, S. G. *et al.* Polymer brushes - Surface immobilized polymers. *Surf. Sci.* **570**, 1–12 (2004).

184. Lemieux, M. *et al.* Reorganization of Binary Polymer Brushes: Reversible Switching of Surface Microstructures and Nanomechanical Properties. *Macromolecules* **36**, 7244–7255 (2003).

185. Hong, S. C. *et al.* Polyolefin graft copolymers via living polymerization techniques: Preparation of poly(n-butyl acrylate)-graft-polyethylene through the combination of Pd-mediated living olefin polymerization and atom transfer radical polymerization. *J. Polym. Sci. Part A Polym. Chem.* **40**, 2736–2749 (2002).

186. Minisci, F. Free-Radical Additions to Olefins in the Presence of Redox Systems. *Acc. Chem. Res.* **8**, 165–171 (1975).

187. Taylor, M. J. W., Eckenhoff, W. T. & Pintauer, T. Copper-catalyzed atom transfer radical addition (ATRA) and cyclization (ATRC) reactions in the presence of environmentally benign ascorbic acid as a reducing agent. *Dalt. Trans.* **39**, 11475–11482 (2010).

188. Hui, C. M. *et al.* Surface-Initiated Polymerization as an Enabling Tool for Multifunctional (Nano-)Engineered Hybrid Materials. *Chem. Mater.* **26**, 745–762 (2014).

189. Kato, M., Kamigaito, M., Sawamoto, M. & Higashimura, T. Polymerization of Methyl Methacrylate with the Carbon Tetrachloride/Dichlorotris-(triphenylphosphine)ruthenium(II)/ Methylaluminum Bis(2,6-di-tert-butylphenoxide) Initiating System: Possibility of Living Radical Polymerization. *Macromolecules* **28**, 1721–

1723 (1995).

190. Di Lena, F. & Matyjaszewski, K. Transition metal catalysts for controlled radical polymerization. *Prog. Polym. Sci.* **35**, 959–1021 (2010).

191. Grimaud, T. & Matyjaszewski, K. Controlled/"Living" Radical Polymerization of Methyl Methacrylate by Atom Transfer Radical Polymerization. *Macromolecules* **30**, 2216–2218 (1997).

192. Fischer, H. The Persistent Radical Effect in Controlled Radical. *J. Polym. Sci. Part A Polym. Chem.* **37**, 1885–1901 (1999).

193. Xiao, D. & Wirth, M. J. Kinetics of surface-initiated atom transfer radical polymerization of acrylamide on silica. *Macromolecules* **35**, 2919–2925 (2002).

194. Tang, W. *et al.* Understanding Atom Transfer Radical Polymerization: Effect of Ligand and Initiator Structures on the Equilibrium Constants. *J. Am. Chem. Soc.* **130**, 10702–10713 (2008).

195. Matyjaszewski, K. & Xia, J. Atom transfer radical polymerization. *Chem. Rev.* **101**, 2921–2990 (2001).

196. Xia, J., Zhang, X. & Matyjaszewski, K. Atom transfer radical polymerization of 4-vinylpyridine. *Macromolecules* **32**, 3531–3533 (1999).

197. Matyjaszewski, K., Mu Jo, S., Paik, H. & Gaynor, S. G. Synthesis of Well-Defined Polyacrylonitrile by Atom Transfer Radical Polymerization. *Macromolecules* **30**, 6398–6400 (1997).

198. Teodorescu, M. & Matyjaszewski, K. Controlled polymerization of (meth)acrylamides by atom transfer radical polymerization. *Macromol. Rapid Commun.* **21**, 190–194 (2000).

199. Göbelt, B. & Matyjaszewski, K. Diimino- and diaminopyridine complexes of CuBr and FeBr2as catalysts in atom transfer radical polymerization (ATRP). *Macromol. Chem. Phys.* **201**, 1619–1624 (2000).

200. Matyjaszewski, K., Göbelt, B., Paik, H. J. & Horwitz, C. P. Tridentate nitrogen-based ligands in Cu-based ATRP: A structure-activity study. *Macromolecules* **34**, 430–440 (2001).

201. Zhang, Y. *et al.* Copper-mediated CRP of methyl acrylate in the presence of metallic copper: Effect of ligand structure on reaction kinetics. *Macromolecules* **45**, 78–86 (2012).

202. Boyer, C. *et al.* Copper-Mediated Living Radical Polymerization (Atom Transfer Radical Polymerization and Copper(0) Mediated Polymerization): From Fundamentals to Bioapplications. *Chem. Rev.* **116**, 1803–1949 (2016).

203. Zhou, D., Gao, X., Wang, W. & Zhu, S. Termination of Surface Radicals and Kinetic Modeling of ATRP Grafting from Flat Surfaces by Addition of Deactivator. *Macromolecules* **45**, 1198–1207 (2012).

204. von Werne, T. & Patten, T. E. Atom transfer radical polymerization from nanoparticles: A tool for the preparation of well-defined hybrid nanostructures and for understanding the chemistry of controlled/"living" radical polymerizations from surfaces. *J. Am. Chem. Soc.* **123**, 7497–7505 (2001).

205. Lele, B. S., Murata, H., Matyjaszewski, K. & Russell, A. J. Synthesis of uniform protein-polymer conjugates. *Biomacromolecules* **6**, 3380–3387 (2005).

206. Carlmark, A. & Malmström, E. Atom transfer radical polymerization from cellulose fibers at ambient temperature. *J. Am. Chem. Soc.* **124**, 900–901 (2002).

207. Matyjaszewski, K., Dong, H., Jakubowski, W., Pietrasik, J. & Kusumo, A. Grafting from Surfaces for “Everyone”: ARGET ATRP in the Presence of Air. *Langmuir* **23**, 4528–4531 (2007).

208. Discekici, E. H. *et al.* Simple Benchtop Approach to Polymer Brush Nanostructures Using Visible-Light-Mediated Metal-Free Atom Transfer Radical Polymerization. *ACS Macro Lett.* **5**, 258–262 (2016).

209. Beuermann, S. *et al.* Critically evaluated rate coefficients for free-radical polymerization, 2.. Propagation rate coefficients for methyl methacrylate. *Macromol. Chem. Phys.* **198**, 1545–1560 (1997).

210. Moad, G., Rizzardo, E. & Thang, S. H. Living radical polymerization by the RAFT process. *Aust. J. Chem.* **58**, 379–410 (2005).

211. Moad, G. RAFT polymerization to form stimuli-responsive polymers. *Polym. Chem.* **8**,

177–219 (2017).

212. Chiefari, J. *et al.* Thiocarbonylthio Compounds (SC(Z)S−R) in Free Radical Polymerization with Reversible Addition-Fragmentation Chain Transfer (RAFT Polymerization). Effect of the Activating Group Z. *Macromolecules* **36**, 2273–2283 (2003).

213. Barner-kowollik, C. *Handbook of RAFT Polymerization*. (Wiley-VCH, 2008).

214. Zoppe, J. O. *et al.* Surface-Initiated Controlled Radical Polymerization: State-of-the-Art, Opportunities, and Challenges in Surface and Interface Engineering with Polymer Brushes. *Chem. Rev.* **117**, 1105–1318 (2017).

215. Pirri, G., Chiari, M., Damin, F. & Meo, A. Microarray glass slides coated with block copolymer brushes obtained by reversible addition chain-transfer polymerization. *Anal. Chem.* **78**, 3118–3124 (2006).

216. Moraes, J., Ohno, K., Gody, G., Maschmeyer, T. & Perrier, S. The synthesis of well-defined poly(vinylbenzyl chloride)-grafted nanoparticles via RAFT polymerization. *Beilstein J. Org. Chem.* **9**, 1226–1234 (2013).

217. Stenzel, M. H., Zhang, L. & Huck, W. T. S. Temperature-responsive glycopolymer brushes synthesized via RAFT polymerization using the Z-group approach. *Macromol. Rapid Commun.* **27**, 1121–1126 (2006).

218. Günay, K. A., Schüwer, N. & Klok, H. A. Synthesis and post-polymerization modification of poly(pentafluorophenyl methacrylate) brushes. *Polym. Chem.* **3**, 2186 (2012).

219. Zamfir, M. *et al.* Controlled growth of protein resistant PHEMA brushes via S-RAFT polymerization. *J. Mater. Chem. B* **1**, 6027 (2013).

220. Zengin, A. & Caykara, T. RAFT-mediated synthesis of poly[(oligoethylene glycol) methyl ether acrylate] brushes for biological functions. *J. Polym. Sci. Part A Polym. Chem.* **50**, 4443–4450 (2012).

221. Islam, M. R., Bach, L. G., Vo, T. S., Tran, T. N. & Lim, K. T. Nondestructive chemical functionalization of MWNTs by poly(2- dimethylaminoethyl methacrylate) and their conjugation with CdSe quantum dots: Synthesis, properties, and cytotoxicity studies. *Appl. Surf. Sci.* **286**, 31–39 (2013).

222. Grande, C. D. *et al.* Grafting of polymers from electrodeposited macro-RAFT initiators on conducting surfaces. *React. Funct. Polym.* **71**, 938–942 (2011).

223. Ye, Y. S. *et al.* Versatile grafting approaches to star-shaped POSS-containing hybrid polymers using RAFT polymerization and click chemistry. *Chem. Commun.* **47**, 10656 (2011).

224. Huang, X. *et al.* Synthesis of Hetero-Polymer Functionalized Nanocarriers by Combining Surface-Initiated ATRP and RAFT Polymerization. *Small* **8**, 3579–3583 (2012).

225. McDonald, J. C. & Whitesides, G. M. Poly(dimethylsiloxane) as a material for fabricating microfluidic devices. *Acc. Chem. Res.* **35**, 491–499 (2002).

226. Lahann, J. Vapor-based polymer coatings for potential biomedical applications. *Polym. Int.* **55**, 1361–1370 (2006).

227. Nandivada, H., Chen, H. Y. & Lahann, J. Vapor-based synthesis of poly[(4-formyl-p-xylylene)-co-(p-xylylene)] and its use for biomimetic surface modifications. *Macromol. Rapid Commun.* **26**, 1794–1799 (2005).

228. Nandivada, H. *et al.* Fabrication of synthetic polymer coatings and their use in feeder-free culture of human embryonic stem cells. *Nat. Protoc.* **6**, 1037–1043 (2011).

229. Young, T. An Essay on the Cohesion of Fluids. *Philos. Trans. R. Soc. London* **95**, 65–87 (1805).

230. Watts, J. F. & Wolstenholme, J. *An Introduction to Surface Analysis by XPS and AES*. (Wiley, 2005).

231. Heide, P. V. d. *X-Ray Photoelectron Spectroscopy: An Introduction to Principles and Practices*. (John Wiley & Sons, Ltd, 2011).

232. O'Connor, D. J., Sexton, B. A. & Smart, R. S. C. *Surface Analysis Methods in Materials Science*. **23**, (Springer-Verlag, 1992).

233. Scofield, J. H. Hartree-Slater subshell photoionization cross-sections at 1254 and 1487 eV. *J. Electron Spectros. Relat. Phenomena* **8**, 129–132 (1976).

234. Parry, K. L. *et al.* ARXPS characterisation of plasma polymerised surface chemical gradients. *Surf. Interface Anal.* **38**, 1497–1504 (2006).

235. Barlow, A. J. *et al.* Chemically specific identification of carbon in XPS imaging using Multivariate Auger Feature Imaging (MAFI). *Carbon* **107**, 190–197 (2016).

236. Muramoto, S., Brison, J. & Castner, D. G. Exploring the Surface Sensitivity of TOF-Secondary Ion Mass Spectrometry by Measuring the Implantation and Sampling Depths of Bin and C60 Ions in Organic Films. *Anal. Chem.* **84**, 365–372 (2012).

237. Vickerman, J. C. & Briggs, D. *ToF-SIMS: Materials Analysis by Mass Spectrometry*. (IM Publications LLP and Surface Spectra Limited, Chichester, 2013).

238. Belu, A. M., Graham, D. J. & Castner, D. G. Time-of-flight secondary ion mass spectrometry: Techniques and applications for the characterization of biomaterial surfaces. *Biomaterials* **24**, 3635–3653 (2003).

239. Benninghoven, A. Chemical Analysis of Inorganic and Organic Surfaces and Thin Films by Static Time-of-Flight Secondary Ion Mass Spectrometry (TOF-SIMS). *Angew. Chem. Int. Ed. Engl.* **33**, 1023–1043 (1994).

240. Hofmann, J. P., Rohnke, M. & Weckhuysen, B. M. Recent advances in secondary ion mass spectrometry of solid acid catalysts: Large zeolite crystals under bombardment. *Phys. Chem. Chem. Phys.* **16**, 5465–5474 (2014).

241. Kumar, R., Kopyeva, I., Cheng, K., Liu, K. & Lahann, J. Examining Nanoparticle Adsorption on Electrostatically "Patchy" Glycopolymer Brushes Using Real-Time ζ-Potential Measurements. *Langmuir* **33**, 6322–6332 (2017).

242. Krajewski, A., Malavolti, R. & Piancastelli, A. Albumin adhesion on some biological and non-biological glasses and connection with their Z-potentials. *Biomaterials* **17**, 53–60 (1996).

243. Abramson, H. A. Electrokinetic phenomena and their application to biology and medicine. *J. Phys. Chem.* **38**, 1128–1129 (1934).

244. Roessler, S., Zimmermann, R., Scharnweber, D., Werner, C. & Worch, H. Characterization of oxide layers on Ti6Al4V and titanium by streaming potential and streaming current measurements. *Colloids Surfaces B Biointerfaces* **26**, 387–395 (2002).

245. Cai, K. *et al.* Surface functionalized titanium thin films: Zeta-potential, protein adsorption

and cell proliferation. *Colloids Surfaces B Biointerfaces* **50**, 1–8 (2006).

246. Walker, S. L., Bhattacharjee, S., Hoek, E. M. V. & Elimelech, M. A novel asymmetric clamping cell for measuring streaming potential of flat surfaces. *Langmuir* **18**, 2193–2198 (2002).

247. Werner, C., Zimmermann, R. & Kratzmüller, T. Streaming potential and streaming current measurements at planar solid/liquid interfaces for simultaneous determination of zeta potential and surface conductivity. *Colloids Surfaces A Physicochem. Eng. Asp.* **192**, 205–213 (2001).

248. Topal, T. *et al.* Acoustic Tweezing Cytometry Induces Rapid Initiation of Human Embryonic Stem Cell Differentiation. *Sci. Rep.* **8**, 1–11 (2018).

249. McCloy, R. A. *et al.* Partial inhibition of Cdk1 in G2phase overrides the SAC and decouples mitotic events. *Cell Cycle* **13**, 1400–1412 (2014).

250. Burgess, A. *et al.* Loss of human Greatwall results in G2 arrest and multiple mitotic defects due to deregulation of the cyclin B-Cdc2/PP2A balance. *Proc. Natl. Acad. Sci.* **107**, 12564–12569 (2010).

251. Schmittgen, T. D. & Livak, K. J. Analyzing real-time PCR data by the comparative CT method. *Nat. Protoc.* **3**, 1101–1108 (2008).

252. Musah, S. *et al.* Glycosaminoglycan-Binding Hydrogels Enable Mechanical Control of Human Pluripotent Stem Cell Self-Renewal. *ACS Nano* **6**, 10168–10177 (2012).

253. Gattazzo, F., Urciuolo, A. & Bonaldo, P. Extracellular matrix: A dynamic microenvironment for stem cell niche. *Biochim. Biophys. Acta* **1840**, 2506–2519 (2014).

254. Wang, Y.-K. & Chen, C. S. Cell adhesion and mechanical stimulation in the regulation of mesenchymal stem cell differentiation. *J. Cell. Mol. Med.* **17**, 823–832 (2013).

255. Kleinman, H. K. & Martin, G. R. Matrigel: Basement membrane matrix with biological activity. *Semin. Cancer Biol.* **15**, 378–386 (2005).

256. Caliari, S. R. & Burdick, J. A. A practical guide to hydrogels for cell culture. *Nat. Methods* **13**, 405–414 (2016).

257. Kolhar, P., Kotamraju, V. R., Hikita, S. T., Clegg, D. O. & Ruoslahti, E. Synthetic surfaces

for human embryonic stem cell culture. *J. Biotechnol.* **146**, 143–146 (2010).

258. Chen, W. *et al.* Nanotopography influences adhesion, spreading, and self-renewal of Human embryonic stem cells. *ACS Nano* **6**, 4094–4103 (2012).

259. Sun, Y. *et al.* Mechanics regulates fate decisions of human embryonic stem cells. *PLoS One* **7**, 1–7 (2012).

260. Pyun, J., Kowalewski, T. & Matyjaszewski, K. Synthesis of Polymer Brushes Using Atom Transfer Radical Polymerization. *Macromol. Rapid Commun.* **24**, 1043–1059 (2003).

261. Husseman, M. *et al.* Controlled Synthesis of Polymer Brushes by 'Living' Free Radical Polymerization Techniques. *Macromolecules* **32**, 1424–1431 (1999).

262. Kratzer, D., Barner, L., Friedmann, C., Bräse, S. & Lahann, J. A Synthetic Route to Sulfobetaine Methacrylates with Varying Charge Distance. *European J. Org. Chem.* **2014**, 8064–8071 (2014).

263. Li, G. *et al.* Ultra low fouling zwitterionic polymers with a biomimetic adhesive group. *Biomaterials* **29**, 4592–4597 (2008).

264. Kuang, J. & Messersmith, P. B. Universal surface-initiated polymerization of antifouling zwitterionic brushes using a mussel-mimetic peptide initiator. *Langmuir* **28**, 7258–7266 (2012).

265. Ratner, B. D., Hoffman, A. S., Schoen, F. J. & Lemons, J. E. *Biomaterials Science*. *Biomaterials Science - An Introduction to Materials in Medicine* (Academic Press, 1996).

266. Tsujii, Y., Ejaz, M., Sato, K., Goto, A. & Fukuda, T. Mechanism and kinetics of RAFT-mediated graft polymerization of styrene on a solid surface. 1. Experimental evidence of surface radical migration. *Macromolecules* **34**, 8872–8878 (2001).

267. Gabler, C. *et al.* Corrosion properties of ammonium based ionic liquids evaluated by SEM-EDX, XPS and ICP-OES. *Green Chem.* **13**, 2869 (2011).

268. Moulder, J. F., Stickle, W. F., Sobol, P. E. & Bomben, K. D. *Handbook of X-ray Photoelectron Spectroscopy*. (Eden Prarie (MN), 1992).

269. Azzaroni, O. Polymer brushes here, there, and everywhere: Recent advances in their practical applications and emerging opportunities in multiple research fields. *J. Polym. Sci.*

Part A Polym. Chem. **50**, 3225–3258 (2012).

270. Huang, J. *et al.* Nonleaching Antibacterial Glass Surfaces via “Grafting Onto”: The Effect of the Number of Quaternary Ammonium Groups on Biocidal Activity. *Langmuir* **24**, 6785–6795 (2008).

271. Edmondson, S., Osborne, V. L. & Huck, W. T. S. Polymer brushes via surface-initiated polymerizations. *Chem. Soc. Rev.* **33**, 14–22 (2004).

272. Zhao, B. & Brittain, W. J. Polymer brushes : surface-immobilized macromolecules. **25**, 677–710 (2000).

273. Farrell, E. & Brousseau, J. *Guide for DLS sample preparation from Brookhaven instruments*. *Brookhaven Instruments*

274. Schulz, D. N. *et al.* Phase behaviour and solution properties of sulphobetaine polymers. *Polymer* **27**, 1734–1742 (1986).

275. Bally-Le Gall, F. *et al.* Co-immobilization of biomolecules on ultrathin reactive chemical vapor deposition coatings using multiple click chemistry strategies. *ACS Appl. Mater. Interfaces* **5**, 9262–8 (2013).

276. Hermanson, G. T. *Bioconjugation Techniques*. (Academic Press, 2013).

277. Starck, P. *et al.* Surface chemistry and rheology of polysulfobetaine-coated silica. *Langmuir* **23**, 7587–7593 (2007).

278. Tan, K. Y., Gautrot, J. E. & Huck, W. T. S. Formation of Pickering emulsions using ion-specific responsive colloids. *Langmuir* **27**, 1251–1259 (2010).

279. Ramstedt, M. *et al.* Synthesis and Characterization of Poly (3-Sulfopropylmethacrylate) Brushes for Potential Antibacterial Applications. *Langmuir* **23**, 3314–3321 (2007).

280. Tan, K. Y. *et al.* Decoupling geometrical and chemical cues directing epidermal stem cell fate on polymer brush-based cell micro-patterns. *Integr. Biol.* **5**, 899 (2013).

281. Elkasabi, Y. *et al.* Partially fluorinated poly-p-xylylenes synthesized by CVD polymerization. *Chem. Vap. Depos.* **15**, 142–149 (2009).

282. Chen, H. Y., Elkasabi, Y. & Lahann, J. Surface modification of confined microgeometries

via vapor-deposited polymer coatings. *J. Am. Chem. Soc.* **128**, 374–380 (2006).

283. Schmid, H. & Michel, B. Siloxane polymers for high-resolution, high-accuracy soft lithography. *Macromolecules* **33**, 3042–3049 (2000).

284. Wu, J., Lin, W., Wang, Z., Chen, S. & Chang, Y. Investigation of the hydration of nonfouling material poly(sulfobetaine methacrylate) by low-field nuclear magnetic resonance. *Langmuir* **28**, 7436–7441 (2012).

285. Gang Cheng, Zheng Zhang, Shenfu Chen, James D. Bryers, and S. J. Inhibition of Bacterial Adhesion and Biofilm Formation on Zwitterionic Surfaces. *Biomaterials* **28**, 4192–4199 (2007).

286. Zhang, Z. *et al.* Polysulfobetaine-grafted surfaces as environmentally benign ultralow fouling marine coatings. *Langmuir* **25**, 13516–13521 (2009).

287. Vickerman, J. C., Briggs, D. & Henderson, A. *Static SIMS Library*. (SurfaceSpectra Ltd., 2012).

288. Siegwart, D. J., Oh, J. K. & Matyjaszewski, K. ATRP in the design of functional materials for biomedical applications. *Prog. Polym. Sci.* **37**, 18–37 (2012).

289. Lowe, A. B. & McCormick, C. L. Synthesis and solution properties of zwitterionic polymers. *Chem. Rev.* **102**, 4177–4189 (2002).

290. Donovan, M. S., Sumerlin, B. S., Lowe, A. B. & McCormick, C. L. Controlled/"living" polymerization of sulfobetaine monomers directly in aqueous media via RAFT. *Macromolecules* **35**, 8663–8666 (2002).

291. Bhuchar, N., Deng, Z., Ishihara, K. & Narain, R. Detailed study of the reversible addition-fragmentation chain transfer polymerization and co-polymerization of 2-methacryloyloxyethyl phosphorylcholine. *Polym. Chem.* **2**, 632–639 (2011).

292. Valdebenito, A. & Encinas, M. V. Effect of solvent on the free radical polymerization of N,N-dimethylacrylamide. *Polym. Int.* **59**, 1246–1251 (2010).

293. Huglin, M. B. & Radwan, M. a. Properties of poly[N-2-(methyacryloyloxy)ethyl-N,N-dimethyl- N-3-sulfopropylammonium betaine] in dilute solution. *Makromol. Chem.* **192**, 2433–2445 (1991).

294. Villa-Diaz, L. G., Kim, J. K., Lahann, J. & Krebsbach, P. H. Derivation and long-term culture of transgene-free human induced pluripotent stem cells on synthetic substrates. *Stem Cells Transl. Med.* **3**, 1410–1417 (2014).

295. Ross, A. M. Biomolecular Interactions with Synthetic Surfaces. (2012).

296. Haruta, Y. & Seon, B. K. Distinct human leukemia-associated cell surface glycoprotein GP160 defined by monoclonal antibody SN6. *Proc. Natl. Acad. Sci.* **83**, 7898–7902 (1986).

297. Nakano, A., Harada, T., Morikawa, S. & Kato, Y. Expression of Leukocyte Common Antigen (CD45) on Various Human Leukemia/Lymphoma Cell Lines. *Pathol. Int.* **40**, 107–115 (1990).

298. O'Connor, M. D. *et al.* Alkaline Phosphatase-Positive Colony Formation Is a Sensitive, Specific, and Quantitative Indicator of Undifferentiated Human Embryonic Stem Cells. *Stem Cells* **26**, 1109–1116 (2008).

299. Hoffman, L. M. & Carpenter, M. K. Characterization and culture of human embryonic stem cells. *Nat. Biotechnol.* **23**, 699–708 (2005).

300. Villa-Diaz, L. G., Kim, J. K., Laperle, A., Palecek, S. P. & Krebsbach, P. H. Inhibition of Focal Adhesion Kinase Signaling by Integrin α6β1 Supports Human Pluripotent Stem Cell Self-Renewal. *Stem Cells* **34**, 1753–1764 (2016).

301. Evans, N. D. *et al.* Substrate stiffness affects early differentiation events in embryonic stem cells. *Eur. Cells Mater.* **18**, 1–13 (2009).

302. Przybyla, L., Lakins, J. N. & Weaver, V. M. Tissue Mechanics Orchestrate Wnt-Dependent Human Embryonic Stem Cell Differentiation. *Cell Stem Cell* **19**, 462–475 (2016).

303. Ameringer, T. *et al.* Surface grafting of electrospun fibers using ATRP and RAFT for the control of biointerfacial interactions. *Biointerphases* **8**, 1–11 (2013).

304. Higaki, Y., Kobayashi, M., Hirai, T. & Takahara, A. Direct polymer brush grafting to polymer fibers and films by surface-initiated polymerization. *Polym. J.* **50**, 101–108 (2018).

305. Wang, X. *et al.* I3DP, a robust 3D printing approach enabling genetic post-printing surface modification. *Chem. Commun.* **49**, 10064–10066 (2013).

306. Jordahl, J. H. *et al.* 3D Jet Writing: Functional Microtissues Based on Tessellated Scaffold

Architectures. *Adv. Mater.* **30**, 1–9 (2018).

307. Cai, M. *et al.* Colloids and Surfaces B : Biointerfaces Synthesis of amphiphilic copolymers containing zwitterionic sulfobetaine as pH and redox responsive drug carriers. *Colloids Surfaces B Biointerfaces* **126**, 1–9 (2015).

308. Xu, Y., Guo, S., Mao, X. & Feng, J. Molecular simulation study on the self-assembly behaviors of zwitterionic heterogemini surfactant in aqueous solution. *J. Dispers. Sci. Technol.* **39**, 443–451 (2018).

309. Duncan, R., Ringsdorf, H. & Satchi-Fainaro, R. Polymer therapeutics - Polymers as drugs, drug and protein conjugates and gene delivery systems: Past, present and future opportunities. *J. Drug Target.* **14**, 337–341 (2006).

310. Greenwald, R. B., Choe, Y. H., McGuire, J. & Conover, C. D. Effective drug delivery by PEGylated drug conjugates. *Adv. Drug Deliv. Rev.* **55**, 217–250 (2003).

311. Lockett, M. R., Phillips, M. F., Jarecki, J. L., Peelen, D. & Smith, L. M. A tetrafluorophenyl activated ester self-assembled monolayer for the immobilization of amine-modified oligonucleotides. *Langmuir* **24**, 69–75 (2008).

312. Bejarano, J. *et al.* Nanoparticles for diagnosis and therapy of atherosclerosis and myocardial infarction: evolution toward prospective theranostic approaches. *Theranostics* **8**, 4710–4732 (2018).

313. García, K. P. *et al.* Zwitterionic-Coated "Stealth" Nanoparticles for Biomedical Applications: Recent Advances in Countering Biomolecular Corona Formation and Uptake by the Mononuclear Phagocyte System. *Small* **10**, 2516–2529 (2014).

314. Rahmani, S., Park, T.-H., Dishman, A. F. & Lahann, J. Multimodal delivery of irinotecan from microparticles with two distinct compartments. *J. Control. Release* **172**, 239–245 (2013).

315. Willcock, H. & O'Reilly, R. K. End group removal and modification of RAFT polymers. *Polym. Chem.* **1**, 149–157 (2010).